Title

Development of Chemical Mechanisms for Predictions of Ozone and Secondary Organic Aerosol Formation From Biomass Burning-Derived Precursors

Author

Jiang, Jia

Publication Date

2021

UNIVERSITY OF CALIFORNIA
RIVERSIDE

Development of Chemical Mechanisms for Predictions of Ozone and Secondary Organic Aerosol Formation From Biomass Burning-Derived Precursors

A dissertation submitted in partial satisfaction
of the requirements for the degree of

Doctor of Philosophy

in

Chemical and Environmental Engineering

by

Jia Jiang

December 2021

Dissertation Committee:
  Dr. Kelley C. Barsanti, Chairperson
  Dr. David R. Cocker III
  Dr. Matthew J. Alvarado

The Dissertation of Jia Jiang is approved:

Committee Chairperson

University of California, Riverside

Acknowledgements

I was fortunate to have many people who supported and encouraged me during my five years of graduate study. I must thank them all for getting me here.

I would like to express my sincerest gratitude to my advisor, Dr. Kelley Barsanti for her guidance and support during my Ph.D. study. Kelley is enthusiastic about her work, and her passion in research has always inspired me to move forward in my own development. She helped me build critical thinking and problem-solving skills, as well as how to work as part of a team. Everything that I've learned from her will benefit me forever. Kelley is not only a fantastic mentor but also a friend I can trust. I'm grateful for the opportunity to be her student.

I would like to thank Dr. William Carter for training me on the SAPRC modeling system. His extensive experience and expertise in gas-phase chemical mechanism development has helped me accomplish a lot and be able to finish this dissertation. He is very knowledgeable and has been extremely patient with all my questions. I truly respect him and enjoy working with him.

I would like to thank Dr. David Cocker for leading me into the world of atmospheric chemistry. I have worked with him and his group on several projects, and I really appreciated his support. I would also like to acknowledge my dissertation committee, Dr. Matthew Alvarado for the valuable feedback and suggestions.

I would like to thank my colleague Qi Li for working together with me in the

camphene SOA study and running all the chamber experiments. We had lots of interesting discussions when we were writing the paper. I would like to thank Dr. Isaac Afreh for his contribution in this project as well. I must acknowledge my other collaborators: Dr. John Orlando, Dr. Julia Lee-Taylor, Dr. Louisa Emmons, Dr. Frank Flocke, Dr. Kirk Baker, Dr. Robert Strongin, Dr. Jiries Meehan-Atrash and Dr. Benjamin Brown-Steiner. It’s my pleasure to work with them.

I am also thankful to Isaac and Dr. Christos Stamatis, for being wonderful colleagues and friends, and giving me so much help in both research and life. Thanks to my other group members: Dr. Lindsay Hatch, Dr. Avi Lav, Dr. Paul Van Rooy, Dr. Laura Kiely, William Lichtenberg, Samiha Binte Shahid, Afsara Tasnia and Guadalupe Lara. Thanks to Dr. Cesunica Ivey, Dr. Don Collins, Dr. Jiacheng Yang, Dr. Xinze Peng, Dr. Weihan Peng, and Chen Le for their assistance and advice.

Special thanks also go to my funding sources, the National Science Foundation grant AGS-1753364, the National Oceanic and Atmospheric Administration grant AC4 NA16OAR4310103, the U.S. Environmental Protection Agency grant EPA STAR 84000701, and Esther F. Hays Graduate Fellowship Award for providing the funds for my research.

Lastly, I would like to thank my husband, Xikui, for being the best husband in the world who loves me, respects me, and brings me happiness. Thanks a lot to my parents, my sister, and my parents-in-law. I will always be grateful for their love and support. I’d like to thank my friends. The past five years have been filled with great memories because of you.

Chapter 2 and Appendix A~B of this dissertation, in full, is a reprinted with permission from “ACS Earth Space Chem. 2020, 4, 1254−1268” with contributing authors William Carter, David Cocker, and Kelley Barsanti entitled “Development and Evaluation of a Detailed Mechanism for Gas-Phase Atmospheric Reactions of Furans”, https://dx.doi.org/10.1021/acsearthspacechem.0c00058. Copyright © 2020 American Chemical Society.

Chapter 4 and Appendix D of this dissertation, in part, is a reprint of the material as has been submitted to Atmospheric Chemistry and Physics (in review) with contributing authors: Qi Li, Isaac Afreh, Kelley Barsanti, and David Cocker entitled “Secondary Organic Aerosol Formation from Camphene Oxidation: Measurements and Modeling”, Atmospheric Chemistry and Physics Discussions, https://doi.org/10.5194/acp-2021-587.

ABSTRACT OF THE DISSERTATION

Development of Chemical Mechanisms for Predictions of Ozone and Secondary Organic Aerosol Formation From Biomass Burning-Derived Precursors

by

Jia Jiang

Doctor of Philosophy, Graduate Program in Chemical and Environmental Engineering
University of California, Riverside, December 2021
Dr. Kelley C. Barsanti, Chairperson

The increase in the frequency, extent, and duration of wildfires has become a great concern for air quality and climate because of the significant quantities of trace gases released from biomass burning (BB). Once in the atmosphere, BB emissions have a strong influence on climate, tropospheric chemistry, and human health. Advances in analytical techniques have recently enabled improved identification and quantification of the gas-phase emissions from BB, including volatile organic compounds (VOCs). A few classes of these BB-derived VOCs have been identified as ozone (O_3) and secondary organic aerosol (SOA) precursors but their reactions in the atmosphere generally are poorly understood and/or are inadequately represented in air quality models. Such classes of VOCs include heterocyclic compounds (e.g., furans), oxygenated aromatics (e.g., phenols), and monoterpenes (e.g., camphene). As presented in this dissertation, the Statewide Air Pollution Research Center (SAPRC) modeling system was used to develop new chemical mechanisms and to conduct mechanistic studies of O_3 and SOA formation from these understudied VOCs emitted from BB.

New gas-phase chemical mechanisms were derived for furans, phenols, and their major oxidation products based on published experimental data, molecular modeling simulations, and estimations from the SAPRC mechanism generation system (MechGen). The new mechanisms were implemented into the SAPRC box model and evaluated based on model-measurement comparisons of VOC consumption, nitric oxide (NO) decay, O_3 formation, and radical levels. The mechanisms were developed with no tuning to fit the experimental data used for evaluation and showed much better model performance compared to the previous versions of mechanisms in simulating chamber experiments for furans and phenols (except for 2,4-dimethylphenol).

MechGen was also used to derive a chemical mechanism for camphene that was applied in the SAPRC box model to investigate the role of peroxy radicals (RO_2) in camphene SOA formation. In the chamber experiments, an unexpected enhancement of SOA formation was observed at higher NO_x levels. SAPRC simulation results suggested that the higher SOA mass yields at higher initial NO_x levels were primarily due to higher production of RO_2 and the generation of highly oxygenated organic molecules (HOMs). Camphene RO_2 reacts with NO and the resultant RO_2 undergo hydrogen (H)-shift isomerization reactions in the presence of NO_x, leading to the formation of HOMs which have significantly lower volatilities than products formed via other pathways.

The research presented in this dissertation has advanced the understanding of gas-phase chemistry for BB-derived VOCs including furans, phenols, and camphene while also

addressing inadequate representations of these compounds in chemical models. For the first time, the chemically detailed SAPRC box model was used to establish the connection between gas-phase chemistry and SOA formation. The findings in this dissertation have aided in the optimization of MechGen estimation methodology and have made it more visible and accessible to the atmospheric chemistry community.

Table of Contents

List of Tables

List of Figures

Chapter 1 Introduction

1.1 Introduction

Emissions from biomass burning (BB), including wildfires, prescribed fires, and agricultural burning, have a strong influence on climate, tropospheric chemistry, and human health. The increase in the frequency, extent, and duration of wildfires in particular has become a great concern for air quality because of the significant quantities of trace gases, such as nitrogen oxides (NO_x), volatile organic compounds (VOCs), and primary particulate matter (PM) emitted from BB (Abatzoglou & Williams, 2016; Harvey, 2016; Heilman et al., 2014; Westerling, 2016). Highly reactive VOCs can undergo photochemical oxidation during plume transport to form air pollutants downwind, including ozone (O_3) and secondary organic aerosol (SOA).

Short-term exposure to high levels of tropospheric O_3 has been found to irritate eyes and impact the respiratory system, as well as increase the susceptibility to inhaled allergens (Bell et al., 2004; EPA, 2021b; WHO, 2003). Long-term exposure to O_3 is associated with the aggravation of asthma and is likely to cause permanent lung damage (Akagi et al., 2011; Bell et al., 2004; EPA, 2021b; Katsouyanni et al., 2009; Lippmann, 1989; WHO, 2003). PM in the atmosphere is known to affect visibility, radiative climatic forcing, cloud droplet formation, and human health (Hallquist et al., 2009; Jacobson & Hansson, 2000; Kanakidou et al., 2005). PM can have direct and indirect impacts on climate, through moderation of the earth's radiative balance or cloud formation (Crutzen &

Andreae, 1990; Hobbs et al., 2003; Reid et al., 2005). In terms of human health, exposure to PM can increase airway inflammation and asthma, or even lead to death from lung and heart diseases due to long-term exposures (Bernstein et al., 2004; Davidson et al., 2005; EPA, 2021a; Katsouyanni et al., 2009; Pöschl, 2005; WHO, 2003).

In order to mitigate the effects of BB on air quality and climate, improvements are needed in the model representation of source emissions and subsequent chemistry. Advances in analytical techniques have recently enabled improved identification and quantification the gas-phase emissions from BB. Efforts to quantify the potential O_3 and SOA formation from these recently identified VOCs have been hindered due to the lack of published information on the reaction kinetics and mechanisms for atmospheric oxidation, as well as lack of information on propensity to form SOA (e.g., chamber-based SOA yields).

1.2 O_3 and SOA Chemistry

The formation of O_3 and SOA in the troposphere is promoted by the presence of VOCs and NO_x. Figure 1.1 shows the generalized reaction schematic of the oxidation of a VOC by the hydroxyl radical (OH) in the presence of NO_x, which is also the tropospheric oxidation pathway of most organic compounds (Hallquist et al., 2009; Jenkin & Clemitshaw, 2000). In the presence of NO_x, OH catalyzes the oxidation of the VOC, leading to the formation of oxidized products with O_3 formed as a by-product. The oxidized products can continue to react through two major pathways: functionalization through the chain-propagating process (Figure 1.1) or fragmentation ultimately to carbon dioxide and water vapor (Ziemann, 2011; Ziemann & Atkinson, 2012). Highly functionalized species typically have lower saturation vapor pressures than the parent VOC, and thus have a greater tendency to condense to the particle phase, leading to the formation of SOA (Odum Jay et al., 1996; Pankow, 1987). In addition to reacting with OH, VOCs can form O_3 and SOA through reactions with other atmospheric oxidants such as nitrate radical (NO_3), O_3, and chlorine radical (Cl).

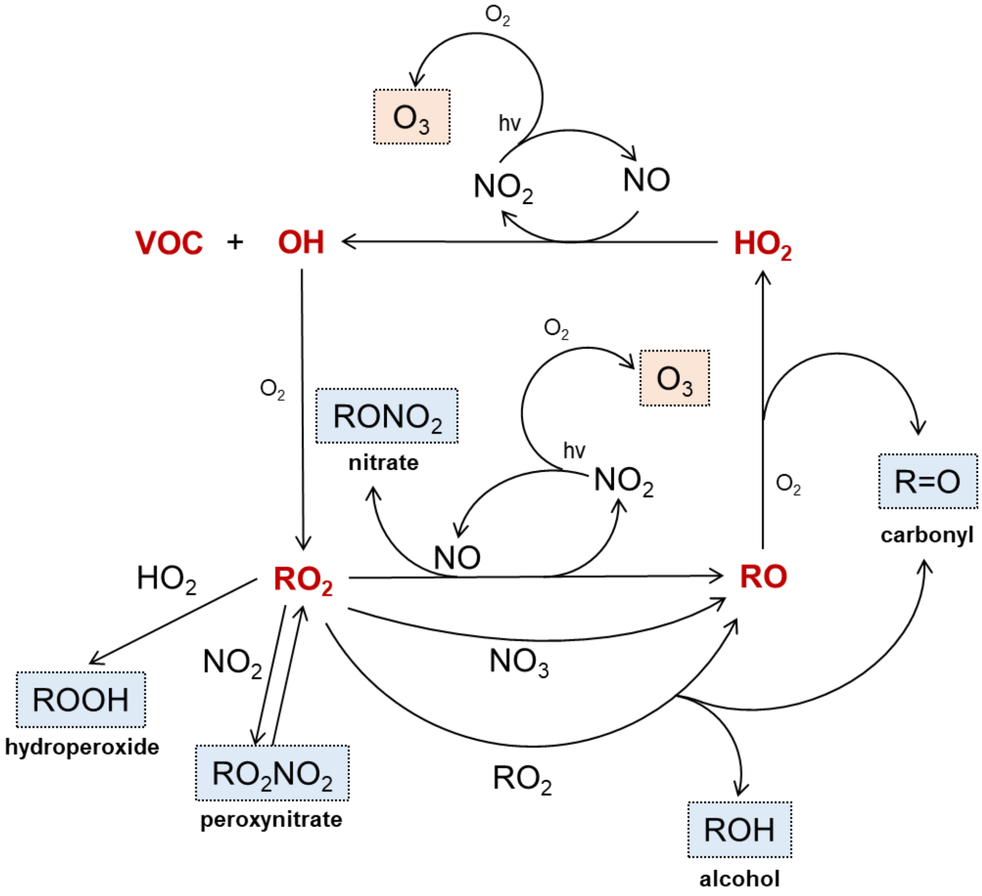

Figure 1.1: Simplified schematic of the OH-initiated oxidation of a generic VOC to form O_3 and 1st generation products in the presence of NO_x.

Different parameters such as NO_x levels, temperature, and relative humidity will all affect atmospheric SOA formation (Cocker et al., 2001; Ng et al., 2007; Song et al., 2005; Svendby et al., 2008). SOA formation has been shown to be highly dependent on gas-phase NO_x concentrations, and more precisely, the chemistry of the peroxy radicals (RO_2) as influenced by the relative ratios of hydroperoxyl radicals (HO_2):nitric oxide (NO):RO_2 (Hartikainen et al., 2018; Henze et al., 2008; Lane et al., 2008; Ng et al., 2007; Pöschl, 2005; Presto et al., 2005; Song et al., 2005; Ziemann & Atkinson, 2012). RO_2 radicals undergo different reaction pathways, dependent on HO_2:NO:RO_2 levels, which lead to products with different molecular weights and functional groups (Figure 1.1). The presence of additional methylene, ketone, ester, aldehyde, nitrate, hydroxyl, hydroperoxyl, peroxycarboxyl, and carboxyl groups will reduce compound vapor pressure by factors of approximately 3, 9, 16, 22, 170, 170, 300, 300, and 3800 respectively (Ziemann & Atkinson, 2012). The different RO_2 reaction pathways will lead to products with different functionalities and different volatilities, and therefore different propensities to form SOA.

In air quality models, it is common to represent SOA formation using two sets of SOA parameters derived by separately fitting chamber experiments carried out under high-NO_x and low-NO_x conditions. Under high-NO_x conditions, the RO_2 + NO pathway will be dominant, forming more volatile compounds such as carbonyls, whereas under low-NO_x conditions, the RO_2 + HO_2 pathway will be dominant, forming less volatile products such as hydroperoxides (Kroll & Seinfeld, 2008). The branching ratio, β, describes the fraction of RO_2 that undergoes bimolecular reaction with NO relative to HO_2 (Pye et al., 2010):

$$\boldsymbol{\beta} = ([\mathbf{NO}] \cdot \boldsymbol{k}_{\mathbf{NO}})/([\mathbf{NO}] \cdot \boldsymbol{k}_{\mathbf{NO}} + [\mathbf{HO_2}] \cdot \boldsymbol{k}_{\mathbf{HO_2}}) \qquad \textbf{Equation 1.1}$$

Where k_{NO} and $k_{\mathrm{HO_2}}$ are rate constants for RO_2 reacting with NO and HO_2. Current chemical transport models, such as GEOS-Chem and CMAQ (Koo et al., 2014; Pye et al., 2010), predict SOA concentrations using β coupled with SOA yield parameters to determine the fractional amounts of hydrocarbon reacted (ΔHC) through the corresponding pathways. The initial concentration of NO_x or the ratio of [VOC]/[NO_x] is mostly used to define the experiments as high NO_x or low NO_x. However, the high-NO_x chamber experiments may not accurately represent the RO_2 + NO pathway when β is equal to 1. Similarly, low-NOx experiments may not represent the RO_2 + HO_2 pathway when β is equal to 0. The fitting of chamber data to derive the SOA parameters does not have a specific connection with the gas-phase mechanism, despite the fact that the gas-phase mechanism can provide critical information regarding reaction pathways, products, O_3, and SOA formation.

1.3 Summary

The goal of the research presented in this dissertation is to advance the understanding and model representation of underrepresented O_3 and SOA precursors emitted from BB. Detailed speciation of VOCs in BB samples has been achieved through measurements using one- and two-dimensional gas chromatography with mass spectrometry (GC(×GC)/MS) and chemical ionization mass spectrometry (CIMS). A few VOC classes have been identified as likely O_3 and SOA precursors but are poorly understood and/or inadequately represented in air quality models: heterocyclic compounds (e.g., furans), oxygenated aromatics (e.g., phenols) and monoterpenes (e.g., camphene) (Akherati et al., 2020; Hatch et al., 2015; Hatch et al., 2017). In the research presented in this dissertation, the Statewide Air Pollution Research Center (SAPRC) modeling system was used to develop new chemical mechanisms for these classes of compounds and to conduct mechanistic studies of O_3 and SOA formation under atmospherically-relevant conditions.

SAPRC is a broad name that refers to the many components of the SAPRC modeling system, which includes several versions of gas-phase chemical mechanisms, an explicit chemical mechanism generator, and a box-model simulation software system. The components of SAPRC were developed by Dr. William Carter at the University of California, Riverside (Carter, 1999, 2009, 2010, 2020a, 2020b, 2020c; Carter & Heo, 2012) and updates to the system have continued since its origin. The SAPRC gas-phase chemical mechanisms represent the gas-phase reactions of VOCs with major atmospheric oxidants in the lower troposphere. They are among the most widely-used chemical mechanisms in current atmospheric models. The major versions used in this dissertation include SAPRC-07 (Carter, 2009), SAPRC-11 (Carter & Heo, 2012), and SAPRC-18 (Carter, 2020a). The SAPRC mechanism generation system (MechGen) (Carter, 2020b) is capable of generating fully explicit mechanisms for the atmospheric reactions of many types of organic compounds and the intermediate radicals they form. MechGen uses experimentally derived rate constants and branching ratios if data are available, and otherwise, uses estimated rate constants and branching ratios based on group additivity and other estimation methods. The SAPRC box-model system (Carter, 2015) has been in use since the mid-1970s for developing and evaluating SAPRC chemical mechanisms. Simulations can be run using multiple versions of the SAPRC gas-phase chemical mechanism, and require inputs such as initial conditions and relevant chemical parameters for environmental chamber experiments. More detailed descriptions of the SAPRC modeling system can be found in Appendix A and the reports published on Dr. William Carter's personal website: https://intra.engr.ucr.edu/~carter/.

Chapter 2 presents a detailed gas-phase mechanism for furans and their major oxidation products, which was developed using a combination of published experimental data, molecular modeling simulations, and MechGen. The detailed furans mechanism was implemented in the SAPRC-18 base mechanism to enable evaluation against environmental chamber experiments. A reduced version of the mechanism was developed that maintains consistency and compatibility with the SAPRC-07/-11 base mechanisms. Relative to the SAPRC-07/-11 mechanisms model skill was improved significantly, especially for methylfurans. Sensitivity simulations were performed to evaluate the relative importance of OH-, NO_3- and O_3- initiated photooxidation.

Chapter 3 presents an updated SAPRC-18 phenols gas-phase mechanism, which was derived based on MechGen and published data. The phenols mechanism was evaluated based on model-measurement comparison of phenols decay, O_3 formation, and NO oxidation rates in 15 environmental chamber experiments. The phenols mechanism was developed with no tuning to fit the experimental data used for evaluation and showed better performance than the standard SAPRC-18 mechanism in simulating phenol and o-cresol experiments (except for 2,4-dimethylphenol).

Chapter 4 presents a mechanistic study of camphene SOA formation. A series of experiments were performed in the UCR environmental chamber to explore camphene SOA mass yields and properties across a range of chemical conditions at atmospherically relevant OH levels. SOA parameterizations were derived from the chamber data using both the two-product (2p) and volatility basis set (VBS) approaches. SAPRC-based simulations of the chamber studies were used to investigate how the RO_2 fates affected observed camphene SOA formation and indicated the formation of highly oxygenated organic molecules (HOMs) at the presence of NO_x. The observed differences in SOA mass yields between experiments with NO_x and without NO_x were largely explained by the gas-phase RO_2 chemistry and the competition between $RO_2 + HO_2$, $RO_2 + NO$, $RO_2 + RO_2$, and RO_2 autoxidation reactions.

References

Abatzoglou, J. T., & Williams, A. P. (2016). Impact of anthropogenic climate change on wildfire across western US forests. *Proceedings of the National Academy of Sciences of the United States of America*, *113*(42), 11770-11775. https://doi.org/10.1073/pnas.1607171113

Akagi, S. K., Yokelson, R. J., Wiedinmyer, C., Alvarado, M. J., Reid, J. S., Karl, T., Crounse, J. D., & Wennberg, P. O. (2011). Emission factors for open and domestic biomass burning for use in atmospheric models. *Atmos. Chem. Phys.*, *11*(9), 4039-4072. https://doi.org/10.5194/acp-11-4039-2011

Akherati, A., He, Y., Coggon, M. M., Koss, A. R., Hodshire, A. L., Sekimoto, K., Warneke, C., De Gouw, J., Yee, L., Seinfeld, J. H., Onasch, T. B., Herndon, S. C., Knighton, W. B., Cappa, C. D., Kleeman, M. J., Lim, C. Y., Kroll, J. H., Pierce, J. R., & Jathar, S. H. (2020). Oxygenated Aromatic Compounds are Important Precursors of Secondary Organic Aerosol in Biomass-Burning Emissions. *Environmental Science and Technology*, *54*(14), 8568-8579. https://doi.org/10.1021/acs.est.0c01345

Bell, M. L., McDermott, A., Zeger, S. L., Samet, J. M., & Dominici, F. (2004). Ozone and Short-term Mortality in 95 US Urban Communities, 1987-2000. *JAMA*, *292*(19), 2372-2378. https://doi.org/10.1001/jama.292.19.2372

Bernstein, J. A., Alexis, N., Barnes, C., Bernstein, I. L., Nel, A., Peden, D., Diaz-Sanchez, D., Tarlo, S. M., Williams, P. B., & Bernstein, J. A. (2004). Health effects of air pollution. *Journal of Allergy and Clinical Immunology*, *114*(5), 1116-1123. https://doi.org/https://doi.org/10.1016/j.jaci.2004.08.030

Carter, W. P. (2015). *Documentation of the SAPRC Chemical Mechanism Modeling Software and Files* (Draft report to California Air Resources Board Contract, Issue.

Carter, W. P. L. (1999). Documentation of the SAPRC-99 Chemical Mechanism for VOC Reactivity Assessment. *Assessment*, *1*, 329-329. http://www.engr.ucr.edu.oca.ucsc.edu/~carter/pubs/s99doc.pdf

Carter, W. P. L. (2009). *Development of the SAPRC-07 Chemical Mechanism and Updated Ozone Reactivity Scales; Final report to the California Air Resources Board Contract No. 03-318, March 2009*. https://intra.engr.ucr.edu/~carter/SAPRC/

Carter, W. P. L. (2010). Development of a condensed SAPRC-07 chemical mechanism. *Atmospheric Environment*, *44*(40), 5336-5345. https://doi.org/10.1016/j.atmosenv.2010.01.024

Carter, W. P. L. (2020a). *Documentation of the SAPRC-18 Mechanism; Report to California Air Resources Board Contract No. 11-761, May, 2020*. https://intra.engr.ucr.edu/~carter/SAPRC/18/

Carter, W. P. L. (2020b). *Estimates and Assignments used in the SAPRC-18 Mechanism Generation System; Report to California Air Resources Board Contract No. 11-761. In preparation. When completed, will be available at http://intra.engr.ucr.edu/~carter/SAPRC/18*.

Carter, W. P. L. (2020c). *Gateway to the SAPRC Mechanism Generation System*. http://mechgen.cert.ucr.edu/

Carter, W. P. L., & Heo, G. (2012). *Development of revised SAPRC aromatics mechanisms. Final Report to the California Air Resources Board, Contracts No. 07-730 and 08-326, April 2012*. https://intra.engr.ucr.edu/~carter/SAPRC/saprc11.pdf

Cocker, D. R., Mader, B. T., Kalberer, M., Flagan, R. C., & Seinfeld, J. H. (2001). The effect of water on gas–particle partitioning of secondary organic aerosol: II. m-xylene and 1,3,5-trimethylbenzene photooxidation systems. *Atmospheric Environment*, *35*(35), 6073-6085. https://doi.org/https://doi.org/10.1016/S1352-2310(01)00405-8

Crutzen, P. J., & Andreae, M. O. (1990). Biomass Burning in the Tropics: Impact on Atmospheric Chemistry and Biogeochemical Cycles. *Science*, *250*(4988), 1669-1678. https://doi.org/doi:10.1126/science.250.4988.1669

Davidson, C. I., Phalen, R. F., & Solomon, P. A. (2005). Airborne Particulate Matter and Human Health: A Review. *Aerosol Science and Technology*, *39*(8), 737-749. https://doi.org/10.1080/02786820500191348

EPA, U. S. (2021a). *Health and Environmental Effects of Particulate Matter (PM)*. https://www.epa.gov/pm-pollution/health-and-environmental-effects-particulate-matter-pm

EPA, U. S. (2021b). *Health Effects of Ozone Pollution*. Retrieved November 4 from https://www.epa.gov/ground-level-ozone-pollution/health-effects-ozone-pollution

Hallquist, M., Wenger, J. C., Baltensperger, U., Rudich, Y., Simpson, D., Claeys, M., Dommen, J., Donahue, N. M., George, C., Goldstein, a. H., Hamilton, J. F., Herrmann, H., Hoffmann, T., Iinuma, Y., Jang, M., Jenkin, M. E., Jimenez, J. L., Kiendler-Scharr, a., Maenhaut, W., McFiggans, G., Mentel, T. F., Monod, a., Prévôt, a. S. H., Seinfeld, J. H., Surratt, J. D., Szmigielski, R., & Wildt, J. (2009). The formation, properties and impact of secondary organic aerosol: current and emerging issues. *Atmos. Chem. Phys.*, *9*(14), 5155-5236. https://doi.org/10.5194/acp-9-5155-2009

Hartikainen, A., Yli-Pirilä, P., Tiitta, P., Leskinen, A., Kortelainen, M., Orasche, J., Schnelle-Kreis, J., Lehtinen, K. E. J., Zimmermann, R., Jokiniemi, J., & Sippula, O. (2018). Volatile organic compounds from logwood combustion: emissions and transformation under dark and photochemical aging conditions in a smog chamber. *Environmental Science and Technology*, *52*(8), 4979-4988. https://doi.org/10.1021/acs.est.7b06269

Harvey, B. J. (2016). Human-caused climate change is now a key driver of forest fire activity in the western United States. In *Proceedings of the National Academy of Sciences of the United States of America* (Vol. 113, pp. 11649-11650): National Academy of Sciences.

Hatch, L. E., Luo, W., Pankow, J. F., Yokelson, R. J., Stockwell, C. E., & Barsanti, K. C. (2015). Identification and quantification of gaseous organic compounds emitted from biomass burning using two-dimensional gas chromatography-time-of-flight mass spectrometry. *Atmospheric Chemistry and Physics*, *15*(4), 1865-1899. https://doi.org/10.5194/acp-15-1865-2015

Hatch, L. E., Yokelson, R. J., Stockwell, C. E., Veres, P. R., Simpson, I. J., Blake, D. R., Orlando, J. J., & Barsanti, K. C. (2017). Multi-instrument comparison and compilation of non-methane organic gas emissions from biomass burning and implications for smoke-derived secondary organic aerosol precursors. *Atmospheric Chemistry and Physics*, *17*(2), 1471-1489. https://doi.org/10.5194/acp-17-1471-2017

Heilman, W. E., Liu, Y., Urbanski, S., Kovalev, V., & Mickler, R. (2014). Wildland fire emissions, carbon, and climate: Plume rise, atmospheric transport, and chemistry processes. *Forest Ecology and Management*, *317*, 70-79. https://doi.org/https://doi.org/10.1016/j.foreco.2013.02.001

Henze, D. K., Seinfeld, J. H., Ng, N. L., Kroll, J. H., Fu, T. M., Jacob, D. J., & Heald, C. L. (2008). Global modeling of secondary organic aerosol formation from aromatic hydrocarbons: high- vs. low-yield pathways. *Atmospheric Chemistry and Physics*, *8*(9), 2405-2420. https://doi.org/10.5194/acp-8-2405-2008

Hobbs, P. V., Sinha, P., Yokelson, R. J., Christian, T. J., Blake, D. R., Gao, S., Kirchstetter, T. W., Novakov, T., & Pilewskie, P. (2003). Evolution of gases and particles from a savanna fire in South Africa. *Journal of Geophysical Research: Atmospheres*, *108*(D13). https://doi.org/https://doi.org/10.1029/2002JD002352

Jacobson, M. C., & Hansson, H. (2000). Organic Atmospheric Aerosols: Review and State of the Science. (1998), 267-294.

Jenkin, M. E., & Clemitshaw, K. C. (2000). Ozone and other secondary photochemical pollutants: chemical processes governing their formation in the planetary boundary layer. *Atmospheric Environment*, *34*(16), 2499-2527. https://doi.org/https://doi.org/10.1016/S1352-2310(99)00478-1

Kanakidou, M., Seinfeld, J. H., Pandis, S. N., Barnes, I., Dentener, F. J., Facchini, M. C., Van Dingenen, R., Ervens, B., Nenes, A., Nielsen, C. J., Swietlicki, E., Putaud, J. P., Balkanski, Y., Fuzzi, S., Horth, J., Moortgat, G. K., Winterhalter, R., Myhre, C. E. L., Tsigaridis, K., Vignati, E., Stephanou, E. G., & Wilson, J. (2005). Organic aerosol and global climate modelling: a review. *Atmospheric Chemistry and Physics*, *5*(4), 1053-1123. https://doi.org/10.5194/acp-5-1053-2005

Katsouyanni, K., Samet, J. M., Anderson, H. R., Atkinson, R., Le Tertre, A., Medina, S., Samoli, E., Touloumi, G., Burnett, R. T., Krewski, D., Ramsay, T., Dominici, F., Peng, R. D., Schwartz, J., Zanobetti, A., & Committee, H. E. I. H. R. (2009). Air pollution and health: a European and North American approach (APHENA). *Research report (Health Effects Institute)*(142), 5-90. http://europepmc.org/abstract/MED/20073322

Koo, B., Knipping, E., & Yarwood, G. (2014). 1.5-Dimensional volatility basis set approach for modeling organic aerosol in CAMx and CMAQ. *Atmospheric Environment*, *95*, 158. https://doi.org/10.1016/j.atmosenv.2014.06.031

Kroll, J. H., & Seinfeld, J. H. (2008). Chemistry of secondary organic aerosol: Formation and evolution of low-volatility organics in the atmosphere. *Atmospheric Environment*, *42*(16), 3593-3624. https://doi.org/10.1016/j.atmosenv.2008.01.003

Lane, T. E., Donahue, N. M., & Pandis, S. N. (2008). Effect of NOx on secondary organic aerosol concentrations. *Environmental Science and Technology*, *42*(16), 6022-6027. https://doi.org/10.1021/es703225a

Lippmann, M. (1989). HEALTH EFFECTS OF OZONE A Critical Review. *JAPCA*, *39*(5), 672-695. https://doi.org/10.1080/08940630.1989.10466554

Ng, N. L., Chhabra, P. S., Chan, A. W. H., Surratt, J. D., Kroll, J. H., Kwan, A. J., McCabe, D. C., Wennberg, P. O., Sorooshian, A., Murphy, S. M., Dalleska, N. F., Flagan, R. C., & Seinfeld, J. H. (2007). Effect of NOx level on secondary organic aerosol (SOA) formation from the photooxidation of terpenes. *Atmospheric Chemistry and Physics*, *7*(19), 5159-5174. https://doi.org/10.5194/acp-7-5159-2007

Odum Jay, R., Hoffmann, T., Bowman, F., Collins, D., Flagan Richard, C., & Seinfeld John, H. (1996). Gas particle partitioning and secondary organic aerosol yields. *Environmental Science and Technology*, *30*(8), 2580-2585. https://doi.org/10.1021/es950943+

Pankow, J. F. (1987). Review and comparative analysis of the theories on partitioning between the gas and aerosol particulate phases in the atmosphere. *Atmospheric Environment (1967)*, *21*(11), 2275-2283. https://doi.org/10.1016/0004-6981(87)90363-5

Pöschl, U. (2005). Atmospheric aerosols: Composition, transformation, climate and health effects. *Angewandte Chemie - International Edition*, *44*(46), 7520-7540. https://doi.org/10.1002/anie.200501122

Presto, A. A., Huff Hartz, K. E., & Donahue, N. M. (2005). Secondary organic aerosol production from terpene ozonolysis. 2. Effect of NOx concentration. *Environmental Science and Technology*, *39*(18), 7046-7054. https://doi.org/10.1021/es050400s

Pye, H. O. T., Chan, A. W. H., Barkley, M. P., & Seinfeld, J. H. (2010). Global modeling of organic aerosol: the importance of reactive nitrogen (NOx and NO3). *Atmos. Chem. Phys.*, *10*(22), 11261-11276. https://doi.org/10.5194/acp-10-11261-2010

Reid, J. S., Koppmann, R., Eck, T. F., & Eleuterio, D. P. (2005). A review of biomass burning emissions part II: intensive physical properties of biomass burning particles. *Atmos. Chem. Phys.*, *5*(3), 799-825. https://doi.org/10.5194/acp-5-799-2005

Song, C., Na, K., & Cocker, D. R. (2005). Impact of the Hydrocarbon to NOx Ratio on Secondary Organic Aerosol Formation. *Environmental Science & Technology*, *39*(9), 3143-3149. https://doi.org/10.1021/es0493244

Svendby, T. M., Lazaridis, M., & Tørseth, K. (2008). Temperature dependent secondary organic aerosol formation from terpenes and aromatics. *Journal of Atmospheric Chemistry*, *59*(1), 25-46. https://doi.org/10.1007/s10874-007-9093-7

Westerling, A. L. R. (2016). Increasing western US forest wildfire activity: Sensitivity to changes in the timing of spring. *Philosophical Transactions of the Royal Society B: Biological Sciences*, *371*(1696), 20150178-20150178. https://doi.org/10.1098/rstb.2015.0178

WHO. (2003). Health aspects of air pollution with particulate matter, ozone and nitrogen dioxide : report on a WHO working group, Bonn, Germany 13-15 January 2003. In: WHO Regional Office for Europe.

Ziemann, P. J. (2011). Effects of molecular structure on the chemistry of aerosol formation from the oh-radical-initiated oxidation of alkanes and alkenes. *International Reviews in Physical Chemistry*, *30*(2), 161-195. https://doi.org/10.1080/0144235X.2010.550728

Ziemann, P. J., & Atkinson, R. (2012). Kinetics, products, and mechanisms of secondary organic aerosol formation. *Chemical Society Reviews*, *41*(19), 6582-6605. https://doi.org/10.1039/c2cs35122f

Chapter 2 Development and Evaluation of a Detailed Mechanism for Gas-Phase Atmospheric Reactions of Furans

2.1 Introduction

Furan and its alkyl-derivatives, hereafter referred to as furans, are heterocyclic compounds emitted to the atmosphere from multiple sources. While furans have historically represented a small fraction of total anthropogenic emissions, emissions from a wider range of sources are of increasing interest, facilitating consideration of the roles of compounds such as furans in atmospheric chemistry. One such source is biomass burning, which includes wildfires, prescribed burns, and agriculture fires. Reported emission factors (mass of compound/mass of fuel burned) for furans are among the highest of all gaseous non-methane organic carbon compounds (Andreae & Merlet, 2001; Ciccioli et al., 2001; Gilman et al., 2015; Hartikainen et al., 2018; Hatch et al., 2015; Hatch et al., 2017; Liu et al., 2017; Yokelson et al., 2007). Biomass burning-derived furan emissions may increase in the future, due to an increase in the frequency, extent, and duration of wildfires (Abatzoglou & Williams, 2016; Harvey, 2016; Westerling, 2016). In addition to pyrogenic sources, alkylfurans derived from biomass, such as 2-methylfuran (2-MF) and 2,5-dimethylfuran (2,5-DMF), are being considered as alternative transportation fuel sources (Eldeeb & Akih-Kumgeh, 2018; Román-Leshkov et al., 2007; Togbé et al., 2014; Tran et al., 2014). Due to their similar physical and chemical properties to gasoline, they can be used without changing the structure of current internal combustion engines (Jiang et al., 2021; Thewes et al., 2011; Wang et al., 2013; Wei et al., 2014). Once put into commercial use, methylfurans emissions from this source may be significant. The photooxidation of isoprene and other dienes is another source of atmospheric furans (Atkinson et al., 1989; Brégonzio-Rozier et al., 2015; Francisco-Márquez et al., 2005; Paulson et al., 1992a, 1992b; Sprengnether et al., 2002). Several studies have reported that isoprene, the most abundant biogenic hydrocarbon (Brégonzio-Rozier et al., 2015; Guenther et al., 2006; Laothawornkitkul et al., 2009) forms the first-generation product 3-methylfuran (3-MF) with a molar yield of ~0.04 (Atkinson et al., 1989; Brégonzio-Rozier et al., 2015; Paulson & Seinfeld, 1992; Tuazon & Atkinson, 1990). While not necessarily new, the contribution of this secondary biogenic source to atmospheric furan chemistry has not been well quantified. Emerging sources and potential increases in atmospheric levels of furans have promoted research into their effects on atmospheric oxidant budgets and potential to form secondary pollutants including ozone (O_3) and secondary organic aerosol (SOA) (Decker et al., 2019; Hatch et al., 2015; Hatch et al., 2017).

Once in the atmosphere, furans can be chemically removed by reactions with hydroxyl radical (OH), O_3, nitrate radical (NO_3), and chlorine radical (Cl). While the reaction of furans with Cl is very fast, the relatively low concentration of Cl outside of the marine boundary layer results in an atmospheric lifetime of several days for furans with Cl (Cabañas et al., 2005), and therefore was not considered in this study. The magnitude of the reaction rate coefficients for individual furans is dependent on the number, length, position, and nature of the substituent groups (Bierbach et al., 1992). Reported rate coefficients for reactions of selected furans with OH, O_3, and NO_3 are listed in Table 2.1. The primary sink for furans during the daytime is the reaction with OH, with atmospheric lifetimes on the order of several hours at typical ambient OH levels. During the nighttime, the dominant sink is the reaction with NO_3. A recent study of nighttime chemical transformations in biomass burning plumes suggested that furans were among the compounds that contributed most to the initial NO_3 reactivity (e.g. approximately 23% for a rice straw fire) (Decker et al., 2019). For some methylfuran derivatives, reactions with O_3 also must be considered. For example, using 24-hr average tropospheric concentrations of OH and 12-hr average O_3 concentrations, the calculated lifetime for 2,5-DMF with O_3 is 0.94 hr, which is approximately a factor of 2 shorter than the lifetime with OH (2.22 hr). This demonstrates that O_3 can be an important sink for 2,5-DMF, even in the daytime.

Table 2.1: Rate coefficients (unit: $cm^3 molecule^{-1} s^{-1}$) for the reactions of furans with OH, O_3, and NO_3 at atmospheric pressure and near room temperature (296K ~ 298K), and calculated tropospheric lifetimes.

Compound	Rate coefficients			Tropospheric lifetimes [i]		
	k_{OH} (10^{-11})	k_{O3} (10^{-17})	k_{NO3} (10^{-11})	τ_{OH} (h)	τ_{O3} (h)	τ_{NO3} (h)
Furan	4.0 [a]	0.242 [c]	0.13 [b]	6.94	163.98	0.89
2-MF	7.31 [d]	NA	2.57 [e]	3.80	NA	0.05
3-MF	8.73 [d]	2.05 [g]	1.26 [f]	3.18	19.36	0.09
2,5-DMF	12.5 [d]	42 [h]	5.78 [e]	2.22	0.94	0.02
2,3-Dimethylfuran (2,3-DMF)	12.6 [d]	NA	5.83 [e]	2.20	NA	0.02
2,4-Dimethylfuran (2,4-DMF)	NA	NA	5.72 [e]	NA	NA	0.02
2,3,4,5-Tetramethylfuran (2,3,4,5-TMF)	NA	NA	11.8 [e]	NA	NA	0.01

[a] Calvert et al. (2015); [b] Cabañas et al. (2004); [c] Atkinson et al. (1983); [d] Aschmann et al. (2011); [e] Kind et al. (1996); [f] Tapia et al. (2011); [g]Alvarado et al. (1996); [h] Matsumoto (2011); [i]Assuming typical tropospheric concentration of [OH] = 1×10^6 radicals cm^{-3} (12h daytime average), [O_3] = 7×10^{11} molecule cm^{-3} (24h average), [NO_3] = 2.4×10^8 radicals cm^{-3} (12h nighttime average) (Fry et al., 2009).

Experimental and computational studies of furans have been performed to elucidate their atmospheric oxidation mechanisms and to quantify the yields of major products. Relative to NO_3 and O_3, reactions with OH are well studied, but inconsistencies still exist in the literature regarding OH reaction pathways and product yields (Anglada, 2008; Aschmann et al., 2011, 2014; Bierbach et al., 1995; Gómez Alvarez et al., 2009; Joo et al., 2019; Strollo & Ziemann, 2013; Tapia et al., 2011; Yuan et al., 2017). The major reaction pathway of furans with OH is addition to the double bond of the furan ring followed by ring-opening. H-atom abstraction from the methyl group or furan ring, accounts for a very small fraction of the overall reaction under atmospheric conditions (Tapia et al., 2011; Yuan et al., 2017). The dominant furans photooxidation products are known to be unsaturated dicarbonyls, hydroxyfuranone, maleic anhydride, glyoxal, and their derivatives. However, product yields are not widely reported with the exception of unsaturated dicarbonyls (Aschmann et al., 2014; Gómez Alvarez et al., 2009; Ji et al., 2017; Strollo & Ziemann, 2013; Tapia et al., 2011).

Despite the fact that furans are highly reactive in the atmosphere, the treatment of furans has generally been over-simplified in gas-phase chemical mechanisms used for air quality predictions and atmospheric modeling studies. Most widely used mechanisms do not represent furans explicitly. For example, in condensed gas-phase chemical mechanisms including SAPRC-07, RADM2, RACM2, and CB05, furans have been assigned to the lumped model species used for xylenes and other higher aromatic compounds (Carter, 2009, 2015, 2016; Stockwell et al., 1990; Yarwood et al., 2005). Furans were assigned to these lumped aromatics because chamber experiments indicated similar reactivity characteristics, and models assuming highly photoreactive products were needed to fit the data. However, as further discussed herein, representing furans as aromatic species does not reproduce the available data well (e.g., furans decay and O_3 formation), and a better alternative is needed when modeling conditions where furans may be important.

There have been a number of simplified furans mechanisms developed for specific applications. Reactions of furans with OH radicals were added to SAPRC-07 and SAPRC-11 to calculate O_3 reactivity (Carter & Heo, 2013; Carter et al., 2010). For those applications, OH was the only oxidant, and a single model species representing 1,4-dicarbonyls was the only organic product of the OH reaction included. Alvarado and Prinn used a similar approach, adding one model species in the Caltech Atmospheric Chemistry Mechanism (CACM) to represent furans for a biomass burning plume modeling study (Alvarado & Prinn, 2009). Explicit reactions of 3-MF (formed from isoprene oxidation) with OH, NO_3, and O_3 are included in the Master Chemical Mechanism (MCM) v3.3.1; 2-methyl-1,4-butenedial is the only organic product of the OH reaction (Jenkin et al., 2015). To model biomass burning plume chemistry, Decker et al. (2019) replaced the reaction mechanism of 3-MF with NO_3 in MCM v3.3.1 to include more pathways and products. Coggon et al. (2019) further extended MCM v3.3.1 to include reactions of other furans (including furan, 2-MF, and 2,5-DMF) with OH based on Aschmann et al (2014).

The highly simplified representations of OH-initiated gas-phase furans chemistry and the absence of NO_3- and O_3-initiated pathways in currently available mechanisms, as well as limited evaluation against atmospherically-relevant laboratory data, limit the reliability of such mechanisms for predicting atmospheric oxidant levels and secondary pollutant levels where furans emissions are significant (e.g., biomass burning-influenced regions). Although mechanisms for SOA formation are beyond the scope of this work, inaccurate predictions of gas-phase chemistry can lead to inaccurate predictions of SOA, given that SOA formation is dependent on gas-phase oxidant and radical levels and some furans may serve as SOA precursors (Gómez Alvarez et al., 2009; Joo et al., 2019; Strollo & Ziemann, 2013). Therefore, a more detailed furans mechanism was developed and evaluated in this work. This detailed mechanism was developed by adding model species and reactions to the recently-developed SAPRC-18 mechanism (Carter, 2020a) to represent four individual furans (furan, 2-MF, 3-MF and 2,5-DMF) and 11 major predicted oxidation products (dicarbonyls and furanones), see Table B2 in the Appendix B.

SAPRC-18 was chosen as the base mechanism because it is considered to represent the current state of the science, and because it includes more model species to more accurately represent organic reaction products. It also has a more explicit representation of peroxy radical chemistry that makes incorporation of more detailed mechanisms more straightforward. The SAPRC-18 mechanism is further described in Appendix A. The detailed furans reactions were also implemented and evaluated in the more widely-used SAPRC-07 and SAPRC-11 mechanisms to facilitate application in existing models used for air quality predictions and atmospheric research (Carter, 2009; Carter & Heo, 2013).

The predictive capabilities of the detailed furans mechanism were evaluated by comparing model simulations with data from 26 environmental chamber experiments previously carried out at the University of California at Riverside (UCR). The experiments were designed as simplified representations of ground-level smog formation. Reactive volatile organic compounds (VOCs) and nitrogen oxides (NO_x) were added to the chamber, and photochemical reactions were then initiated by turning on blacklights or an Argon arc light (see Appendix B.4 for further details on reaction initiation). While the levels of furans, and in the earliest experiments the levels of NO_x, were generally higher than in the atmosphere, this is the best available dataset to evaluate model predictions of gas-phase furans reactions under conditions approximating atmospheric relevance.

2.2 Furans Mechanism

The detailed furans mechanism developed in this work incorporates results of quantum calculations, published literature (cited in Table 2.1, Table 2.2, Table B3 and Table B4) and estimation methods developed for the SAPRC mechanisms (Carter, 2020b; Yuan et al., 2017). The rate constants for the reactions of the furans and their major products were obtained from the literature or estimated using structure-reactivity methods (see Table 2.1 for furans and Table 2.2 for their major products). The OH-initiated furans reactions were derived mainly using the high-level quantum chemistry and kinetic calculation results published by Yuan et al. (2017). Yuan et al. (2017) included detailed information for the furan reactions and demonstrated good agreement with experimental data from five published chamber studies (Anglada, 2008; Aschmann et al., 2014; Bierbach et al., 1995; Gómez Alvarez et al., 2009; Tapia et al., 2011; Yuan et al., 2017; Ziemann & Atkinson, 2012).

Table 2.2: Rate coefficients (unit: $cm^3 molecule^{-1} s^{-1}$) for dicarbonyls at atmospheric pressure and near room temperature (296K ~ 298K) used in this work.

Parent VOC	Product	OH (10^{-11})	NO_3 (10^{-14})	O_3 (10^{-18})	Photolysis
Furan	(Z)-2-Butene-1,4-dial	5.21 [a]	0.208 [c]	1.6 [d]	p(NO_2) × 0.16 [e]
	(E)-2-Butene-1,4-dial	3.45 [b]			
2-MF	4-Oxo-2-pentenal	5.67 [a]	1.0 [a]	4.8 [f]	p(NO_2) × 0.19 [e]
3-MF	2-Methyl-1,4-butenedial	4.71 [g]	0.313 [a]	4.8 [h]	p(NO_2) × 0.19 [i]
2,5-DMF	Z-3-Hexene-2,5-dione	5.90 [g]	3.0 [a]	1.8 [j]	Slow [c]
	E-3-Hexene-2,5-dione	4.45 [g]	1.0 [a]	8.3 [a]	Slow [c]

[a] Bierbach et al. (1994).
[b] Martin et al. (2013).
[c] Photolysis of unsaturated 1,4-diketones assumed to be slow (Carter, 2020c).
[d] Liu et al. (1999).
[e] Given as the ratio of total rate coefficient for loss of the product by photolysis to the photolysis rate of nitrogen dioxide (NO2), p(NO2), measured in the European Photoreactor (EUPHORE), as reported by Newland et al. (2019).
[f] Recommended by Calvert et al. (2015).
[g] Aschmann et al. (2011).
[h] Assumed in this work to be the same as that used for 4-oxo-2-pentenal.
[i] Estimated to be the same as that for photolysis of 4-oxo-2-pentenal and 2-methyl-1,4-butenedial, assuming that the ratio of overall quantum yields for the non-radical to the radical is the same for both compounds.
[j] Tuazon et al. (1985)

Mechanistic studies of NO_3- and O_3- initiated furans reactions are significantly limited in published literature (Joo et al., 2019; Tapia et al., 2011). Therefore, the reactions in these two pathways were derived using the SAPRC mechanism generation system (MechGen), with the exception of the initial step in the NO_3-initiated pathway (Carter, 2020a, 2020b, 2020c). The NO_3-initiated reactions were derived by analogy with the OH-initiated mechanism of Yuan et al. (2017). Schematics of NO_3 and O_3 pathways are shown in Figure B1 and Figure B2 in the Appendix B. MechGen, further described in the Appendix A, uses experimentally derived rate constants and branching ratios if data are available, and otherwise uses estimated rate constants and branching ratios based on group-additivity and other estimation methods (Carter, 2020b, 2020c). Theoretically-calculated branching ratios from Yuan et al. (2017) were also added to the MechGen assignments for this study. Detailed reactions and corresponding references are presented in Table B3 and Table B4.

A schematic of the OH-initiated furans reactions is shown in Figure 2.1. The yields of 1st generation products at 298K were calculated based on Yuan et al. (2017) in which good agreement with five experimental studies was demonstrated. As suggested by Yuan et al. (2017), the barriers for additions to C2 and C5 positions are much lower than those to C3 and C4. The reaction starts with OH addition to the C2/C5-position to form highly chemically activated radicals. These radicals are either stabilized by collision to form ring-retaining radicals or isomerized by breaking the furan C-O bond to form aliphatic radicals. Under atmospheric conditions, the ring-retaining radicals react with O_2 to form peroxy radicals and are then converted to hydroxyfuranone and epoxide compounds while the aliphatic radicals react with O_2 to form unsaturated 1,4-dicarbonyl compounds. For figure clarity, only the major NO reaction pathways are presented in Figure 2.1. Other reaction pathways for furans peroxy radicals (with: NO that form nitrates, NO_3, hydroperoxyl radicals (HO_2), and other peroxy radicals) were estimated using MechGen and are included in the mechanism (not shown here).

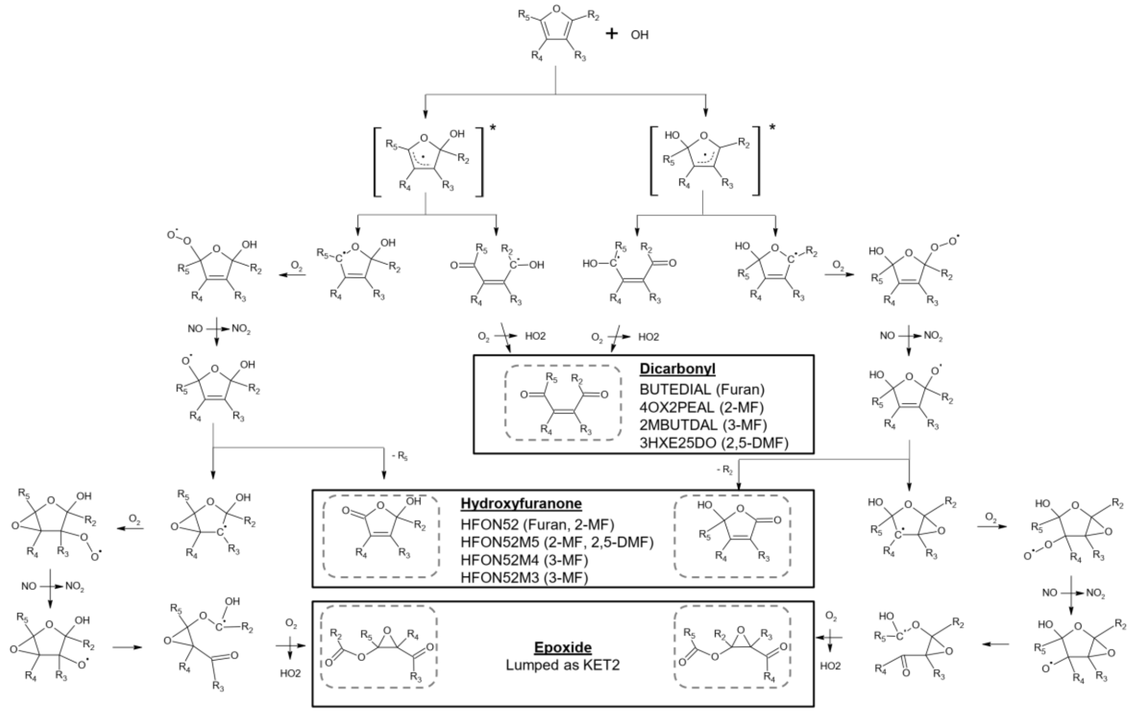

Figure 2.1: Schematic of the OH-initiated oxidation of furans in the detailed furans mechanism at 298K and atmospheric pressure in the presence of NO_x. For figure clarity, only the major reaction pathways of furans peroxy radicals are shown in this figure. The other reaction pathways for peroxy radicals are listed in Table B4.

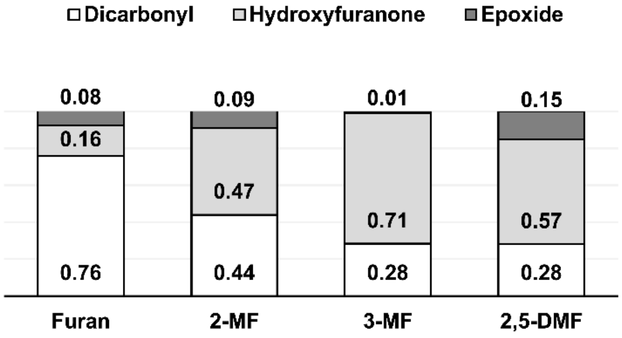

Figure 2.2: Molar yields of major 1st generation products in the OH-initiated oxidation of furans at 298K and atmospheric pressure calculated based on Yuan et al. (2017).

As illustrated in Figure 2.2, the major 1st generation products formed in the reactions of furans with OH are various unsaturated 1,4-dicarbonyls and hydroxyfuranones; epoxides are also formed in lower yields. Unsaturated 1,4-dicarbonyls can photolyze quickly if at least one of the carbonyls is in an aldehyde group. Photolysis is thought to be the primary sink for such compounds in the atmosphere with the exception of 3-hexene-2,5-dione (Aschmann et al., 2011; Bierbach et al., 1994; Liu et al., 1999; Martín et al., 2013; Newland et al., 2019; Tang & Zhu, 2005; Xiang et al., 2007). Loss rates due to photolysis, relative to NO_2 under solar conditions, have been measured for the E- and Z- isomers of 2-butene-1,4-dial and 4-oxo-2-pentenal by Newland et al. (2019), and correspond to photolysis lifetimes of only 6~8 minutes with direct overhead sunlight (Newland et al., 2019).

The exact mechanisms for the photolysis of unsaturated 1,4-dicarbonyl aldehydes are uncertain, but product data suggest that at least three routes occur: 1) rearrangements to form the observed non-radical furanone products such as 2(3H)-furanone from 2-butene-1,4-dial; 2) fragmentation to form maleic anhydride or related compounds, with OH and HO_2 radicals also being formed in the process; and 3) unknown processes involving the formation of carbon monoxide (CO), and unidentified products that are assumed to also form radicals (Newland et al., 2019). Based on observed furanone yields reported by Newland et al. (2019), it was assumed that the non-radical pathway occurs ~40% of the time from 2-butene-1,4-dial and ~30% of the time from 4-oxo-2-pentenal. It was also assumed that the photolysis rates for 2-butene-1,4-dial are approximately the same as for 4-oxo-2-pentenal. Although the product data suggest that the radical formation mechanism may be more complicated, for simplicity it was assumed that this mechanism can be represented by a process involving the anhydride + OH + HO_2 formation.

Unsaturated dicarbonyl products were represented explicitly in the detailed furans mechanisms because of their relatively high yields and high photolysis rates, and (for the aldehydes) their importance in contributing to the overall reactivity of furans. While furanones and hydroxyfuranones are not photoreactive, they were also represented explicitly because of the high yields as 1st and 2nd generation products, and because they are not particularly well represented by existing lumped SARPC model species. There have been few studies in the literature that report reaction pathways and products of 1,4-dicarbonyls and hydroxyfuranones. Their explicit reactions were mainly derived here using MechGen. The other products, either formed in lower yields or estimated to be relatively unreactive (e.g., anhydrides), are represented by SAPRC-18 lumped model species (Table S5). No adjustments to the rate constants or product yields were made to improve the fit for individual simulations.

Table 2.3: List of major products formed in the reactions of the furans with OH, O_3, and NO_3; and from the rapid photolysis of the photoreactive dicarbonyl product formed in the OH-initiated reactions.

Structure [a]	Model Species [b]	Yield [c]			
		OH	O_3	NO_3	hv [d]
Furan and Products					
HC(O)CH=CHCHO	BUTEDIAL	76%			
HOCH*CH=CHC(O)O*	HFON52	16%			
$CH*=CHOC(O)CH_2*$	3HF2ONE				31%
CH*=CHC(O)OC(O)*	MALAH				45%
HC(O)OCH*OCH*CHO	RCHO	8%	100%	31%	
$O_2NOCH*CH=CHC(O)O*$	RCNO3			65%	
NO_2	NO2			31%	
$O_2NOCH*CH=CHCH(ONO_2)O*$	RDNO3			3%	
2-MF and Products					
$CH_3C(O)CH=CHCHO$	4OX2PEAL	44%			
$CH_3C*(OH)CH=CHC(O)O*$	HFON52M5	26%			
HOCH*CH=CHC(O)O*	HFON52	17%			
$CH_3C*=CHCH_2C(O)O*$	3HF2ONM5				13%
CH*=CHC(O)OC(O)*	MALAH				31%
HCHO	HCHO	17%		31%	31%
$CH_3C*(OCHO)OCH*CHO$	RCHO	7%		12%	
HC(O)OCH*OCH*CHO	RCHO	2%	59%	3%	
$HC(O)OC*=CHC(O)OCH_2*$	OLEP		20%		
$CH_2=C(CHO)OCHO$	OLEA1		19%		
CO_2	CO2		16%		
CO	CO		3%		
NO_2	NO2			15%	
$CH_3C*(ONO_2)CH=CHC(O)O*$	RCNO3			46%	
$O_2NOCH*CH=CHC(O)O*$	RCNO3			31%	
$CH_3C*(ONO_2)CH=CHCH(ONO_2)O*$	RDNO3			6%	
3-MF and Products					
$CH_3C(CHO)=CHCHO$	2MBUTDAL	27%			
$CH_3C*=CHC(O)OCH*OH$	HFON52M4	59%			
$CH_3C*=CHCH(OH)OC(O)*$	HFON52M3	8%			
$CH_3C*=CHOC(O)CH_2*$	3HF2ONM4				8%
$CH_3C*=CHCH(ONO_2)OCH*OH$	RHNO3	4%			
$CH_3C*(CHO)OCH*OCHO$	RCHO	1%	41%		
$CH_3C(O)CH*OCH*OCHO$	KET2		59%		
$CH_3C*=CHC(O)OCH*ONO_2$	RCNO3			81%	1%
HCHO	MEO2				3%
CH3-C*=CH-CH(ONO2)-O-CO*	RCNO3			11%	

Structure [a]	Model Species [b]	Yield [c]			
		OH	O_3	NO_3	hv [d]
$CH_3C*=CHCH(ONO_2)OCH*ONO_2$	RDNO3			6%	
$HOOC(O)OCH=C(CH_3)C(O)OO.$	MACO3				9%
$CH_3C*=CHC(O)OC(O)*$	AFG3				5%
HC(O)C(O)OCHO	MGLY				3%
2,5-DMF and Products					
$CH_3C*(OH)CH=CHC(O)O*$	HFON52M5	50%			
$CH_3C(O)CH=CHC(O)CH_3$	3HXE25DO	28%		56%	
HCHO	HCHO	50%		32%	
$CH_3C(O)OC*(CH_3)OCH*CHO$	RCHO	12%			
$CH_3C*(OH)CH=CHC(CH_3)(ONO_2)O*$	RHNO3	9%			
$CH_3C(O)OC*=CHC(O)OCH_2*$	OLEP		50%		
$CH_2=C(CHO)OC(O)CH_3$	OLEA1		44%		
CO_2	CO2		37%		
CO	CO		7%		
$CH_2=C(OC(O)CH_3)CH(ONO_2)C(O)OOH$	RCNO3		5%		
$CH_3C*(ONO_2)CH=CHC(O)O*$	RCNO3			69%	
$CH_3C*(ONO_2)CH=CHC(CH_3)(ONO_2)O*$	RDNO3			12%	
NO_2	NO2			12%	
$CH_3C*(CHO)OC(O)C(CH_3)(ONO_2)O*$	RCNO3			4%	
$CH_3C*(ONO_2)OC**(CH_3)OCH**CH*ONO_2$	RDNO3			2%	

[a] The symbols "*" and "**" are used to indicate groups that are bonded in ring structures.

[b] Model species used to represent these products. Underlined species indicate new model species added in this work to represent compounds explicitly. Non-underlined species are existing SAPRC-18 explicit or lumped model species.

[c] Product yields in the presence of NO_x, under conditions where reaction with NO dominates over other bimolecular reactions. Not shown are: products not formed in yields > 2% in any reactions shown, secondary products other than those from the rapid photolysis of dicarbonyl products, and products from the thermal reactions of the photoreactive products. See Table B4 in the Appendix B for a complete list of products, and the associated model species when implemented using the SAPRC-07/-11 base mechanism.

[d] Yields in the "hv" column are yields from the photolysis of the photoreactive dicarbonyl product (first product listed, where applicable), multiplied by the yield of the dicarbonyl product. Not applicable for 2,5-DMF, whose major dicarbonyl product is assumed not to be photoreactive.

[e] Substituted maleic anhydrides are represented by the maleic anhydride model species. These compounds are relatively unreactive.

Table 2.3 lists the major products predicted when the furans and their major dicarbonyl products react in the presence of NO_x. Yields are estimated based on rate constants for the reaction pathways, assuming that the reactions of peroxy radicals with NO dominate over other bimolecular reactions, and that photolysis is the dominant loss process for the photoreactive dicarbonyls. Peroxy radicals also react with NO_3 radicals, but these reactions are assumed to form the same products as reaction with NO, except that formation of organic nitrates from the addition reaction is assumed not to occur. Products formed in yields of less than 2% in any of the reactions shown, products formed from peroxy + HO_2 reactions, or from non-photolysis reactions of the dicarbonyl products are not shown. These additional products are listed in Table B4 in the Appendix B.

2.3 Chamber Modeling Methods

The furans mechanism was evaluated by simulating 26 furans-NO_x chamber experiments that were carried out in two different environmental chambers during four separate time periods between 1983 and 2011, summarized in Table 4. The chambers, UCR Indoor Teflon Chamber (ITC) and UCR/CE-CERT environmental chamber (hereafter referred to as EPA chamber), and associated measurement techniques, have been described previously (Carter et al., 2005; Carter et al., 1993). These experiments were designed to represent simplified atmospheric conditions (VOC + NO_x) and did not contain additional reactants except as shown in the table. Once the lights were turned on, the reactions were initiated primarily by radical-forming reactions of the furans with O_3 or NO_3, and then by photolysis of the photoreactive products. Calculations and modeling simulations indicated that OH radicals formed from the reactions of H_2O with oxygen atom O(1D), and OH radicals formed from photolysis of background nitrous acid (HONO) in the chamber, played minor roles in these experiments (Carter et al., 1993). The experiments were carried out with additional experiments to characterize light intensity and background and wall effects (Carter et al., 2005; Carter et al., 1993). The data used to evaluate the detailed furans mechanism were time-dependent mixing ratios of O_3 (UV absorption), NO and NO_x (chemiluminescence), and furans (gas chromatography).

The experiments were classified based on the furans precursor, experimental conditions and chamber used (see Table 2.4). The furan-NO_x experiments designated as “Furan-1”, were carried out in 1983 at relatively high reactant concentrations and ~50% RH using ITC chamber with a blacklight light source as described in Carter et al. (1993). The remainder of the furan-NO_x experiments were conducted under dry conditions (RH < 0.1%) in the EPA chamber with either arc light or blacklight light sources (Carter et al., 2005); experiments in the “Furan-2”, “2-MF”, “3-MF” and “2,5-DMF” groups were carried out in 2004-2005 and 2009. The most recent furan-NO_x experiments designated as “Furan-3”, were carried out in 2011 and had ethylene added as a surrogate to represent the chemistry of reactive atmospheric VOCs. All the experiments, except for the “Furan-3” group, have been used for SAPRC-07 and SAPRC-11 evaluations and are described in further detail in associated publications (Carter, 1999, 2009; Carter & Heo, 2013; Carter & Lurmann, 1991; Nakao et al., 2012; Yarwood et al., 2012). The experimental data, input files for modeling experiments, and box model software are available online (Carter, 2017).

Table 2.4: List of chamber experiments used to evaluate model performance.

Group	Run ID	Light	Duration (mins)	RH [f] (%)	NO	NO_2	Furans	Ethylene
					Initial concentration (ppb)			
Furan-1	ITC711	BL[a]	285	50	367	144	423	
	ITC713	BL[a]	360	50	769	206	406	
	ITC715	BL[a]	360	50	391	98	225	
	ITC743	BL[a]	375	50	420	120	389	
Furan-2	EPA355A	Arc [b]	312	Dry	101	7	40	
	EPA355B	Arc [b]	312	Dry	26	~0 [g]	41	
	EPA371A	BL[c]	314	Dry	90	7	37	
	EPA371B	BL[c]	314	Dry	27	1	38	
Furan-3	EPA1402A	BL[d]	288	Dry	3	10	129	1102
	EPA1403A	BL[d]	289	Dry	~0	13	47	981
	EPA1403B	BL[d]	289	Dry	~0	14	50	1056
	EPA1448A	BL[d]	469	Dry	15	~0 [g]	130	878
2-MF	EPA356A	Arc [b]	321	Dry	100	~0 [g]	51	
	EPA356B	Arc [b]	321	Dry	31	2	51	
	EPA996A	BL[e]	509	Dry	40	1	50	
	EPA996B	BL[e]	473	Dry	40	1	50	
	EPA999A	BL[e]	479	Dry	52	~0 [g]	600	
	EPA999B	BL[e]	479	Dry	50	~0[g]	293	
3-MF	EPA358A	Arc [b]	340	Dry	93	7	62	
	EPA358B	Arc [b]	340	Dry	28	2	65	
	EPA359A	BL[c]	308	Dry	96	4	55	
	EPA359B	BL[c]	308	Dry	28	2	55	
	EPA418A	Arc [b]	362	Dry	104	7	48	
	EPA418B	Arc [b]	362	Dry	26	2	49	
2,5-DMF	EPA357A	Arc [b]	294	Dry	96	3	47	
	EPA357B	Arc [b]	294	Dry	22	1	50	

[a] Blacklight, light intensity k_1 (NO_2 photolysis rate as measured by actinometry) = 0.35 min^{-1}.

[b] Argon arc light, k_1 = 0.26 min^{-1}.

[c] Blacklight, k_1 = 0.163 min^{-1}.

[d] Blacklight, k_1 = 0.401 min^{-1}.

[e] Blacklight, k_1 = 0.131 min^{-1}.

[f] Dry condition, RH < 0.1%.

[g] Below detection limit (less than 1 ppb).

Table 2.5: List of model simulations. The mechanisms developed in this work are identified with the label "Standard".

Simulation Label	Mechanism for Furans	Base Mechanism
Lumped_S11Base	Lumped furans mechanism developed before this study [a]	SAPRC-11
Standard_S18Base	Detailed furans mechanism developed in this study [b]	SARPC-18
Standard-NO3_S18Base	Detailed furans mechanism developed in this study [b], NO_3 pathway turned off for furans	SAPRC-18
Standard-O3_S18Base	Detailed furans mechanism developed in this study [b], O_3 pathway turned off for furans	SAPRC-18
ARO2_S11Base	Furans are represented as ARO2 model species [c]	SAPRC-11
Standard_S11Base	Reduced furans mechanism derived from the detailed furans mechanism developed in this study [d]	SAPRC-11
Standard_S07Base	Reduced furans mechanism derived from the detailed furans mechanism developed in this study [d]	SAPRC-07

[a] Table B1.
[b] Table B5.
[c] ARO2 used to represent all furans, aromatics with $kOH > 2\times10^4$ ppm^{-1} min^{-1}.
[d] Table B6.

In this work, model simulations of the chamber experiments were performed for each furan or methylfuran experiment using the SAPRC-18 base mechanism with the detailed furans mechanism, and also using the SAPRC-11 base mechanism with the lumped furan reactions previously used for O_3 reactivity modeling (Table B1). The initial conditions were defined based on the reported experimental conditions and resultant data. Additional sensitivity simulations with the detailed furans mechanism were performed to explore the relative importance of different reaction pathways and the effects of lumping furans with aromatics. The chamber experiments were also modeled using the detailed furans mechanism implemented in the SAPRC-07 and SAPRC-11 base mechanisms. The model simulations carried out in this study are summarized in Table 2.5 and the mechanisms developed in this work are identified with the label “Standard”.

2.4 Results and Discussion

2.4.1 Quantification of model performance

The performance of the detailed furans mechanism implemented with the SAPRC-18 base mechanism was evaluated based on model-measurement comparison of furans mixing ratios and $\Delta([O_3]-[NO])$ values for the chamber experiments summarized in Table 2.4. Final O_3 concentrations were not used as an indicator of model error, because they are highly dependent on the initial concentrations of NO, which are relatively high in these experiments and must be consumed before significant O_3 formation occurs. The quantity $\Delta([O_3]-[NO])$ has been used previously to evaluate the rate of NO oxidation by peroxy radicals (Carter, 1999, 2009, 2020a). The quantity is calculated by: $([O_3]_t - [NO]_t) - ([O_3]_0 - [NO]_0)$, where $[O_3]_0$, $[NO]_0$, $[O_3]_t$, and $[NO]_t$ are the initial and time = t concentrations of O_3 and NO, respectively.

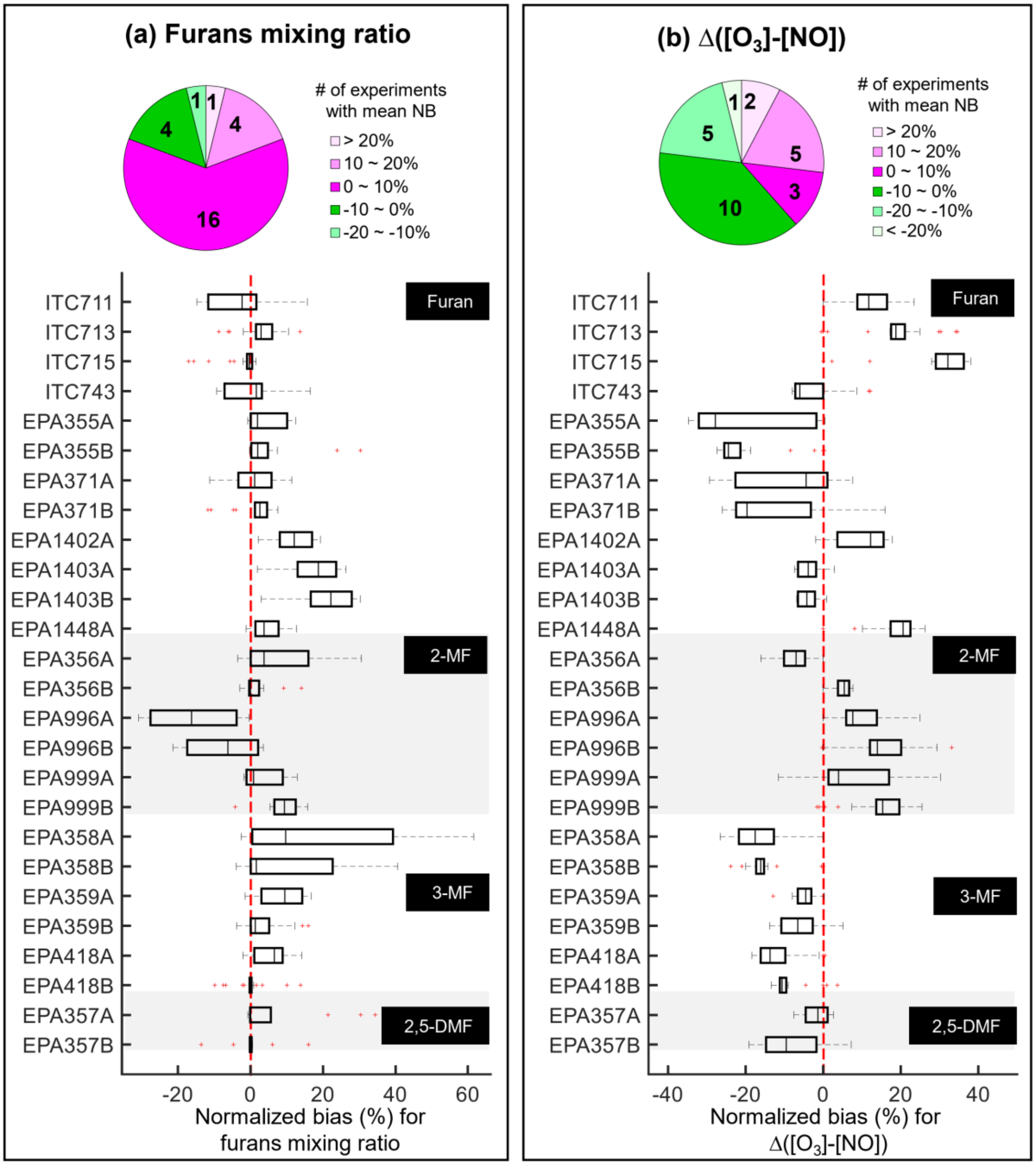

Figure 2.3: Normalized bias for the detailed furans mechanism implemented in the SAPRC-18 base mechanism ("Standard_S18Base"): a) furans mixing ratios; b) Δ([O_3]-[NO]). Pie chart: classification of mean normalized bias by the number of experiments. Box-and-whisker plots: distribution and median of the normalized bias over the duration of the experiment.

Normalized bias (NB) was calculated for the furans mixing ratios and $\Delta([O_3]-[NO])$ values. Figure 2.3 shows the distribution and median of NB values over the duration of each experiment (5-minutes intervals) based on the "Standard_S18Base" simulations. As shown in Figure 2.3a, the mean NB values for furans consumption are within ±20% for 25 (out of 26) experiments; 20 experiments have NB mean values ±10%. The mechanism predicts a slower decay of furans than measured for most experiments; this results in the overestimation of the furans mixing ratio as shown in the Figure 2.3a box plot. For $\Delta([O_3]-[NO])$ shown in Figure 2.3b, 23 (out of 26) experiments had mean NB values ±20%; 13 experiments had mean NB values ±10%. Generally, the mechanism underestimated $\Delta([O_3]-[NO])$ values for the experiments in the "Furan-2", "3-MF", and "2,5-DMF" groups, and overestimated values for the experiments in the "Furan-1" and "2-MF" groups with the exception of ITC743 and EPA356A. Methylfuran simulations typically had smaller model deviations than the furan simulations.

2.4.2 Simulating chamber experiments using the detailed and lumped furans mechanisms

Furan experiments that were assigned to the same group showed similar sensitivity to changes in a mechanism. Therefore, only one experiment from each of the three groups of furan experiments and one of each methylfuran experiments were selected for further discussion. These experiments were chosen because of the relatively small model error when the detailed furans mechanism was applied. This gives increased confidence in the radical level evaluations and sensitivity simulations. Results for all other experiments are presented in the Appendix B.

Figure 2.4 shows the mixing ratio time profiles (furan consumption, O_3 formation, NO decay) for three furan experiments. Chamber data are indicated using solid triangles. The 1st set of simulations ("Lumped_S11Base", blue solid line) were performed using the lumped furans mechanism and the 2nd set of simulations ("Standard_S18Base", red solid line) were performed using the detailed furans mechanism.

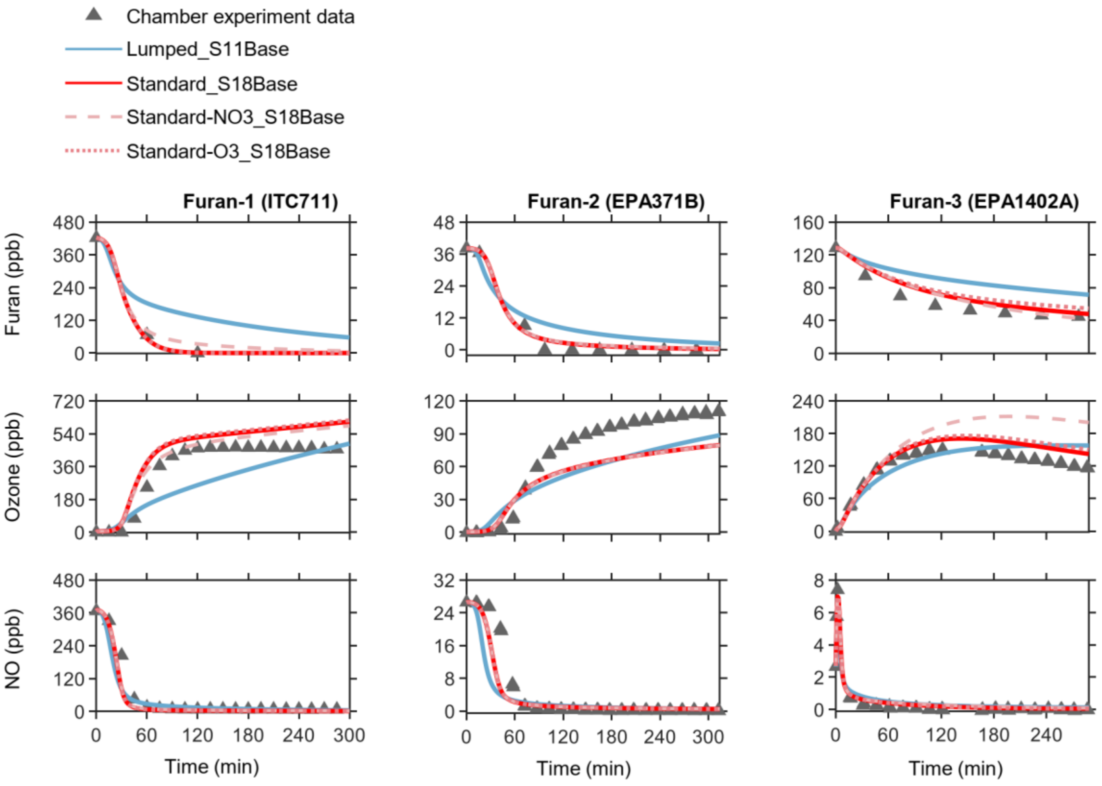

Figure 2.4: Comparison of chamber data (triangles) and model simulation results (lines) for the photooxidation of furan in the presence of NO_x.

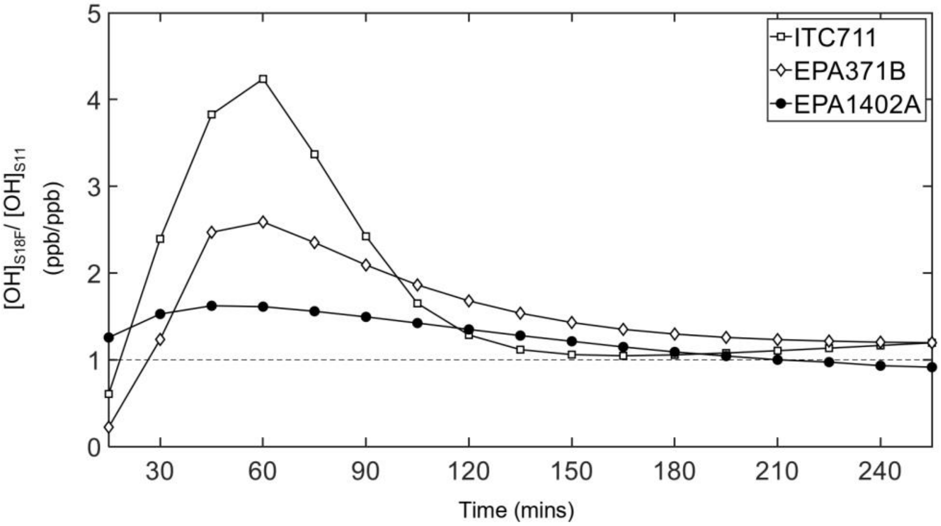

Figure 2.5: The ratio of simulated OH mixing ratios between the detailed furans mechanism ("S18F" short for "Standard_S18Base") and lumped furans mechanism in SAPRC-11 ("S11" short for "Lumped_S11Base") as a function of time (from 15 minutes to 255 minutes, 15-minute intervals).

As shown in Figure 2.4, the "Standard_S18Base" simulation results exhibited improved model performance in predicting the furan consumption rate and final furan mixing ratio compared to "Lumped_S11Base" in all three chamber experiments shown, as well as in the other furan experiments (Figure B4 through Figure B6). At the beginning of the photooxidation period, the "Standard_S18Base" simulation predicted slower furan decay for experiment ITC711 than "Lumped_S11Base" simulations. After approximately 20 minutes, the rate of furan oxidation increased relative to "Lumped_S11Base", such that the net rate of furan decay and overall furan consumption were greater with the detailed mechanism. Similar model behavior was observed for experiment EPA371B. For experiment EPA1402A, the detailed mechanism predicted a faster furan decay than the lumped mechanism throughout the experiment, including at the beginning of the photooxidation period. Figure 2.5 shows the ratio of simulated OH mixing ratios between the "Standard_S18Base" and "Lumped_S11Base" simulations for all three furan experiments. For ITC711, at the onset of photooxidation, the OH concentration was lower with the detailed mechanism; the OH level rapidly increased and after the first 20 minutes, exceeded the "Lumped_S11Base" values. The change of the OH ratio is similar for EPA371B and is consistent with the differences in modeled furan decay shown in Figure 2.4. In contrast, for EPA1402A, the OH mixing ratio calculated using the detailed mechanism was higher than that calculated in "Lumped_S11Base" in the first 3 hours, and then lower (ratio slightly below 1) thereafter.

Given that the reaction rate constant of furan + OH is the same in both mechanisms, the consistency between the time-dependent furan consumption and OH mixing ratio for experiments ITC743 and EPA371B, indicate that OH is the major sink of furan in these experiments (also see Table B7). The improved predictions of furan decay are a consequence of more accurate simulation of OH levels with the detailed mechanism as photooxidation proceeds. Although the photoreactive model species yields used in the "Lumped_S11Base" simulations (Table B1) were adjusted during the model derivation to minimize errors in model simulations of chamber O_3 and NO (Carter & Heo, 2012), the initial rate of NO oxidation was overpredicted and the final O_3 yields were underpredicted. The detailed furans mechanism developed in this work results in better representation of the initial rates of furan consumption and NO oxidation in most of the furan experiments.

The main exceptions to improved model performance with the detailed furans mechanism are the two older ITC furan experiments with the lowest furan/NO_x ratios, where the "Standard_S18Base" simulations overpredicted O_3 formation (also see Figure B4). The "Standard_S18Base" simulations predicted that the total NO had almost reacted away at the end of the experiment even though measurements indicated there was still about tens to one hundred ppb remaining. The relatively small deviation in the NO levels (8% of consumed NO for ITC713 and 6% for ITC715) resulted in large overpredictions of the final O_3 mixing ratios (over 200 %). For experiments in the same group for which the "Standard_S18Base" simulation predicts a more accurate final NO level (ITC711 and ITC743), the O_3 predictions are also more accurate than with the lumped mechanism in SAPRC-11. To illustrate, time profiles of $\Delta([O_3]-[NO])$ in ITC713 and ITC715 are shown in Figure S10; $\Delta([O_3]-[NO])$ values are overpredicted but to a much lesser extent than the final O_3 mixing ratio in Figure B4.

Both mechanisms underestimated O_3 for EPA371B and the other experiments in the "Furan-2" group (Figure 2.4, also see Figure B5). Relative to the "Lumped_S11Base" simulations, the "Standard_S18Base" simulations did not show an improvement in the maximum predicted O_3 mixing ratio. However, the detailed furans mechanism predicted a time profile of O_3 formation that better fit the data, especially in the first hour of EPA371B when the initial oxidation of furan was occurring. While it is known that the reaction pathways and product yields for the later generation products are more uncertain than the initial oxidation products and yields, a specific explanation for the underprediction of final O_3 mixing ratios in the "Furan-2" group could not be determined. The detailed furans mechanism was not tuned to improve the model performance.

The detailed furans mechanism demonstrated marked improvement for simulating EPA1402A and other experiments in the “Furan-3” group (Figure B6). In EPA1402A, the inclusion of 1.1 ppm of ethylene, at almost 10 times the initial furan concentration, promoted effective competition for OH; this reduced the furan decay and the differences in OH levels predicted between the “Standard_S18Base” and “Lumped_S11Base” simulations (Figure 2.5). As with most furan-NO_x experiments, the use of the more detailed furan mechanism improved the model prediction of furan decay in EPA1402A. While the “Lumped_S11Base” simulation results showed a steady increase in O_3 throughout the experiments, the “Standard_S18Base” captured the reduction in O_3 at the end of the experiments. As shown in Figure 2.5, the “Standard_S18Base” simulations predicted that for EPA1402A the OH concentration after 3 hours was slightly lower than that of “Lumped_S11Base”, which did not result in a slower decay rate of furan. This indicates that there are other furan sinks, as discussed further in the following analysis.

Figure 2.6 shows the mixing ratio time profiles for selected 2-MF, 3-MF, and 2,5-DMF experiments, analogous to Figure 2.4 for furan. Similar plots for the other methylfurans experiments are shown in Figure B7 through Figure B9 in Appendix B. The “Standard_S18Base” simulations using the detailed furans mechanism significantly improved model performance as compared to the “Lumped_S11Base” simulations, for all experiments except for EPA358B in which both mechanisms represented furans decay and O_3 formation well. This is in contrast to furan, for which final O_3 yields were better simulated using “Lumped_S11Base” in a few experiments.

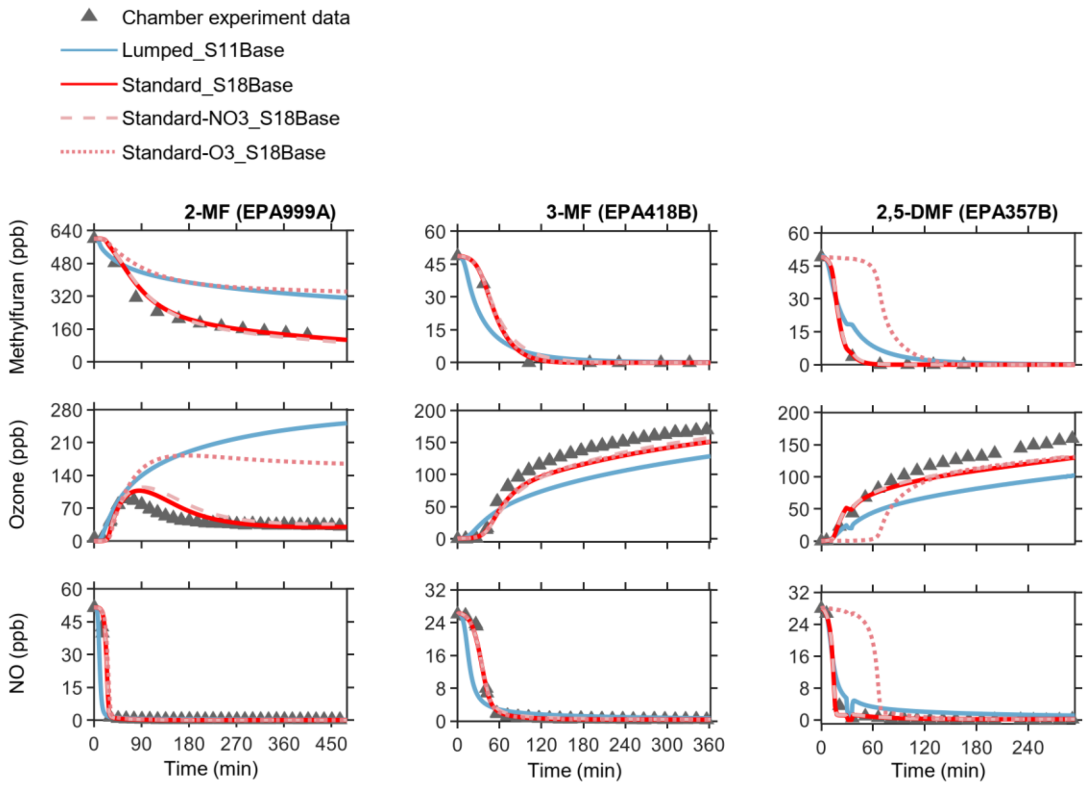

Figure 2.6: Comparison of chamber data (triangles) and box model simulation results (lines) for the photooxidation of methylfurans in the presence of NO$_x$.

2.4.3 Sensitivities to reactions of furans with NO$_3$ and O$_3$

Table 2.6 summarizes the fractions of furans calculated to react with OH, NO$_3$, and O$_3$ in the “Standard_S18Base” simulations; results of the individual experiments are summarized in Table B7. Even though the OH pathway was dominant, non-negligible amounts of furans were oxidized by NO$_3$ and/or O$_3$ except for in the “Furan-2” group experiments. Figure B12 shows the time profiles of the consumption rates during representative experiments, where it can be seen that the NO$_3$ and O$_3$ reactions become non-negligible only in the later stages of the experiments when the initially present NO has been reacted and O_3 formation begins. Since NO_3 is formed by the reaction of O_3 with NO_2, and also reacts rapidly with NO, NO consumption is also necessary before NO_3 levels become non-negligible. Sensitivity simulations were run to evaluate the effects of excluding NO_3- and O_3- initiated oxidation in the detailed furans mechanism. In the "Standard-NO3_S18Base" simulations (Figure 2.4 and Figure 2.6, red dashed lines), NO_3-initiated furans reactions were turned off; in the "Standard-O3_S18Base" simulations (Figure 2.4 and Figure 2.6, red dotted lines), O_3-initiated furans reactions were turned off.

Table 2.6: Fractions of furans reacted with different oxidants for each group of experiments as calculated using the detailed mechanism (see Table B7 and Figure B12 of results for individual experiments).

Group of Experiments	Fractions Furans Reacting with:		
	OH	NO_3	O_3
Furan-1	84 - 92%	7 - 15%	~1%
Furan-2	97 - 100%	0 - 2%	~0%
Furan-3	69 - 78%	10 - 22%	9 - 12%
2-MF	60 - 88%	4 - 13%	2 - 36%
3-MF	83 - 90%	8 - 12%	2 - 5%
2,5-DMF	79 - 85%	~5%	9 - 16%

In the case of furan, when the NO_3-initiated reactions were turned off, only minor differences were observed for most experiments. However, the NO_3-initiated pathway did have observable effects on simulations of EPA1402A and the other experiments in the “Furan-3” group. When the NO_3 pathway was turned off, the formation of the lumped model species for hydroxy nitrates, one of the major sinks of NO_x, was greatly reduced and eventually resulted in higher concentrations of other nitrogen-containing gas-phase compounds leading to overestimation of the final O_3 levels. There was no significant difference when the O_3-initiated furan reactions were turned off, as shown in Figure 2.4 and Figure B4 through Figure B6. The insensitivity to turning off O_3-initiated reactions of furan is supported by the relative unimportance of this pathway predicted by the full mechanism; it does not lead to the formation of new radicals, which then initiate further reactions. For the methylfurans experiments, when the NO_3-initiated reactions were turned off, minimal differences were observed in the simulation results for the three experiments shown in Figure 2.6, as well as the other methylfurans experiments (Figure B7 through Figure B9), with the exception of one 2-MF experiment EPA999B. The relative insensitivity to turning off NO_3-initiated reactions is likely due to the relatively small fraction of methylfurans oxidation by NO_3 relative to OH (Figure 2.6). In addition, when NO_3-initiated reactions were turned off, they were replaced by OH-initiated reactions, and the radical levels were not affected.

In contrast with the furan experiments, the methylfurans experiments sensitivity simulations demonstrated that the O_3-initiated reactions were non-negligible (Figure 2.6). In EPA999A, most of the injected NO (99%) was converted to NO_2 by oxidation with peroxy radicals in approximately 30 minutes. Both the "Standard_S18Base" and the "Standard-O3_S18Base" simulations show temporal profiles of 2-MF, O_3, and NO that are in good agreement with measurement data in the first 30 minutes (Figure 2.6 and Figure B7) and over half of the total 2-MF remained in the chamber. After 30 minutes, O_3 started to take over the oxidation of 2-MF (Figure B12). In EPA999A and EPA999B, approximately 30% of the total 2-MF reacted with O_3. Reaction with O_3 was the major sink in the latter half of the experiment, resulting in a decrease in O_3 (see Figure 2.6), which can also be confirmed by the 2-MF consumption rate shown in Figure B12.

Unlike the other methylfurans, with 2,5-DMF the rates of NO and furans consumption and O_3 formation were grossly underpredicted when the O_3-initiated reactions were turned off. This is largely due to the fact that 3-hexene-2,5-dione, the unsaturated 1,4-dicarbonyl formed in the OH reactions, is a diketone that is believed to be much less photoreactive than the aldehyde-containing dicarbonyls formed from the other furans (Calvert et al., 2011). The relatively unreactive diketone reduces the radical source from this reaction and makes other radical source processes more important. Unlike other furans, the 2,5-DMF + O_3 reaction is assumed to be a major pathway that forms new radicals, and which as demonstrated here has a significant effect on reaction rates in the 2,5-DMF experiments. In addition, the lower OH radical levels caused by the lower dicarbonyl photolysis rates mean that consumption by reaction with O_3 is relatively more important.

In EPA357A and EPA357B, the measured consumption rate of 2,5-DMF (Figure B12) drops suddenly, approximately 30 minutes after the start of the experiment; analysis of the data log reveals that the lights were off at that time for a duration of 10 minutes. When the lights were off in experiment EPA357A, the remaining OH was rapidly reacted away; thereby reducing the consumption rate of 2,5-DMF. One might expect continued decay of 2,5-DMF due to reaction with accumulated NO_3 and/or O_3. However, the NO_3 level was low due to the low level of O_3, which served as the major source of NO_3 (formed from NO_2 + O_3) at this stage of the experiment. Under the relatively high NO_x conditions (EPA357A), the initial oxidation of furans resulted in lower O_3 levels than under the relatively lower NO_x conditions (EPA357B), because O_3 was consumed in the reaction with NO to form NO_2. The differences in the O_3 levels during the first one to two hours of these 2,5-DMF experiments reflect this difference in the higher vs. lower NO_x chemistry. In EPA357A, the consumption of 2,5-DMF did not resume until the lights were turned on again. However, in EPA357B, when the lights were off and OH was rapidly reacted away, the accumulated O_3 was sufficient to drive the oxidation of 2,5-DMF.

2.4.4 Effects of lumping furans with aromatics

Currently, in most chemical transport models used for air quality predictions and atmospheric modeling studies, furans are not represented explicitly but are lumped with more reactive aromatics such as xylenes. In order to assess the performance of this representation in fitting these chamber data, the chamber experiments were simulated using the SAPRC-11 base mechanism with the furans represented by the lumped aromatic model species ARO2. The "ARO2_S11Base" simulations results for O_3 are shown in Figure 2.7 for selected chamber experiments (one of each type is presented in Table 2.4), and in Figure B13 and Figure B14 for all other experiments (green dashed line). It can be seen that this representation approximates the O_3 reactivity of the furans; but the lumped furans mechanism in SAPRC-11 ("Lumped_S11Base") improves model performance (Figure B3), and the detailed mechanism developed in this work ("Standard_S18Base") further improves model performance (Figure B3 and Figure 2.7). The aromatic representation largely underpredicted the oxidation rate of furans in all simulations and gave generally unsatisfactory fits to O_3 formation.

2.4.5 Detailed furans mechanism coupling with SAPRC-07/-11 base mechanisms

Given the widespread use of SARPC-07, a reduced furans mechanism that is compatible with the SAPRC-07 (“Standard_S07Base”) and SAPRC-11 (“Standard_S11Base”) base mechanisms was derived from the detailed furans mechanism developed in this work. The rate coefficients, reaction pathways, and products yields are the same for furans and their major photooxidation products. Because of the changes made to the SAPRC-18 base mechanism relative to the earlier versions of SAPRC, some of the products are represented as different model species in SAPRC-07 and SAPRC-11; these are shown in Table B6. The SAPRC-07 and SAPRC-11 base mechanisms are essentially the same, with the exception of the reactions of aromatics. Since the furans mechanism does not include any aromatics, the reduced furans mechanism can be applied using either base mechanism. This is confirmed by identical simulation results for the 26 chamber experiments using “Standard_S07Base” and “Standard_S11Base”; only the “Standard_S11Base” simulations are presented here.

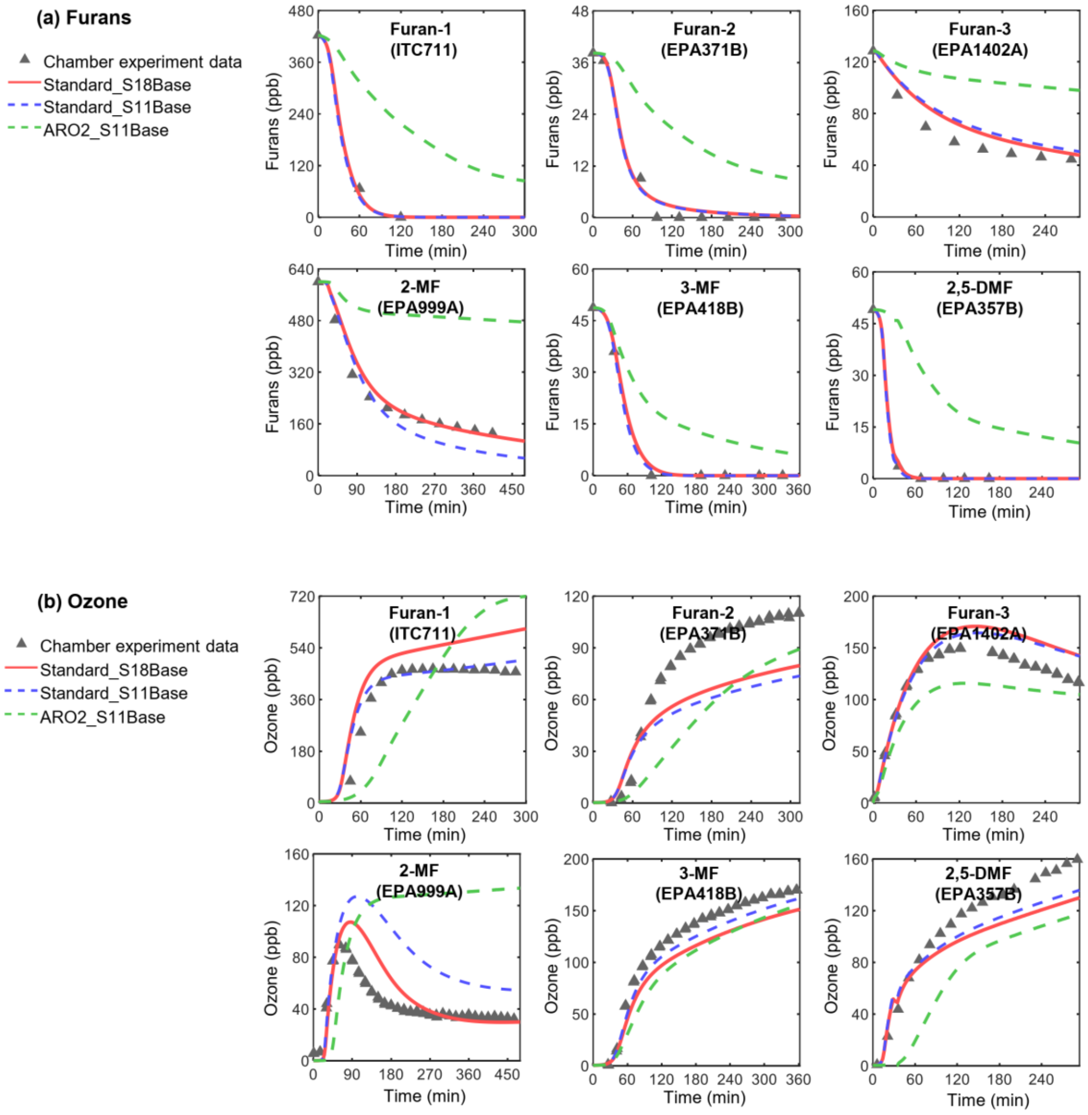

Figure 2.7: Model simulation comparison for representative furan and methylfuran experiments using the standard mechanisms developed in this work and the mechanism where furans are lumped with higher aromatics: a) furans, b) O_3.

The relative performance of the detailed furans mechanism coupled with the SAPRC-18 and SAPRC-11 base mechanisms in simulating chamber experiments is shown in Figure 2.7 for selected experiments, and Figure B13 (furans mixing ratio time profiles) and Figure B14 (O_3 time profiles) for all other experiments. While the “Standard_S11Base” configuration resulted in lower O_3 levels for the ITC furan experiments and higher O_3 levels for 2-MF experiments (EPA999A and EPA999B) compared to the “Standard_S18Base” configuration, the performance of the two mechanisms was consistent, producing similar time profiles for all measured constituents. The consistency of model performance with the SAPRC-18 and SAPRC-07/-11 base mechanisms, as well as the improved performance relative to the lumped furans mechanism with the SAPRC-11 base mechanism, support current and future applicability and compatibility of the detailed furans mechanism developed in this work.

2.5 Conclusions

A detailed gas-phase furans chemical mechanism was developed in this work using a combination of published experimental data and molecular modeling simulations, and the SAPRC mechanism generation system, MechGen (Carter, 2020b). The mechanism was evaluated based on model-measurement comparison of furans decay, O_3 formation, and NO oxidation rates in 26 environmental chamber experiments carried out between 1983 and 2011. The skill in capturing the measured time profiles is directly related to the skill in approximating radical levels, which is critical for models in which gas-phase chemical mechanisms are used. The detailed furans mechanism performs significantly better than the simplified and approximate representations that are currently available.

Model simulations and analysis demonstrated that the high reactivity observed in furan, 2-MF, and 3-MF experiments was due to the rapid photolysis of the unsaturated 1,4-dicarbonyls formed in the OH-initiated reactions. Although absorption cross sections of representative dicarbonyls have been measured and data are available on their overall photolysis rates in sunlight, uncertainties exist regarding the dependencies of the quantum yields on wavelength and effects of structure on the measured photolysis rates (Calvert et al., 2011). 2,5-DMF differs from the other furans studied in that the predicted dicarbonyl product, 3-hexene-2,5-dione, is expected to be much less photoreactive than the unsaturated 1,4-dicarbonyls formed from by other furans. The detailed mechanism also predicts less reactive products, such as hydroxyfuranones and epoxides, are formed in comparable or higher yields than the dicarbonyls. Mechanisms for these hydroxyfuranone and epoxide products have not been published and thus were derived here solely using various structure-reactivity estimation methods incorporated into MechGen. The uncertainty associated with using MechGen to derive these reactions is considered to be less important in simulating gas-phase furans chemistry than the uncertainties associated with the photolysis rates, products, and yields of the more reactive dicarbonyls.

During the daytime, the major sinks of furans are OH-initiated reactions, but reactions of furans with NO_3 and O_3 can become non-negligible under conditions of high O_3. Reactions with O_3 were found to be particularly important in initiating reactivity in experiments with 2,5-DMF, because of the assumed lack of photoreactivity of the unsaturated diketone product. The fact that the lumped mechanism ("Lumped_S11Base") can approximately predict initial 2,5-DMF and NO consumption rates, despite the absence of the O_3 pathway, is a result of compensating errors created when the yields of photoreactive model species were adjusted to improve the simulation results (Carter, 2009). This illustrates the potential danger of using oversimplified mechanisms with adjustable parameters. Although rate constants for furans with NO_3 and O_3 have been measured, products and yields of these reactions have not been well studied, and thus were estimated in this work. The effects of the uncertainties in products and yields have not been assessed and will depend on atmospheric conditions.

Further evaluation of the detailed furans mechanism will require additional data, which are currently unavailable. The chamber experiments used in this work were focused on assessing O_3 reactivity, and the available data were insufficient to evaluate predicted product yields. In addition, the experiments were carried out with relatively high reactant concentrations and simpler reactant mixtures than exist in the atmosphere, and are not sufficient to thoroughly evaluate the mechanism under low NO_x conditions. Some confidence in the mechanism for predicting photooxidation of furans under low NO_x conditions can be gained by looking at the extent to which peroxy radicals reacted with NO relative to other pathways (i.e., HO_2), as summarized in Table B7 for all the experiments. Even in those experiments for which a sufficient amount of peroxy radicals reacted with HO_2 (up to ~50%), furans decay and O_3 formation were well represented by the mechanism. Within the experimental and mechanism uncertainties, the detailed mechanism is consistent with the available experimental data.

Despite the uncertainties, the detailed furans mechanism represents the current state of the science. It is not completely explicit in that the reactions of most of the minor and 2nd generation products are represented by lumped model species, but the initial reactions of furans, and the reactions of their major dicarbonyl and hydroxyfuranone products are represented explicitly. The detailed furans mechanism may have more reactions and products than necessary for many model applications. Future work will focus on the development and evaluation of a condensed version of the detailed furans mechanism, including over a wider range of atmospherically relevant conditions.

References

Abatzoglou, J. T., & Williams, A. P. (2016). Impact of anthropogenic climate change on wildfire across western US forests. *Proceedings of the National Academy of Sciences of the United States of America*, *113*(42), 11770-11775. https://doi.org/10.1073/pnas.1607171113

Alvarado, A., Atkinson, R., & Arey, J. (1996). Kinetics of the gas-phase reactions of NO3 radicals and O3 with 3-methylfuran and the OH radical yield from the O3 reaction. *International Journal of Chemical Kinetics*, *28*(12), 905-909. https://doi.org/10.1002/(SICI)1097-4601(1996)28:12<905::AID-KIN7>3.0.CO;2-R

Alvarado, M. J., & Prinn, R. G. (2009). Formation of ozone and growth of aerosols in young smoke plumes from biomass burning: 1. Lagrangian parcel studies. *Journal of Geophysical Research Atmospheres*, *114*(9), D09306-D09306. https://doi.org/10.1029/2008JD011144

Andreae, M. O., & Merlet, P. (2001). Emission of trace gases and aerosols from biomass burning. *Global Biogeochemical Cycles*, *15*(4), 955-966. https://doi.org/10.1029/2000GB001382

Anglada, J. M. (2008). The Gas Phase HO-Initiated Oxidation of Furan: A Theoretical Investigation on the Reaction Mechanism. *The Open Chemical Physics Journal*, *1*(1), 80-93. https://doi.org/10.2174/1874412500801010080

Aschmann, S. M., Nishino, N., Arey, J., & Atkinson, R. (2011). Kinetics of the Reactions of OH Radicals with 2- and 3-Methylfuran, 2,3- and 2,5-Dimethylfuran, and E- and Z-3-Hexene-2,5-dione, and Products of OH + 2,5-Dimethylfuran. *Environmental Science and Technology*, *45*(5), 1859-1865. https://doi.org/10.1021/es103207k

Aschmann, S. M., Nishino, N., Arey, J., & Atkinson, R. (2014). Products of the OH radical-initiated reactions of furan, 2- and 3-methylfuran, and 2,3- and 2,5-dimethylfuran in the presence of NO. *Journal of Physical Chemistry A*, *118*(2), 457-466. https://doi.org/10.1021/jp410345k

Atkinson, R., Aschmann, S. M., & Carter, W. P. L. (1983). Kinetics of the reactions of O3 and OH radicals with furan and thiophene at 298 ± 2 K. *International Journal of Chemical Kinetics*, *15*(1), 51-61. https://doi.org/10.1002/kin.550150106

Atkinson, R., Aschmann, S. M., Tuazon, E. C., Arey, J., & Zielinska, B. (1989). Formation of 3-Methylfuran from the gas-phase reaction of OH radicals with isoprene and the rate constant for its reaction with the OH radical. *International Journal of Chemical Kinetics*, *21*(7), 593-604. https://doi.org/10.1002/kin.550210709

Bierbach, A., Barnes, I., & Becker, K. H. (1992). Rate coefficients for the gas-phase reactions of hydroxyl radicals with furan, 2-methylfuran, 2-ethylfuran and 2,5-dimethylfuran at 300 ± 2 K. *Atmospheric Environment Part A, General Topics*, *26*(5), 813-817. https://doi.org/10.1016/0960-1686(92)90241-C

Bierbach, A., Barnes, I., & Becker, K. H. (1995). Product and kinetic study of the oh-initiated gas-phase oxidation of Furan, 2-methylfuran and furanaldehydes at ≈ 300 K. *Atmospheric Environment*, *29*(19), 2651-2660. https://doi.org/10.1016/1352-2310(95)00096-H

Bierbach, A., Barnes, I., Becker, K. H., & Wiesen, E. (1994). Atmospheric chemistry of unsaturated carbonyls: butenedial, 4-oxo-2-pentenal, 3-hexene-2,5-dione, maleic anhydride, 3h-furan-2-one, and 5-methyl-3h-furan-2-one. *Environmental Science and Technology*, *28*(4), 715-729. https://doi.org/10.1021/es00053a028

Brégonzio-Rozier, L., Siekmann, F., Giorio, C., Pangui, E., Morales, S. B., Temime-Roussel, B., Gratien, A., Michoud, V., Ravier, S., Cazaunau, M., Tapparo, A., Monod, A., & Doussin, J. F. (2015). Gaseous products and secondary organic aerosol formation during long term oxidation of isoprene and methacrolein. *Atmospheric Chemistry and Physics*, *15*(6), 2953-2968. https://doi.org/10.5194/acp-15-2953-2015

Cabañas, B., Baeza, M. T., Salgado, S., Martín, P., Taccone, R., & Martínez, E. (2004). Oxidation of heterocycles in the atmosphere: Kinetic study of their reactions with NO3 radical. *Journal of Physical Chemistry A*, *108*(49), 10818-10823. https://doi.org/10.1021/jp046524t

Cabañas, B., Villanueva, F., Martín, P., Baeza, M. T., Salgado, S., & Jiménez, E. (2005). Study of reaction processes of furan and some furan derivatives initiated by Cl atoms. *Atmospheric Environment*, *39*(10), 1935-1944. https://doi.org/10.1016/j.atmosenv.2004.12.013

Calvert, J., Mellouki, A., & Orlando, J. (2011). *Mechanisms of Atmospheric Oxidation of the Oxygenates*. https://doi.org/10.15713/ins.mmj.3

Calvert, J. G., Orlando, J. J., Stockwell, W. R., & Wallington, T. J. (2015). *The Mechanisms of Reactions Infuencing Atmospheric Ozone*. https://doi.org/10.15713/ins.mmj.3

Carter, W. P. L. (1999). Documentation of the SAPRC-99 Chemical Mechanism for VOC Reactivity Assessment. *Assessment*, *1*, 329-329. http://www.engr.ucr.edu.oca.ucsc.edu/~carter/pubs/s99doc.pdf

Carter, W. P. L. (2009). *Development of the SAPRC-07 Chemical Mechanism and Updated Ozone Reactivity Scales; Final report to the California Air Resources Board Contract No. 03-318, March 2009*. https://intra.engr.ucr.edu/~carter/SAPRC/

Carter, W. P. L. (2015). Development of a database for chemical mechanism assignments for volatile organic emissions. *Journal of the Air and Waste Management Association*, *65*(10), 1171-1184. https://doi.org/10.1080/10962247.2015.1013646

Carter, W. P. L. (2016). *Development of an Improved Chemical Speciation Database for Processing Emissions of Volatile Organic Compounds for Air Quality Models*. http://intra.engr.ucr.edu/~carter/emitdb/

Carter, W. P. L. (2017). *SAPRC-07 and SAPRC-11 Chemical Mechanisms, Test Simulations, and Environmental Chamber Simulation Files*. https://www.cert.ucr.edu/~carter/SAPRC/SAPRCfiles.htm

Carter, W. P. L. (2020a). *Documentation of the SAPRC-18 Mechanism; Report to California Air Resources Board Contract No. 11-761, May, 2020*. https://intra.engr.ucr.edu/~carter/SAPRC/18/

Carter, W. P. L. (2020b). *Estimates and Assignments used in the SAPRC-18 Mechanism Generation System; Report to California Air Resources Board Contract No. 11-761. In preparation. When completed, will be available at http://intra.engr.ucr.edu/~carter/SAPRC/18*.

Carter, W. P. L. (2020c). *Gateway to the SAPRC Mechanism Generation System*. http://mechgen.cert.ucr.edu/

Carter, W. P. L., Cocker, D. R., Fitz, D. R., Malkina, I. L., Bumiller, K., Sauer, C. G., Pisano, J. T., Bufalino, C., & Song, C. (2005). A new environmental chamber for evaluation of gas-phase chemical mechanisms and secondary aerosol formation. *Atmospheric Environment*, *39*(40), 7768-7788. https://doi.org/10.1016/j.atmosenv.2005.08.040

Carter, W. P. L., & Heo, G. (2012). *Development of revised SAPRC aromatics mechanisms. Final Report to the California Air Resources Board, Contracts No. 07-730 and 08-326, April 2012*. https://intra.engr.ucr.edu/~carter/SAPRC/saprc11.pdf

Carter, W. P. L., & Heo, G. (2013). Development of revised SAPRC aromatics mechanisms. *Atmospheric Environment*, *77*, 404-414. https://doi.org/10.1016/j.atmosenv.2013.05.021

Carter, W. P. L., Luo, D., & Malkina, I. L. (2010). *"Investigation of Atmospheric Reactivities of Selected Consumer Product VOCs", Final Report to California Air Resources Board Contract No. 95-308, May 2010.* http://intra.engr.ucr.edu/~carter/absts.htm#cpreport

Carter, W. P. L., Luo, D., Malkina, I. L., & Fitz, D. (1993). *The University of California, Riverside Environmental Chamber Data Base for Evaluating Oxidant Mechanism. Indoor Chamber Experiments through 1993; Report submitted to the U. S. Environmental Protection Agency, EPA/AREAL*. http://intra.engr.ucr.edu/~carter/absts.htm#databas

Carter, W. P. L., & Lurmann, F. W. (1991). Evaluation of a detailed gas-phase atmospheric reaction mechanism using environmental chamber data. *Atmospheric Environment. Part A. General Topics*, *25*(12), 2771-2806. https://doi.org/10.1016/0960-1686(91)90206-M

Ciccioli, P., Brancaleoni, E., Frattoni, M., Cecinato, A., & Pinciarelli, L. (2001). Determination of volatile organic compounds (VOC) emitted from biomass burning of Mediterranean vegetation species by GC-MS. *Analytical Letters*, *34*(6), 937-955. https://doi.org/10.1081/AL-100103604

Coggon, M. M., Lim, C. Y., Koss, A. R., Sekimoto, K., Yuan, B., Gilman, J. B., Hagan, D. H., Selimovic, V., Zarzana, K. J., Brown, S. S., M Roberts, J., Müller, M., Yokelson, R., Wisthaler, A., Krechmer, J. E., Jimenez, J. L., Cappa, C., Kroll, J. H., De Gouw, J., & Warneke, C. (2019). OH chemistry of non-methane organic gases (NMOGs) emitted from laboratory and ambient biomass burning smoke: Evaluating the influence of furans and oxygenated aromatics on ozone and secondary NMOG formation. *Atmospheric Chemistry and Physics*, *19*(23), 14875-14899. https://doi.org/10.5194/ACP-19-14875-2019

Decker, Z. C. J., Zarzana, K. J., Coggon, M., Min, K. E., Pollack, I., Ryerson, T. B., Peischl, J., Edwards, P., Dubé, W. P., Markovic, M. Z., Roberts, J. M., Veres, P. R., Graus, M., Warneke, C., De Gouw, J., Hatch, L. E., Barsanti, K. C., & Brown, S. S. (2019). Nighttime Chemical Transformation in Biomass Burning Plumes: A Box Model Analysis Initialized with Aircraft Observations. *Environmental Science and Technology*, *53*(5), 2529-2538. https://doi.org/10.1021/acs.est.8b05359

Eldeeb, M. A., & Akih-Kumgeh, B. (2018). Recent Trends in the Production, Combustion and Modeling of Furan-Based Fuels. *Energies*, *11*(3), 512. https://www.mdpi.com/1996-1073/11/3/512

Francisco-Márquez, M., Raúl Alvarez-Idaboy, J., Galano, A., & Vivier-Bunge, A. (2005). A possible mechanism for furan formation in the tropospheric oxidation of dienes. *Environmental Science and Technology*, *39*(22), 8797-8802. https://doi.org/10.1021/es0500714

Fry, J. L., Kiendler-Scharr, A., Rollins, A. W., Wooldridge, P. J., Brown, S. S., Fuchs, H., Dubé, W., Mensah, A., Dal Maso, M., Tillmann, R., Dorn, H. P., Brauers, T., & Cohen, R. C. (2009). Organic nitrate and secondary organic aerosol yield from NO3 oxidation of β-pinene evaluated using a gas-phase kinetics/aerosol partitioning model. *Atmospheric Chemistry and Physics*, *9*(4), 1431-1449. https://doi.org/10.5194/acp-9-1431-2009

Gilman, J. B., Lerner, B. M., Kuster, W. C., Goldan, P. D., Warneke, C., Veres, P. R., Roberts, J. M., De Gouw, J. A., Burling, I. R., & Yokelson, R. J. (2015). Biomass burning emissions and potential air quality impacts of volatile organic compounds and other trace gases from fuels common in the US. *Atmospheric Chemistry and Physics*, *15*(24), 13915-13938. https://doi.org/10.5194/acp-15-13915-2015

Gómez Alvarez, E., Borrás, E., Viidanoja, J., & Hjorth, J. (2009). Unsaturated dicarbonyl products from the OH-initiated photo-oxidation of furan, 2-methylfuran and 3-methylfuran. *Atmospheric Environment*, *43*(9), 1603-1612. https://doi.org/10.1016/j.atmosenv.2008.12.019

Guenther, A., Karl, T., Harley, P., Wiedinmyer, C., Palmer, P. I., & Geron, C. (2006). Estimates of global terrestrial isoprene emissions using MEGAN (Model of Emissions of Gases and Aerosols from Nature). *Atmospheric Chemistry and Physics*, *6*(11), 3181-3210. https://doi.org/10.5194/acp-6-3181-2006

Hartikainen, A., Yli-Pirilä, P., Tiitta, P., Leskinen, A., Kortelainen, M., Orasche, J., Schnelle-Kreis, J., Lehtinen, K. E. J., Zimmermann, R., Jokiniemi, J., & Sippula, O. (2018). Volatile organic compounds from logwood combustion: emissions and transformation under dark and photochemical aging conditions in a smog chamber. *Environmental Science and Technology*, *52*(8), 4979-4988. https://doi.org/10.1021/acs.est.7b06269

Harvey, B. J. (2016). Human-caused climate change is now a key driver of forest fire activity in the western United States. In *Proceedings of the National Academy of Sciences of the United States of America* (Vol. 113, pp. 11649-11650): National Academy of Sciences.

Hatch, L. E., Luo, W., Pankow, J. F., Yokelson, R. J., Stockwell, C. E., & Barsanti, K. C. (2015). Identification and quantification of gaseous organic compounds emitted from biomass burning using two-dimensional gas chromatography-time-of-flight mass spectrometry. *Atmospheric Chemistry and Physics*, *15*(4), 1865-1899. https://doi.org/10.5194/acp-15-1865-2015

Hatch, L. E., Yokelson, R. J., Stockwell, C. E., Veres, P. R., Simpson, I. J., Blake, D. R., Orlando, J. J., & Barsanti, K. C. (2017). Multi-instrument comparison and compilation of non-methane organic gas emissions from biomass burning and implications for smoke-derived secondary organic aerosol precursors. *Atmospheric Chemistry and Physics*, *17*(2), 1471-1489. https://doi.org/10.5194/acp-17-1471-2017

Jenkin, M. E., Young, J. C., & Rickard, A. R. (2015). The MCM v3.3.1 degradation scheme for isoprene. *Atmospheric Chemistry and Physics*, *15*(20), 11433-11459. https://doi.org/10.5194/acp-15-11433-2015

Ji, Y., Zhao, J., Terazono, H., Misawa, K., Levitt, N. P., Li, Y., Lin, Y., Peng, J., Wang, Y., Duan, L., Pan, B., Zhang, F., Feng, X., An, T., Marrero-Ortiz, W., Secrest, J., Zhang, A. L., Shibuya, K., Molina, M. J., & Zhang, R. (2017). Reassessing the atmospheric oxidation mechanism of toluene. *Proceedings of the National Academy of Sciences of the United States of America*, *114*(31), 8169-8174. https://doi.org/10.1073/pnas.1705463114

Jiang, C., Wang, C., Xu, H., Liu, H., & Ma, X. (2021). Engine performance and emissions of furan-series biofuels under stratified lean-burn combustion mode. *Fuel*, *285*, 119113. https://doi.org/https://doi.org/10.1016/j.fuel.2020.119113

Joo, T., Rivera-Rios, J. C., Takeuchi, M., Alvarado, M. J., & Ng, N. L. (2019). Secondary Organic Aerosol Formation from Reaction of 3-Methylfuran with Nitrate Radicals. *ACS Earth and Space Chemistry*, *3*(6), 922-934. https://doi.org/10.1021/acsearthspacechem.9b00068

Kind, I., Berndt, T., Böge, O., & Rolle, W. (1996). Gas-phase rate constants for the reaction of NO3 radicals with furan and methyl-substituted furans. *Chemical Physics Letters*, *256*(6), 679-683. https://doi.org/10.1016/0009-2614(96)00513-1

Laothawornkitkul, J., Taylor, J. E., Paul, N. D., & Hewitt, C. N. (2009). Biogenic volatile organic compounds in the Earth system: Tansley review. *New Phytologist*, *183*(1), 27-51. https://doi.org/10.1111/j.1469-8137.2009.02859.x

Liu, X., Huey, L. G., Yokelson, R. J., Selimovic, V., Simpson, I. J., Müller, M., Jimenez, J. L., Campuzano-Jost, P., Beyersdorf, A. J., Blake, D. R., Butterfield, Z., Choi, Y., Crounse, J. D., Day, D. A., Diskin, G. S., Dubey, M. K., Fortner, E., Hanisco, T. F., Hu, W., King, L. E., Kleinman, L., Meinardi, S., Mikoviny, T., Onasch, T. B., Palm, B. B., Peischl, J., Pollack, I. B., Ryerson, T. B., Sachse, G. W., Sedlacek, A. J., Shilling, J. E., Springston, S., St. Clair, J. M., Tanner, D. J., Teng, A. P., Wennberg, P. O., Wisthaler, A., & Wolfe, G. M. (2017). Airborne measurements of western U.S. wildfire emissions: Comparison with prescribed burning and air quality implications. *Journal of Geophysical Research*, *122*(11), 6108-6129. https://doi.org/10.1002/2016JD026315

Liu, X., Jeffries, H. E., & Sexton, K. G. (1999). Atmospheric photochemical degradation of 1,4-unsaturated dicarbonyls. *Environmental Science and Technology*, *33*(23), 4212-4220. https://doi.org/10.1021/es990469y

Martín, P., Cabañas, B., Colmenar, I., Salgado, M. S., Villanueva, F., & Tapia, A. (2013). Reactivity of E-butenedial with the major atmospheric oxidants. *Atmospheric Environment*, *70*, 351-360. https://doi.org/10.1016/j.atmosenv.2013.01.041

Matsumoto, J. (2011). Kinetics of the reactions of ozone with 2,5-dimethylfuran and its atmospheric implications. *Chemistry Letters*, *40*(6), 582-583. https://doi.org/10.1246/cl.2011.582

Nakao, S., Liu, Y., Tang, P., Chen, C. L., Zhang, J., & Cocker, D. R. (2012). Chamber studies of SOA formation from aromatic hydrocarbons: observation of limited glyoxal uptake. *Atmospheric Chemistry and Physics*, *12*(9), 3927-3937. https://doi.org/10.5194/acp-12-3927-2012

Newland, M. J., Rea, G. J., Thüner, L. P., Henderson, A. P., Golding, B. T., Rickard, A. R., Barnes, I., & Wenger, J. (2019). Photochemistry of 2-butenedial and 4-oxo-2-pentenal under atmospheric boundary layer conditions. *Physical Chemistry Chemical Physics*, *21*(3), 1160-1171. https://doi.org/10.1039/c8cp06437g

Paulson, S. E., Flagan, R. C., & Seinfeld, J. H. (1992a). Atmospheric photooxidation of isoprene part I: The hydroxyl radical and ground state atomic oxygen reactions. *International Journal of Chemical Kinetics*, *24*(1), 79-101. https://doi.org/10.1002/kin.550240109

Paulson, S. E., Flagan, R. C., & Seinfeld, J. H. (1992b). Atmospheric photooxidation of isoprene part II: The ozone-isoprene reaction. *International Journal of Chemical Kinetics*, *24*(1), 103-125. https://doi.org/10.1002/kin.550240110

Paulson, S. E., & Seinfeld, J. H. (1992). Development and evaluation of a photooxidation mechanism for isoprene. *Journal of Geophysical Research*, *97*(D18), 20703-20703. https://doi.org/10.1029/92jd01914

Román-Leshkov, Y., Barrett, C. J., Liu, Z. Y., & Dumesic, J. A. (2007). Production of dimethylfuran for liquid fuels from biomass-derived carbohydrates. *Nature*, *447*(7147), 982-985. https://doi.org/10.1038/nature05923

Sprengnether, M., Demerjian, K. L., Donahue, N. M., & Anderson, J. G. (2002). Product analysis of the OH oxidation of isoprene and 1,3-butadiene in the presence of NO. *Journal of Geophysical Research Atmospheres*, *107*(15), 4268-4268. https://doi.org/10.1029/2001JD000716

Stockwell, W. R., Middleton, P., Chang, J. S., & Xiaoyan, T. (1990). The second generation regional acid deposition model chemical mechanism for regional air quality modeling. *Journal of Geophysical Research*, *95*(D10). https://doi.org/10.1029/jd095id10p16343

Strollo, C. M., & Ziemann, P. J. (2013). Products and mechanism of secondary organic aerosol formation from the reaction of 3-methylfuran with OH radicals in the presence of NOx. *Atmospheric Environment*, *77*, 534-543. https://doi.org/10.1016/j.atmosenv.2013.05.033

Tang, Y., & Zhu, L. (2005). Photolysis of butenedial at 193, 248, 280, 308, 351, 400, and 450 nm. *Chemical Physics Letters*, *409*(4-6), 151-156. https://doi.org/10.1016/j.cplett.2005.05.007

Tapia, A., Villanueva, F., Salgado, M. S., Cabañas, B., Martínez, E., & Martín, P. (2011). Atmospheric degradation of 3-methylfuran: kinetic and products study. *Atmospheric Chemistry and Physics*, *11*(7), 3227-3241. https://doi.org/10.5194/acp-11-3227-2011

Thewes, M., Muether, M., Pischinger, S., Budde, M., Brunn, A., Sehr, A., Adomeit, P., & Klankermayer, J. (2011). Analysis of the impact of 2-methylfuran on mixture formation and combustion in a direct-injection spark-ignition engine. *Energy and Fuels*, *25*(12), 5549-5561. https://doi.org/10.1021/ef201021a

Togbé, C., Tran, L. S., Liu, D., Felsmann, D., Oßwald, P., Glaude, P. A., Sirjean, B., Fournet, R., Battin-Leclerc, F., & Kohse-Höinghaus, K. (2014). Combustion chemistry and flame structure of furan group biofuels using molecular-beam mass spectrometry and gas chromatography - Part III: 2,5-Dimethylfuran. *Combustion and Flame*, *161*(3), 780-797. https://doi.org/10.1016/j.combustflame.2013.05.026

Tran, L. S., Togbé, C., Liu, D., Felsmann, D., Oßwald, P., Glaude, P. A., Fournet, R., Sirjean, B., Battin-Leclerc, F., & Kohse-Höinghaus, K. (2014). Combustion chemistry and flame structure of furan group biofuels using molecular-beam mass spectrometry and gas chromatography - Part II: 2-Methylfuran. *Combustion and Flame*, *161*(3), 766-779. https://doi.org/10.1016/j.combustflame.2013.05.027

Tuazon, E. C., & Atkinson, R. (1990). A product study of the gas-phase reaction of Isoprene with the OH radical in the presence of NOx. *International Journal of Chemical Kinetics*, *22*(12), 1221-1236. https://doi.org/10.1002/kin.550221202

Tuazon, E. C., Atkinson, R., & Carter, W. P. L. (1985). Atmospheric chemistry of cis-and trans-3-hexene-2, 5-dione. *Environmental Science and Technology*, *19*(3), 265-269. https://doi.org/10.1021/es00133a009

Wang, C., Xu, H., Daniel, R., Ghafourian, A., Herreros, J. M., Shuai, S., & Ma, X. (2013). Combustion characteristics and emissions of 2-methylfuran compared to 2,5-dimethylfuran, gasoline and ethanol in a DISI engine. *Fuel*, *103*, 200-211. https://doi.org/10.1016/j.fuel.2012.05.043

Wei, H., Feng, D., Shu, G., Pan, M., Guo, Y., Gao, D., & Li, W. (2014). Experimental investigation on the combustion and emissions characteristics of 2-methylfuran gasoline blend fuel in spark-ignition engine. *Applied Energy*, *132*, 317-324. https://doi.org/10.1016/j.apenergy.2014.07.009

Westerling, A. L. R. (2016). Increasing western US forest wildfire activity: Sensitivity to changes in the timing of spring. *Philosophical Transactions of the Royal Society B: Biological Sciences*, *371*(1696), 20150178-20150178. https://doi.org/10.1098/rstb.2015.0178

Xiang, B., Zhu, L., & Tang, Y. (2007). Photolysis of 4-oxo-2-pentenal in the 190-460 nm region. *Journal of Physical Chemistry A*, *111*(37), 9025-9033. https://doi.org/10.1021/jp0739972

Yarwood, G., Heo, G., William, C.-C., Carter, P. L., Gary, C.-C., Whitten, Z., & McDonald-Buller, E. C. (2012). *Environmental Chamber Experiments to Evaluate NOx Sinks and Recycling in Atmospheric Chemical Mechanisms; Final report to AQRP Project 10-042, February 2012*. http://aqrp.ceer.utexas.edu/projectinfo%5C10-042%5C10-042 Final Report.pdf.

Yarwood, G., Rao, S., Yocke, M., & Whitten, G. Z. (2005). *Updates to the Carbon Bond chemical mechanism: CB05; Final report to the U.S. EPA, RT-0400675, December 2005*.

Yokelson, R. J., Karl, T., Artaxo, P., Blake, D. R., Christian, T. J., Griffith, D. W. T., Guenther, A., & Hao, W. M. (2007). The tropical forest and fire emissions experiment: Overview and airborne fire emission factor measurements. *Atmospheric Chemistry and Physics*, *7*(19), 5175-5196. https://doi.org/10.5194/acp-7-5175-2007

Yuan, Y., Zhao, X., Wang, S., & Wang, L. (2017). Atmospheric oxidation of furan and methyl-substituted furans initiated by hydroxyl radicals. *Journal of Physical Chemistry A*, *121*(48), 9306-9319. https://doi.org/10.1021/acs.jpca.7b09741

Ziemann, P. J., & Atkinson, R. (2012). Kinetics, products, and mechanisms of secondary organic aerosol formation. *Chemical Society Reviews*, *41*(19), 6582-6605. https://doi.org/10.1039/c2cs35122f

Chapter 3 Mechanism Development and Evaluation for the Gas-Phase Reactions of Phenolic Compounds under Atmospherically Relevant Conditions

3.1 Introduction

While wildfires are a natural environmental process, they are becoming more frequent and more widespread as a result of human activities and climate change (Abatzoglou & Williams, 2016; Harvey, 2016; Heilman et al., 2014; Mohammed & Mohammed, 2021; Westerling, 2016; Zhuang et al., 2021). Wildfire emissions have a strong influence on climate, tropospheric chemistry, and human health. Specifically, volatile organic compounds (VOCs) released from wildfires undergo oxidation in the troposphere, significantly affecting tropospheric ozone (O_3) and secondary organic aerosols (SOA) levels. Oxygenated aromatics (e.g., benzaldehyde and phenolic compounds) represent a large mass fraction of VOCs emitted from BB; further, of the BB-derived VOCs, their SOA formation potential is among the highest (50~75% depending on the fuel) (Akherati et al., 2020; Derwent et al., 2010; Gilman et al., 2015; Hatch et al., 2017). Phenolic compounds, hereafter referred to as phenols, are also key intermediates from photooxidation of aromatic hydrocarbons in the atmosphere (e.g., 0.03 to 0.385 cresol formation from toluene oxidation with hydroxyl radicals (OH)) (Bloss et al., 2005; Calvert et al., 2002). Thus, accurate representation of the chemistry of these oxygenated aromatics is critical for representing SOA formation when such compounds contribute measurably to emissions.

Table 3.1: Rate coefficients and atmospheric lifetimes for the reactions of OH and NO_3 radicals with selected phenolic compounds at atmospheric pressure and near room temperature (294K ~ 302K).

compound	rate coefficient [a] (10^{-11} cm^3 $molecule^{-1}$ s^{-1})			atmospheric lifetime [c]	
	k_{OH}	k_{NO3}	k_{NO3}/k_{OH}	τ_{OH} (h)	τ_{NO3} (min)
phenol	2.70	0.40	0.15	6.4	8.3
2-methylphenol (o-cresol)	4.10	1.4	0.34	4.2	2.4
3-methylphenol (m-cresol)	6.80	1.1	0.16	2.6	3.0
4-methylphenol (p-cresol)	5.00	1.1	0.22	3.5	3.0
2,3-dimethylphenol (2,3-DMP)	8.30	2.90	0.35	2.1	1.1
2,4-dimethylphenol (2,4-DMP)	7.40	3.12	0.42	2.3	1.1
2,5-dimethylphenol (2,5-DMP)	8.80	3	0.34	2.0	1.1
2,6-dimethylphenol (2,6-DMP)	6.70	4.9	0.73	2.6	0.7
3,4-dimethylphenol (3,4-DMP)	8.30	2.5	0.30	2.1	1.3
3,5-dimethylphenol (3,5-DMP)	11.40	1.1	0.10	1.5	3.0
2,3,5-trimethylphenol	12.50	11.2 [b]	0.90	1.4	0.3
2,3,6-trimethylphenol	11.80	7.48 [b]	0.63	1.5	0.4
1,2-dihydroxybenzene (catechol)	10.40	9.80	0.94	1.7	0.3
1,2-dihydroxy-3-methylbenzene	20.50	17.1	0.83	0.8	0.2
1,2-dihydroxy-4-methylbenzene	15.60	14.7	0.94	1.1	0.2

[a] Based on Calvert et al. (2011) and Thüner et al. (2004).

[b] Estimated by SAPRC mechanism generation system (MechGen) (Carter, 2020b, 2020c).

[c] $\tau_{OH}=1/k_{OH}[OH]$, where 12 h daily average $[OH] = 1.6 \times 10^6$ molecule cm^{-3}; $\tau NO3= 1/k_{NO3}[NO_3]$, where 12 h daily average $[NO_3] = 5 \times 10^8$ molecule cm^{-3}.

The major atmospheric loss processes for phenols are gas-phase reactions with OH and nitrate (NO_3) radicals. There have been a few studies on the oxidation of phenols, with a focus on reaction kinetics (Albarran & Schuler, 2007; Berndt & Böge, 2003; Bolzacchini et al., 2001; Coeur-Tourneur et al., 2006; Lauraguais et al., 2016; Liu et al., 2001; Raghavan & Steenken, 1980; Roger et al., 1992; Sandhiya et al., 2013; Semadeni et al., 1995; Thüner et al., 2004; Zhang et al., 2016). Table 3.1 lists the rate coefficients of selected phenols reacting with OH and NO_3 radicals, and the associated atmospheric lifetimes under ambient conditions. Reactions of phenols in the atmosphere are very rapid and are enhanced by the presence of alkyl substituents on the aromatic ring. The reactivity of phenols increases with the number of substituents –OH or $-CH_3$ groups, as shown in Table 3.1. The position and identity of the –OH and $-CH_3$ substituents on the ring also appears to influence reactivity as well; compounds with the same number of substituents activate the aromatic ring more efficiently with –OH groups (Thüner et al., 2004).

The mechanism of the OH reaction with phenols proceeds by three pathways: 1) addition to the aromatic ring; 2) abstraction of H atom from the OH group; and 3) abstraction of H atoms from alkyl groups attached to the aromatic ring. The dominant pathway under ambient conditions is OH addition, resulting in the formation of dihydroxybenzenes with yields of 70~80% for phenol and 64~73% for cresols (Atkinson et al., 1992; Berndt & Böge, 2003; Olariu et al., 2002). Olariu et al. (2002) compared the reported rate coefficients for the reaction of the OH-adducts with O_2 and NO_2 at atmospheric pressure and room temperature (listed in Table 3.2). While the rate constants for the reaction between the OH-adducts and NO_2 are the same order of magnitude, the rate constants for the O_2 reactions are much faster (> 2 magnitudes larger) for phenol and m-cresol than benzene and toluene, which makes the O_2 pathway even more dominate. For both phenol and creosols, the H-atom abstraction from the –OH group will lead to the formation of nitrophenols with a yield of ~10% (Atkinson, 1994; Kiliç et al., 2007; Lundqvist & Eriksson, 2000; Raghavan & Steenken, 1980; Xu & Wang, 2013). The NO_3 reactions of phenolic compounds proceed via a different mechanism. They mainly appear to occur (at least in part) through net abstraction of H from the –OH group, followed by

NO_2 addition at the adjacent site to form a nitrophenol-type species (Atkinson et al., 1992; Calvert et al., 2011; Mayorga et al., 2020).

Table 3.2: Rate coefficients for the reaction of the OH-adducts with O_2 and NO_2 at atmospheric pressure and room temperature

	rate coefficients (cm^3 s^{-1}) [a]	
adducts	O_2	NO_2
OH-phenol	3.0×10^{-14}	3.6×10^{-11}
OH-m-cresol	8.0×10^{-14}	4.0×10^{-11}
OH-benzene	2.1×10^{-16}	3.6×10^{-11}
OH-toluene	6.0×10^{-16}	3.6×10^{-11}

[a] Rate coefficients are from Olariu et al. (2002) and corresponding references.

The OH-initiated oxidations of phenols and nighttime/dark NO_3-initiated oxidations represent a significant source of SOA formation in the atmosphere (Coeur-Tourneur et al., 2010; Finewax et al., 2018; Frka et al., 2016; Kitanovski et al., 2014; Lauraguais et al., 2016; Mayorga et al., 2020; Nakao et al., 2011; Schwantes et al., 2017; Yee et al., 2013). Large amounts of BrC have been observed in both laboratory and field experiments, which were attributed to the substantial formation of nitrophenol products (Bluvshtein et al., 2017; Fleming et al., 2020; Lin et al., 2017; Lin et al., 2018). Phenols can affect atmospheric oxidant levels due to their short lifetimes, and will rapidly form SOA in the first few hours after emission. Thus, there is an urgent need to account for the emissions of phenols from wildfires, as well as to better represent phenols in chemical mechanisms used to simulate the air quality impacts of wildfires.

SAPRC gas-phase chemical mechanisms, which have been developed at UCR to represent the gas-phase reactions of VOCs with major atmospheric oxidants in the lower troposphere, are among the most widely used chemical mechanisms in current atmospheric models. The most recent version of the SAPRC gas-phase mechanism, SAPRC-18 (Carter, 2020a), includes more model species to represent organic reaction products and is considered to represent the current state of the science. The SAPRC-18 mechanism is further described in Appendix A. Table C1 in Appendix C lists the phenol reactions in the SAPRC-18 base mechanisms and the reaction rate constants at 298K, hereafter referred to as SAPRC-18-STD. PHEN is the model species that represents phenol; CRES is the model species that represents cresol isomers (o-, m-, p-cresol), for which the mechanism was derived based on o-cresol; XYNL is the model species that represents xylenols and higher alkylphenols, for which the mechanism was derived based on 2,4-DMP; SVPHE is the model species that represents unspecified semi-volatile, non-nitrogen-containing products of the reactions of OH and NO_3 with phenolic compounds, for which the mechanism was derived based on catechol. More details about the other model species listed in Table C1 can be found in Carter (2020a). The current phenols mechanism in SAPRC-18-STD is highly simplified and highly parameterized with product model species and parameters adjusted to give best fits to chamber data. The extent to which this mechanism can represent atmospheric reactions of phenols is uncertain and largely untested.

The SAPRC mechanism generation system (MechGen) is a mechanism generator that predicts fully explicit mechanisms for the atmospheric reactions of organic compounds, and the intermediate radicals they form, using estimated rate constants and branching ratios based on group additivity and other estimation methods Carter (2020b). Carter (2020a) and Jiang et al. (2020) have presented MechGen as a tool for developing fully explicit mechanisms for the atmospheric reactions of many types of organic compounds and the intermediate radicals they form. In this work, we derived a new phenols mechanism in which MechGen estimations were supplemented with available published data on branching ratios and product yields (shown in section 3.2). The ability of MechGen to represent reactions of phenols was evaluated by comparing SAPRC box-model simulations with data from environmental chamber experiments previously carried out at the University of California at Riverside (UCR).

3.2 Chemical Mechanism for Phenols

The standard and new mechanisms evaluated in this work are listed in Table 3.3. SAPRC-18-STD already has model species for phenol reactions such as PHEN, SVPHE, CRES, and XYNL (see Table C1), where only PHEN represents a single compound, phenol. The reactions of the model species SVPHE, CRES, and XYNL each were derived from a single compound (catechol in the case of SVPHE, o-cresol in the case of CRES, and 2,4-DMP in the case of XYNL), though they are sed as lumped model species to represent a group of other compounds assigned to them. MG-PHEN refers to the phenols mechanism directly derived from MechGen (Table C2), and MG-PHEN-MOD refers to the modified MG-PHEN based on reported data including rate constants and product yields (Table C3). In MG-PHEN and MG-PHEN-MOD, the model species listed in Table 3.3 only represent single one compound. The MG-PHEN-MOD mechanism was then implemented into SAPRC-18-STD to replace the original mechanism of PHEN and the lumped model species SVPHE, CRES, and XYNL by updating their reactions from MG-PHEN-MOD.

This updated version of SAPRC-18-STD phenols mechanism was named as SAPRC-18-PHEN (Table C4). Furthermore, HCHDO in MG-PHEN-MOD, which represents 2-hydroxy-3,5-cyclohexadienone, was not originally included in SAPRC-18-STD and was added as a new model species in SAPRC-18-PHEN.

Table 3.3: List of phenols mechanisms.

Label of Mechanism		SAPRC-18-STD[a]	MG-PHEN[b]	MG-PHEN-MOD [c]	SAPRC-18-PHEN [d]
Model Species	phenol	PHEN	PHENOL	PHENOL	PHEN
	catechol	SVPHE	CATECHOL	CATECHOL	SVPHE
	2-hydroxy-3,5-cyclohexadienone		HCHDO	HCHDO	HCHDO
	o-cresol	CRES	O-CRESOL	O-CRESOL	CRES
	m-cresol				
	p-cresol				
	2,4-DMP	XYNL	24M-PHEN	24M-PHEN	XYNL

[a] The standard SAPRC-18 mechanism.
[b] MechGen-derived phenols mechanism.
[c] Modified MechGen-derived phenols mechanism: phenol and o-cresol mechanisms are modified based on literature.
[d] Updated SAPRC-18-STD phenols mechanism. Reactions of PHEN, SVPHE, CRES and XYNL were replace by MG-PHEN-MOD; new species HCHDO was added.

3.2.1 Phenol

At atmospherically relevant temperatures, OH addition is considered as dominate for phenol photooxidation under chamber conditions. H-atom abstraction of phenol accounts for around 12% of the OH oxidation at 298 K and less at lower temperatures. In the presence of NO_x, the yield of 6-nitrophenol through phenol + OH is 6%, indicating that at least 6% of the reactions happen through the abstraction pathway (Atkinson et al., 1992;

Olariu et al., 2002). The major OH oxidation product, catechol, can only be formed via the addition pathway, for which addition at the position ortho to the OH substituent is dominant (Olariu et al., 2002; Xu & Wang, 2013). Berndt and Böge (2003) investigated the products of phenol + OH reactions in a flow tube reactor at varying NO_x levels from 266 to 364 K. Catechol (yield of 0.73~0.78), along with 2-nitrophenol, and 1,4-benzoquinone were the major products, consistent with the smog chamber study of Olariu et al. (2002) in which a catechol yield of 0.80 was reported.

Figure 3.1 shows the reaction schematic for the OH-initiated oxidation of phenol at room temperature and atmospheric pressure in which OH addition occurs at the ortho position. From there, three reaction pathways have been identified leading to catechol formation (A~C in Figure 3.1). Most studies have suggested that catechol is formed directly from pathway A, which involves the HO_2-elimination of the phenol RO_2, PHENOL_P1, after the O_2 addition to the radical intermediate PHENOL_A1 (Berndt & Böge, 2003; Calvert et al., 2011; Olariu et al., 2002). Xu and Wang (2013) proposed that the major pathway of PHENOL_P1 undergoes intramolecular H-shift and then HO_2-elimination to form 2-hydroxy-3,5-cyclohexadienone, HCHDO, via pathway B. HCHDO is very unstable, and the presence of water or phenol molecules can aid tautomerization to form catechol quickly (Xu & Wang, 2013). Xu and Wang (2013) also suggested the possibole formation of catechol through the reaction of PHENOL_A1 with NO_2 (through pathway C in Figure 3.1), which is consistant from the observation in the study of Berndt and Böge (2003). They observed the formation of catechol (~35% yield) and 2-nitrophenol (~18% yield) at 0.1 ~ 10 ppm NO_2 in the absence of O_2.

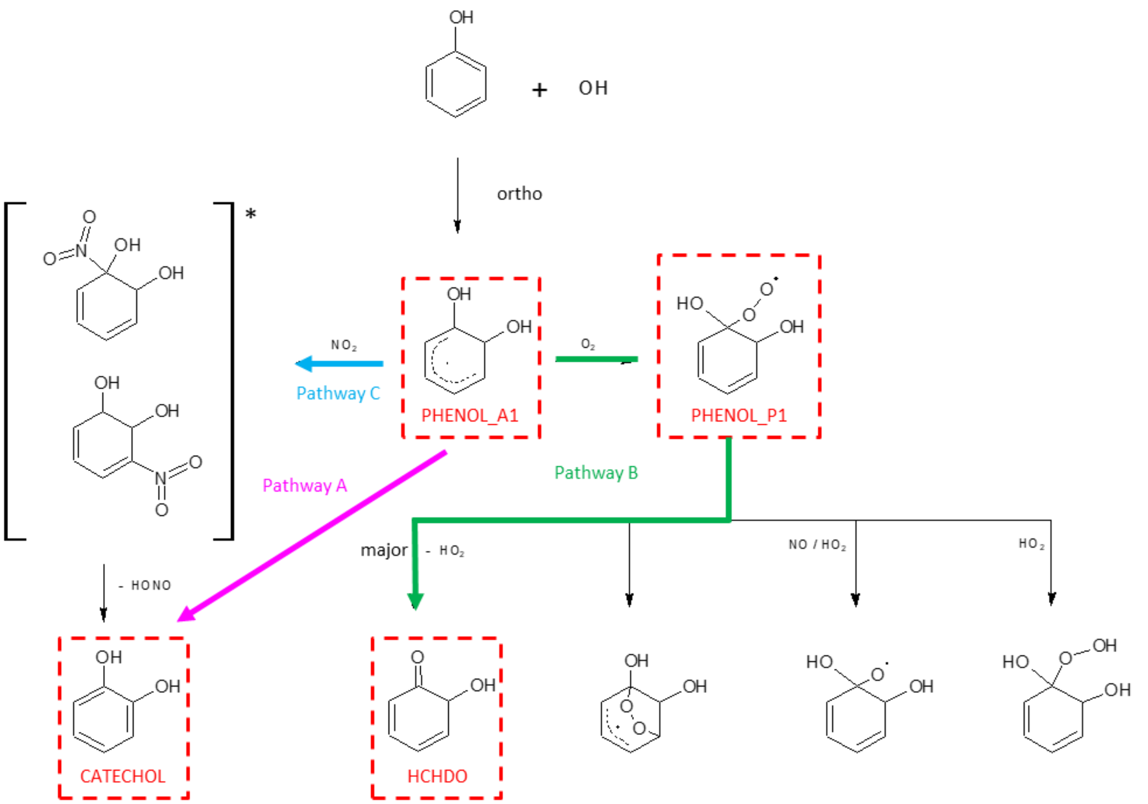

Figure 3.1: Schematic of the OH-initiated oxidation of phenol (ortho addition) at room temperature and atmospheric pressure in the presence of NO_x.

Table 3.4 lists the OH- and NO_3- initiated reactions of phenols directly derived from MechGen in MG-PHEN. Except for catechol and HCHDO, the 1st generation products were all represented by the lumped model species defined by the SAPRC-18 base mechanism. Catechol (“CATECHOL”) and HCHDO were explicitly represented because of their high yields as 1st generation products, with reactions entirely derived from MechGen due to a lack of published data. In MG-PHEN, MechGen predicted a 6.2% fraction for OH abstraction and a 93.8% fraction for OH addition with 49% occurring on the ortho position, which is inconsistent with the values reported in previous studies (Kiliç et al., 2007; Wu et al., 2012; Xu & Wang, 2013).

Table 3.4: OH- and NO_3- initiated oxidation of phenol in MG-PHEN mechanism[a]

Reactions [b]	Rate Constant at 298K (cm^3 $molecule^{-1}$ s^{-1})
PHENOL + OH = #.49 PHENOL _P1 + #.449 HO2 + #.189 XYNL + #.126 OLEA1 + #.104 OLEA2 + #.062 BZO + #.029 OLEP + #-0.91 XC + #.49 SumRO	2.78E-11
PHENOL + NO3 = BZO + XN	4.50E-12
CATECHOL + OH = #.774 HO2 + #.386 OLEP + #.197 CATECHOL_P1 + #.132 OLEA1 + #.123 XYNL + #.087 OLEA2 + #.045 LVKS + #.03 BZO + #-2.228 XC + #.197 SumRO2	6.23E-11
CATECHOL + NO3 = BZO + XN	6.43E-11
HCHDO + OH = #.989 HCHDO_P1 + #.011 BACL + #.011 HO2 + #.022 XC + #.989 SumRO2	1.73E-10
HCHDO + O3 = #.75 AFG2A + #.643 HO2 + #.613 OH + #.25 RCHO + #.137 CO2 + #1.113 XC	3.77E-17
HCHDO + HV = OLEP + CO + #-5 XC	PF=MVK-16

[a] The complete mechanism of MG-PHEN is listed in Table C2.

[b] PHENOL _P1: phenol RO_2 (see Figure 3.1); BZO: phenoxy or substituted phenoxy radicals; XN: lost nitrogen or nitrogen in unreactive products; other species: see Carter (2020a) for more details.

Table 3.5: Modified OH- and NO_3- initiated oxidation of phenol in MG-PHEN-MOD mechanism[a]

Reactions[b]	Rate Constant at 298K (cm^3 $molecule^{-1}$ s^{-1})
PHENOL + OH = #.94 PHENOL _A1 + #.06 BZO	2.78E-11
PHENOL_A1 + O2 = #.25 PHENOL _P1 + #.75 CATECHOL + #.75 HO2	3.10E-14
PHENOL_A1 + NO2 = CATECHOL + HONO	3.60E-11
PHENOL + NO3 = BZO + HNO3	4.50E-12
CATECHOL + OH = #.774 HO2 + #.386 OLEP + #.197 CATECHOL_P1 + #.132 OLEA1 + #.123 XYNL + #.087 OLEA2 + #.045 LVKS + #.03 BZO + #-2.228 XC + #.197 SumRO2	1.04E-10
CATECHOL + NO3 = BZO + XN	9.80E-11

[a] The complete mechanism of MG-PHEN-MOD is listed in Table C3.

[b] PHENOL_A1: phenol alkyl radical (see Figure 3.1); PHEN_P1: phenol RO_2 (see Figure 3.1); BZO: phenoxy or substituted phenoxy radicals; other species: see Carter (2020a) for more details.

In MG-PHEN-MOD, the phenol + OH mechanism in MG-PHEN was modified to be consistent with the literature, and the reactions shown in Figure 3.1 were manually added. The NO_3-initiated oxidation of phenol occurs via abstraction from the –OH group to form a phenoxy radical (BZO) that reacts with NO_2 to form 2-nitrophenol, but the details of the reaction are unknown. As a result, no changes were made other than replacing the model species "XN" with "HNO3" to achieve atom balance. Table 3.5 lists the modified OH- and NO_3- initiated phenol oxidation in MG-PHEN-MOD; the reaction mechanisms of CATECHOL and HCHDO remain unchanged, and the reactions of the intermediates are not shown in the table but are included in the full mechanism show in Table C2. In addition, when compared to reported data, MG-PHEN has much slower rate constants for catechol oxidations. As a result, the rate constants for CATECHOL in MG-PHEN-MOD were adjusted in accordance with Table 3.1.

3.2.2 Cresols

When additional CH_3 groups are added to the aromatic ring in cresols, the oxidation rate coefficient increases significantly when compared to phenol. The reported major products of OH-initiated oxidation of cresols are dihydroxybenzene, benzoquinone and nitrophenol, and with the highest yields of dihydroxybenzene (Figure C9): ~73% yield of 1,2-dihydroxy-3-methylbenzene from o-cresol; ~69% yield of 1,2-dihydroxy-3-methylbenzene and ~10% yield of 1,2-dihydroxy-4-methylbenzen from m-cresol; and ~64% yield of 1,2-dihydroxy-4-methylbenzene from p-cresol (Olariu et al., 2002). The only products identified for the NO_3-initiated oxidation of cresols were nitrophenols, and it is commonly assumed that this is the only pathway. Table 3.6 lists the MG-PHEN o-cresol reactions (OH- and NO_3- initiated oxidations). MechGen predicted a 3.8% fraction for OH abstraction and a 96.2% fraction for OH addition, with 42% occurring on the ortho position, which leads to the formation of 1,2-dihydroxy-3-methylbenzene. These values in MG-PHEN are inconsistent with the findings from previous studies (Olariu et al., 2002; Schwantes et al., 2017).

Table 3.6: OH- and NO_3- initiated oxidation of o-cresol in MG-PHEN mechanism[a]

Reactions[b]	Rate Constant at 298K (cm^3 $molecule^{-1}$ s^{-1})
O-CRESOL + OH = #.542 HO2 + #.42 O-CRESOL_P1 + #.169 OLEP + #.129 OLEA1 + #.114 XYNL + #.07 OLEA2 + #.059 LVKS + #.038 BZO + #-0.716 XC + #.42 SumRO2	4.10E-11
O-CRESOL + NO3 = BZO + XC + XN	1.40E-11

[a] The complete mechanism of MG-PHEN is listed in Table C2.
[b] O-CRESOL_P1: o-cresol RO_2; BZO: phenoxy or substituted phenoxy radicals; XN: lost nitrogen or nitrogen in unreactive products; other species: see Carter (2020a) for more details.

Table 3.7: OH-initiated oxidation of o-cresol in MG-PHEN-MOD mechanism [a]

Reactions[b]	Rate Constant at 298K (cm^3 $molecule^{-1}$ s^{-1})
O-CRESOL + OH = #.73 XYNL + #.73 HO2 + #.2 O-CRESOL_P1 + #.07 BZO + #-0.66 XC + 2 SumRO2	4.10E-11

[a] The complete mechanism of MG-PHEN-MOD is listed in Table C3.
[b] O-CRESOL_P1: o-cresol RO_2 (see Figure 3.1); XYNL: xylenols and higher alkylphenols; BZO: phenoxy or substituted phenoxy radicals; XC: Lost Carbon or carbon in unreactive products; other species: see Carter (2020a) for more details.

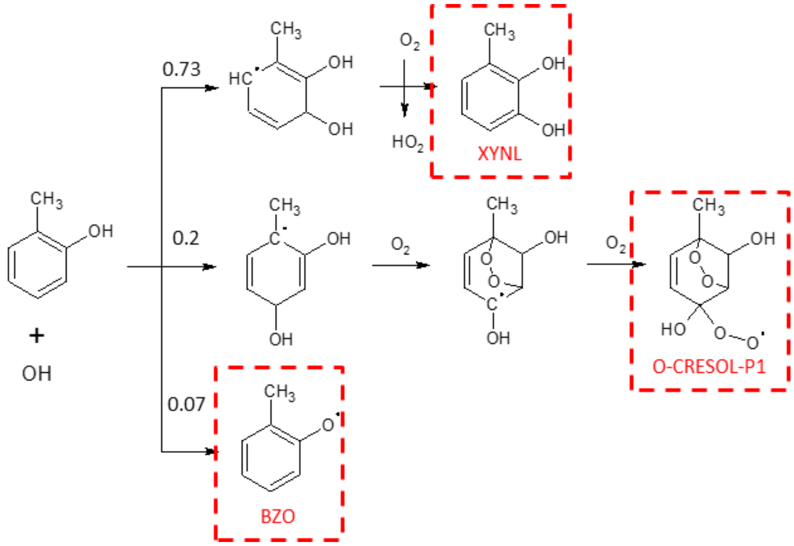

Figure 3.2: Schematic of the OH-initiated oxidation of o-cresol at room temperature and atmospheric pressure in the presence of NO$_x$.

Thus, in MG-PHEN-MOD, the MG-PHEN mechanism was modified to be consistent with the literature. The schematic of the OH-initiated oxidation of o-cresol in MG-PHEN-MOD at room temperature and atmospheric pressure in the presence of NO$_x$ is shown in Figure 3.2. H-atom abstraction accounts for a yield of 0.07 in the OH-initiated oxidation of o-cresol (Atkinson et al., 1992; Coeur-Tourneur et al., 2006; Olariu et al., 2002), and 2-dihydroxy-3-methylbenzene formed from the ortho position has a yield of 0.73 (Olariu et al., 2002); thus, the addition to the ipso position is assumed to have a fraction of 20%. Nitrophenol is the only known product of NO$_3$-initiated o-cresol oxidation, but the detailed mechanism of the reaction is unknown. As a result, no changes were made. Table 3.7 lists the modified OH-initiated o-cresol oxidation reactions in MG-PHEN-MOD; the intermediate reactions are not shown in the table but are included in the full mechanism file in Table C3. The lumped model species was used to represent all of the 1st generation products.

3.2.3 Dimethylphenols

Similarly, in the reaction rate constants with OH and NO_3, the position of $–CH_3$ substituents on the ring appears to have an opposite effect, similar to creosols. The reactions of 2,4-DMP (OH- and NO_3- initiated oxidations) in MG-PHEN are listed in Table 3.8. MechGen predicted an OH abstraction fraction of 1.1% and an OH addition fraction of 98.9%. The reaction of OH or NO_3 with dimethylphenols is expected to proceed primarily as in the reactions of phenol and cresols, but the detailed mechanisms are unknown. As a result, no modifications to the 2,4-DMP were made.

Table 3.8: OH- and NO_3- initiated oxidation of 2,4-DMP in MG-PHEN and MG-PHEN-MOD[a]

Reactions[b]	Rate Constant at 298K (cm^3 $molecule^{-1}$ s^{-1})
24M-PHEN + OH = #.877 HO2 + #.658 OLEP + #.112 24M-PHEN_P1 + #.105 OLEA2 + #.062 XYNL + #.036 OLEA1 + #.017 LVKS + #.011 BZO + #-1.44 XC + #.112 SumRO2	7.30E-11 or 7.40E-11[c]
24M-PHEN + NO3 = BZO + #2 XC + XN	3.12E-11

[a] The complete mechanism of MG-PHEN is listed in Table C2; The complete mechanism of MG-PHEN-MOD is listed in Table C3.
[b] 24M-PHEN_P1: 2,4-methylphenol RO_2; BZO: phenoxy or substituted phenoxy radicals; XN: lost nitrogen or nitrogen in unreactive products; other species: see Carter (2020a) for more details.
[c] 7.30E-11 for MG-PHEN, 7.40E-11 for MG-PHEN-MOD.

3.3 Modeling Methods

The mechanisms in Table 3.3 were evaluated by simulating 15 phenols-NO_x chamber experiments summarized in Table 3.9. The UCR/CE-CERT environmental chamber (hereafter referred to as EPA chamber), and associated measurement techniques, have previously been described in Chapter 2 and in Carter et al. (2005). These experiments were designed to represent simplified atmospheric conditions (VOC + NO_x) and did not contain additional reactants. The data used to evaluate the phenols mechanism were time-dependent mixing ratios of O_3 (UV absorption), NO and NO_x (chemiluminescence), and phenols (gas chromatography). The experiments were classified based on the phenol precursor, experimental conditions (see Table 3.9). The EPA chamber experiments were all conducted under dry conditions (RH < 0.1%) with blacklight light sources (Carter et al., 2005).

Table 3.9: List of chamber experiments used to evaluate model performance.

Group	Run ID	Light[a]	k_1[b]	Duration (mins)	HC	NO_x	$[HC]_0/[NO_x]_0$
					Initial Mixing Ratio (ppb)		(ppb/ppb)
phenol	EPA1219A	BL	0.401	546	140	147	1.0
	EPA1219B	BL	0.401	546	140	76	1.8
	EPA1273A	BL	0.401	276	106	23	4.6
	EPA1273B	BL	0.401	276	106	53	2.0
	EPA1289B	BL	0.401	236	84	106	0.8
o-cresol	EPA1260A	BL	0.401	231	62	15	4.1
	EPA1260B	BL	0.401	201	62	56	1.1
	EPA1279A	BL	0.401	224	80	27	3.0
	EPA1279B	BL	0.401	238	80	57	1.4
	EPA1350A	BL	0.401	326	312	718	0.4
	EPA1350B	BL	0.401	326	301	384	0.8
2,4-DMP	EPA1275A	BL	0.401	259	40	22	1.8
	EPA1275B	BL	0.401	259	40	53	0.8
	EPA1277A	BL	0.401	223	94	23	4.1
	EPA1277B	BL	0.401	236	94	51	1.8

[a] BL: blacklight, Arc: Argon arc light.
[b] Light intensity k_1 (NO_2 photolysis rate as measured by actinometry), unit: min^{-1}.

3.4 Results and Discussion

The performance of the standard and new mechanisms was evaluated based on model-measurement comparison of phenols consumption, NO decay, O_3 formation and $\Delta([O_3]-[NO])$ value. The quantity $\Delta([O_3]-[NO])$ has been used previously to evaluate the rate of NO oxidation by peroxy radicals (Carter, 1999, 2009, 2020a). The quantity is calculated by: $([O_3]_t - [NO]_t) - ([O_3]_0 - [NO]_0)$, where $[O_3]_0$, $[NO]_0$, $[O_3]_t$, and $[NO]_t$ are the initial and time = t concentrations of O_3 and NO, respectively.

3.4.1 Quantification of mechanism performance

The overall performance of SAPRC-18-PHEN mechanism was evaluated based on model-measurement comparison of phenols mixing ratios and $\Delta([O_3]-[NO])$ values for the chamber experiments summarized in Table 3.9. The quantity $\Delta([O_3]-[NO])$ was used instead of final O_3 concentration in order to evaluate the rate of NO oxidation by peroxy radicals. Normalized bias (NB) was calculated for the phenols mixing ratios and $\Delta([O_3]-[NO])$ values. Figure 3.3 shows the distribution and median of NB values over the duration of each experiment based on the SAPRC-18-PHEN simulations. SAPRC-18-PHEN mechanism predicted a faster decay rate of phenol than chamber observations, underestimated $\Delta([O_3]-[NO])$ values for phenol under relatively high NO_x conditions ($[HC]_0/[NO_x]_0 < 2$), and overestimated $\Delta([O_3]-[NO])$ values under relatively low NO_x conditions ($[HC]_0/[NO_x]_0 \geq 2$). SAPRC-18-PHEN simulations for o-cresol experiments were highly compatible with experimental data. SAPRC-18-PHEN predicted a faster consumption of 2,4-DMP (except for EPA1350B) and underestimated Δ([O_3]-[NO]) values in all 2,4-DMP experiments.

Similar to Figure 3.3 for SAPRC-18-PHEN, Figure C7 shows the distribution and median of NB values for SAPRC-18-STD. The classifications of mean normalized bias by the number of experiments are shown in Figure C8 for both SAPRC-18-STD and SAPRC-18-PHEN mechanisms. For SAPRC-18-STD, the mean NB values for phenols consumption are within ±20% for 13 (out of 15) experiments; 9 experiments have NB mean values ±10%; the mean NB values for Δ([O_3]-[NO]) values are within ±20% for 11 (out of 15) experiments; 4 experiments have NB mean values ±10%. For SAPRC-18-PHEN, the mean NB values for phenols consumption are within ±20% for 13 (out of 15) experiments; 10 experiments have NB mean values ±10%; the mean NB values for Δ([O_3]-[NO]) values are within ±20% for 14 (out of 15) experiments; 8 experiments have NB mean values ±10%. In this instance, we may infer that SAPRC-18-PHEN exhibits overall better performance in modeling phenols experiments when compared to the SAPRC-18-STD mechanism.

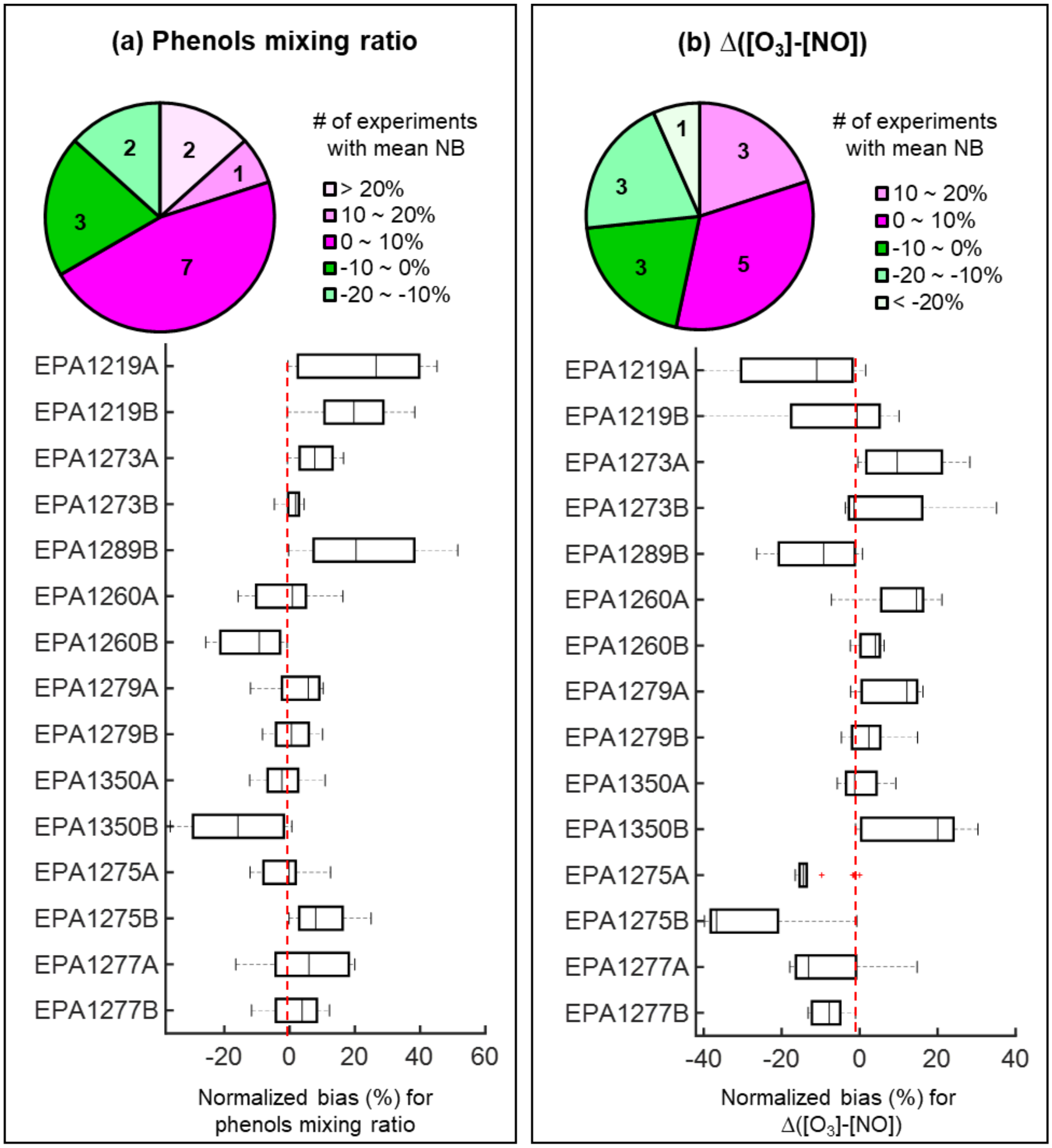

Figure 3.3: Normalized bias for the SAPRC-18-PHEN mechanism: a) phenols mixing ratios; b) Δ($[O_3]$-[NO]). Pie chart: classification of mean normalized bias by the number of experiments. Box-and-whisker plots: distribution and median of the normalized bias over the duration of the experiment.

3.4.2 Simulating phenol chamber experiments

The phenol experiments were carried out under various NO_x conditions, with the initial NO mixing ratio ranging from 23 ppb to 147 ppb and the $[HC]_0/[NO_x]_0$ ratio ranging from 0.8~4.6. EPA1219A and EPA1219B showed similar behavior for both chamber observations and model simulations of all mechanism, as did EPA1273A and EPA1273B. Only one experiment from each similarity group was chosen for further discussion, including EPA1289B, EPA1219B, and EPA1273B, all of which were performed in the same chamber bag. The mixing ratio time profiles for these three phenol experiments are shown in Figure 3.4, and the results of EPA1219A and EPA1273A are shown in Figure C1 in Appendix C. Solid triangles are used to represent chamber data in Figure 3.4. The difference in simulation results between SAPRC-18-STD (solid blue line), MG-PHEN (solid green line), and MG-PHEN-MOD (dashed green line) is quite significant, indicating a fundamental change in the mechanisms. The difference between MG-PHEN-MODE and SAPRC-18-PHEN (solid red line) is negligible because the mechanism of phenol in SAPRC-18-PHEN will not be affected by mechanism changes caused by updating model species CRES and XYNL.

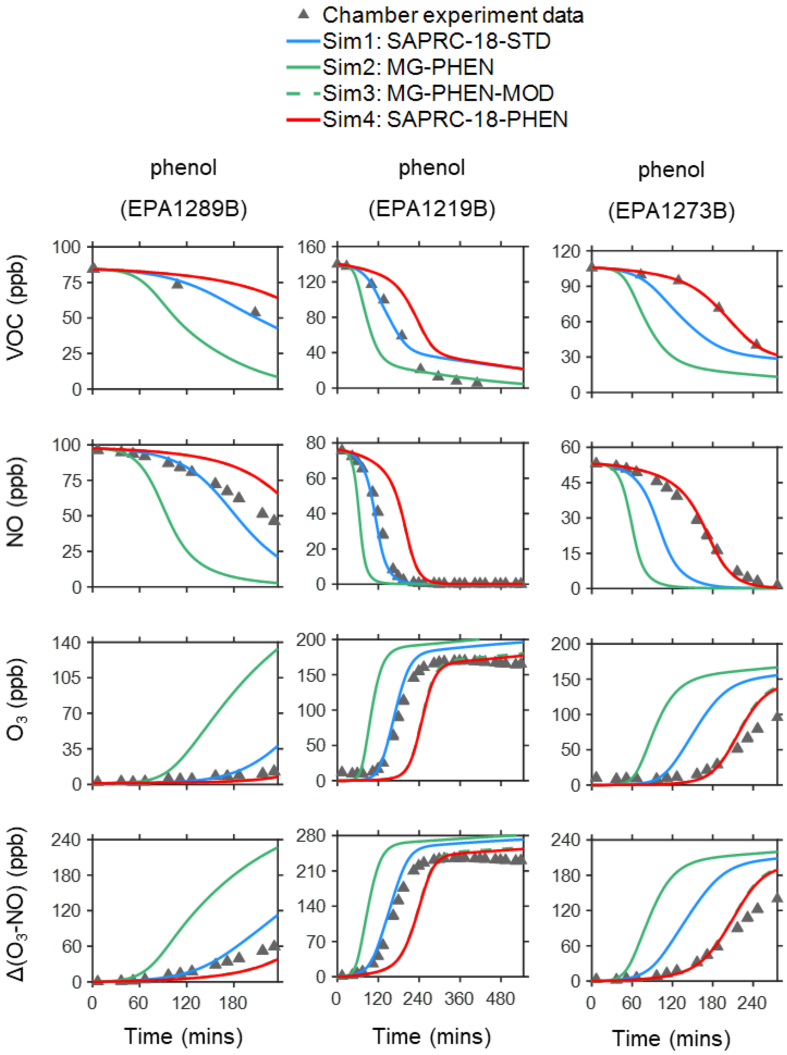

Figure 3.4: Comparison of chamber data (triangles) and model simulation results (lines) for the photooxidation of phenol in the presence of NO_x. The difference between MG-PHEN-MODE and SAPRC-18-PHEN is negligible because the mechanism of phenol in SAPRC-18-PHEN will not be affected by mechanism changes caused by updating model species CRES and XYNL.

Unfortunately, no mechanism fit all of the experiments perfectly. Generally, the SAPRC-18-STD mechanism overestimated the reactivity of the phenol and subsequent products. It was able to reproduce the observations at the start of the experiments, but after a maximum of two hours, the predicted rate of NO decay and O_3 formation was faster, and the rate of phenol consumption was slower. This was most likely due to uncertainties in product yields, which were manually adjusted to achieve the lowest overall model bias but were not based on reported product yields or branching ratios. MG-PHEN has the worst model performance across all experiments, vastly overestimating radical level and recycling while providing the fastest rate for phenol consumption, NO decay, and O_3 formation. This is because in MG-PHEN, MechGen predicted a relatively low yield of catechol compared to published literature values, but high yields of other photoreactive products such as unsaturated dicarbonyls, which can enhance radical recycling and speed up reactions. For MG-PHEN-MOD, the yield of catechol was increased from 0.49 to 0.71 based on published data, and thus the yields of the photoreactive products were decreased, resulting in a considerably slower consumption of the precursors, which is too slow for some experiments (e.g., EPA1289B and EPA1218B). Nonetheless, relative to SAPRC-18-STD, MG-PHEN-MOD better captured the concentration changes of phenol, NO, and O_3 in experiments EPA1273B ($[HC]_0/[NOx]_0=2.0$, Figure 3.4) and EPA1273A ($[HC]_0/[NOx]_0=4.6$, Figure C1) . The overall improvement in model performance using MG-PHEN-MOD to simulate the phenol experiments, particularly for lower NO_x conditions ($[HC]_0/[NO_x]_0 \geq 2$) that are more representative of atmospheric conditions, is notable given than no tuning of the mechanism was performed.

Figure C3 illustrates the phenol consumption rates as a function of time for SAPRC-18-STD and SAPRC-18-PHEN over a 540-minute simulation, allowing a direct comparison between different mechanisms and experiments. Because the durations of some experiments are shorter than the simulation times (as shown in Table 3.9), stop times of the experiments are indicated with a dashed grey line. The dominant reaction pathway in the phenol experiments was phenol reacting with OH. SAPRC-18-STD and SAPRC-18-PHEN both predicted that experiments EPA1219A and EPA1289B had some fraction of phenol consumed by NO_3, whereas in EPA1289B, almost all of the phenol was consumed by OH. The higher phenol concentration in SAPRC-18-PHEN at each time point indicated that the OH level predicted by SAPRC-18-PHEN was much lower than that predicted by SAPRC-18-STD. The rate constant for catechol + OH in SAPRC-18-STD was significantly higher than in SAPRC-18-PHEN; the latter was adjusted downward to be consistent with published literature. One sensitivity simulation was performed to test the sensitivities of phenol consumption and O_3 formation to the catechol rate constant, as shown in Figure C6. Instead of using published data, the simulation results would be much closer to those predicted by SAPRC-18-STD if the rate constants of catechol in SAPRC-18-PHEN were adjusted to be the same as in SAPRC-18-STD. Even though this manually adjusted mechanism performed better with experiment data for EPA1289B and EPA1219B, it performed worse for EPA1273B. This adjustment is not particularly necessary if not all experiments improved and were not taken into consideration in this study.

3.4.3 Simulating o-cresol chamber experiments

The o-cresol experiments were carried out under various NOx conditions, with the initial NO mixing ratio ranging from 15 ppb to 718 ppb and the $[HC]_0/[NO_x]_0$ ratio ranging from 0.4~4.1. Experiments EPA1260A and EPA1279A showed similar behavior for both chamber observations and model simulations of all mechanisms, while EPA1260B and EPA1279B had similar behavior as well. Only one experiment from each similarity group, including EPA1279A, EPA1279B, EPA1350A, and EPA1350B, was chosen for further discussion. The mixing ratio time profiles for selected o-cresol experiments are shown in Figure 3.5, which is analogous to Figure 3.4 for phenol. Figure C2 in Appendix C shows similar plots for the other two o-cresol experiments.

Again, MG-PHEN showed the poorest model performance across all experiments by overestimating the system's reactivity while providing the fastest rates for phenol consumption, NO decay and O_3 formation. MG-PHEN-MOD had a slower reaction rate and better fitted experiment results after being modified based on reported data. Unlike phenol, there is a clear distinction between MG-PHEN-MOD and SAPRC-18-PHEN due to the major 1st generation product 1,2-dihydroxy-3-methylbenzene (0.73 yield), which was represented by the lumped model species XYNL. While the XYNL mechanism in MG-PHEN-MOD was the same as in SAPRC-18-STD, the XYNL mechanism in SAPRC-18-PHEN was updated to use the new 2,4-DMP mechanism, which will be discussed later.

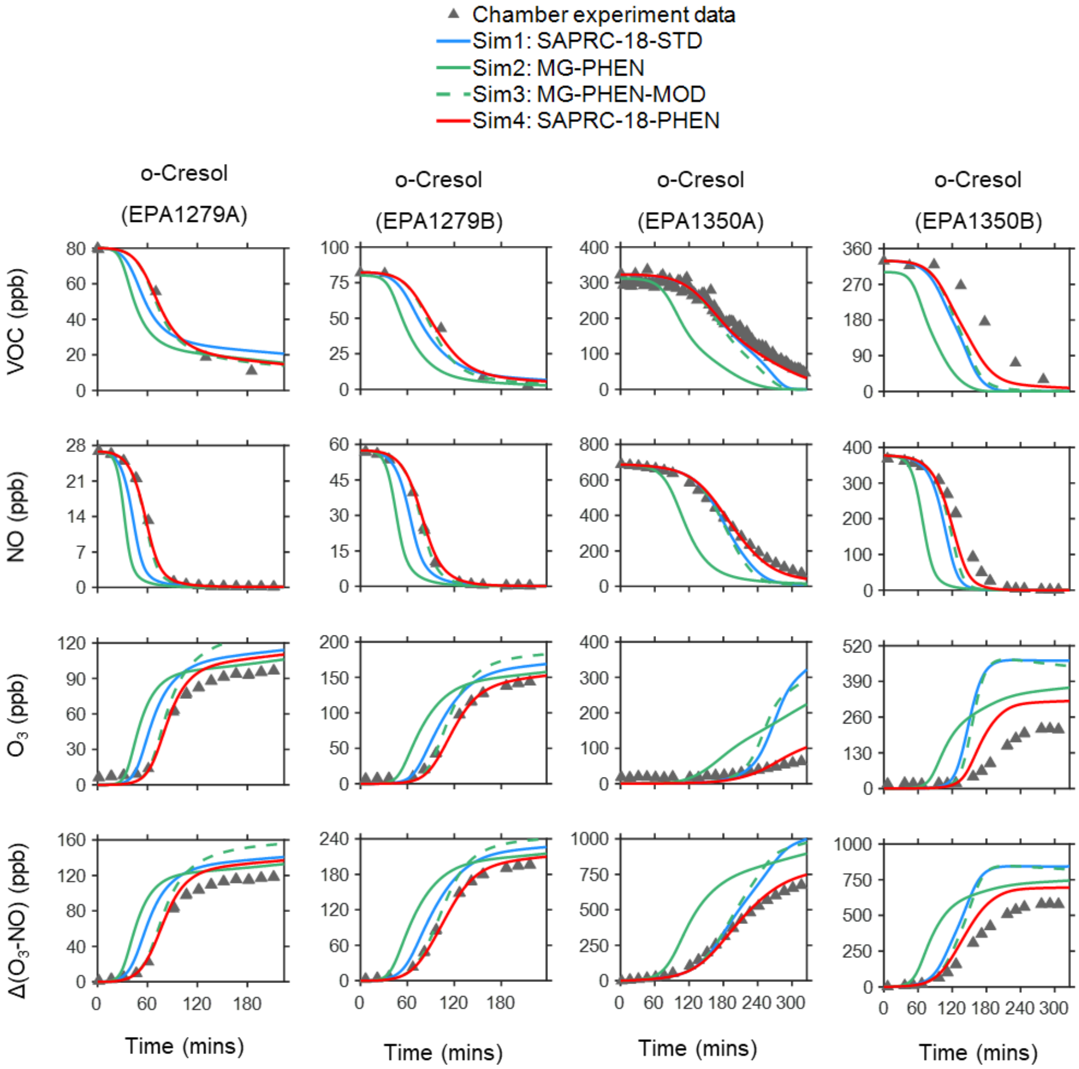

Figure 3.5: Comparison of chamber data (triangles) and model simulation results (lines) for the photooxidation of o-cresol in the presence of NO$_x$.

In contrast to the phenol experiments, the SAPRC-18-PHEN simulations significantly improved model performance for all six o-cresol experiments when compared to SAPRC-18-STD. While SAPRC-18-STD largely overpredicted O_3 formation in experiments with high concentrations and high NO_x levels (shown in Figure 3.4, EPA1350A and EPA1350B), SAPRC-18-PHEN reduced the overprediction to a much lower level. SAPRC-18-PHEN very well captured the time-dependence of all valuables for experiments performed under relatively lower NOx conditions, regardless of final concentration or overall reaction rate. The reaction with OH was the dominant oxidation pathway of o-cresol, as shown in Figure C4, which is analogous to Figure C3 for phenol. In experiments EPA1350A and EPA1350B, the NO_3 pathway began to play a role in the latter half of the experiments, but it only contributed to a small fraction of o-cresol oxidation consumption.

3.4.4 Simulating 2,4-DMP chamber experiments

The 2,4-DMP experiments were carried out under various NOx conditions, with the initial NO mixing ratio ranging from 22 ppb to 53 ppb and the $[HC]_0/[NO_x]_0$ ratio ranging from 0.8~4.1. Figure 3.6 depicts the mixing ratio time profiles for 2,4-DMP experiments, which are analogous to Figure 3.4 and Figure 3.5 for phenol and o-cresol, respectively. The differences between MG-PHEN, MG-PHEN-MOD, and SAPRC-18-PHEN simulations are negligible because the 2,4-DMP mechanism was completely derived from MechGen with only minor modifications in MG-PHEN-MOD: the rate constant with OH was changed from 7.3×10^{-11} to 7.4×10^{-11} (Table 3.8). When compared to SAPRC-18-STD, SAPRC-18-PHEN better captured the 2,4-DMP consumption and NO to NO_2 conversion rates except for experiment EPA1275B, but underestimated the O_3 formation rate in all experiments.

Despite the fact that SAPRC-18-STD was parameterized to fit the chamber data, it may still be useful to estimate radical levels in 2,4-DMP experiments due to the better model-measurement agreement compared to SAPRC-18-PHEN. Given the lower concentration of 2,4-DMP in SAPRC-18-PHEN at each time point, it is clear that the OH level predicted by SAPRC-18-PHEN was significantly lower than that predicted by SAPRC-18-STD. Manually adjusting the product distribution would improve the O_3 prediction for 2,4-DMP; however, the change in 2,4-DMF mechanism will reflect in the change of the lumped model species XYNL in SAPRC-18-PHEN and affect the model performance for the o-cresol experiments. As a result of the trade-off effects and the lack of published data, no adjustment was taken for the 2,4-DMF mechanism in SAPRC-18-PHEN.

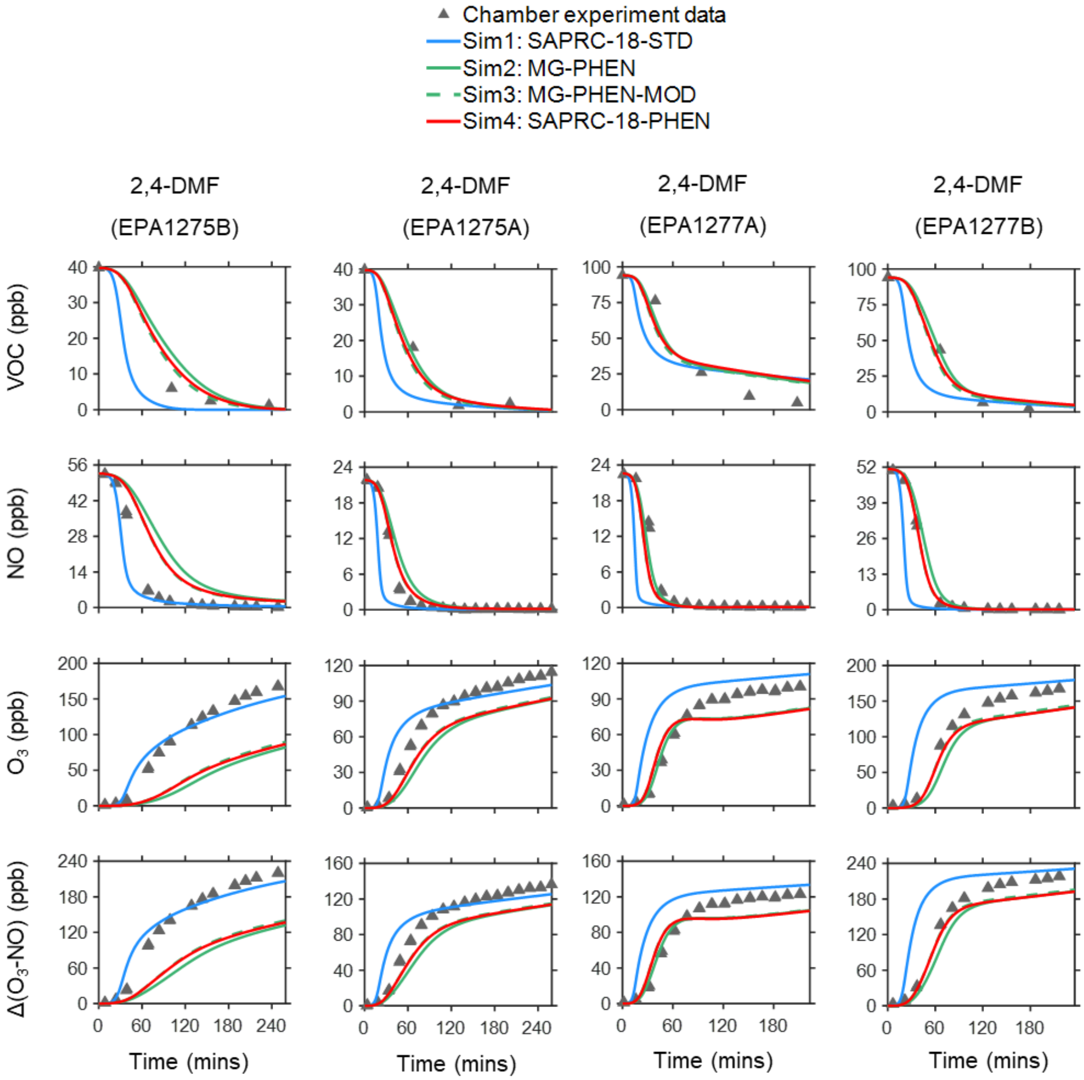

Figure 3.6: Comparison of chamber data (triangles) and model simulation results (lines) for the photooxidation of 2,4-DMP in the presence of NO_x.

3.5 Conclusions

A new phenols chemical mechanism, MG-PHEN-MOD, was developed using a combination of published experimental data and molecular modeling simulations, and the SAPRC mechanism generation system, MechGen (Carter, 2020b). The MG-PHEN-MOD mechanism was then incorporated into the SAPRC-18-STD mechanism to replace the previous phenols species, and the updated mechanism was renamed as SAPRC-18-PHEN. SAPRC-18-PHEN mechanism was evaluated based on model-measurement comparison of phenols decay, O_3 formation, and NO oxidation rates in 15 environmental chamber experiments. The SAPRC-18-PHEN mechanism showed a better performance than SAPRC-18-STD mechanism in simulating phenol and o-cresol experiments, and it is deemed to have equal performance in simulating 2,4-DMP experiments.

SAPRC MechGen used in this work to generate chemical mechanisms for oxidation of phenols under ambient conditions using structure-reactivity estimation methods. The uncertainties in the mechanisms were demonstrated using modified versions of the standard mechanism, SAPRC-18-STD, largely by updating product yields and branching ratios based on published data. While there have been numerous mechanism and product studies published for phenol and o-cresol, and thus the SAPRC-18-PHEN mechanism demonstrated better performance than SAPRC-18-STD. There is significantly less published data for 2,4-DMP and thus the default MechGen derived mechanism without modification was found to be unsatisfactory, and didn't show improved model performance compared to SAPRC-18-STD. Furthermore, the reactivity of the phenols is not only controlled by the precursor VOC, but it is also greatly influenced by the 1st generation and higher products. Further improvements in the representations of phenols in models will require additional product studies under ambient conditions. Despite the uncertainties, the SAPRC-18-PHEN mechanism represents the current state of the science, and no manual adjustment was done to fit the chamber data.

The phenols experiments in this study were carried out with relatively high reactant concentrations and simpler reactant mixtures than exist in the atmosphere, and are not sufficient to thoroughly evaluate the mechanism under low NO_x conditions. In addition, given the importance of phenols as an emission source from wildfires, the nighttime NO_3 chemistry of phenols is critical and needs to be further addressed. Phenols are also important intermediates in the photooxidation of aromatic hydrocarbons like benzene and toluene, and they can be produced in large quantities. Thus, it is recommended that SAPRC-18-PHEN be evaluated using aromatic hydrocarbon chamber experiments in the future.

References

Abatzoglou, J. T., & Williams, A. P. (2016). Impact of anthropogenic climate change on wildfire across western US forests. *Proceedings of the National Academy of Sciences of the United States of America*, *113*(42), 11770-11775. https://doi.org/10.1073/pnas.1607171113

Akherati, A., He, Y., Coggon, M. M., Koss, A. R., Hodshire, A. L., Sekimoto, K., Warneke, C., De Gouw, J., Yee, L., Seinfeld, J. H., Onasch, T. B., Herndon, S. C., Knighton, W. B., Cappa, C. D., Kleeman, M. J., Lim, C. Y., Kroll, J. H., Pierce, J. R., & Jathar, S. H. (2020). Oxygenated Aromatic Compounds are Important Precursors of Secondary Organic Aerosol in Biomass-Burning Emissions. *Environmental Science and Technology*, *54*(14), 8568-8579. https://doi.org/10.1021/acs.est.0c01345

Albarran, G., & Schuler, R. H. (2007). Hydroxyl radical as a probe of the charge distribution in aromatics: Phenol. *Journal of Physical Chemistry A*, *111*(13), 2507-2510. https://doi.org/10.1021/jp068736r

Atkinson, R. (1994). Gas-phase tropospheric chemistry of volatile organic compounds. *J. Phys. Chem. Ref. Data Monog*, *2*, 11-216.

Atkinson, R., Aschmann, S. M., & Arey, J. (1992). Reactions of hydroxyl and nitrogen trioxide radicals with phenol, cresols, and 2-nitrophenol at 296.+-. 2 K. *Environmental Science & Technology*, *26*(7), 1397-1403.

Berndt, T., & Böge, O. (2003). Gas-phase reaction of OH radicals with phenol. *Physical Chemistry Chemical Physics*, *5*(2), 342-350. https://doi.org/10.1039/b208187c

Bloss, C., Wagner, V., Bonzanini, A., Jenkin, M. E., Wirtz, K., Martin-Reviejo, M., & Pilling, M. J. (2005). Evaluation of detailed aromatic mechanisms (MCMv3 and MCMv3.1) against environmental chamber data. *Atmospheric Chemistry and Physics*, *5*(3), 623-639. https://doi.org/10.5194/acp-5-623-2005

Bluvshtein, N., Lin, P., Michel Flores, J., Segev, L., Mazar, Y., Tas, E., Snider, G., Weagle, C., Brown, S. S., Laskin, A., & Rudich, Y. (2017). Broadband optical properties of biomass-burning aerosol and identification of brown carbon chromophores. *Journal of Geophysical Research*, *122*(10), 5441-5456. https://doi.org/10.1002/2016JD026230

Bolzacchini, E., Bruschi, M., Hjorth, J., Meinardi, S., Orlandi, M., Rindone, B., & Rosenbohm, E. (2001). Gas-phase reaction of phenol with NO3. *Environmental Science and Technology*, *35*(9), 1791-1797. https://doi.org/10.1021/es001290m

Calvert, J., Mellouki, A., & Orlando, J. (2011). *Mechanisms of Atmospheric Oxidation of the Oxygenates*. https://doi.org/10.15713/ins.mmj.3

Calvert, J. G., Atkinson, R., Becker, K. H., Kamens, R. M., Seinfeld, J. H., Wallington, T. H., & Yarwood, G. (2002). The mechanisms of atmospheric oxidation of the aromatic hydrocarbons.

Carter, W. P. L. (1999). Documentation of the SAPRC-99 Chemical Mechanism for VOC Reactivity Assessment. *Assessment*, *1*, 329-329. http://www.engr.ucr.edu.oca.ucsc.edu/~carter/pubs/s99doc.pdf

Carter, W. P. L. (2009). *Development of the SAPRC-07 Chemical Mechanism and Updated Ozone Reactivity Scales; Final report to the California Air Resources Board Contract No. 03-318, March 2009*. https://intra.engr.ucr.edu/~carter/SAPRC/

Carter, W. P. L. (2020a). *Documentation of the SAPRC-18 Mechanism; Report to California Air Resources Board Contract No. 11-761, May, 2020*. https://intra.engr.ucr.edu/~carter/SAPRC/18/

Carter, W. P. L. (2020b). *Estimates and Assignments used in the SAPRC-18 Mechanism Generation System; Report to California Air Resources Board Contract No. 11-761. In preparation. When completed, will be available at http://intra.engr.ucr.edu/~carter/SAPRC/18*.

Carter, W. P. L. (2020c). *Gateway to the SAPRC Mechanism Generation System*. http://mechgen.cert.ucr.edu/

Carter, W. P. L., Cocker, D. R., Fitz, D. R., Malkina, I. L., Bumiller, K., Sauer, C. G., Pisano, J. T., Bufalino, C., & Song, C. (2005). A new environmental chamber for evaluation of gas-phase chemical mechanisms and secondary aerosol formation. *Atmospheric Environment*, *39*(40), 7768-7788. https://doi.org/10.1016/j.atmosenv.2005.08.040

Coeur-Tourneur, C., Foulon, V., & Laréal, M. (2010). Determination of aerosol yields from 3-methylcatechol and 4-methylcatechol ozonolysis in a simulation chamber. *Atmospheric Environment*, *44*(6), 852-857. https://doi.org/10.1016/j.atmosenv.2009.11.027

Coeur-Tourneur, C., Henry, F., Janquin, M.-A., & Brutier, L. (2006). Gas-phase reaction of hydroxyl radicals withm-,o- andp-cresol. *International Journal of Chemical Kinetics*, *38*(9), 553-562. https://doi.org/10.1002/kin.20186

Derwent, R. G., Jenkin, M. E., Utembe, S. R., Shallcross, D. E., Murrells, T. P., & Passant, N. R. (2010). Secondary organic aerosol formation from a large number of reactive man-made organic compounds. *Science of The Total Environment*, *408*(16), 3374-3381. https://www.sciencedirect.com/science/article/abs/pii/S0048969710003918?via%3Dihub

Finewax, Z., De Gouw, J. A., & Ziemann, P. J. (2018). Identification and Quantification of 4-Nitrocatechol Formed from OH and NO3 Radical-Initiated Reactions of Catechol in Air in the Presence of NOx: Implications for Secondary Organic Aerosol Formation from Biomass Burning. *Environmental Science and Technology*, *52*(4), 1981-1989. https://doi.org/10.1021/acs.est.7b05864

Fleming, L. T., Lin, P., Roberts, J. M., Selimovic, V., Yokelson, R., Laskin, J., Laskin, A., & Nizkorodov, S. A. (2020). Molecular composition and photochemical lifetimes of brown carbon chromophores in biomass burning organic aerosol. *Atmospheric Chemistry and Physics*, *20*(2), 1105-1129. https://doi.org/10.5194/acp-20-1105-2020

Frka, S., Sala, M., Kroflic, A., Hus, M., Cusak, A., & Grgic, I. (2016). Quantum chemical calculations resolved identification of methylnitrocatechols in atmospheric aerosols. *Environmental Science & Technology*, *50*(11), 5526-5535.

Gilman, J., Lerner, B., Kuster, W., Goldan, P. D., Warneke, C., Veres, P., Roberts, J., De Gouw, J., Burling, I., & Yokelson, R. (2015). Biomass burning emissions and potential air quality impacts of volatile organic compounds and other trace gases from fuels common in the US. *Atmospheric Chemistry and Physics*, *15*(24), 13915-13938.

Harvey, B. J. (2016). Human-caused climate change is now a key driver of forest fire activity in the western United States. In *Proceedings of the National Academy of Sciences of the United States of America* (Vol. 113, pp. 11649-11650): National Academy of Sciences.

Hatch, L. E., Yokelson, R. J., Stockwell, C. E., Veres, P. R., Simpson, I. J., Blake, D. R., Orlando, J. J., & Barsanti, K. C. (2017). Multi-instrument comparison and compilation of non-methane organic gas emissions from biomass burning and implications for smoke-derived secondary organic aerosol precursors. *Atmospheric Chemistry and Physics*, *17*(2), 1471-1489. https://doi.org/10.5194/acp-17-1471-2017

Heilman, W. E., Liu, Y., Urbanski, S., Kovalev, V., & Mickler, R. (2014). Wildland fire emissions, carbon, and climate: Plume rise, atmospheric transport, and chemistry processes. *Forest Ecology and Management*, *317*, 70-79. https://doi.org/https://doi.org/10.1016/j.foreco.2013.02.001

Jiang, J., Carter, W. P. L., Cocker, D. R., & Barsanti, K. C. (2020). Development and Evaluation of a Detailed Mechanism for Gas-Phase Atmospheric Reactions of Furans. *ACS Earth and Space Chemistry*, *4*(8), 1254-1268. https://doi.org/10.1021/acsearthspacechem.0c00058

Kiliç, M., Koçtürk, G., San, N., & Çinar, Z. (2007). A model for prediction of product distributions for the reactions of phenol derivatives with hydroxyl radicals. *Chemosphere*, *69*(9), 1396-1408. https://doi.org/10.1016/j.chemosphere.2007.05.002

Kitanovski, Z., Čusak, A., Grgić, I., & Claeys, M. (2014). Chemical characterization of the main products formed through aqueous-phase photonitration of guaiacol. *Atmospheric Measurement Techniques*, *7*(8), 2457-2470.

Lauraguais, A., El Zein, A., Coeur, C., Obeid, E., Cassez, A., Rayez, M. T., & Rayez, J. C. (2016). Kinetic Study of the Gas-Phase Reactions of Nitrate Radicals with Methoxyphenol Compounds: Experimental and Theoretical Approaches. *Journal of Physical Chemistry A*, *120*(17), 2691-2699. https://doi.org/10.1021/acs.jpca.6b02729

Lin, P., Bluvshtein, N., Rudich, Y., Nizkorodov, S. A., Laskin, J., & Laskin, A. (2017). Molecular chemistry of atmospheric brown carbon inferred from a nationwide biomass burning event. *Environmental Science & Technology*, *51*(20), 11561-11570.

Lin, P., Fleming, L. T., Nizkorodov, S. A., Laskin, J., & Laskin, A. (2018). Comprehensive molecular characterization of atmospheric brown carbon by high resolution mass spectrometry with electrospray and atmospheric pressure photoionization. *Analytical chemistry*, *90*(21), 12493-12502. https://pubs.acs.org/doi/10.1021/acs.analchem.8b02177

Liu, C., Liu, Y., Chen, T., Liu, J., & He, H. (2001). Rate constant and secondary organic aerosol formation from the gas-phase reaction of eugenol with hydroxyl radicals. *Atmos. Chem. Phys*, *19*. https://doi.org/10.5194/acp-19-2001-2019

Lundqvist, M. J., & Eriksson, L. A. (2000). Hydroxyl Radical Reactions with Phenol as a Model for Generation of Biologically Reactive Tyrosyl Radicals. *Journal of Physical Chemistry B*, *104*(4), 848-855. https://doi.org/10.1021/jp993011r

Mayorga, R. J., Zhao, Z., & Zhang, H. (2020). Formation of secondary organic aerosol from nitrate radical oxidation of phenolic VOCs: Implications for nitration mechanisms and brown carbon formation. *Atmospheric Environment*, *244*, 117910-117910. https://doi.org/10.1016/j.atmosenv.2020.117910

Mohammed, H., & Mohammed, H. (2021). *Mapping wildfires around the world*. AL JAZEERA. https://www.aljazeera.com/news/2021/8/19/mapping-wildfires-around-the-world-interactive

Nakao, S., Clark, C., Tang, P., Sato, K., & Cocker, D. (2011). Secondary organic aerosol formation from phenolic compounds in the absence of NOx. *Atmospheric Chemistry and Physics*, *11*(20), 10649-10660. https://doi.org/10.5194/acp-11-10649-2011

Olariu, R. I., Klotz, B., Barnes, I., Becker, K. H., & Mocanu, R. (2002). FT-IR study of the ring-retaining products from the reaction of OH radicals with phenol, o-, m-, and p-cresol. *Atmospheric Environment*, *36*(22), 3685-3697. https://doi.org/10.1016/S1352-2310(02)00202-9

Raghavan, N. V., & Steenken, S. (1980). Electrophilic reaction of the hydroxyl radical with phenol. Determination of the distribution of isomeric dihydroxycyclohexadienyl radicals. *Journal of the American Chemical Society*, *102*(10), 3495-3499. https://doi.org/10.1021/ja00530a031

Roger, A., Aschmann, S. M., & Janet, A. (1992). Reactions of Hydroxyl and Nitrogen Trioxide Radicals with Phenol, Cresols, and 2-Nitrophenol at 296 ± 2K. *Environmental Science and Technology*, *26*(7), 1397-1403. https://doi.org/10.1021/es00031a018

Sandhiya, L., Kolandaivel, P., & Senthilkumar, K. (2013). Mechanism and kinetics of the atmospheric oxidative degradation of dimethylphenol isomers initiated by OH radical. *Journal of Physical Chemistry A*, *117*(22), 4611-4626. https://doi.org/10.1021/jp3120868

Schwantes, R. H., Schilling, K. A., McVay, R. C., Lignell, H., Coggon, M. M., Zhang, X., Wennberg, P. O., & Seinfeld, J. H. (2017). Formation of highly oxygenated low-volatility products from cresol oxidation. *Atmospheric Chemistry and Physics*, *17*(5), 3453-3474. https://doi.org/10.5194/acp-17-3453-2017

Semadeni, M., Stocker, D. W., & Kerr, J. A. (1995). The temperature dependence of the OH radical reactions with some aromatic compounds under simulated tropospheric conditions. *International Journal of Chemical Kinetics*, *27*(3), 287-304. https://doi.org/10.1002/kin.550270307

Thüner, L. P., Bardini, P., Rea, G. J., & Wenger, J. C. (2004). Kinetics of the gas-phase reactions of OH and NO3 radicals with dimethylphenols. *Journal of Physical Chemistry A*, *108*(50), 11019-11025. https://doi.org/10.1021/jp046358p

Westerling, A. L. R. (2016). Increasing western US forest wildfire activity: Sensitivity to changes in the timing of spring. *Philosophical Transactions of the Royal Society B: Biological Sciences*, *371*(1696), 20150178-20150178. https://doi.org/10.1098/rstb.2015.0178

Wu, P., Li, J., Li, S., & Tao, F. M. (2012). Theoretical study of mechanism and kinetics for the addition of hydroxyl radical to phenol. *Science China Chemistry*, *55*(2), 270-276. https://doi.org/10.1007/s11426-011-4380-1

Xu, C., & Wang, L. (2013). Atmospheric oxidation mechanism of phenol initiated by OH radical. *Journal of Physical Chemistry A*, *117*(11), 2358-2364. https://doi.org/10.1021/jp308856b

Yee, L. D., Kautzman, K. E., Loza, C. L., Schilling, K. A., Coggon, M. M., Chhabra, P. S., Chan, M. N., Chan, A. W. H., Hersey, S. P., Crounse, J. D., Wennberg, P. O., Flagan, R. C., & Seinfeld, J. H. (2013). Secondary organic aerosol formation from biomass burning intermediates: phenol and methoxyphenols. *Atmospheric Chemistry and Physics*, *13*(16), 8019-8043. https://doi.org/10.5194/acp-13-8019-2013

Zhang, H., Yang, B., Wang, Y., Shu, J., Zhang, P., Ma, P., & Li, Z. (2016). Gas-Phase Reactions of Methoxyphenols with NO3 Radicals: Kinetics, Products, and Mechanisms. *Journal of Physical Chemistry A*, *120*(8), 1213-1221. https://doi.org/10.1021/acs.jpca.5b10406

Zhuang, Y., Fu, R., Santer, B. D., Dickinson, R. E., & Hall, A. (2021). Quantifying contributions of natural variability and anthropogenic forcings on increased fire weather risk over the western United States. *Proceedings of the National Academy of Sciences*, *118*(45), e2111875118. https://doi.org/10.1073/pnas.2111875118

Chapter 4 Modeling the Role of Peroxy Radicals in Camphene Secondary Organic Aerosol Formation

4.1 Introduction

On a global scale, biogenic monoterpene emissions are estimated to contribute 14% of the total reactive volatile organic compound (VOC) flux (Tg C) (Guenther et al., 1995). Camphene is a ubiquitous monoterpene emitted from biogenic sources (Geron et al., 2000; Hayward et al., 2001; Ludley et al., 2009; Maleknia et al., 2007; White et al., 2008) and pyrogenic sources (Akagi et al., 2013; Gilman et al., 2015; Hatch et al., 2015). Many studies have reported camphene as a top contributor by mass in measured biogenic and pyrogenic monoterpene emissions (Benelli et al., 2018; Hatch et al., 2019; Komenda & Koppmann, 2002; Mazza & Cottrell, 1999; Moukhtar et al., 2006). For example, in measurements of laboratory and prescribed fires reported by (Hatch et al., 2019), camphene was among the top two monoterpenes emitted from subalpine and Douglas fir fires based on emission factors (mass of compound emitted/mass of fuel burned).

When emitted to the atmosphere, monoterpenes form oxygenated compounds through reactions with oxidants such as hydroxyl radicals (OH), ozone (O_3), and nitrate radicals (NO_3); compounds with sufficiently low volatility can then condense to form secondary organic aerosol (SOA). Figure 4.1 shows the chemical structure of camphene and its reaction rate constants with major atmospheric oxidants. The SOA formation potential of individual monoterpenes can vary greatly based on their molecular structure, atmospheric lifetimes, and the volatility of their oxidation products (Atkinson & Arey, 2003; Griffin et al., 1999; N. Ng et al., 2007; Zhang et al., 1992). Previous experimental studies of other monoterpenes (such as α-pinene, β-pinene, d-limonene, etc.) have reported SOA mass yields from ~10% to 50% through OH oxidation and from ~0 to 65% through NO_3 oxidation; among the studied monoterpenes, d-limonene often has the highest reported yields (Fry et al., 2014; Griffin et al., 1999; Mutzel et al., 2016; N. L. Ng et al., 2007). Few studies have been published regarding camphene SOA formation.

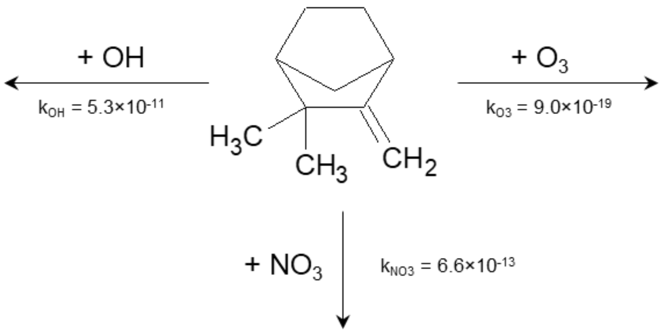

Figure 4.1: Camphene chemical structure and reaction rate constants (unit: cm^3 $molecule^{-1}$ s^{-1}) with major atmospheric oxidants.

Past experimental studies of camphene largely have been focused on gas-phase reactivity with OH, NO_3, and/or O_3 and gas-phase product identification (Atkinson et al., 1990; Gaona-Colmán et al., 2017; Hakola et al., 1994). Baruah et al. (2018) performed a kinetic and mechanism study of the camphene oxidation initiated by OH radicals using density functional theory (DFT), in which the rate constant and atmospheric lifetime were reported. It was also suggested that addition at the terminal double bond carbon atom could account for 98.4% of the initial OH-addition. A product study by Gaona-Colmán et al. (2017) showed obvious NO_x dependence in OH + camphene experiments, in which the molar yield of acetone was enhanced by a factor of 3, 33% relative to 10%, in the presence of NO_x (2–2.3 ppmv of NO).

Hatfield and Huff-Hartz studied SOA formation from ozonolysis of VOC mixtures, in which the added camphene was considered a non-reactive VOC and assumed to have little to no effect on SOA mass yields (Hatfield & Hartz, 2011). Mehra et al. (2020) recently published a compositional analysis study of camphene SOA. Although SOA mass yields were not provided, they demonstrated the potential contribution of highly oxygenated organic molecules (HOMs) and oligomers to camphene SOA formed in an oxidation flow reactor (OFR). Afreh et al. (2021) presented the first mechanistic modeling study of camphene SOA formation. While relatively high SOA mass yields were reported (with final SOA mass and yields twice that of α-pinene), no chamber-based SOA data were available for measurement–model comparison at that time.

SOA formation has been shown to be highly dependent on gas-phase NO_x concentrations; and more precisely, the relative ratios of NO:HO_2, hydroperoxyl radicals:RO_2, peroxy radicals (Henze et al., 2008; Kroll & Seinfeld, 2008; N. L. Ng et al., 2007; Presto et al., 2005; Song et al., 2005; Ziemann & Atkinson, 2012). During chamber experiments, VOCs are subject to oxidation by OH, O_3 and/or NO_3. For some precursors, NO_x levels influence the amount of SOA produced in the initial oxidation steps by controlling the relative proportions of oxidants, the fractional reactivity with those oxidants, and thus the volatility distribution of the products formed (Hurley et al., 2001; Kroll & Seinfeld, 2008; Nøjgaard et al., 2006). For other precursors, NO_x levels influence the amount of SOA produced via fate of RO_2. The reactions between RO_2 and HO_2 form hydroperoxides, which can have sufficiently low volatility to condense into the particle phase. In the presence of NO_x, RO_2 will react with NO, forming organic nitrate and carbonyl compounds that have higher volatilities than the products formed through the HO_2 pathway (Kroll & Seinfeld, 2008; Ziemann & Atkinson, 2012). Previous studies of relatively small compounds (carbon number ≤ 10), including monoterpenes such as α-pinene, have reported that SOA mass yields generally increase as initial NO_x decreases, with a proposed mechanism of competitive chemistry between $RO_2 + HO_2$ and $RO_2 + NO$ pathways, of which the latter would form more volatile products (Kroll et al., 2006; N. L. Ng et al., 2007; Song et al., 2005). The NO_x dependence of camphene oxidation and SOA formation has been relatively understudied.

The atmospheric gas-phase autoxidation of RO_2 has been identified as another key pathway of SOA formation (Bianchi et al., 2019; Crounse et al., 2013; Ehn et al., 2017; Jokinen et al., 2014). The RO_2 radical undergoes intramolecular H-atom abstraction reactions to form a hydroperoxide functionality and an alkyl radical (RO), to which a new RO_2 will be formed by adding O_2. The autoxidation process can repeat several times until terminated by other pathways and will form low-volatility compounds known as highly oxygenated organic molecules (HOMs) (Bianchi et al., 2019). Recent theoretical and experimental studies have been conducted to understand HOM formation from monoterpenes such as α-pinene and β-pinene (Pullinen et al., 2020; Quéléver et al., 2019; Xavier et al., 2019; Ye et al., 2019; Zhang et al., 2017), but the potential importance and mechanisms of HOM formation from camphene have not been well investigated.

Here, we present the first systematic study of SOA formation from camphene using laboratory-based chamber experiments and a chemically detailed box model. The experiments were conducted at varying NO_x levels and the chamber data were used to provide SOA parameterizations based on the two-product (Odum Jay et al., 1996) and volatility basis set (VBS) modeling approaches (Donahue et al., 2009; Donahue et al., 2006). The chemically detailed box models, Statewide Air Pollution Research Center (SAPRC) was used to provide mechanistic insights into the chamber observations and to elucidate the connections between the fate of RO_2, HOM forming mechanisms, and camphene SOA formation.

4.2 Method

4.2.1 Chamber experimental conditions

The camphene photooxidation experiments were conducted in the University of California, Riverside (UCR) dual indoor environmental chamber. The initial conditions of the chamber experiments are summarized in Table 4.1. Chamber characterization and features have been previously described in detail (Carter et al., 2005). A series of 13 camphene photooxidation experiments were carried out under varying levels of camphene and NO_x (Table 4.1) with approximately 1 ppm H_2O_2 to control reaction activity of the chamber experiments. No seed aerosol was used in this study. All experiments were conducted under UV black lights and dry conditions (relative humidity < 0.1 %) at 300 K. More detailed information about the chamber experiments can be found in Li et al. (2021).

Table 4.1: Summary of initial conditions for chamber experiments and box model simulations.

	Expt.	Initial Conditions for Chamber Experiments and SAPRC Simulations			
		Camphene (ppb)	Added NO_x (ppb)	H_2O_2 [a] (ppb)	HC/NO_x (ppb/ppb)
without NO_x	WO1	7		854	
	WO2	9		1148	
	WO3	28		1212	
	WO4	57		1182	
	WO5	120		1212	
	WO6	223		1576	
with NO_x	W1	7	89	854	0.08
	W2	25	138	1040	0.18
	W3	32	62	1136	0.51
	W4	43	7	860	5.91
	W5	60	94	1227	0.64
	W6	131	98	1167	1.33
	W7	172	60	1121	2.88

[a] H_2O_2 mixing ratio was targeted at 1ppm but corrected based on tracer (perfluorohexane or perfluorobutane) concentration to offset initial reactor volume bias. Corrected H_2O_2 mixing ratios were used in SAPRC modeling.

4.2.2 SAPRC model configurations and conditions

A gas-phase oxidation mechanism was derived using the SAPRC mechanism generation system (MechGen) with modified initial rate constants (camphene with OH, NO_3 and O_3) based on published literature data (Atkinson et al., 1990). MechGen, described elsewhere (Carter, 2020a, 2020b; Jiang et al., 2020), is capable of generating fully explicit mechanisms for the atmospheric reactions of many types of organic compounds and the intermediate radicals they form. MechGen uses experimentally derived rate constants and branching ratios if data are available and otherwise uses estimated rate constants and branching ratios based on group additivity and other estimation methods. This system was used to derive reactions of explicit and lumped organic compounds and products in the development of the SAPRC-18 mechanism (Carter, 2020a) and a detailed SAPRC furans mechanism (Jiang et al., 2020).

The MechGen-derived camphene mechanism was implemented into the SAPRC box model to simulate chamber experiments under the same chemical conditions as the chamber experiments, where the initial hydrocarbon concentrations and NO_x levels were as defined in Table 4.1. The SAPRC box model system has been used for chemical mechanism development, evaluation, and box modeling applications since the mid-1970s (Carter, 1999, 2009, 2010, 2020a, 2020b, 2020c; Carter & Heo, 2012). The initial conditions and relevant chemical parameters for environmental chamber experiments are required inputs; simulations can be performed using multiple versions of the SAPRC gas-phase chemical mechanism. In this work, the recently published version, SAPRC-18 (Carter, 2020a), was selected as the base mechanism because it represents the current state of the science and includes the most up-to-date model species and explicit representation of RO_2 chemistry.

4.3 Experimental and Modeling Results

Table 4.2 summarizes the measured initial NO/NO_2 mixing ratios, initial camphene concentration ($[HC]_0$), reacted camphene concentration ($\Delta[HC]$), SOA mass (M_o) formed, photochemical aging time, irradiation time, and SOA mass yield (SOA mass formed,

M_o/hydrocarbon reacted, ΔHC) for all 13 experiments. Except for Figure 4.4, in which SOA mass yields are shown as a function of photochemical age, all SOA mass yields refer to the mass at the end of the experiments (~6 hours).

Table 4.2: Chamber SOA data, WO indicates experiments without added NO_x and W with added NO_x.

Expt.	Initial NO/NO_2	$[HC]_0$	Δ[HC]	M_o	Irradiation time	Photochemical aging time	Mass Yield
	ppb	μg m^{-3}	μg m^{-3}	μg m^{-3}	hour	hour	
WO1	0/0	41	41	6.1	4.9	16.1	0.15
WO2	0/0	49	49	3.7	5.0	16.7	0.08
WO3	0/0	155	153	42.0	6.1	17.7	0.27
WO4	0/0	313	305	84.4	6.7	15.8	0.28
WO5	0/0	663	597	158.6	6.7	9.5	0.27
WO6	0/0	1230	844	162.4	6.1	5.0	0.19
W1	86/2	40	40	14.6	5.1	50.6	0.36
W2	114/24	140	140	46.1	5.2	40.6	0.33
W3	51/11	177	177	112.3	6.0	42.0	0.64
W4	5/2	238	237	96.0	5.9	16.1	0.41
W5	45/49	334	334	199.5	5.8	33.6	0.60
W6	42/56	724	724	428.8	5.8	12.7	0.59
W7	45/15	956	950	494.3	6.4	8.75	0.52

4.3.1 Gas-phase reactivity

Figure 4.2 shows measured and predicted camphene consumption for the 13 photooxidation experiments, and the calculated time-dependent *β* values (ratio of RO_2 + NO to the sum of RO_2 + NO and RO_2 + HO_2) (Henze et al., 2008; Pye et al., 2010) based on SAPRC predictions for each experimental condition. Additional comparisons of measured and predicted gas-phase species are shown in Figure D1. Experimental OH mixing ratio was calculated as:

$$[\mathbf{OH}]_{\mathbf{exp}} = \frac{\frac{\mathrm{d[Cam]_{exp}}}{\mathrm{dt}} - k_{\mathrm{O3}}[\mathrm{Cam}]_{\mathrm{exp}}[\mathrm{O_3}] - k_{\mathrm{NO3}}[\mathrm{Cam}]_{\mathrm{exp}}[\mathrm{NO_3}]_{\mathrm{exp}}}{k_{\mathrm{OH}}[\mathrm{Cam}]_{\mathrm{exp}}} \qquad \textbf{Equation 4.1}$$

where $[OH]_{exp}$ is the OH mixing ratio averaged throughout the experiment until complete consumption of camphene; $[Cam]_{exp}$ is the camphene mixing ratio; $[NO_3]_{exp}$ is the NO_3 mixing ratio which was assumed to be the same as the simulation NO_3 mixing ratio; k_{OH}, k_{NO3} and k_{O3} are the camphene reaction rate constants with OH, NO_3 and O_3 at 298K under atmospheric conditions (Figure 4.1).

Higher camphene decay rates and higher OH levels (0.15–0.88 ppt with added NO_x; 0.05–0.29 ppt without added NO_x) were observed and predicted for experiments with added NO_x than without; likely due to the fast recycling of OH when NO_x was present (Figure 4.2). For all experiments, the *β* values changed as a function of time due to changing chemical conditions. Note that due to off-gassing of NO_x from the Teflon reactor (Carter et al., 2005), *β* values simulated here were larger than 0 even for experiments without added NO_x. Experiments with added NO_x have *β* values from 0.12~1, while experiments without added NO_x have values < 0.12.

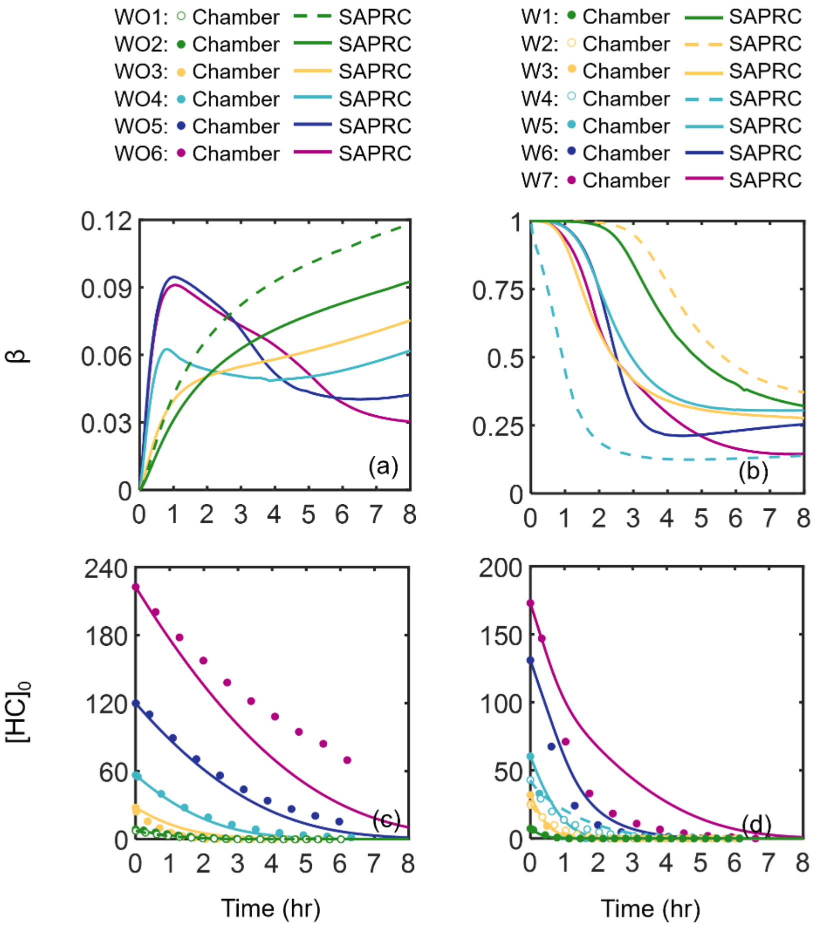

Figure 4.2: SAPRC predicted *β* values: (a) without added NO_x, and (b) with added NO_x. Measured (circles) and predicted (lines) camphene consumption as a function of irradiation time: (c) without added NO_x, and (d) with added NO_x. The hollow makers used in (c) and (d) are equivalent to dashed lines defined in the legends.

For all parameters (camphene consumption, NO_x decay, O_3 formation, and OH levels), the SAPRC simulation results were generally in good agreement with the experimental data. The exception to the generally good agreement was O_3 predictions in experiments without added NO_x, which have a relatively strong dependence on the HONO off-gassing rate. The quantity $\Delta([O_3]-[NO])$ has been used to evaluate the rate of NO oxidation by RO_2 for VOC-NO_x systems in SAPRC mechanism development (Carter, 1999, 2009, 2020a; Carter & Lurmann, 1991). Figure D2 shows the comparison of the $\Delta([O_3]-[NO])$ values between chamber measurements and SAPRC simulations for experiments with added NO_x. The SAPRC box model captures the rates of RO_2+NO well, and supports the use of the SAPRC model to interpret chamber observations especially in the presence of NO_x. Unfortunately, it is hard to quantify how well constrained the other RO_2 reaction rates and product yields are without corresponding measurements, which are not available. In this case, the SAPRC model was largely used to probe the mechanism (diagnostic) and not to predict yields (prognostic).

4.3.2 SOA mass and yield

Measured SOA mass yields are shown in Figure 4.3 as a function of SOA mass (M_o) for experiments with (circles) and without (squares) added NO_x. The SOA mass yields were much higher in experiments with added NO_x (0.33~0.64) than experiments without added NO_x (0.08~0.28). The observed trends in SOA mass yields were unexpected based on prior chamber studies of SOA formation from monoterpenes, such as OH oxidation studies of α- and β-pinene, in which SOA mass yields were reported to be suppressed under high-NO_x conditions (Eddingsaas et al., 2012; Pullinen et al., 2020; Sarrafzadeh et al., 2016).

Figure 4.3 shows another unexpected observation: the SOA mass yields decreased at high SOA mass under both NO_x conditions. In the presence of NO_x, the observed SOA mass yields increased with M_o for $M_o \leq 112$ μg m^{-3}, plateaued between 112 μg m^{-3} $< M_o \leq$

429 μg m^{-3}, and then decreased for $M_o > 429$ μg m^{-3}. Without NO_x, the observed SOA mass yields increased for $M_o \leq 42$ μg m^{-3}, plateaued between 42 μg m^{-3} $< M_o \leq 159$ μg m^{-3}, and then decreased for $M_o > 159$ μg m^{-3}. These unexpected trends in SOA mass yields were further investigated and largely explained by the RO_2 fate based on box model simulations (see Sect. 4.4).

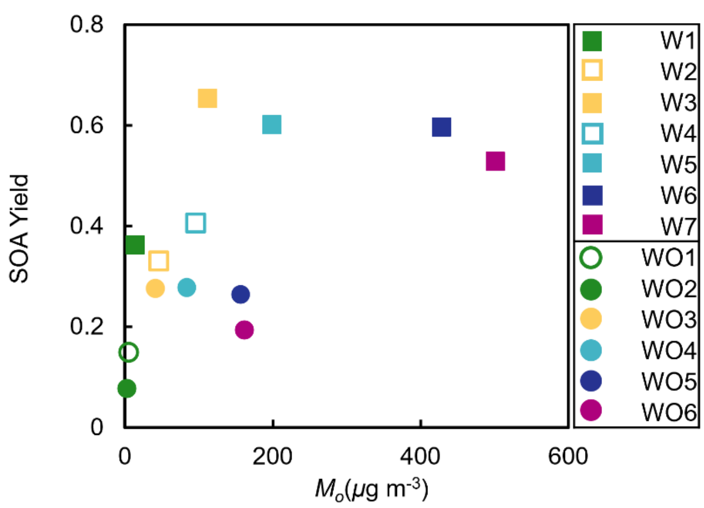

Figure 4.3: Measured camphene SOA mass yields as a function of SOA mass (M_o). Squares indicate experiments with (W) and circles without (WO) added NO_x. Initial HC mixing ratios are differentiated by color; open symbols are used to indicate replicate initial HC mixing ratios.

The varying [OH] levels in the chamber experiments led to a wide range of photochemical aging times, from hours to days. The irradiation time was converted to equivalent photochemical aging time in the ambient atmosphere using Equation 4.2 (Aumont et al., 2012):

$$\boldsymbol{\tau} = \frac{\mathbf{1}}{[\mathbf{OH}]_{\mathbf{atm}}} \int_{\mathbf{0}}^{\mathbf{t}} [\mathbf{OH}]_{\mathbf{sim}} \mathbf{dt} \qquad \textbf{Equation 4.2}$$

where $[OH]_{atm}$ was assumed to be 2×10^6 molecule cm^{-3}. Figure 4.4 shows the measured SOA mass yields as a function of photochemical aging time calculated using OH values predicted by SAPRC ($[OH]_{sim}$). The SOA mass yields are dependent on OH levels and thus photochemical aging time. The yield curves for most experiments plateaued or nearly plateaued by the end of the experiment. Higher $[HC]_0$ generally led to steeper increases in SOA mass yield as a function of aging time. Experiments with added NO_x generally had longer photochemical aging times than experiments without added NO_x; even at the same aging time (Figure D6), the SOA yields were higher in the with added NO_x experiments. The higher SOA mass yields in experiments with added NOx may partially be attributed to the difference in [OH] levels and extents of aging. Similar NO_x effects have been reported in many previous studies (N. L. Ng et al., 2007; Sarrafzadeh et al., 2016). Sarrafzadeh et al. (2016) proposed that in a study of β-pinene the OH level was the main factor that accounted for differences in SOA mass yields under varying $[NO_x]_0$. In the camphene experiments presented herein, the aging effects were determined to be less important than RO_2 chemistry, since the SOA mass yield curves as a function of photochemical aging already plateau or nearly plateau by the end of experiments (Figure 4.4).

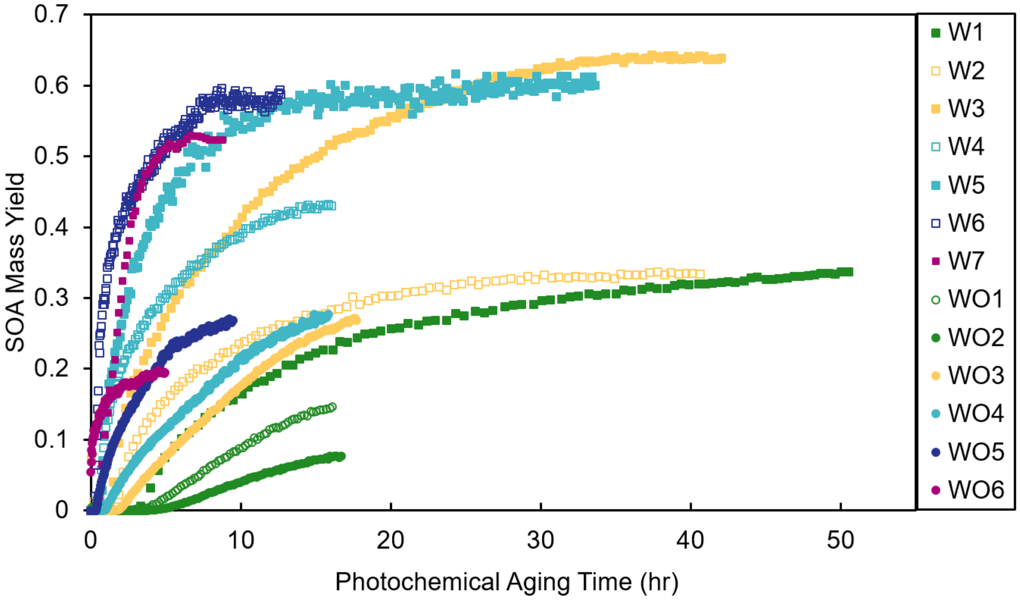

Figure 4.4: Measured SOA mass yields as a function of photochemical aging time in experiments with added NO$_x$ (squares) and experiments without added NO$_x$ (circles).

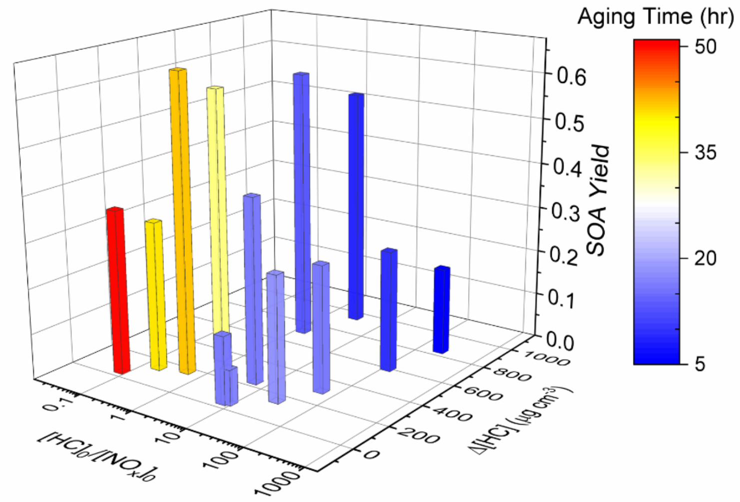

Figure 4.5: SOA mass yields dependence on [HC]$_0$/[NO$_x$]$_0$, Δ[HC], and photochemical aging time.

SOA mass yields are shown as a function of Δ[HC], $[HC]_0/[NO_x]_0$, and photochemical aging time in Figure 4.5. For the experiments without added NO_x, a constant value of 1 ppb was used in the calculations of $[HC]_0/[NO_x]_0$ to account for NO_x off-gassing from the Teflon reactors. Based on recent characterization experiments, the UCR chamber has a NO_x off-gassing rate of 2.8 ppt/min in the form of HONO; the camphene experiments lasted for ~300 to 360 mins. Over low Δ[HC] ranges, when Δ[HC] increases, SOA mass yield increases as well. When Δ[HC] is larger than approximately 200 ug m^{-3}, this correlation becomes less apparent, due to the high sensitivity of SOA formation on $[HC]_0/[NO_x]_0$ over the range of Δ[HC] sampled. At a given Δ[HC] level, a relatively smaller $[HC]_0/[NO_x]_0$ (when it was within 0.5~200) would lead to a higher SOA mass yield (decreasing $[HC]_0/[NO_x]_0$ by approximately 100 times may double the SOA mass yield). The chamber data presented here exhibit a general trend that, under the regular regime (distinguished from the extreme $[NO_x]$ regime), higher SOA mass yields are observed from camphene oxidation at higher Δ[HC] and smaller $[HC]_0/[NO_x]_0$. This is different from studies of α-pinene, in which smaller $[HC]_0/[NO_x]_0$ generally led to lower SOA mass yield (Eddingsaas et al., 2012; Li et al., 2007).

4.3.3 $[HC]_0/[NOx]_0$ and the fate of peroxy radicals

Table D1 shows the experimental $[HC]_0/[NO_x]_0$ and the SAPRC predicted fate of total RO_2 (calculated as the summation of RO_2 radicals that undergo bimolecular reactions) for all the chamber runs. In Figure 4.6, the fate of total RO_2 is shown as a function of $[HC]_0/[NO_x]_0$. The majority of RO_2 was predicted to undergo bimolecular reactions with

HO_2 or NO across the range of $[HC]_0/[NO_x]_0$ values sampled. At $[HC]_0/[NO_x]_0 < 6$, > 50% of the RO_2 was predicted to react with NO; and at $[HC]_0/[NO_x]_0 > 10$, > 50% of the RO_2 was predicted to react with HO_2. A roughly 50:50 branching of RO_2 between NO and HO_2 was reached when $[HC]_0/[NO_x]_0$ was 6:1, which is close to the ratio that was suggested in (Presto et al., 2005). When $[HC]_0/[NO_x]_0$ increased over 50, the total fraction of bimolecular $RO_2 + RO_2$ increased from 0 to 30%. In addition, the normalized total RO_2 concentration (total $[RO_2]/[HC]_0$, ppbv/ppbv) increased as $[HC]_0/[NO_x]_0$ decreased (Figure 4.7), suggesting more oxygenated RO_2s were formed by NO pathway than others, which is consistent with the formation of HOMs with added NO_x. There is a general trend of increasing SOA mass yield with decreasing $[HC]_0/[NO_x]_0$ (Figure 4.5 and Figure 4.7), with the exception of four outliers (W1, W2, WO1, and WO2) that have relatively low SOA mass yields. Experiments WO1, WO2, W1 had the lowest $\Delta[HC]$ (49, 41, and 40 $\mu g/m^3$, respectively, Table 4.2), indicating the SOA mass yields were influenced by $\Delta[HC]$ as well as RO_2 chemistry. The connections between the fate of RO_2 and observed SOA mass yields are further discussed in Sect. 4.4. Though vapor wall loss has been found to be negligible in previous UCR chamber experiments, such experiments were typically conducted at higher $[HC]_0$. Thus, it is acknowledged that vapor wall loss could affect the measured SOA yields, particularly for experiments W1~2 and WO1~2 with low $[HC]_0$ (or M_o). A vapor wall loss correction for those experiments would increase the measured SOA, but would not affect the following discussion or conclusions regarding the role of RO_2 chemistry.

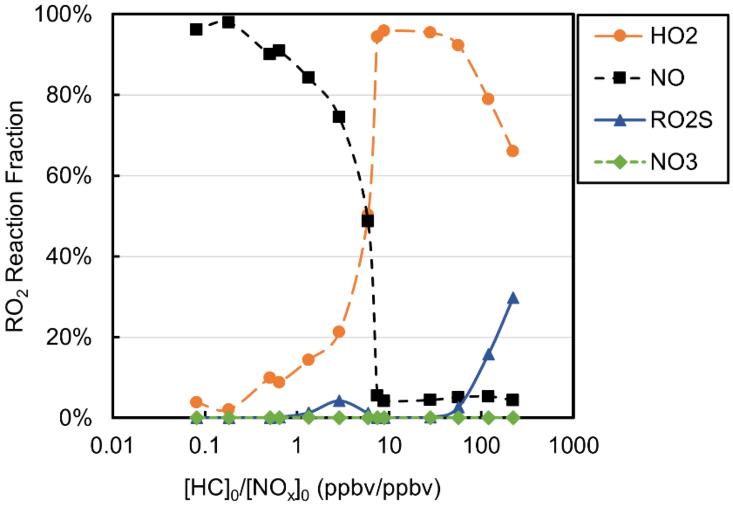

Figure 4.6: Fractions of total RO_2 reactions of each type as a function of $[HC]_0/[NOx]_0$ based on Table S1.

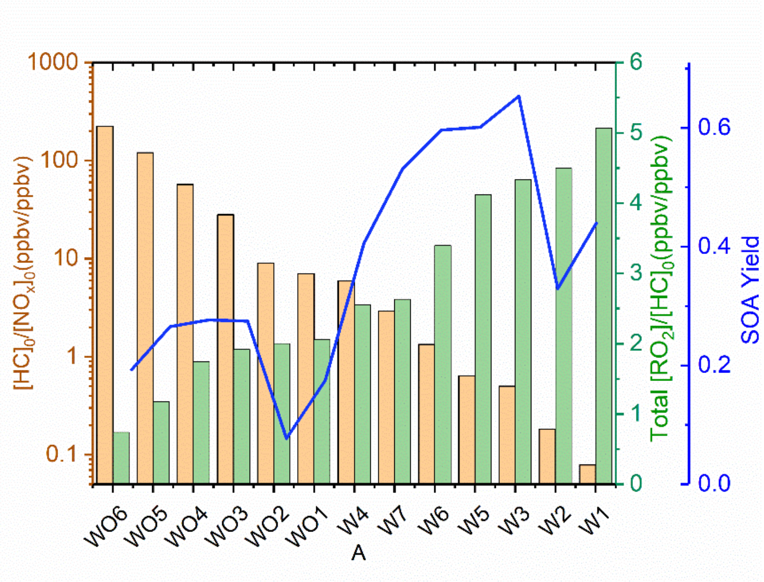

Figure 4.7: Relationship between total $[RO_2]/[HC]_0$, $[HC]_0/[NO_x]_0$, and SOA mass yields.

By assuming the gas-phase chemistry and product distribution were similar when RO_2 + NO accounted for more than 80% of the total RO_2 consumption and when RO_2 + HO_2 accounted for more than 80% of the total RO_2 consumption, experiments with (W1~3, 5~6) and without (WO1~4) added NO_x were grouped and used to derive SOA parameters using the two-product (Odum Jay et al., 1996) and VBS approaches (Donahue et al., 2009; Donahue et al., 2006). The resultant parameters are shown in Table 4.3 (two-product) and Table 4.4 (VBS).

Table 4.3: Two-Product Model SOA parameters.

	α_1	$\log_{10} C^*_1$	α_2	$\log_{10} C^*_2$
Without NO_x	0.0017	1.08	0.3139	0.92
With NO_x	0.4484	1.77	0.2398	-2.94

Table 4.4: VBS Model SOA parameters.

C^*	α_{wo} [a]	α_w [b]
0.1	0.0001	0.2657
1	0.0152	0.0008
10	0.3069	0.0357
100	0.0001	0.4222
1000	0.0003	0.0000

[a] wo refers to without added NO_x.
[b] w refers to with added NO_x.

4.4 Discussion

The reaction rate constant of camphene with O_3 is relatively low compared to OH, and thus it is expected that OH is the dominant oxidant in the photooxidation of camphene under chamber conditions, especially with the high initial H_2O_2 (~1 ppm) concentrations. This is supported by SAPRC simulation results (see Figure D3 in Appendix D), in which O_3 accounts for 0~3% and NO_3 for 0~16% of camphene oxidation, demonstrating the important role of OH oxidation in these studies.

4.4.1 Camphene + OH gas-phase mechanism

Figure 4.8 shows the MechGen predicted reactions and products of OH-initiated oxidation of camphene in the presence of NO_x through one major pathway, which had a yield of 0.83 (a more detailed reaction mechanism schematic is presented in Figure D4). The reaction starts with OH addition to the CH_2=(C) position to form a ring-retaining alkyl radical, which further reacts with O_2 to form the camphene peroxy radical, RO_2-a. RO_2-a can react with oxidants (NO, NO_3, HO_2, and/or other RO_2) to create an alkoxy radical, RO-a, with NO to NO_2 conversion; or form stable products such as organic nitrate (NO3CAMP1), hydroperoxide (HO2CAMP1), and alcohol (RO2CAMP1) compounds. The cyclic alkoxy radical RO-a can undergo prompt beta (β)-scission ring-opening reaction, and then O_2 addition to form another peroxy radical, RO_2-b. In the presence of NO_x, rapid β-scission decomposition, or ring-opening reactions of the camphene alkoxy radicals (RO-b and RO-c) occur through the RO_2 + NO pathway, leading to the generation of the peroxy radical RO_2-d with lower carbon number and higher O:C ratio (increases from 0.30 for RO_2-a to 0.71 for RO_2-d).

MechGen predicted that RO_2-d could undergo 1,5 H-shift isomerization nearly instantaneously, even in the presence of ~ 100 ppb NO_x. Subsequent rapid addition of O_2 can form a new peroxy radical RO_2-d* which can undergo 1,7 H-shift isomerization and form the peroxy radical RO_2-d**. RO_2-d** can participate in termination reactions with NO and HO_2 to form organic nitrate (NO3CAMP4) and hydroperoxide (HO2CAMP4) products, which are known as highly oxygenated organic molecules (HOMs). In the presence of NO_x, RO_2-d** can also react with NO to form the alkoxy radical RO-d that can undergo 1,4 H-shift isomerization and then O_2 addition to form the new peroxy radical RO_2-e which will also lead to the formation of HOMs such as NO3CAMP5, HO2CAMP5, and UNICAMP. A recent SOA study by Mehra et al. (2020) demonstrated the formation of HOMs in camphene chamber experiments under both low NO_x (30 ppb camphene, ~ 0 ppb NO_x) and medium NO_x (30 ppb camphene, 2.2 ppb NO, 58.4 ppb NO_2) conditions. Based on their observations and analysis, the average molecular formula of the camphene SOA was $C_{7.26}H_{9.85}O_{4.03}$ for low NO_x and $C_{6.63}H_{9.7}N_{0.12}O_{4.21}$ for the medium NO_x conditions, which also suggest the occurrence of ring-opening and decomposition reactions during camphene photooxidation, as predicted by MechGen.

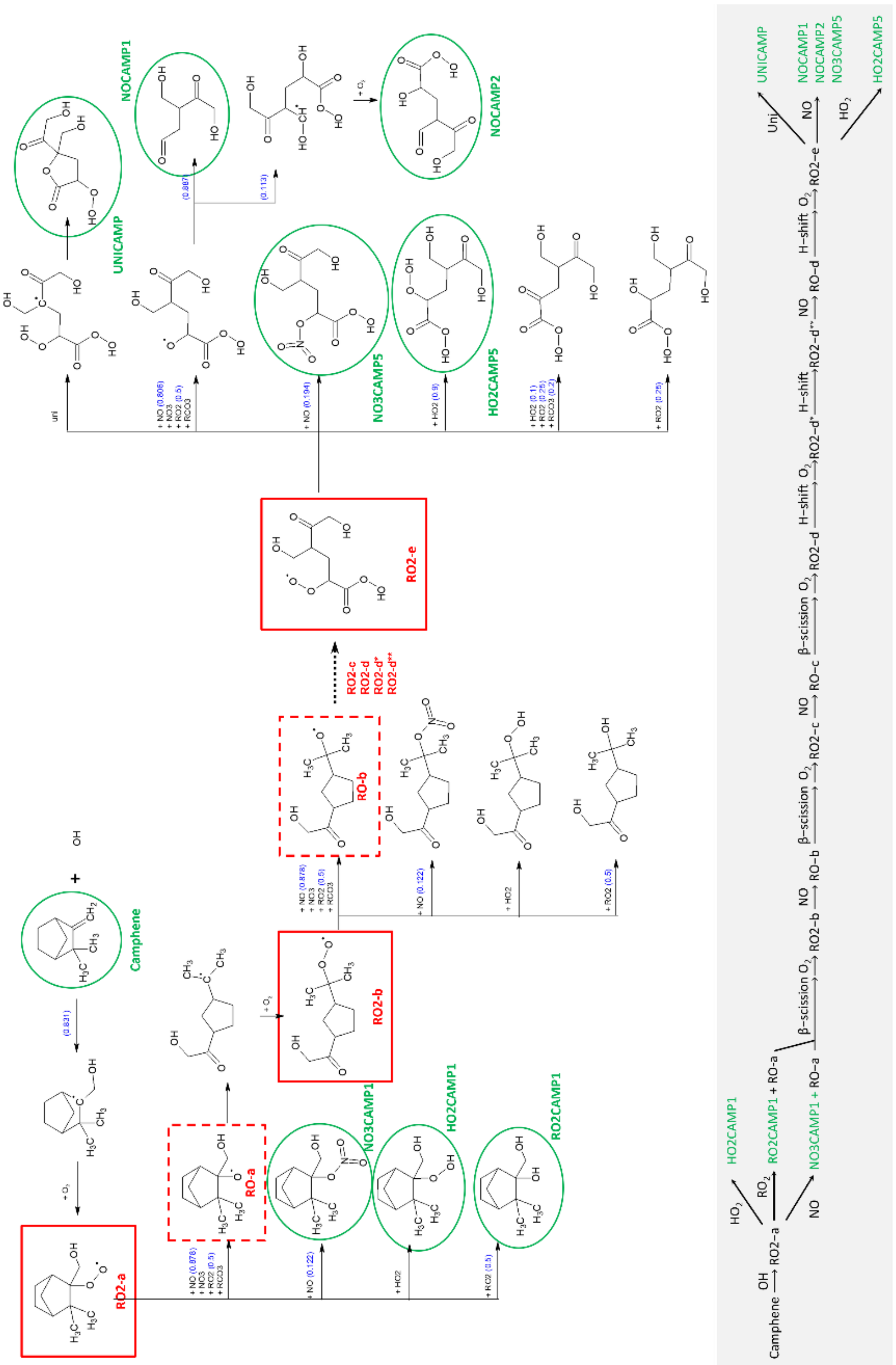

Figure 4.8: Schematic of the OH-initiated oxidation of camphene mechanism in SAPRC at 298 K and atmospheric pressure in the presence of NO$_x$. Check Figure D4 for more details.

4.4.2 The formation of HOMs and influence on SOA mass yields

Table 4.5: Log_{10} C^* value for selected 1st generation of stable end products formed from camphene reactions with OH.

Species	Atom				O:C	$\log_{10} C^*$
	C	H	O	N		
RO2CAMP1	10	18	2	0	0.20	3.8
HO2CAMP1	10	18	3	0	0.30	2.5
HO2CAMP2	10	18	4	0	0.40	1.7
HO2CAMP3	7	12	4	0	0.57	2.5
HO2CAMP4	7	12	7	0	1.00	-1.3
HO2CAMP5	7	12	8	0	1.14	-4.3
NO3CAMP1	10	17	4	1	0.40	3.5
NO3CAMP2	10	17	5	1	0.50	2.6
NO3CAMP3	7	11	5	1	0.71	3.5
NO3CAMP4	7	11	8	1	1.14	-0.1
NO3CAMP5	7	11	9	1	1.29	-2.8
NOCAMP1	6	10	4	0	0.67	2.6
NOCAMP2	7	10	7	0	1.00	-1.1
UNICAMP	7	10	7	0	1.00	-3.9

Table 4.5 lists the log C^* values and O:C ratios for the major camphene products predicted; vapor pressures of products were calculated based on the Nannoolal method (Nannoolal et al., 2008). HOMs have much lower volatilities than the earlier terminal products such as NO3CAMP1, HO2CAMP1, and RO2CAMP1. HOMs formed by autoxidation steps in camphene radical chain reactions are mediated by the H-shift isomerization of RO_2-d and RO-d. Table 6 shows the SAPRC predicted fate of RO_2-a for all chamber runs; the fate of summed RO_2 is shown in Table S1, which includes RO_2-a~d and all the RO_2 radicals formed from other minor pathways. For the experiments without added NO_x (WO1~6), once the initial peroxy radical RO_2-a was formed, a large fraction of RO_2-a (0.54~0.98) quickly reacted with HO_2 to form the terminal product HO2CAMP1,

while only 2~3% of RO_2-a reacted through the NO pathway and led to the generation of HOMs. For the experiments with added NO_x (W1~7), much higher RO_2-a + NO fractions (0.65~1.00) were predicted by SAPRC. The fates of summed RO_2 also suggested that not only RO_2-a, but also the other RO_2 radical intermediates would tend to favor further reactions through the NO reaction chain to form lower volatility products.

Based on the predicted fate of RO_2 in SAPRC simulations, the higher SOA mass yields in experiments with NO_x were due to the formation of HOMs through autoxidation in the presence of NO_x. In general, faster RO_2 reaction with NO, HO_2 or other RO_2 limits HOM formation by autoxidation (Bianchi et al., 2019). In previous monoterpene SOA studies, HOM formation was often observed when NO_x was absent or under lower NO_x conditions (Pye et al., 2019; Schervish & Donahue, 2020; Zhao et al., 2018). For example, Zhao et al. (2018) demonstrated that autoxidation for some RO_2 is competitive with RO_2 + NO at ppb levels of NO for O_3-initiated α-pinene oxidation. They also reported that HOM formation decreased as the initial NO concentration increased from 0 ppb to 30 ppb. In the camphene experiments presented herein, the reverse trend was observed (see experiments WO4, W4 and W5 conducted with ~50 ppb camphene at different NO_x levels). This was due to the key RO_2 species, RO_2-d, which was predicted to form only in the presence of NO_x and had a fast enough autoxidation rate constant to effectively compete with bimolecular reactions.

Table 4.6: Fractions of peroxy radical RO2-a reactions of each type, calculated based on SAPRC simulations.

Expt.	$[HC]_0$ (ppb)	$[HC]_0/[NO_x]_0$ [a] (ppbv/ppbv)	SOA Mass Yield	Fraction of RO_2-a Reaction			
				NO	HO_2	RO_2s [b]	NO_3
WO1	7	7	0.15	0.03	0.97	0	0
WO2	9	9	0.08	0.02	0.98	0	0
WO3	28	28	0.27	0.02	0.97	0	0
WO4	57	57	0.28	0.03	0.89	0.08	0
WO5	120	120	0.27	0.03	0.64	0.32	0
WO6	223	223	0.19	0.03	0.54	0.43	0
W1	7	0.08	0.36	1.00	0	0	0
W2	25	0.18	0.33	1.00	0	0	0
W3	32	0.51	0.64	0.97	0.03	0	0
W4	43	5.91	0.41	0.46	0.53	0.01	0
W5	60	0.64	0.60	0.97	0.03	0	0
W6	131	1.33	0.59	0.88	0.12	0.02	0
W7	172	2.88	0.52	0.65	0.30	0.01	0

[a] The $[HC]_0/[NO_x]_0$ for WO1~6 experiments were estimated assuming 1 ppb of NO_x.
[b] "RO_2s" refers to the sum of RO_2 reacting with RO_2 and with RCO_3.

The decreasing SOA mass yields at high $[HC]_0$ and M_o in all experiments (shown in Figure 4.3) can also be explained by RO_2 chemistry. For experiments with added NO_x, the decreasing SOA mass yield trend was most likely due to the shift of RO_2 reaction pathways from NO to HO_2. The fraction of RO_2-a + NO decreased from 0.97 (W5) to 0.65 (W7) while the fraction of RO_2-a + HO_2 increased from 0.03 (W5) to 0.3 (W7). For the experiments without NO_x, the shift from RO_2 + HO_2 to self- and cross-reactions of RO_2 at high $[HC]_0$ and M_o led to decreasing SOA mass yields. When $[HC]_0$ increased from 57 ppb to 223 ppb, the fractions of RO_2-a + HO_2 decreased from 0.89 (WO4) to 0.54 (WO6) and the fraction of RO_2-a + RO_2 increased by a factor of five, from 0.08 to 0.41. Moreover, this shift from bimolecular reactions with HO_2 to RO_2 as $[HC]_0$ increased also occurred in the context of the total RO_2 (Table D1). Generally, products that were predicted to form from one RO_2 reacting with another RO_2 in the absence of NO_x, had relatively higher volatility than those formed from that RO_2 reacting with HO_2; for example, RO2CAMP1 formed from RO_2-a + RO_2 was more volatile than HO2CAMP1 formed from RO_2-a + HO_2 (Table 4.5). The increasing fraction of self- and cross-reactions of RO_2 therefore is one likely explanation for the decreasing SOA mass yields at high ΔHC and M_o in the experiments without NO_x.

In experiments W1 and W2, the relatively low SOA mass yields (0.36 and 0.33) can be partially attributed to differences in product distribution. A comparison of the product distributions between W1, W2, W3 and W5 suggested similar yields of NO3CAMP1~5 and NOCAMP1~2, but major differences in yields of UNICAMP and HO2CAMP1–5 (Figure D5). Experiments W3 and W5 were selected for comparison because of their closest total RO_2 fractional reaction distribution (approximately 90% RO_2 + NO and 10% RO_2 + HO_2) to W2 (98% RO_2 + NO and 2% RO_2 + HO_2) and W1 (96% RO_2 + NO and 4% RO_2 + HO_2) but higher SOA mass yield (0.64 and 0.6). W1 and W2 were predicted to have much smaller SOA mass yield than W3 and W5 in the low volatility products HO2CAMP1~5 (especially product HO2CAMP5, the lowest volatility among all listed products in Table 4.5, $\log_{10}C^* = -4.3$) and UNICAMP (the second lowest volatility shown in Table 4.5, $\log_{10}C^* = -3.9$), which can contribute to the lower SOA mass yield. Further analysis of W1 and W2 revealed a likely cause for the different yields of HO2CAMP1–5 and UNICAMP. W1 and W2 were predicted to have delayed peaks of [OH] (after 3–4 hours of irradiation) which likely was due to the high NO_x concentrations (Fig. S2). Correspondingly, the [HO_2] was highly suppressed during the first 2 hours of irradiation. Under high [NO_x], the RO_2-e + HO_2 pathway shown in Fig. 8 therefore could be suppressed, resulting in a lower yield of HO2CAMP5. This indicates a second regime may exist at high [NO_x] and significantly lower $[HC]_0/[NO_x]_0$.

4.5 Conclusions

The first SOA mass yields from oxidation of camphene based on experiments performed in UCR environmental chamber with varying $[NO_x]_0$ are presented herein. Higher SOA mass yields were measured with added NO_x (0.33~0.64) than without added NO_x (0.08~0.26) at atmospherically relevant OH concentrations. SOA formation from the oxidation of camphene showed different NO_x dependence than what has previously been reported for other monoterpenes (e.g., α-pinene, d-limonene) and n-alkanes (carbon$\leq$ 10), in which higher SOA mass yields were measured when [NO_x] was lower (N. L. Ng et al., 2007). For camphene oxidation, higher Δ[HC] and lower $[HC]_0/[NO_x]_0$ (within 0.5~200) generally led to higher SOA mass yields. Similar NO_x dependence has been observed for two sesquiterpenes (longifolene and aromadendrene) but was attributed to the production of nonvolatile organic nitrates with no detailed mechanistic analysis provided at that time (N. L. Ng et al., 2007).

Although $[HC]_0/[NO_x]_0$ shows clear correlation with SOA mass yield, this quantity cannot completely represent the underlying RO_2 chemistry. The RO_2 chemistry and the competition between varying bimolecular RO_2 and unimolecular RO_2 reaction pathways, explored using SAPRC MechGen, can be used to explain the dependence of SOA mass yields on HC and NO_x. The RO_2 + NO pathway favored in experiments with added NO_x formed HOMs with much lower volatilities than products formed in other pathways. In addition to the regular regime introduced above, the results suggested an extreme regime where significantly high [NO_x] may suppress SOA mass yield. High NO_x concentration may suppress the HO_2 concentration at the beginning of the reactions, causing a subsequent reduction in yield of low volatility products such as UNICAMP and HO2CAMP5. This indicates that if the reactions happened under NO_x-rich environment with extremely high ratios of NO to HO_2 (NO/HO_2), the SOA mass yield from oxidation of camphene might be significantly suppressed. As demonstrated here, simulations with chemically detailed box models such as SAPRC are useful for identifying SOA formation regimes.

Overall, SOA formation from oxidation of camphene may be larger in polluted environments (e.g., urban environments) than NO_x-free environments. This reveals a possible underestimation of SOA formed from oxidation of camphene and potentially other VOCs that are assumed to have lower SOA mass yields at higher NO_x levels. Further chamber and modeling studies of other understudied VOCs will be important for identifying other systems in which moderate NO_x levels can promote HOM formation.

References

Afreh, I. K., Aumont, B., Camredon, M., & Barsanti, K. C. (2021). Using GECKO-A to derive mechanistic understanding of secondary organic aerosol formation from the ubiquitous but understudied camphene. *Atmos. Chem. Phys.*, *21*(14), 11467-11487. https://doi.org/10.5194/acp-21-11467-2021

Akagi, S., Yokelson, R. J., Burling, I., Meinardi, S., Simpson, I., Blake, D. R., McMeeking, G., Sullivan, A., Lee, T., & Kreidenweis, S. (2013). Measurements of reactive trace gases and variable O 3 formation rates in some South Carolina biomass burning plumes. *Atmospheric Chemistry and Physics*, *13*(3), 1141-1165.

Atkinson, R., & Arey, J. (2003). Atmospheric Degradation of Volatile Organic Compounds Atmospheric Degradation of Volatile Organic Compounds. *Chemical Reviews*, *103*(3), 4605-4638. https://doi.org/10.1021/cr0206420

Atkinson, R., Aschmann, S. M., & Arey, J. (1990). Rate constants for the gas-phase reactions of OH and NO3 radicals and O3 with sabinene and camphene at 296±2 K. *Atmospheric Environment. Part A. General Topics*, *24*(10), 2647-2654.

Aumont, B., Valorso, R., Mouchel-Vallon, C., Camredon, M., Lee-Taylor, J., & Madronich, S. (2012). Modeling SOA formation from the oxidation of intermediate volatility n-alkanes. *Atmospheric Chemistry and Physics*, *12*(16), 7577-7589. https://doi.org/10.5194/acp-12-7577-2012

Baruah, S. D., Gour, N. K., Sarma, P. J., & Deka, R. C. (2018). OH-initiated mechanistic pathways and kinetics of camphene and fate of product radical: a DFT approach. *Environmental Science and Pollution Research*, *25*(3), 2147-2156.

Benelli, G., Govindarajan, M., Rajeswary, M., Vaseeharan, B., Alyahya, S. A., Alharbi, N. S., Kadaikunnan, S., Khaled, J. M., & Maggi, F. (2018). Insecticidal activity of camphene, zerumbone and α-humulene from Cheilocostus speciosus rhizome essential oil against the Old-World bollworm, Helicoverpa armigera. *Ecotoxicology and environmental safety*, *148*, 781-786.

Bianchi, F., Kurtén, T., Riva, M., Mohr, C., Rissanen, M. P., Roldin, P., Berndt, T., Crounse, J. D., Wennberg, P. O., Mentel, T. F., Wildt, J., Junninen, H., Jokinen, T., Kulmala, M., Worsnop, D. R., Thornton, J. A., Donahue, N., Kjaergaard, H. G., & Ehn, M. (2019). Highly Oxygenated Organic Molecules (HOM) from Gas-Phase Autoxidation Involving Peroxy Radicals: A Key Contributor to Atmospheric Aerosol. *Chemical Reviews*, *119*(6), 3472-3509. https://doi.org/10.1021/acs.chemrev.8b00395

Carter, W. P. L. (1999). Documentation of the SAPRC-99 Chemical Mechanism for VOC Reactivity Assessment. *Assessment*, *1*, 329-329. http://www.engr.ucr.edu.oca.ucsc.edu/~carter/pubs/s99doc.pdf

Carter, W. P. L. (2009). *Development of the SAPRC-07 Chemical Mechanism and Updated Ozone Reactivity Scales; Final report to the California Air Resources Board Contract No. 03-318, March 2009*. https://intra.engr.ucr.edu/~carter/SAPRC/

Carter, W. P. L. (2010). Development of a condensed SAPRC-07 chemical mechanism. *Atmospheric Environment*, *44*(40), 5336-5345. https://doi.org/10.1016/j.atmosenv.2010.01.024

Carter, W. P. L. (2020a). *Documentation of the SAPRC-18 Mechanism; Report to California Air Resources Board Contract No. 11-761, May, 2020*. https://intra.engr.ucr.edu/~carter/SAPRC/18/

Carter, W. P. L. (2020b). *Estimates and Assignments used in the SAPRC-18 Mechanism Generation System; Report to California Air Resources Board Contract No. 11-761. In preparation. When completed, will be available at http://intra.engr.ucr.edu/~carter/SAPRC/18*.

Carter, W. P. L. (2020c). *Gateway to the SAPRC Mechanism Generation System*. http://mechgen.cert.ucr.edu/

Carter, W. P. L., Cocker, D. R., Fitz, D. R., Malkina, I. L., Bumiller, K., Sauer, C. G., Pisano, J. T., Bufalino, C., & Song, C. (2005). A new environmental chamber for evaluation of gas-phase chemical mechanisms and secondary aerosol formation. *Atmospheric Environment*, *39*(40), 7768-7788. https://doi.org/10.1016/j.atmosenv.2005.08.040

Carter, W. P. L., & Heo, G. (2012). *Development of revised SAPRC aromatics mechanisms. Final Report to the California Air Resources Board, Contracts No. 07-730 and 08-326, April 2012*. https://intra.engr.ucr.edu/~carter/SAPRC/saprc11.pdf

Carter, W. P. L., & Lurmann, F. W. (1991). Evaluation of a detailed gas-phase atmospheric reaction mechanism using environmental chamber data. *Atmospheric Environment. Part A. General Topics*, *25*(12), 2771-2806. https://doi.org/10.1016/0960-1686(91)90206-M

Crounse, J. D., Nielsen, L. B., Jørgensen, S., Kjaergaard, H. G., & Wennberg, P. O. (2013). Autoxidation of Organic Compounds in the Atmosphere. *The Journal of Physical Chemistry Letters*, *4*(20), 3513-3520. https://doi.org/10.1021/jz4019207

Donahue, N. M., Robinson, A. L., & Pandis, S. N. (2009). Atmospheric organic particulate matter: From smoke to secondary organic aerosol. *Atmospheric Environment*, *43*(1), 94-106. https://doi.org/10.1016/j.atmosenv.2008.09.055

Donahue, N. M., Robinson, A. L., Stanier, C. O., & Pandis, S. N. (2006). Coupled partitioning, dilution, and chemical aging of semivolatile organics. *Environmental Science and Technology*, *40*(8), 2635-2643. https://doi.org/10.1021/es052297c

Eddingsaas, N., Loza, C., Yee, L., Chan, M., Schilling, K., Chhabra, P., Seinfeld, J., & Wennberg, P. (2012). α-pinene photooxidation under controlled chemical conditions–Part 2: SOA yield and composition in low-and high-NO x environments. *Atmospheric Chemistry and Physics*, *12*(16), 7413-7427.

Ehn, M., Berndt, T., Wildt, J., & Mentel, T. (2017). Highly oxygenated molecules from atmospheric autoxidation of hydrocarbons: a prominent challenge for chemical kinetics studies. *International Journal of Chemical Kinetics*, *49*(11), 821-831.

Fry, J. L., Draper, D. C., Barsanti, K. C., Smith, J. N., Ortega, J., Winkle, P. M., Lawler, M. J., Brown, S. S., Edwards, P. M., Cohen, R. C., & Lee, L. (2014). Secondary Organic Aerosol Formation and Organic Nitrate Yield from NO3 Oxidation of Biogenic Hydrocarbons. *Environmental Science & Technology*, *48*(20), 11944-11953. https://doi.org/10.1021/es502204x

Gaona-Colmán, E., Blanco, M. B., Barnes, I., Wiesen, P., & Teruel, M. A. (2017). OH- and O3-initiated atmospheric degradation of camphene: temperature dependent rate coefficients, product yields and mechanisms. *RSC Advances*, *7*(5), 2733-2744. https://doi.org/10.1039/c6ra26656h

Geron, C., Rasmussen, R., Arnts, R. R., & Guenther, A. (2000). A review and synthesis of monoterpene speciation from forests in the United States. *Atmospheric Environment*, *34*(11), 1761-1781.

Gilman, J. B., Lerner, B. M., Kuster, W. C., Goldan, P. D., Warneke, C., Veres, P. R., Roberts, J. M., De Gouw, J. A., Burling, I. R., & Yokelson, R. J. (2015). Biomass burning emissions and potential air quality impacts of volatile organic compounds and other trace gases from fuels common in the US. *Atmospheric Chemistry and Physics*, *15*(24), 13915-13938. https://doi.org/10.5194/acp-15-13915-2015

Griffin, R. J., Cocker, D. R., Flagan, R. C., & Seinfeld, J. H. (1999). Organic aerosol formation from the oxidation of biogenic hydrocarbons. *Journal of Geophysical Research Atmospheres*, *104*(D3), 3555-3567. https://doi.org/10.1029/1998JD100049

Guenther, A., Hewitt, C. N., Erickson, D., Fall, R., Geron, C., Graedel, T., Harley, P., Klinger, L., Lerdau, M., & McKay, W. (1995). A global model of natural volatile organic compound emissions. *Journal of Geophysical Research: Atmospheres*, *100*(D5), 8873-8892.

Hakola, H., Arey, J., Aschmann, S. M., & Atkinson, R. (1994). Product formation from the gas-phase reactions of OH radicals and O 3 with a series of monoterpenes. *Journal of Atmospheric Chemistry*, *18*(1), 75-102.

Hatch, L. E., Jen, C. N., Kreisberg, N. M., Selimovic, V., Yokelson, R. J., Stamatis, C., York, R. A., Foster, D., Stephens, S. L., Goldstein, A. H., & Barsanti, K. C. (2019). Highly Speciated Measurements of Terpenoids Emitted from Laboratory and Mixed-Conifer Forest Prescribed Fires. *Environmental Science & Technology*, *53*(16), 9418-9428. https://doi.org/10.1021/acs.est.9b02612

Hatch, L. E., Luo, W., Pankow, J. F., Yokelson, R. J., Stockwell, C. E., & Barsanti, K. C. (2015). Identification and quantification of gaseous organic compounds emitted from biomass burning using two-dimensional gas chromatography-time-of-flight mass spectrometry. *Atmospheric Chemistry and Physics*, *15*(4), 1865-1899. https://doi.org/10.5194/acp-15-1865-2015

Hatfield, M. L., & Hartz, K. E. H. (2011). Secondary organic aerosol from biogenic volatile organic compound mixtures. *Atmospheric Environment*, *45*(13), 2211-2219.

Hayward, S., Muncey, R., James, A., Halsall, C. J., & Hewitt, C. N. (2001). Monoterpene emissions from soil in a Sitka spruce forest. *Atmospheric Environment*, *35*(24), 4081-4087.

Henze, D. K., Seinfeld, J. H., Ng, N. L., Kroll, J. H., Fu, T. M., Jacob, D. J., & Heald, C. L. (2008). Global modeling of secondary organic aerosol formation from aromatic hydrocarbons: high- vs. low-yield pathways. *Atmospheric Chemistry and Physics*, *8*(9), 2405-2420. https://doi.org/10.5194/acp-8-2405-2008

Hurley, M. D., Sokolov, O., & Wallington, T. J. (2001). Organic aerosol formation during the atmospheric degradation of toluene. *Environmental Science and Technology*, *35*(7), 1358-1366. https://doi.org/10.1021/es0013733

Jiang, J., Carter, W. P. L., Cocker, D. R., & Barsanti, K. C. (2020). Development and Evaluation of a Detailed Mechanism for Gas-Phase Atmospheric Reactions of Furans. *ACS Earth and Space Chemistry*, *4*(8), 1254-1268. https://doi.org/10.1021/acsearthspacechem.0c00058

Jokinen, T., Sipilä, M., Richters, S., Kerminen, V. M., Paasonen, P., Stratmann, F., Worsnop, D., Kulmala, M., Ehn, M., & Herrmann, H. (2014). Rapid autoxidation forms highly oxidized RO2 radicals in the atmosphere. *Angewandte Chemie International Edition*, *53*(52), 14596-14600.

Komenda, M., & Koppmann, R. (2002). Monoterpene emissions from Scots pine (Pinus sylvestris): Field studies of emission rate variabilities. *Journal of Geophysical Research: Atmospheres*, *107*(D13), ACH 1-1-ACH 1-13. https://doi.org/https://doi.org/10.1029/2001JD000691

Kroll, J. H., Ng, N. L., Murphy, S. M., Flagan, R. C., & Seinfeld, J. H. (2006). Secondary organic aerosol formation from isoprene photooxidation. *Environmental Science & Technology*, *40*(6), 1869-1877.

Kroll, J. H., & Seinfeld, J. H. (2008). Chemistry of secondary organic aerosol: Formation and evolution of low-volatility organics in the atmosphere. *Atmospheric Environment*, *42*(16), 3593-3624. https://doi.org/10.1016/j.atmosenv.2008.01.003

Li, Q., Hu, D., Leungsakul, S., & Kamens, R. M. (2007). Large outdoor chamber experiments and computer simulations:(I) Secondary organic aerosol formation from the oxidation of a mixture of d-limonene and α-pinene. *Atmospheric Environment*, *41*(40), 9341-9352.

Li, Q., Jiang, J., Afreh, I., Barsanti, K. C., & Cocker Iii, D. R. (2021). Secondary Organic Aerosol Formation from Camphene Oxidation: Measurements and Modeling. *Atmos. Chem. Phys. Discuss.*, *2021*, 1-27. https://doi.org/10.5194/acp-2021-587

Ludley, K. E., Jickells, S. M., Chamberlain, P. M., Whitaker, J., & Robinson, C. H. (2009). Distribution of monoterpenes between organic resources in upper soil horizons under monocultures of Picea abies, Picea sitchensis and Pinus sylvestris. *Soil Biology and Biochemistry*, *41*(6), 1050-1059.

Maleknia, S. D., Bell, T. L., & Adams, M. A. (2007). PTR-MS analysis of reference and plant-emitted volatile organic compounds. *International Journal of Mass Spectrometry*, *262*(3), 203-210.

Mazza, G., & Cottrell, T. (1999). Volatile components of roots, stems, leaves, and flowers of Echinacea species. *Journal of agricultural and food chemistry*, *47*(8), 3081-3085.

Mehra, A., Krechmer, J. E., Lambe, A., Sarkar, C., Williams, L., Khalaj, F., Guenther, A., Jayne, J., Coe, H., & Worsnop, D. (2020). Oligomer and highly oxygenated organic molecule formation from oxidation of oxygenated monoterpenes emitted by California sage plants. *Atmospheric Chemistry and Physics*, *20*(18), 10953-10965.

Moukhtar, S., Couret, C., Rouil, L., & Simon, V. (2006). Biogenic volatile organic compounds (BVOCs) emissions from Abies alba in a French forest. *Science of The Total Environment*, *354*(2-3), 232-245.

Mutzel, A., Rodigast, M., Iinuma, Y., Böge, O., & Herrmann, H. (2016). Monoterpene SOA–Contribution of first-generation oxidation products to formation and chemical composition. *Atmospheric Environment*, *130*, 136-144.

Nannoolal, Y., Rarey, J., & Ramjugernath, D. (2008). Estimation of pure component properties: Part 3. Estimation of the vapor pressure of non-electrolyte organic compounds via group contributions and group interactions. *Fluid Phase Equilibria*, *269*(1-2), 117-133.

Ng, N., Chhabra, P., Chan, A., Surratt, J., Kroll, J., Kwan, A., McCabe, D., Wennberg, P., Sorooshian, A., & Murphy, S. (2007). Effect of NO x level on secondary organic aerosol (SOA) formation from the photooxidation of terpenes. *Atmospheric Chemistry and Physics*, *7*(19), 5159-5174.

Ng, N. L., Chhabra, P. S., Chan, A. W. H., Surratt, J. D., Kroll, J. H., Kwan, A. J., McCabe, D. C., Wennberg, P. O., Sorooshian, A., Murphy, S. M., Dalleska, N. F., Flagan, R. C., & Seinfeld, J. H. (2007). Effect of NOx level on secondary organic aerosol (SOA) formation from the photooxidation of terpenes. *Atmospheric Chemistry and Physics*, *7*(19), 5159-5174. https://doi.org/10.5194/acp-7-5159-2007

Nøjgaard, J. K., Bilde, M., Stenby, C., Nielsen, O. J., & Wolkoff, P. (2006). The effect of nitrogen dioxide on particle formation during ozonolysis of two abundant monoterpenes indoors. *Atmospheric Environment*, *40*(6), 1030-1042.

Odum Jay, R., Hoffmann, T., Bowman, F., Collins, D., Flagan Richard, C., & Seinfeld John, H. (1996). Gas particle partitioning and secondary organic aerosol yields. *Environmental Science and Technology*, *30*(8), 2580-2585. https://doi.org/10.1021/es950943+

Presto, A. A., Huff Hartz, K. E., & Donahue, N. M. (2005). Secondary organic aerosol production from terpene ozonolysis. 2. Effect of NOx concentration. *Environmental Science and Technology*, *39*(18), 7046-7054. https://doi.org/10.1021/es050400s

Pullinen, I., Schmitt, S., Kang, S., Sarrafzadeh, M., Schlag, P., Andres, S., Kleist, E., Mentel, T. F., Rohrer, F., Springer, M., Tillmann, R., Wildt, J., Wu, C., Zhao, D., Wahner, A., & Kiendler-Scharr, A. (2020). Impact of NOxon secondary organic aerosol (SOA) formation from α-pinene and β-pinene photooxidation: The role of highly oxygenated organic nitrates. *Atmospheric Chemistry and Physics*, *20*(17), 10125-10147. https://doi.org/10.5194/ACP-20-10125-2020

Pye, H. O. T., Chan, A. W. H., Barkley, M. P., & Seinfeld, J. H. (2010). Global modeling of organic aerosol: the importance of reactive nitrogen (NOx and NO3). *Atmos. Chem. Phys.*, *10*(22), 11261-11276. https://doi.org/10.5194/acp-10-11261-2010

Pye, H. O. T., D'Ambro, E. L., Lee, B. H., Schobesberger, S., Takeuchi, M., Zhao, Y., Lopez-Hilfiker, F., Liu, J., Shilling, J. E., Xing, J., Mathur, R., Middlebrook, A. M., Liao, J., Welti, A., Graus, M., Warneke, C., de Gouw, J. A., Holloway, J. S., Ryerson, T. B., Pollack, I. B., & Thornton, J. A. (2019). Anthropogenic enhancements to production of highly oxygenated molecules from autoxidation. *Proceedings of the National Academy of Sciences of the United States of America*, *116*(14), 6641-6646. https://doi.org/10.1073/pnas.1810774116

Quéléver, L. L., Kristensen, K., Normann Jensen, L., Rosati, B., Teiwes, R., Daellenbach, K. R., Peräkylä, O., Roldin, P., Bossi, R., & Pedersen, H. B. (2019). Effect of temperature on the formation of highly oxygenated organic molecules (HOMs) from alpha-pinene ozonolysis. *Atmospheric Chemistry and Physics*, *19*(11), 7609-7625.

Sarrafzadeh, M., Wildt, J., Pullinen, I., Springer, M., Kleist, E., Tillmann, R., Schmitt, S. H., Wu, C., Mentel, T. F., & Zhao, D. (2016). Impact of NO x and OH on secondary organic aerosol formation from β-pinene photooxidation. *Atmospheric Chemistry and Physics*, *16*(17), 11237-11248.

Schervish, M., & Donahue, N. M. (2020). Peroxy radical chemistry and the volatility basis set. *Atmospheric Chemistry and Physics*, *20*(2), 1183-1199.

Song, C., Na, K., & Cocker, D. R. (2005). Impact of the Hydrocarbon to NOx Ratio on Secondary Organic Aerosol Formation. *Environmental Science & Technology*, *39*(9), 3143-3149. https://doi.org/10.1021/es0493244

White, M. L., Russo, R. S., Zhou, Y., Mao, H., Varner, R. K., Ambrose, J., Veres, P., Wingenter, O. W., Haase, K., & Stutz, J. (2008). Volatile organic compounds in northern New England marine and continental environments during the ICARTT 2004 campaign. *Journal of Geophysical Research: Atmospheres*, *113*(D8).

Xavier, C., Rusanen, A., Zhou, P., Dean, C., Pichelstorfer, L., Roldin, P., & Boy, M. (2019). Aerosol mass yields of selected biogenic volatile organic compounds–a theoretical study with nearly explicit gas-phase chemistry. *Atmospheric Chemistry and Physics*, *19*(22), 13741-13758.

Ye, Q., Wang, M., Hofbauer, V., Stolzenburg, D., Chen, D., Schervish, M., Vogel, A., Mauldin, R. L., Baalbaki, R., & Brilke, S. (2019). Molecular Composition and Volatility of Nucleated Particles from α-Pinene Oxidation between− 50° C and+ 25° C. *Environmental Science & Technology*, *53*(21), 12357-12365.

Zhang, S. H., Shaw, M., Seinfeld, J. H., & Flagan, R. C. (1992). Photochemical aerosol formation from α-pinene-and β-pinene. *Journal of Geophysical Research: Atmospheres*, *97*(D18), 20717-20729.

Zhang, X., Lambe, A. T., Upshur, M. A., Brooks, W. A., Gray Bé, A., Thomson, R. J., Geiger, F. M., Surratt, J. D., Zhang, Z., & Gold, A. (2017). Highly oxygenated multifunctional compounds in α-pinene secondary organic aerosol. *Environmental Science & Technology*, *51*(11), 5932-5940.

Zhao, Y., Thornton, J. A., & Pye, H. O. T. (2018). Quantitative constraints on autoxidation and dimer formation from direct probing of monoterpene-derived peroxy radical chemistry. *Proceedings of the National Academy of Sciences of the United States of America*, *115*(48), 12142-12147. https://doi.org/10.1073/pnas.1812147115

Ziemann, P. J., & Atkinson, R. (2012). Kinetics, products, and mechanisms of secondary organic aerosol formation. *Chemical Society Reviews*, *41*(19), 6582-6605. https://doi.org/10.1039/c2cs35122f

Chapter 5 Conclusions & Future Work

Overall, the research presented in this dissertation has sought to advance the understanding and model representation of O_3 and SOA precursors, largely emitted from BB, that are needed for predictions of the effects of fires on air quality and climate. Specific efforts were made in developing and testing gas-phase chemical mechanisms and gaining mechanistic insights into SOA formation based on gas-phase chemistry. The mechanism generator, MechGen, within the SAPRC modeling system was used to derive new chemical mechanisms for furans and phenols. The model performance of the mechanisms was evaluated based on model-measurement comparison using chamber data. MechGen was also used to develop a chemical mechanism for camphene and the chemically-detailed SAPRC box model was used to explore how the fates of RO_2 influence camphene SOA formation and to improve the understanding of RO_2 chemistry leading to HOM formation particularly in the presence of intermediate NO_x levels.

The detailed gas-phase mechanism derived for furans and their major oxidation products was implemented into the SAPRC-18 mechanism. Relative to the SAPRC-11 mechanism, model skill was improved in predicting furans consumption (21 of 26 experiments) and $\Delta([O3]-[NO])$. For the latter, mean model bias was reduced to +/-10% for 13 experiments (4 for SAPRC-11); and was > +/- 20% for only 3 experiments (11 for SAPRC-11). Sensitivity simulations showed that while OH-initiated reactions are the major sink for furans, reactions with NO_3 and O_3 become non-negligible or even of equal importance under dark or high O_3 conditions, such as may be expected during biomass burning events. The detailed furans mechanism was developed with no tuning to fit the experimental data used for evaluation and to facilitate broad application of the mechanism for atmospheric and air quality modeling.

The updated phenols gas-phase chemical mechanism was derived for SAPRC-18 and was evaluated relative to the standard SAPRC-18 mechanism. Relative to the standard SAPRC-18 mechanism, model skill was improved in predicting both phenols consumption and $\Delta([O_3]-[NO])$. For the latter, mean model bias was reduced to +/-10% for 8 experiments (4 for SAPRC-18); and was > +/- 20% for only 1 experiment (4 for SAPRC-18). The phenols mechanism was developed with no tuning to fit the experimental data used for evaluation and showed better performance than the standard SAPRC-18 mechanism in simulating phenol and o-cresol experiments. The mechanisms had equal performance in simulating the 2,4-DMP experiments.

A series of camphene experiments were performed in the UCR environmental chamber across a range of chemical conditions at atmospherically relevant OH levels. Experiments performed with added nitrogen oxides (NO_x) resulted in higher SOA mass yields (up to 64%) than experiments performed without added NO_x (up to 28%). In addition, camphene SOA mass yields increased with SOA mass (M_o) at lower mass loadings, but a threshold was reached at higher mass loadings in which the SOA mass yields no longer increased with M_o. SAPRC predicted that in the presence of NO_x, camphene RO_2 reacts with NO and the resultant RO_2 undergo hydrogen (H)-shift isomerization reactions; as has been documented previously, such reactions rapidly add oxygen and lead to products with very low volatility (i.e., HOMs). The end products formed in the presence of NO_x have significantly lower volatilities, and higher O:C ratios, than those formed by initial camphene RO_2 reacting with HO_2 or other RO_2.

The research presented in this dissertation has advanced the understanding of gas-phase chemistry for BB-derived VOCs including furans, phenols and camphene while also addressing inadequate representations of these compounds in chemical models. For the first time, the chemically detailed SAPRC box model was used to establish the connection between gas-phase chemistry and SOA formation. The findings in this dissertation have aided in the optimization of MechGen estimation methodology, making it more visible and accessible to the atmospheric chemistry community. In future work, the furans and phenols mechanisms will be implemented into plume/box models and chemical transport models to simulate wildfire events, including under dark/nighttime NO_3 oxidation conditions. Additional chamber and modeling studies of other understudied VOCs with structures similar to camphene should be performed to better understand this NO-driven HOM chemistry and the impacts on SOA formation.

Appendixes

Appendix A: SAPRC Modeling System

A.1 SAPRC Base Mechanisms

The SAPRC-07 mechanism is currently the most widely used of the SAPRC mechanisms (Carter, 2009, 2010). The SAPRC-11 mechanism is an incremental update of SAPRC-07 that is the same in most respects except for an updated representation of aromatics that gives better fits to available chamber data (Carter & Heo, 2013). Additional information about SAPRC-07 and links to download files are available at https://intra.cert.ucr.edu/~carter/SAPRC/files.htm.

The SAPRC-18 mechanism represents the results of the first complete update of all aspects of the SAPRC series of mechanisms since the development of SAPRC-07 and the incremental update to SAPRC-11(Carter, 2009, 2010; Carter & Heo, 2013). The SAPRC-18 mechanism is discussed in detail in the report of Carter (2020a). Additional information about SAPRC-18 and links to download files are available at https://intra.engr.ucr.edu/~carter/SAPRC/18/. The mechanisms used in SAPRC-18 for most individual compounds were derived from MechGen as discussed in Section A.3.

A.2 Types of SAPRC Gas-Phase Chemical Mechanisms

The terms "Base", "Explicit", "Detailed", “Lumped” and "Reduced" are used in this work to characterize the types of mechanisms. These terms are defined as follows:

A "Base" mechanism is the mechanism used to represent the atmospheric or chamber reactions of inorganics; explicitly represented organics, intermediates and products; and lumped model species. The reactions of the individual compounds that are not part of the base mechanism are represented separately for the purpose of developing or evaluating their mechanisms, and were added to the base mechanism for the purpose of the model simulations when needed. The base mechanisms, which have many reactions and model species, are provided in the mechanism documentation, and thus are not listed here.

An "Explicit" mechanism is a mechanism that gives each individual reaction as an elementary process, with each model species corresponding to an individual compound or radical. This includes fast reactions such as additions of alkyl radicals with O_2, and has no lumping or combining of reactions or model species, except perhaps for isomers that are assumed to have the same mechanisms. For example, the mechanisms derived using the MechGen (discussed below in Section A.3) (Carter, 2020b) are considered as “explicit” mechanisms.

A "Detailed" mechanism is an explicit mechanism that has been processed for use with a particular base mechanism by applying the minimum set of reduction procedures associated with that mechanism. These were derived directly from the explicit mechanism. The minimum set of reduction procedures are as follows:

(1) Intermediates that react rapidly and have only unimolecular or O_2 reactions are removed from the model by applying the steady state approximation and replacing them with the products that they form, which is justifiable because they don't depend on conditions for a given temperature and O_2 concentration. For example, alkyl radicals are replaced by the peroxy radicals formed when they react with O_2; alkoxy radicals are replaced with the mixture of compounds and radicals ultimately formed after they react with O_2, decompose or isomerize; and peroxy radicals that isomerize rapidly are replaced by the peroxy radicals or mixture of products formed after their isomerization.

(2) The steady state method is not used to remove peroxy radical intermediates because their fates, and the products they ultimately form, depend on relative, and in some cases absolute, concentrations of NO_x and peroxy species. Instead, different methods are used to represent peroxy radical reactions with reduced numbers of model species, depending on the base mechanism. In the case of SAPRC-07 and -11, this involves using various chemical "operators" to represent the net effects of various peroxy radical reactions. In the case of SAPRC-18, the peroxy radicals and their reactions are represented more explicitly, though radicals formed in the same reaction and reacting in parallel with approximately the same rate constants typically are lumped together to reduce the numbers of peroxy species that need to be added. This peroxy lumping is done when processing the output of MechGen, though was not done when deriving the detailed SAPRC-18 furan mechanisms. The peroxy radical representation methods for both mechanisms are discussed further below.

(3) Minor products are represented using lumped model species in the base mechanism. This avoids the need to derive mechanisms and add model species for each minor product predicted, while still having an appropriate representation of the contributions of these products to the overall reactivity, which may not be negligible when taken as a whole.

A "Lumped" mechanism is a mechanism that uses reactions and model species that do not directly correspond to any explicit mechanism, to represent large numbers of reactions and products. In this case, the products are represented by lumped model species whose yields and photolysis rates were adjusted to fit environmental chamber data.

A "Reduced" mechanism is a mechanism that is derived from the more detailed mechanism while some of the organic reactants and products are represented using lumped model species, while the high yield and highly reactive species are represented explicitly.

A.3 SAPRC Mechanism Generation System, MechGen

The SAPRC-18 mechanism generation system, or MechGen, is capable of generating fully explicit mechanisms for the atmospheric reactions of many types of organic compounds and the intermediate radicals they form (Carter, 2020b). The system uses assigned rate constants and branching ratios where data are available and uses various methods to estimate rate constants or branching ratios in all other cases. Its operation is similar to the Generator for Explicit Chemistry and Kinetics of Organics in the Atmosphere (GECKO-A) system developed by Aumont and co-workers (Aumont et al., 2005;

Camredon et al., 2007; Valorso et al., 2011), except that MechGen is designed to generate explicit mechanisms for individual compounds for integration into SAPRC, rather than to conduct simulations using multi-generation explicit oxidation mechanisms to assess effects of chemical complexity, as is the usual procedure for GECKO-A.

The operation of MechGen is described by Carter (2020c), and the documentation of the estimation methods and assignments is in preparation and can be obtained online: http://mechgen.cert.ucr.edu/. MechGen uses the web-based system to run selected reactions, generate explicit mechanisms of selected VOCs to form stable products, process these explicit mechanisms for implementation into SAPRC-18, and obtain documentation information. The MechGen system can also be accessed by authorized users using a text-based interface for the purpose of updating its programming or estimation methods, inputting assignment data, and processing reactions of multiple compounds and complex mixtures for the purpose of updating SAPRC-18 as a whole.

References

Aumont, B., Szopa, S., & Madronich, S. (2005). Modelling the evolution of organic carbon during its gas-phase tropospheric oxidation: development of an explicit model based on a self generating approach. *Atmospheric Chemistry and Physics*, *5*(9), 2497-2517. https://doi.org/10.5194/acp-5-2497-2005

Camredon, M., Aumont, B., Lee-Taylor, J., & Madronich, S. (2007). The SOA/VOC/NO_x system: an explicit model of secondary organic aerosol formation. *Atmos. Chem. Phys.*, *7*(21), 5599-5610. https://doi.org/10.5194/acpd-7-11223-2007

Carter, W. P. L. (2009). *Development of the SAPRC-07 Chemical Mechanism and Updated Ozone Reactivity Scales; Final report to the California Air Resources Board Contract No. 03-318, March 2009*. https://intra.engr.ucr.edu/~carter/SAPRC/

Carter, W. P. L. (2010). *Development of the SAPRC-07 Chemical Mechanism and Updated Ozone Reactivity Scales*. www.cert.ucr.edu/~carter/SAPRC

Carter, W. P. L. (2020a). *Documentation of the SAPRC-18 Mechanism; Report to California Air Resources Board Contract No. 11-761, May, 2020*. https://intra.engr.ucr.edu/~carter/SAPRC/18/

Carter, W. P. L. (2020b). *Estimates and Assignments used in the SAPRC-18 Mechanism Generation System; Report to California Air Resources Board Contract No. 11-761. In preparation. When completed, will be available at http://intra.engr.ucr.edu/~carter/SAPRC/18*.

Carter, W. P. L. (2020c). *Gateway to the SAPRC Mechanism Generation System*. http://mechgen.cert.ucr.edu/

Carter, W. P. L., & Heo, G. (2013). Development of revised SAPRC aromatics mechanisms. *Atmospheric Environment*, *77*, 404-414. https://doi.org/10.1016/j.atmosenv.2013.05.021

Valorso, R., Aumont, B., Camredon, M., Raventos-Duran, T., Mouchel-Vallon, C., Ng, N. L., Seinfeld, J. H., Lee-Taylor, J., & Madronich, S. (2011). Explicit modelling of SOA formation from α-pinene photooxidation: Sensitivity to vapour pressure estimation. *Atmospheric Chemistry and Physics*, *11*(14), 6895-6910. https://doi.org/10.5194/acp-11-6895-2011

Appendix B: Supplementary Information for Chapter 2

B.1 Listing of Furans Mechanisms

Table B1: Representation of condensed reactions of the individual furans in the current SAPRC-11 mechanism.

a) Reactions of furans (added to base mechanism)

Reaction	k(298) (cm^{3}molecule^{-1}s^{-1})
FURAN + OH = HO2 + 0.25 AFG1 + 0.75 AFG2	4.03E-11
2M-FURAN + OH = HO2 + 0.25 AFG1 + 0.75 AFG2	6.19E-11
3M-FURAN + OH = HO2 + 0.15 AFG1 + 0.85 AFG2	9.35E-11
25M-FUR + OH = HO2 + 0.25 AFG1 + 0.75 AFG2	1.32E-10

b) Lumped photoreactive aromatic fragmentation products (already in base SAPRC-11)

Product	Description
AFG1	Lumped products whose photolysis leads to radicals. Also reacts with OH. Mechanism based on unsaturated 1,4-dicarbonyls.
AFG2	Lumped products whose photolysis leads to non-radical products. Also reacts with OH with the same mechanism as AFG1.

Table B2: List of model species used in the SAPRC-18 and SAPRC-07/-11 furans mechanisms.

Name	Description
Explicit furans and their photoreactive dicarbonyl products (added to both SAPRC-18 and SAPRC-07/-11)	
FURAN	Furan
2M-FURAN	2-Methylfuran
3M-FURAN	3-Methylfuran
25M-FUR	2,5-Dimethylfuran
BUTEDIAL	2-Butene-1,4-dial (formed from furan)
4OX2PEAL	4-Oxo-2-penteneal (formed from 2-methylfuran)
2MBUTDAL	2-Methyl-2-butene-1,4-dial (formed from 3-methylfuran)
3HXE25DO	3-Hexene-2,5-dione (formed from 2,5-dimethylfuran)
Furanones and other products (used for SAPRC-18)	
HFON52	5-Hydroxy-2(5H)-furanone (formed from furan)
HFON52M5	5-Methyl-5-hydroxy-2(5H)-furanone (formed from 2-methyl and 2,5-dimethylfurans)
HFON52M4	4-Methyl-5-hydroxy-2(5H)-furanone (formed from 3-methylfuran)
HFON52M3	3-Methyl-5-hydroxy-2(5H)-furanone (formed from 3-methylfuran)
3HF2ONE	3H-furan-2-one (formed from 2-butene 1,4-dial photolysis)
3HF2ONM5	5-Methyl-3H-furan-2-one (formed from 4-oxo-2-pentenal photolysis)
3HF2ONM4	4-Methyl-3H-furan-2-one (formed from 2-methyl-2-butene-1,4-dial photolysis)
MALAH	Maleic anhydride and alkyl-substituted analogues
Lumped furanones and other products (used for SAPRC-07/-11)	
HFONS	Lumped furanones and hydroxyfuranones
MALAH	Maleic anhydride and alkyl-substituted analogues
Base SAPRC-18 and SAPRC-07/-11 (only species formed in furan reactions are shown)	
O2	Oxygen
H2O	Water
HV	Light
O3	Ozone
NO	Nitric Oxide
NO2	Nitrogen Dioxide
NO3	Nitrate Radical
HNO3	Nitric Acid

Name	Description
CO	Carbon Monoxide
OH	Hydroxyl Radicals
HO2	Hydroperoxide Radicals
HCHO	Formaldehyde (explicit)
GLY	Glyoxal (explicit)
MGLY	Methyl Glyoxal and other compounds with RC(O)C(O)H structures
BACL	Biacetyl and other compounds with RC(O)C(O)R' structures
RCHO	C_{4+} saturated aldehydes with 9 or fewer carbons
ROOH	Other hydroperoxides with 3+ carbons and vapor pressure greater than 1 ppb
AFG3	Monounsaturated 1,4-diketone aromatic products
CO2	Carbon Dioxide
MEO2	Methyl peroxy radicals
MECO3	Acetyl Peroxy Radicals (forms PAN)
MACO3	Peroxyacyl radicals formed from methacrolein and other unsaturated aldehydes (forms MAPAN)
RCHO2	Stabilized Criegee biradicals (other than HCHO2 from ethane)
XC	Lost carbon in reaction due to lumping
XN	Lost nitrogen in reaction due to lumping
	(The following are used in most peroxy radical reaction representations for SAPRC-07 but are used only to represent minor peroxy reactions and products in SAPRC-18 in order to reduce the number of reactions needed to represent relatively minor processes.)
RO2C	Peroxy radical operator representing NO to NO_2 and NO_3 to NO_2 conversions, and the effects of peroxy radical reactions on acyl peroxy and other peroxy radicals.
RO2XC	Peroxy radical operator representing NO consumption (used in conjunction with organic nitrate formation), and the effects of peroxy radical reactions on NO_3, acyl peroxy radicals, and other peroxy radicals.
z(Product)	Formation of the organic nitrate model species after reactions of a peroxy radical with NO
Base SAPRC-18 only	
MECHO	Acetaldehyde
MALAH	Maleic anhydride
KET2	Photoreactive saturated ketones
OLEA1	Unsaturated aldehydes with C=C next to -CHO (mostly from aromatics)
OLEP	Non-photoreactive, non-hydrocarbon compounds with C=C double bonds
RCNO3	Volatile organic carbonyl nitrates

Name	Description
RHNO3	Volatile organic hydroxy nitrates
RDNO3	Volatile organic dinitrates
RUOOH	Hydroperoxides with C=C double bonds
HPALD	Unsaturated hydroperoxy carbonyls with CO-C=C-OOH structures
CROOH	Hydroperoxy carbonyls (other than HPALDs)
IEPOX	Any 3-member ring cyclic ether with at least 2 OH groups.
OTH1	Volatile saturated compounds that react only with OH, and have kOH between 1.4 x 10^{-13} and 1.7 x 10^{-12} cm3 molec-1 s-1
OTH3	Volatile saturated compounds that react only with OH, and have kOH between 3.4 x 10-12 and 1.0 x 10-11 cm3 molec-1 s-1
NROG	Any lumped product assumed to be unreactive
R2CO3	Higher saturated peroxy acyl radicals (forms PAN2)
SumRO2	Counter species used to calculate total peroxy radical concentrations [a]
SumRCO3	Counter species used to calculate total acyl peroxy radical concentrations [a]
Base SAPRC-07/-11 only	
CCHO	Acetaldehyde
ALK3	Alkanes and other non-aromatic compounds that react only with OH, and have kOH between 1.7E-12 and 3.4E-12 cm^3 $molec^{-1}$ s^{-1}
PROD2	Ketones and other non-aldehyde oxygenated products which react with OH radicals faster than 5E-12 cm^3 $molec^{-1}$ s^{-1}
MACR	Acroleins (based on methacrolein)
RCOOH	C_{2+} organic acids and peroxy acids (mechanism based on propionic acid).
OLE2	Alkenes with kOH > 4.7E-11 cm^3 $molec^{-1}$ s^{-1}
RNO3	Lumped Organic Nitrates
ROOH	Lumped organic hydroperoxides with 2-4 carbons. Mechanism based on that estimated for n-propyl hydroperoxide.
RCO3	Peroxy Propionyl and higher peroxy acyl Radicals
x(Product)	Formation of (product) from alkoxy radicals formed in peroxy radical reactions with NO and NO_3 (100% yields) and other peroxy radicals (50% yields)
y(Product)	Formation of a hydroperoxide (product) following peroxy + HO_2 reactions, or formation of H-shift disproportionation products (represented by MEK) in the peroxy + acyl peroxy reactions and (in 50% yields) peroxy + peroxy reactions.

Table B3: List of rate constant and branching ratio assignments added to the SAPRC-18 mechanism generation assignments used when generating explicit mechanisms for the furans and their major products.

a) Rate constant assignments

Reactant	Oxidant	k(298)	Reference or note.
Furan	OH	3.97E-11 =1.30E-11*exp(333/T)	Calvert et al. (2015)
	NO_3	1.36E-12 =1.30E-13*exp(700/T)	Cabañas et al. (2005)
	O_3	2.42E-18	Atkinson et al. (1983)
2-Methylfuran	OH	7.31E-11	Aschmann et al. (2011)
	NO_3	2.57E-11	Kind et al. (1996)
	O_3	2.00E-17	See note [a]
3-Methylfuran	OH	8.73E-11	Aschmann et al. (2011)
	NO_3	1.26E-11	Tapia et al. (2011)
	O_3	2.05E-17	Alvarado et al. (1996)
2,5-Dimethylfuran	OH	1.25E-10	Aschmann et al. (2011)
	NO_3	5.78E-11	Kind et al. (1996)
	O_3	4.20E-16	Matsumoto (2011)
2-Butene-1,4-dial	OH	4.22E-11	See note [b]
	NO_3	2.08E-15	Carter (2020)
	O_3	1.60E-18	Liu et al. (1999)
4-Oxo-2-penteneal	OH	5.67E-11	Bierbach et al. (1994)
	O_3	4.80E-18	Calvert et al. (2015)
	NO_3	1.00E-14	Bierbach et al. (1994)
2-Methyl-2-butene-1,4-dial	OH	4.15E-11	Bierbach et al. (1994)
	NO_3	3.13E-15	Bierbach et al. (1994)
	O_3	4.80E-18	See note [c]
3-Hexene-2,5-dione	OH	4.71E-11	Aschmann et al. (2011)
	NO_3	1.64E-14	See note [d]
	O_3	1.80E-18	Tuazon et al. (1985)
3H-furan-2-one	OH	4.45E-11	Aschmann et al. (2011)

[a] Estimated to be the same as that given for 3-methylfuran, which is from Alvarado et al. (1996).

[b] The measured rate constants of 5.21E-11 cm^3 molec^{-1} s^{-1} for the Z-isomer and 3.45E-11 for the E-isomer (Alvarado et al., 1996; Martín et al., 2013). Yuan et al. (2017) derive the isomer mixture as 44% and 56% for the Z and E isomers, respectively. The rate constant used is derived from this ratio for these rate constants.

[c] Assumed to be the same as that used for 4-oxo-2-pentenal, which is recommended by Calvert et al. (2015).

[d] The overall rate constant was calculated based on the branching ration of the two isomers as the product formed by 2,5-dimethylfuran and OH photooxidation, which is 32% for Z-3-hexene-2,5-dione and 68% for E-3-hexene-2,5-dione from Yuan et al. (2017). Rate constant for specific isomers from Bierbach et al. (1994).

b) Branching Ratio Assignments

Ratio	Reaction
OH Reactions	
Furan	
24%	CH*=CH-O-CH=CH* + OH -> HO-CH*-aCH[.]-aCH-aCH[.]-O*
76%	CH*=CH-O-CH=CH* + OH -> HCO-aCH[.]-aCH-aCH[.]-OH
2-Methylfuran	
30%	CH3-C*=CH-CH=CH-O* + OH -> CH3-C*(OH)-aCH[.]-aCH-aCH[.]-O*
26%	CH3-C*=CH-CH=CH-O* + OH -> CH3-aC[.]*-O-CH(OH)-aCH[.]-aCH*
18%	CH3-C*=CH-CH=CH-O* + OH -> CH3-aC[.](OH)-aCH-aCH[.]-CHO
26%	CH3-C*=CH-CH=CH-O* + OH -> CH3-CO-aCH[.]-aCH-aCH[.]-OH
3-Methylfuran	
63%	CH3-C*=CH-O-CH=CH* + OH -> CH3-aC[.]*-CH(OH)-O-aCH[.]-aCH*
10%	CH3-C*=CH-O-CH=CH* + OH -> CH3-aC*-aCH[.]-O-CH(OH)-aCH[.]*
18%	CH3-C*=CH-O-CH=CH* + OH -> CH3-aC(aCH[.]-CHO)-aCH[.]-OH
9%	CH3-C*=CH-O-CH=CH* + OH -> CH3-aC[.](CHO)-aCH-aCH[.]-OH
2,5-Dimethylfuran	
28%	CH3-C*=CH-CH=C(CH3)-O* + OH -> CH3-CO-aCH[.]-aCH-aC[.](CH3)-OH
72%	CH3-C*=CH-CH=C(CH3)-O* + OH -> CH3-aC[.]*-O-C(CH3)(OH)-aCH[.]-aCH*
	Branching ratios based on quantum calculations for the reactions of furan by Yuan et al. (2017). These represent the net effects of adducts that then decompose before stabilization.

Ratio	Reaction
	NO_3 Reactions
Furan	
100%	CH*=CH-O-CH=CH* + NO3 -> O2NO-CH*-aCH[.]-aCH-aCH[.]-O*
2-Methylfuran	
54%	CH3-C*=CH-CH=CH-O* + NO3 -> CH3-C*(ONO2)-aCH[.]-aCH-aCH[.]-O*
46%	CH3-C*=CH-CH=CH-O* + NO3 -> CH3-aC[.]*-O-CH(ONO2)-aCH[.]-aCH*
3-Methylfuran	
86%	CH3-C*=CH-O-CH=CH* + NO3 -> CH3-aC[.]*-CH(ONO2)-O-aCH[.]-aCH*
14%	CH3-C*=CH-O-CH=CH* + NO3 -> CH3-aC*-aCH[.]-O-CH(ONO2)-aCH[.]*
2,5-Dimethylfuran	
100%	CH3-C*=CH-CH=C(CH3)-O* + NO3 -> CH3-aC[.]*-O-C(CH3)(ONO2)-aCH[.]-aCH*
	These represent the effects of NO_3 addition followed by stabilization. Decomposition such as occurs with the OH adduct is assumed to be less important because of lower excitation energy of the adduct.
	Photolysis Reactions
2-Butene-1,4-dial (formed from furan)	
59%	HCO-CH=CH-CHO + HV -> CO[.]-CH=CH-CHO + H.
41%	HCO-CH=CH-CHO + HV -> CH*=CH-O-CO-CH2*
4-Oxo-2-pentenal (formed from 2-methylfuran)	
70%	CH3-CO-CH=CH-CHO + HV -> CO[.]-CH=CH-CHO + CH3.
30%	CH3-CO-CH=CH-CHO + HV -> CH3-C*=CH-CH2-CO-O*

Ratio	Reaction
	Overall quantum yields for decomposition by photolysis derived from the ratios of photolysis rates for 2-butene-1,4-dial and 4-oxo-2-penteneal relative to NO_2 in the EUPHOR outdoor chamber Newland et al. (2019). Ratios of quantum yields for the formation of stable products via the furanone route is derived based on product data of Newland et al. (2019) for the photolysis of these compounds. Quantum yields for radical production derived from the difference between the total quantum yield and the quantum yield for stable product formation. Although the photolysis forming radicals may be more complex than shown, the product data indicate that much if not most of the radical forming reaction is as shown, and this is used to represent all radical forming pathways. Overall quantum yield used for 2-butene 1,4-dial is 0.288.
2-Methyl-2-butene-1,4-dial (formed from 3-methylfuran)	
70% 30%	CH3-C(CHO)=CH-CHO + HV -> CH3-aC*-aCH[.]-CO-O-aCH[.]* + H. CH3-C(CHO)=CH-CHO + HV -> CH3-C*=CH-O-CO-CH2*
	See comments above for 2-butene 1,4-dial and 4-Oxo-2-pentenal. However, no information is available concerning the quantum yields for photolysis of 2-methyl-1,4-butenedial. It is assumed to have the same photolysis rates as 4-oxo-2-pentenal. The overall quantum yield used for these compounds is 0.342.
Radical Reactions	
Allylic radicals formed after -OH or -ONO_2 addition.	
100%	HO-CH*-aCH[.]-aCH-aCH[.]-O* + O2 -> HO-CH*-CH=CH-CH[OO.]-O*
100%	O2NO-CH*-aCH[.]-aCH-aCH[.]-O* + O2 -> O2NO-CH*-CH=CH-CH[OO.]-O*
100%	CH3-C*(OH)-aCH[.]-aCH-aCH[.]-O* + O2 -> CH3-C*(OH)-CH=CH-CH[OO.]-O*
100%	CH3-aC[.]*-O-CH(OH)-aCH[.]-aCH* + O2 -> CH3-C[OO.]*-CH=CH-CH(OH)-O*
100%	CH3-C*(ONO2)-aCH[.]-aCH-aCH[.]-O* + O2 -> CH3-C*(ONO2)-CH=CH-CH[OO.]-O*
100%	CH3-aC[.]*-O-CH(ONO2)-aCH[.]-aCH* + O2 -> CH3-C[OO.]*-CH=CH-CH(ONO2)-O*
100%	CH3-aC[.]*-CH(OH)-O-aCH[.]-aCH* + O2 -> CH3-C*=CH-CH[OO.]-O-CH*-OH

Ratio	Reaction
100%	CH3-aC*-aCH[.]-O-CH(OH)-aCH[.]* + O2 -> CH3-C*=CH-CH(OH)-O-CH[OO.]*
100%	CH3-aC[.]*-CH(ONO2)-O-aCH[.]-aCH* + O2 -> CH3-C*=CH-CH[OO.]-O-CH*-ONO2
100%	CH3-aC*-aCH[.]-O-CH(ONO2)-aCH[.]* + O2 -> CH3-C*=CH-CH(ONO2)-O-CH[OO.]*
	Addition to the position next to the ether group is calculated to be the dominant pathway by Yuan et al. (2017).
Alkoxy radicals formed after OH additions.	
33% 67%	HO-CH*-CH=CH-CH[O.]-O* -> HO-CH*1-CH[.]-CH*2-O-CH*2-O*1 HO-CH*-CH=CH-CH[O.]-O* -> HO-CH*-CH=CH-CO-O* + H.
8% 92%	CH3-C*(OH)-CH=CH-CH[O.]-O* -> CH3-C*1(OH)-CH[.]-CH*2-O-CH*2-O*1 CH3-C*(OH)-CH=CH-CH[O.]-O* -> CH3-C*(OH)-CH=CH-CO-O* + H.
21% 79%	CH3-C[O.]*-CH=CH-C(CH3)(OH)-O* -> CH3-C*1(OH)-CH[.]-CH*2-O-C*2(CH3)-O*1 CH3-C[O.]*-CH=CH-C(CH3)(OH)-O* -> CH3-C*(OH)-CH=CH-CO-O* + CH3.
100%	CH3-C*=CH-CH[O.]-O-CH*-OH -> CH3-C*=CH-CO-O-CH*-OH + H.
11% 89%	CH3-C*=CH-CH(OH)-O-CH[O.]* -> CH3-C*12-CH[.]-CH(OH)-O-CH*1-O*2 CH3-C*=CH-CH(OH)-O-CH[O.]* -> CH3-C*=CH-CH(OH)-O-CO* + H.
	Branching ratio for cyclization vs hydroxyfuranone formation is based on the mechanism and calculations or estimates of Yuan et al. (2017), as used in the furans mechanism of this work with the H-elimination reaction being used to represent the effect of the reaction of this radical with O_2. (Both H-elimination and O_2 abstraction are estimated to occur at competitive rates, but the same products are eventually formed after H reacts with O_2, and the H-atom reaction is used to represent both processes for simplicity of the assignments.) This ratio is only valid for 1 atm air.
29% 71%	CH3-C[O.]*-CH=CH-CH(OH)-O* -> CH3-C*12-O-CH(OH)-CH[.]-CH*1-O*2 CH3-C[O.]*-CH=CH-CH(OH)-O* -> HO-CH*-CH=CH-CO-O* + CH3.
	Assigned based on the results of Yuan et al (Yuan et al., 2017).

Ratio	Reaction
100%	HO-CH*1-CH[O.]-CH*2-O-CH*2-O*1 -> HCO-CH*-O-CH*-O-CH[.]-OH
100%	CH3-C*12-O-CH(OH)-CH[O.]-CH*1-O*2 -> CH3-C*(O-CH[.]-OH)-O-CH*-CHO
100%	CH3-C*12-CH[O.]-CH(OH)-O-CH*1-O*2 -> CH3-C*(CHO)-O-CH*-O-CH[.]-OH
	These are based on the estimates and calculations of Yuan et al. (2017). Although decomposition forming HCO-CH(OH)-O-CH*-CH[.]-O* is estimated to occur ~25% of the time, this route is assumed to be minor to be consistent with the furans mechanism developed in this work.
Alkoxy radicals formed after NO_3 additions.	
33%	O2NO-CH*-CH=CH-CH[O.]-O* -> O2NO-CH*1-CH[.]-CH*2-O-CH*2-O*1
67%	O2NO-CH*-CH=CH-CH[O.]-O* -> O2NO-CH*-CH=CH-CO-O* + H.
8%	CH3-C*(ONO2)-CH=CH-CH[O.]-O* -> CH3-C*1(ONO2)-CH[.]-CH*2-O-CH*2-O*1
92%	CH3-C*(ONO2)-CH=CH-CH[O.]-O* -> CH3-C*(ONO2)-CH=CH-CO-O* + H.
21%	CH3-C[O.]*-CH=CH-C(CH3)(ONO2)-O* -> CH3-C*1(ONO2)-CH[.]-CH*2-O-C*2(CH3)-O*1
79%	CH3-C[O.]*-CH=CH-C(CH3)(ONO2)-O* -> CH3-C*(ONO2)-CH=CH-CO-O* + CH3.
100%	CH3-C*=CH-CH[O.]-O-CH*-OH -> CH3-C*=CH-CO-O-CH*-OH + H.
11%	CH3-C*=CH-CH(ONO2)-O-CH[O.]* -> CH3-C*12-CH[.]-CH(ONO2)-O-CH*1-O*2
89%	CH3-C*=CH-CH(ONO2)-O-CH[O.]* -> CH3-C*=CH-CH(ONO2)-O-CO* + H.
	Branching ratio for cyclization vs. hydroxyfuranone formation following NO_3 addition is assumed to be the same as calculated or estimated by Yuan et al. (2017) for the analogous radicals formed after OH addition. Both H-elimination and O_2 abstraction are estimated to occur at competitive rates, but the same products are eventually formed after H reacts with O_2, and the H-atom reaction is used to represent both processes for simplicity of the assignments. This ratio is only valid for 1 atm air.

Ratio	Reaction
100%	O2NO-CH*1-CH[O.]-CH*2-O-CH*2-O*1 -> HCO-CH*-O-CH*-O-CH[.]-ONO2
100%	CH3-C*12-O-CH(ONO2)-CH[O.]-CH*1-O*2 -> CH3-C*(O-CH[.]-ONO2)-O-CH*-CHO
100%	CH3-C*12-CH[O.]-CH(ONO2)-O-CH*1-O*2 -> CH3-C*(CHO)-O-CH*-O-CH[.]-ONO2
	These are based on the estimates and calculations of Yuan et al. (2017) for the analogous radical with -ONO2 replaced by -OH. Although decomposition of HO-CH*1-CH[O.]-CH*2-O-CH*2-O*1 forming HCO-CH(ONO2)-O-CH*-CH[.]-O* is estimated to occur ~15% of the time, this is assumed to be minor here.
29% 71%	CH3-C[O.]*-CH=CH-CH(ONO2)-O* -> CH3-C*12-O-CH(ONO2)-CH[.]-CH*1-O*2 CH3-C[O.]*-CH=CH-CH(ONO2)-O* -> O2NO-CH*-CH=CH-CO-O* + CH3.
	Assumed to have the same branching ratio as assigned based on the results of Yuan et al. (2017) for the analogous radical where -ONO2 is replaced by -OH.

Table B4: Listing of the furan reactants and the products they are predicted to form. Yields of products from the initial reactions of the furans or their photoreactive products when they react in the presence of NO_x are also shown.

Structure [a]	Model Species [b]		Yield in reactions [c]			
	SAPRC-18	SAPRC-07	OH	O3	NO3	hv
Furan and Products						
CH*=CH-O-CH=CH*	FURAN (explicit)					
HCO-CH=CH-CHO	BUTEDIAL (explicit)		76%			
HO-CH*-CH=CH-CO-O*	HFON52	HFONS	16%			
CH*=CH-O-CO-CH2*	3HF2ONE	HFONS				31%
CH*=CH-CO-O-CO*	MALAH	MALAH				45%
HCO-O-CH*-O-CH*-CHO	RCHO	RCHO	8%	100%	31%	
HO-CH*-CH=CH-CH(ONO2)-O*	RHNO3	RNO3	1%			
HO-CH*1-O-CH*2-O-CH*2-CH*1-ONO2	RHNO3	RNO3	0.2%			
NO2	NO2	NO2			31%	
O2NO-CH*-CH=CH-CO-O*	RCNO3	RNO3			65%	
O2NO-CH*1-O-CH*2-O-CH*2-CH*1-ONO2	RDNO3	RNO3			1%	
O2NO-CH*-CH=CH-CH(ONO2)-O*	RDNO3	RNO3			3%	
Maximum NO Consumption [d]			<32%		<132%	
Maximum yields of peroxy + HO2 products listed below [e]						
HO-O-CH*-CH=CH-CH(OH)-O*	RUOOH	ROOH	<22%			
HO-O-CH*1-CH(OH)-O-CH*2-O-CH*21	ROOH	ROOH	<8%			
HO-CH*-CH=CH-CO-O*	HFON52	HFONS	<2%			
HO-O-CH*-CH=CH-CH(ONO2)-O*	RHNO3	RNO3			<90%	
HO-O-CH*1-CH(ONO2)-O-CH*2-O-CH*21	RHNO3	RNO3			<32%	
O2NO-CH*-CH=CH-CO-O*	RCNO3	RNO3			<10%	
2-Methylfuran and Products						
CH3-C*=CH-CH=CH-O*	2M-FURAN (explicit)					
CH3-CO-CH=CH-CHO	4OX2PEAL (explicit)		44%			
HO-CH*-CH=CH-CO-O*	HFON52	HFONS	17%			
CH3-C*=CH-CH2-CO-O*	3HF2ONM5	HFONS				13%
CH*=CH-CO-O-CO*	MALAH	MALAH				31%
HCHO	HCHO	HCHO	17%		31%	31%
CH3-C*(O-CHO)-O-CH*-CHO	RCHO	RCHO	7%		12%	
CH3-CO-O-CH*-O-CH*-CHO	RCHO	RCHO	2%	59%	3%	
CH3-C*(OH)-CH=CH-CH(ONO2)-O*	RHNO3	RNO3	2%			
CH3-C*(ONO2)-CH=CH-CH(OH)-O*	RHNO3	RNO3	2%			
CH3-C*12-O-CH(OH)-CH(ONO2)-CH*1-O*2	RHNO3	RNO3	0%			
CH3-C*1(OH)-O-CH*2-O-CH*2-CH*1-ONO2	RHNO3	RNO3	0%			
HCO-O-C*=CH-CO-O-CH2*	OLEP	OLE2		20%		
CH2=C(CHO)-O-CHO	OLEA1	MACR		19%		
CO2	CO2	CO2		16%		
CO	CO	CO		3%		
CH2=C(O-CHO)-CH(ONO2)-CO-O-OH	RCNO3	RNO3		1%		
CH2=C(O-CHO)-CH(CHO)-ONO2	RCNO3	RNO3		0%		
CH3-C*(ONO2)-CH=CH-CO-O*	RCNO3	RNO3			46%	
NO2	NO2	NO2			15%	
O2NO-CH*-CH=CH-CO-O*	RCNO3	RNO3			31%	
CH3-C*(ONO2)-CH=CH-CH(ONO2)-O*	RDNO3	RNO3			6%	
Maximum NO Consumption [d]			<65%	<20%	<117%	
Maximum yields of peroxy + HO2 products listed below [e]						
CH3-C*(OH)-CH=CH-CH(O-OH)-O*	RUOOH	ROOH	<27%			

Structure [a]	**Model Species [b]**		**Yield in reactions [c]**			
	SAPRC-18	**SAPRC-07**	**OH**	**O3**	**NO3**	**hv**
CH3-C*(CH=CH-CH(OH)-O*)-O-OH	RUOOH	ROOH	<26%			
CH3-C*12-O-CH(OH)-CH(O-OH)-CH*1-O*2	ROOH	ROOH	<7%			
CH3-C*(OH)-CH=CH-CO-O*	HFON52M5	HFONS	<3%			
CH3-C*1(OH)-O-CH*2-O-CH*2-CH*1-O-OH	ROOH	ROOH	<2%			
CH2=C(O-CHO)-CH(CO-O-OH)-O-OH	RUOOH	ROOH		<13%		
CH2=C(CO-CO-O-OH)-O-CHO	BACL	BACL		<1%		
CH3-C*(ONO2)-CH=CH-CH(O-OH)-O*	RHNO3	RNO3			<48%	
CH3-C*(CH=CH-CH(ONO2)-O*)-O-OH	RHNO3	RNO3			<46%	
CH3-C*12-O-CH(ONO2)-CH(O-OH)-CH*1-O*2	RCNO3	RNO3			<13%	
CH3-C*(ONO2)-CH=CH-CO-O*	RCNO3	RNO3			<5%	
CH3-C*1(ONO2)-O-CH*2-O-CH*2-CH*1-O-OH	RHNO3	RNO3			<4%	
3-Methylfuran and Products						
CH3-C*=CH-O-CH=CH*	3M-FURAN (explicit)					
CH3-C(CHO)=CH-CHO	2MBUTDAL (explicit)		27%			
CH3-C*=CH-CH(ONO2)-O-CH*-OH	RHNO3	RNO3	4%			
CH3-C*=CH-CO-O-CH*-OH	HFON52M4	HFONS	59%			
CH3-C*=CH-CH(OH)-O-CO*	HFON52M3	HFONS	8%			
CH3-C*=CH-O-CO-CH2*	3HF2ONM4	HFONS				8%
CH3-C*(CHO)-O-CH*-O-CHO	RCHO	RCHO	1%	41%	1%	
CH3-C*=CH-CH(OH)-O-CH*-ONO2	RHNO3	RNO3	1%			
CH3-C*12-O-CH*1-O-CH(OH)-CH*2-ONO2	RHNO3	RNO3	0%			
CH3-CO-CH*-O-CH*-O-CHO	KET2	PROD2		59%		
CH3-C*=CH-CO-O-CH*-ONO2	RCNO3	RNO3			81%	1%
CH3-C*=CH-CH(ONO2)-O-CO*	RCNO3	RNO3			11%	
CH3-C*=CH-CH(ONO2)-O-CH*-ONO2	RDNO3	RNO3			6%	
NO2	NO2	NO2			1%	
CH3-C(CO[OO.])=CH-O-CO-O-OH	MACO3	MACO3				9%
CH3-C*=CH-CO-O-CO*	MALAH	NROG				5%
HCHO	HCHO	HCHO				3%
HCO-CO-O-CHO	MGLY	MGLY				3%
CH3-C*=CH-O-CO-CH*-ONO2	RCNO3	RNO3				1%
Maximum NO Consumption [d]			<74%		<101%	<70%
Maximum yields of peroxy + HO2 products listed below [e]						
CH3-C*=CH-CH(O-OH)-O-CH*-OH	RUOOH	ROOH	<57%			
CH3-C*=CH-CH(OH)-O-CH*-O-OH	RUOOH	ROOH	<9%			
CH3-C*=CH-CO-O-CH*-OH	HFON52M4	HFONS	<6%			
CH3-C*12-O-CH*1-O-CH(OH)-CH*2-O-OH	ROOH	ROOH	<1%			
CH3-C*=CH-CH(OH)-O-CO*	HFON52M3	HFONS	<1%			
CH3-C*=CH-CH(O-OH)-O-CH*-ONO2	RHNO3	RNO3			<78%	
CH3-C*=CH-CH(ONO2)-O-CH*-O-OH	RHNO3	RNO3			<12%	
CH3-C*=CH-CO-O-CH*-ONO2	RCNO3	RNO3			<9%	
CH3-C*12-O-CH*1-O-CH(ONO2)-CH*2-O-OH	RHNO3	RNO3			<1%	
CH3-C*=CH-CH(ONO2)-O-CO*	RCNO3	RNO3			<1%	
CH3-C*=CH-O-CO-CH*-O-OH	RUOOH	ROOH				<31%
CH3-C*=CH-CO-O-CH*-O-OH	HPALD	ROOH				<31%
CH3-C*=CH-O-CO-CO*	BACL	BACL				<3%
CH3-C*=CH-CO-O-CO*	AFG3	AFG3				<3%
2,5-Dimethyl Furan and Products						
CH3-C*=CH-CH=C(CH3)-O*	25M-FUR (explicit)					
CH3-C*(OH)-CH=CH-CO-O*	HFON52M5 (explicit)		50%			

Structure [a]	Model Species [b]		Yield in reactions [c]			
	SAPRC-18	SAPRC-07	OH	O3	NO3	hv
CH3-CO-CH=CH-CO-CH3	3HXE25DO (explicit)		28%			
HCHO	HCHO	HCHO	50%		69%	
CH3-CO-O-C*(CH3)-O-CH*-CHO	RCHO	RCHO	12%		12%	
CH3-C*(OH)-CH=CH-C(CH3)(ONO2)-O*	RHNO3	RNO3	9%			
CH3-C*1(OH)-O-C*2(CH3)-O-CH*2-CH*1-ONO2	RHNO3	RNO3	2%			
CH3-CO-O-C*=CH-CO-O-CH2*	OLEP	OLE2		50%		
CH2=C(CHO)-O-CO-CH3	OLEA1	MACR		44%		
CO2	CO2	CO2		37%		
CO	CO	CO		7%		
CH2=C(O-CO-CH3)-CH(ONO2)-CO-O-OH	RCNO3	RNO3		5%		
CH2=C(O-CO-CH3)-CH(CHO)-ONO2	RCNO3	RNO3		1%		
CH3-C*(ONO2)-CH=CH-CO-O*	RCNO3	RNO3			69%	
CH3-C*(ONO2)-CH=CH-C(CH3)(ONO2)-O*	RDNO3	RNO3			12%	
NO2	NO2	NO2			12%	
CH3-C*(CHO)-O-CO-C(CH3)(ONO2)-O*	RCNO3	RNO3			4%	
CH3-C*1(ONO2)-O-C*2(CH3)-O-CH*2-CH*1-ONO2	RDNO3	RNO3			2%	
Maximum NO Consumption [d]			<85%	<50%	<118%	
Maximum yields of peroxy + HO2 products listed below [e]						
CH3-C*(OH)-CH=CH-C(CH3)(O-OH)-O*	RUOOH	ROOH	<72%			
CH3-C*1(OH)-O-C*2(CH3)-O-CH*2-CH*1-O-OH	ROOH	ROOH	<13%			
CH2=C(O-CO-CH3)-CH(CO-O-OH)-O-OH	RUOOH	ROOH		<33%		
CH2=C(CO-CO-O-OH)-O-CO-CH3	BACL	BACL		<4%		
CH3-C*(ONO2)-CH=CH-C(CH3)(O-OH)-O*	RHNO3	RNO3			<100%	
CH3-C*1(ONO2)-O-C*2(CH3)-O-CH*2-CH*1-O-OH	RHNO3	RNO3			<18%	

[a] Structures are given in MechGen format. The symbols "*", "*1", "*2", and "*12" are used to indicate groups that are bonded in ring structures.

[b] Model species used to represent these products in the SAPRC-18 or SAPRC-07/-11 mechanisms. The notation "(explicit)" means that that the reactions of these species are added to these mechanisms.

[c] Yield of the compound in the reactions of the furan with OH or O_3, or yield of the compound in the photolysis of the photoreactive dicarbonyl product x the dicarbonyl product yield in the OH reaction, in the presence of NO_x and under conditions where reaction with NO dominates over other bimolecular reactions of peroxy radicals. Yields of other secondary products and products from the thermal reactions of the photoreactive products are not shown.

[d] Maximum amount of NO reacting with peroxy radicals to form either NO_2 or an organic nitrate. Shown as upper limits because other bimolecular reactions of peroxy radicals can occur under lower NO_x conditions, reducing the amounts reacting with NO.

[e] These are products formed in the reactions of intermediate peroxy radicals with HO_2. Their yields depend on experimental conditions, and their maximum possible yields are shown. In general, the actual yields of these peroxy + HO_2 products will be much lower, especially when NO_x is present. Therefore, they are shown as upper limits.

Table B5: Detailed mechanism for the furans and their explicitly represented products, for use with the SAPRC-18 base mechanism.

Reaction [a]	k(298) [b]
Furan	
FURAN + OH = #.76 BUTEDIAL + #.76 HO2 + #.24 FURAN_P1 + #.24 SumRO2	3.97E-11
FURAN + O3 = RCHO	2.42E-18
FURAN + NO3 = FURAN_P2 + SumRO2	1.36E-12
FURAN_P1 + NO = #.974 NO2 + #.652 HFON52 + #.652 HO2 + #.323 FURAN_P3 + #.026 RHNO3 + #-0.108 XC + #.323 SumRO2	9.13E-12
FURAN_P1 + NO3 = NO2 + #.669 HFON52 + #.669 HO2 + #.331 FURAN_P3 + #.331 SumRO2	2.30E-12
FURAN_P1 + HO2 = #.9 RUOOH + #.1 HFON52 + #-1.8 XC	1.61E-11
FURAN_P1 + SumRO2 = SumRO2 + #.585 HFON52 + #.335 HO2 + #.25 OLEP + #.166 FURAN_P3 + #-1.004 XC + #.166 SumRO2	2.57E-12
FURAN_P1 + SumRCO3 = SumRCO3 + #.735 HFON52 + #.535 HO2 + #.265 FURAN_P3 + #.265 SumRO2	1.37E-11
FURAN_P2 + NO = #.974 NO2 + #.653 RCNO3 + #.653 HO2 + #.322 FURAN_P4 + #.026 RDNO3 + #-0.108 XC + #-0.001 XN + #.322 SumRO2	9.13E-12
FURAN_P2 + NO3 = NO2 + #.67 RCNO3 + #.67 HO2 + #.33 FURAN_P4 + #.33 SumRO2	2.30E-12
FURAN_P2 + HO2 = #.9 RHNO3 + #.1 RCNO3 + #-3.6 XC	1.61E-11
FURAN_P2 + SumRO2 = SumRO2 + #.585 RCNO3 + #.335 HO2 + #.25 RHNO3 + #.165 FURAN_P4 + #-1 XC + #.165 SumRO2	2.57E-12
FURAN_P2 + SumRCO3 = SumRCO3 + #.736 RCNO3 + #.536 HO2 + #.264 FURAN_P4 + #.264 SumRO2	1.37E-11
FURAN_P3 + NO = #.974 RCHO + #.974 HO2 + #.974 NO2 + #.026 RHNO3 + #-0.104 XC	9.13E-12
FURAN_P3 + NO3 = RCHO + HO2 + NO2	2.30E-12
FURAN_P3 + HO2 = ROOH + #-1 XC	1.61E-11
FURAN_P3 + SumRO2 = SumRO2 + #.5 RCHO + #.5 HO2 + #.25 KET2 + #.25 IEPOX + #-0.75 XC	2.57E-12
FURAN_P3 + SumRCO3 = SumRCO3 + #.8 RCHO + #.8 HO2 + #.2 KET2 + #-0.4 XC	1.37E-11
FURAN_P4 + NO = #1.949 NO2 + #.974 RCHO + #.026 RDNO3 + #-0.104 XC + #-0.001 XN	9.13E-12
FURAN_P4 + NO3 = #2 NO2 + RCHO	2.30E-12
FURAN_P4 + HO2 = RHNO3 + #-4 XC	1.61E-11
FURAN_P4 + SumRO2 = SumRO2 + #.5 RCHO + #.5 NO2 + #.25 RCNO3 + #.25 RHNO3 + #-1 XC	2.57E-12
FURAN_P4 + SumRCO3 = SumRCO3 + #.8 RCHO + #.8 NO2 + #.2 RCNO3	1.37E-11
2-Methylfuran	
2M-FURAN + OH = #.56 2M-FURAN_P1 + #.44 4OX2PEAL + #.44 HO2 + #.56 SumRO2	7.31E-11
2M-FURAN + O3 = #.613 OH + #.591 RCHO + #.204 OLEP + #.204 2M-FURAN_R1 + #-0.016 XC	2.00E-17
2M-FURAN + NO3 = 2M-FURAN_P2 + SumRO2	2.57E-11

Reaction [a]	k(298) [b]
2M-FURAN_P1 + NO = #.938 NO2 + #.462 HFON52M5 + #.462 HO2 + #.309 HFON52 + #.309 MEO2 + #.167 2M-FURAN_P3 + #.062 RHNO3 + #-0.186 XC + #.476 SumRO2	9.13E-12
2M-FURAN_P1 + NO3 = NO2 + #.493 HFON52M5 + #.493 HO2 + #.33 HFON52 + #.33 MEO2 + #.177 2M-FURAN_P3 + #.507 SumRO2	2.30E-12
2M-FURAN_P1 + HO2 = #.946 RUOOH + #.054 HFON52M5 + #-0.946 XC	1.78E-11
2M-FURAN_P1 + SumRO2 = SumRO2 + #.38 HFON52M5 + #.366 OLEP + #.246 HO2 + #.165 HFON52 + #.165 MEO2 + #.089 2M-FURAN_P3 + #-1.098 XC + #.254 SumRO2	1.38E-12
2M-FURAN_P1 + SumRCO3 = SumRCO3 + #.501 HFON52M5 + #.394 HO2 + #.33 HFON52 + #.33 MEO2 + #.169 2M-FURAN_P3 + #.499 SumRO2	1.37E-11
2M-FURAN_R1 = 2M-FURAN_P4 + SumRO2	0.60
2M-FURAN_R1 + NO = #.938 OLEA1 + #.938 CO + #.938 HO2 + #.938 NO2 + #.062 RCNO3 + #-1.814 XC	9.13E-12
2M-FURAN_P2 + NO = #.938 NO2 + #.772 RCNO3 + #.463 HO2 + #.309 MEO2 + #.166 2M-FURAN_P5 + #.062 RDNO3 + #.277 XC + #.475 SumRO2	9.13E-12
2M-FURAN_P2 + NO3 = NO2 + #.823 RCNO3 + #.493 HO2 + #.329 MEO2 + #.177 2M-FURAN_P5 + #.494 XC + #.506 SumRO2	2.30E-12
2M-FURAN_P2 + HO2 = #.946 RHNO3 + #.054 RCNO3 + #-2.784 XC	1.78E-11
2M-FURAN_P2 + SumRO2 = SumRO2 + #.545 RCNO3 + #.366 RHNO3 + #.247 HO2 + #.165 MEO2 + #.089 2M-FURAN_P5 + #-0.718 XC + #.254 SumRO2	1.38E-12
2M-FURAN_P2 + SumRCO3 = SumRCO3 + #.831 RCNO3 + #.394 HO2 + #.329 MEO2 + #.169 2M-FURAN_P5 + #.502 XC + #.498 SumRO2	1.37E-11
2M-FURAN_P3 + NO = #.938 RCHO + #.938 HO2 + #.938 NO2 + #.062 RHNO3 + #.752 XC	9.13E-12
2M-FURAN_P3 + NO3 = RCHO + HO2 + NO2 + XC	2.30E-12
2M-FURAN_P3 + HO2 = ROOH	1.78E-11
2M-FURAN_P3 + SumRO2 = SumRO2 + #.5 RCHO + #.5 HO2 + #.25 KET2 + #.25 IEPOX + #.25 XC	2.57E-12
2M-FURAN_P3 + SumRCO3 = SumRCO3 + #.8 RCHO + #.8 HO2 + #.2 KET2 + #.6 XC	1.37E-11
2M-FURAN_P4 + NO = #.938 OLEA1 + #.938 CO2 + #.938 OH + #.938 NO2 + #.062 RCNO3 + #-1.814 XC	9.13E-12
2M-FURAN_P4 + NO3 = OLEA1 + CO2 + OH + NO2 + #-2 XC	2.30E-12
2M-FURAN_P4 + HO2 = #.9 RUOOH + #.1 BACL + #-0.8 XC	1.78E-11
2M-FURAN_P4 + SumRO2 = SumRO2 + #.5 OLEA1 + #.5 CO2 + #.5 OH + #.25 BACL + #.25 RUOOH + #-1 XC	2.57E-12
2M-FURAN_P4 + SumRCO3 = SumRCO3 + #.8 OLEA1 + #.8 CO2 + #.8 OH + #.2 BACL + #-1.4 XC	1.37E-11
2M-FURAN_P5 + NO = #1.82 NO2 + #.882 RCHO + #.062 RDNO3 + #.056 RCNO3 + #.056 OH + #.752 XC	9.13E-12
2M-FURAN_P5 + NO3 = #1.94 NO2 + #.94 RCHO + #.06 RCNO3 + #.06 OH + XC	2.30E-12
2M-FURAN_P5 + HO2 = RHNO3 + #-3 XC	1.78E-11
2M-FURAN_P5 + SumRO2 = SumRO2 + #.47 RCHO + #.47 NO2 + #.28 RCNO3 + #.25 RHNO3 + #.03 OH	2.57E-12

Reaction [a]	k(298) [b]
2M-FURAN_P5 + SumRCO3 = SumRCO3 + #.752 RCHO + #.752 NO2 + #.248 RCNO3 + #.048 OH + XC	1.37E-11
3-Methylfuran	
3M-FURAN + OH = #.73 3M-FURAN_P1 + #.27 2MBUTDAL + #.27 HO2 + #.73 SumRO2	8.73E-11
3M-FURAN + O3 = #.591 KET2 + #.409 RCHO + #-0.182 XC	2.05E-17
3M-FURAN + NO3 = 3M-FURAN_P2 + SumRO2	1.26E-11
3M-FURAN_P1 + NO = #.938 NO2 + #.937 HO2 + #.81 HFON52M4 + #.114 HFON52M3 + #.062 RHNO3 + #.013 RO2C + #.013 RCHO + #.001 RO2XC + #.001 zRHNO3 + #-0.176 XC + #.014 SumRO2	9.13E-12
3M-FURAN_P1 + NO3 = NO2 + #.999 HO2 + #.863 HFON52M4 + #.122 HFON52M3 + #.014 RO2C + #.014 RCHO + #.001 RO2XC + #.001 zRHNO3 + #.011 XC + #.015 SumRO2	2.30E-12
3M-FURAN_P1 + HO2 = #.9 RUOOH + #.086 HFON52M4 + #.014 HFON52M3 + #-0.9 XC	1.78E-11
3M-FURAN_P1 + SumRO2 = SumRO2 + #.647 HFON52M4 + #.5 HO2 + #.25 OLEP + #.095 HFON52M3 + #.007 RO2C + #.007 RCHO + #-0.738 XC + #.007 SumRO2	2.57E-12
3M-FURAN_P1 + SumRCO3 = SumRCO3 + #.863 HFON52M4 + #.799 HO2 + #.125 HFON52M3 + #.011 RO2C + #.011 RCHO + #.001 RO2XC + #.001 zRHNO3 + #.008 XC + #.012 SumRO2	1.37E-11
3M-FURAN_P2 + NO = #.951 NO2 + #.924 RCNO3 + #.924 HO2 + #.278 CO + #.062 RDNO3 + #.013 RO2C + #.013 RCHO + #.001 RO2XC + #.001 zRDNO3 + #.47 XC + #.014 SumRO2	9.13E-12
3M-FURAN_P2 + NO3 = #1.014 NO2 + #.985 RCNO3 + #.985 HO2 + #.296 CO + #.014 RO2C + #.014 RCHO + #.001 RO2XC + #.001 zRDNO3 + #.7 XC + #.015 SumRO2	2.30E-12
3M-FURAN_P2 + HO2 = #.9 RHNO3 + #.1 RCNO3 + #-2.6 XC	1.78E-11
3M-FURAN_P2 + SumRO2 = SumRO2 + #.742 RCNO3 + #.492 HO2 + #.25 RHNO3 + #.148 CO + #.008 NO2 + #.007 RO2C + #.007 RCHO + #-0.144 XC + #.007 SumRO2	2.57E-12
3M-FURAN_P2 + SumRCO3 = SumRCO3 + #.988 RCNO3 + #.788 HO2 + #.237 CO + #.011 NO2 + #.011 RO2C + #.011 RCHO + #.001 RO2XC + #.001 zRDNO3 + #.759 XC + #.012 SumRO2	1.37E-11
2,5-Dimethylfuran	
25M-FUR + OH = #.72 25M-FUR_P1 + #.28 3HXE25DO + #.28 HO2 + #.72 SumRO2	1.26E-10
25M-FUR + O3 = #1.5 OH + #.5 OLEP + #.5 25M-FUR_R1 + #-1 XC	4.20E-16
25M-FUR + NO3 = 25M-FUR_P2 + SumRO2	5.80E-11
25M-FUR_P1 + NO = #.876 NO2 + #.692 HFON52M5 + #.692 MEO2 + #.184 25M-FUR_P3 + #.124 RHNO3 + #-0.248 XC + #.876 SumRO2	9.13E-12
25M-FUR_P1 + NO3 = NO2 + #.79 HFON52M5 + #.79 MEO2 + #.21 25M-FUR_P3 + SumRO2	2.30E-12
25M-FUR_P1 + HO2 = RUOOH	1.95E-11
25M-FUR_P1 + SumRO2 = SumRO2 + #.5 OLEP + #.395 HFON52M5 + #.395 MEO2 + #.105 25M-FUR_P3 + #-1 XC + #.5 SumRO2	3.71E-16
25M-FUR_P1 + SumRCO3 = SumRCO3 + #.79 HFON52M5 + #.79 MEO2 + #.21 25M-FUR_P3 + SumRO2	1.37E-11
25M-FUR_R1 = 25M-FUR_P4 + SumRO2	6.00E-1

Reaction [a]	k(298) [b]
25M-FUR_R1 + NO = #.876 OLEA1 + #.876 CO + #.876 HO2 + #.876 NO2 + #.124 RCNO3 + #-0.628 XC	9.13E-12
25M-FUR_P2 + NO = #.876 NO2 + #.692 RCNO3 + #.692 MEO2 + #.184 25M-FUR_P5 + #.124 RDNO3 + #.444 XC + #.876 SumRO2	9.13E-12
25M-FUR_P2 + NO3 = NO2 + #.79 RCNO3 + #.79 MEO2 + #.21 25M-FUR_P5 + #.79 XC + SumRO2	2.30E-12
25M-FUR_P2 + HO2 = RHNO3 + #-2 XC	1.95E-11
25M-FUR_P2 + SumRO2 = SumRO2 + #.5 RHNO3 + #.395 RCNO3 + #.395 MEO2 + #.105 25M-FUR_P5 + #-0.605 XC + #.5 SumRO2	3.71E-16
25M-FUR_P2 + SumRCO3 = SumRCO3 + #.79 RCNO3 + #.79 MEO2 + #.21 25M-FUR_P5 + #.79 XC + SumRO2	1.37E-11
25M-FUR_P3 + NO = #.876 RCHO + #.876 HO2 + #.876 NO2 + #.124 RHNO3 + #1.504 XC	9.13E-12
25M-FUR_P3 + NO3 = RCHO + HO2 + NO2 + #2 XC	2.30E-12
25M-FUR_P3 + HO2 = ROOH + XC	1.95E-11
25M-FUR_P3 + SumRO2 = SumRO2 + #.5 RCHO + #.5 HO2 + #.25 KET2 + #.25 IEPOX + #1.25 XC	2.57E-12
25M-FUR_P3 + SumRCO3 = SumRCO3 + #.8 RCHO + #.8 HO2 + #.2 KET2 + #1.6 XC	1.37E-11
25M-FUR_P4 + NO = #.876 OLEA1 + #.876 CO2 + #.876 OH + #.876 NO2 + #.124 RCNO3 + #-0.628 XC	9.13E-12
25M-FUR_P4 + NO3 = OLEA1 + CO2 + OH + NO2 + #-1 XC	2.30E-12
25M-FUR_P4 + HO2 = #.9 RUOOH + #.1 BACL + #.2 XC	1.95E-11
25M-FUR_P4 + SumRO2 = SumRO2 + #.5 OLEA1 + #.5 CO2 + #.5 OH + #.25 BACL + #.25 RUOOH	2.57E-12
25M-FUR_P4 + SumRCO3 = SumRCO3 + #.8 OLEA1 + #.8 CO2 + #.8 OH + #.2 BACL + #-0.4 XC	1.37E-11
25M-FUR_P5 + NO = #1.536 NO2 + #.66 RCHO + #.216 RCNO3 + #.216 OH + #.124 RDNO3 + #1.504 XC	9.13E-12
25M-FUR_P5 + NO3 = #1.753 NO2 + #.753 RCHO + #.247 RCNO3 + #.247 OH + #2 XC	2.30E-12
25M-FUR_P5 + HO2 = RHNO3 + #-2 XC	1.95E-11
25M-FUR_P5 + SumRO2 = SumRO2 + #.376 RCHO + #.376 NO2 + #.374 RCNO3 + #.25 RHNO3 + #.124 OH + XC	2.57E-12
25M-FUR_P5 + SumRCO3 = SumRCO3 + #.602 RCHO + #.602 NO2 + #.398 RCNO3 + #.198 OH + #2 XC	1.37E-11
2-butene-1,4-dial (formed from furan)	
BUTEDIAL + OH = #.83 OH + #.759 MALAH + #.17 BUTEDIAL_R1 + #.071 ROOH + #-0.071 XC	4.22E-11
BUTEDIAL + O3 = GLY + #.668 HO2 + #.607 CO2 + #.393 RCHO2 + #.334 CO + #.273 HCHO + #-0.393 XC	1.60E-18
BUTEDIAL + NO3 = #.995 OH + #.955 MALAH + #.045 RCNO3 + #.005 RO2C + #.005 CO + #.005 HO2 + #-0.005 XC + #.955 XN + #.005 SumRO2	2.08E-15
BUTEDIAL + HV = #.59 MALAH + #.59 OH + #.59 HO2 + #.41 3HF2ONE	qy=0.288
BUTEDIAL_R1 = ROOH + OH + #-1 XC	0.60

Reaction [a]	k(298) [b]
BUTEDIAL_R1 + NO = #.974 HO2 + #.974 NO2 + #.884 GLY + #.884 MGLY + #.09 CROOH + #.09 CO + #.026 RCNO3 + #-1.334 XC	9.13E-12
4-Oxo-2-penteneal (formed from 2-methylfuran)	
4OX2PEAL + OH = #.386 4OX2PEAL_R1 + #.377 MACO3 + #.237 4OX2PEAL_P1 + #.377 XC + #.237 SumRO2 + #.377 SumRCO3	5.67E-11
4OX2PEAL + O3 = #.742 MGLY + #.496 HO2 + #.451 CO2 + #.421 RCHO2 + #.377 CO + #.258 GLY + #.203 HCHO + #.129 4OX2PEAL_P2 + #.129 OH + #-0.294 XC + #.129 SumRO2	4.80E-18
4OX2PEAL + NO3 = #.931 MACO3 + #.058 4OX2PEAL_P3 + #.008 RO2C + #.008 RCNO3 + #.008 CO2 + #.008 OH + #.002 RO2XC + #.002 zRCNO3 + #.938 XC + #.934 XN + #.068 SumRO2 + #.931 SumRCO3	1.00E-14
4OX2PEAL + HV = #.7 MALAH + #.7 OH + #.7 MEO2 + #.3 3HF2ONM5 + #.7 SumRO2	qy=0.342
4OX2PEAL_R1 = 4OX2PEAL_P4 + SumRO2	0.60
4OX2PEAL_R1 + NO = #.948 HO2 + #.948 NO2 + #.86 MGLY + #.86 GLY + #.088 RCHO + #.088 CO + #.052 RCNO3 + #.052 XC	9.13E-12
4OX2PEAL_P1 + NO = #.938 NO2 + #.75 MECO3 + #.75 CROOH + #.376 MGLY + #.188 HO2 + #.062 RCNO3 + #-3.876 XC + #.75 SumRCO3	9.13E-12
4OX2PEAL_P1 + NO3 = NO2 + #.8 MECO3 + #.8 CROOH + #.401 MGLY + #.2 HO2 + #-4.203 XC + #.8 SumRCO3	2.30E-12
4OX2PEAL_P1 + HO2 = #.9 CROOH + #.1 BACL + #-2.6 XC	1.78E-11
4OX2PEAL_P1 + SumRO2 = SumRO2 + #.65 CROOH + #.4 MECO3 + #.25 BACL + #.2 MGLY + #.1 HO2 + #-2.6 XC + #.4 SumRCO3	2.57E-12
4OX2PEAL_P1 + SumRCO3 = SumRCO3 + #.64 MECO3 + #.64 CROOH + #.32 MGLY + #.2 BACL + #.16 HO2 + #-3.16 XC + #.64 SumRCO3	1.37E-11
4OX2PEAL_P2 + NO = NO2 + #.749 MGLY + #.749 HO2 + #.251 CO2 + #.251 HCHO + #.251 OH + #-0.749 XC	9.13E-12
4OX2PEAL_P2 + NO3 = NO2 + #.749 MGLY + #.749 HO2 + #.251 CO2 + #.251 HCHO + #.251 OH + #-0.749 XC	2.30E-12
4OX2PEAL_P2 + HO2 = #.9 CROOH + #.1 MGLY + #-5.5 XC	1.27E-11
4OX2PEAL_P2 + SumRO2 = SumRO2 + #.624 MGLY + #.374 HO2 + #.25 CROOH + #.126 CO2 + #.126 HCHO + #.126 OH + #-2.124 XC	2.03E-13
4OX2PEAL_P2 + SumRCO3 = SumRCO3 + #.799 MGLY + #.599 HO2 + #.201 CO2 + #.201 HCHO + #.201 OH + #-0.799 XC	1.37E-11
4OX2PEAL_P3 + NO = RCNO3 + #.938 MECO3 + #.938 NO2 + #-0.876 XC + #.062 XN + #.938 SumRCO3	9.13E-12
4OX2PEAL_P3 + NO3 = MECO3 + RCNO3 + NO2 + #-1 XC + SumRCO3	2.30E-12
4OX2PEAL_P3 + HO2 = RCNO3 + XC	1.78E-11
4OX2PEAL_P3 + SumRO2 = SumRO2 + RCNO3 + #.5 MECO3 + #.5 SumRCO3	2.57E-12
4OX2PEAL_P3 + SumRCO3 = SumRCO3 + RCNO3 + #.8 MECO3 + #-0.6 XC + #.8 SumRCO3	1.37E-11
4OX2PEAL_P4 + NO = #.938 NO2 + #.899 RCHO + #.899 CO2 + #.899 OH + #.078 MGLY + #.062 RCNO3 + #.039 HO2 + #.023 XC	9.13E-12

Reaction [a]	k(298) [b]
4OX2PEAL_P4 + NO3 = NO2 + #.959 RCHO + #.959 CO2 + #.959 OH + #.083 MGLY + #.041 HO2 + #-0.044 XC	2.30E-12
4OX2PEAL_P4 + HO2 = #.9 CROOH + #.1 BACL + #-2.6 XC	1.78E-11
4OX2PEAL_P4 + SumRO2 = SumRO2 + #.479 RCHO + #.479 CO2 + #.479 OH + #.25 BACL + #.25 CROOH + #.041 MGLY + #.021 HO2 + #-0.518 XC	2.57E-12
4OX2PEAL_P4 + SumRCO3 = SumRCO3 + #.767 RCHO + #.767 CO2 + #.767 OH + #.2 BACL + #.066 MGLY + #.033 HO2 + #.167 XC	1.37E-11
2-Methyl-2-butene-1,4-dial (formed from 3-methylfuran)	
2MBUTDAL + OH = #.782 OH + #.691 MALAH + #.157 2MBUTDAL_R2 + #.091 ROOH + #.061 2MBUTDAL_R1 + #-0.691 XC	4.15E-11
2MBUTDAL + NO3 = #.582 OH + #.418 2MBUTDAL_R3 + #.408 MALAH + #.174 RCNO3 + #-0.234 XC + #.408 XN	3.13E-15
2MBUTDAL + O3 = #.5 GLY + #.5 MGLY + #.447 RCHO2 + #.417 CO + #.334 HO2 + #.303 CO2 + #.25 2MBUTDAL_P1 + #.25 OH + #.137 HCHO + #-0.198 XC + #.25 SumRO2	4.80E-18
2MBUTDAL + HV = #.7 2MBUTDAL_P2 + #.7 HO2 + #.3 3HF2ONM4 + #.7 SumRO2	qy=0.342
2MBUTDAL_R1 = ROOH + OH	0.60
2MBUTDAL_R1 + NO = #.938 HO2 + #.938 NO2 + #.585 BACL + #.585 GLY + #.353 CROOH + #.353 CO + #.062 RCNO3 + #-1.935 XC	9.13E-12
2MBUTDAL_R2 = ROOH + OH	0.60
2MBUTDAL_R2 + NO = #1.825 MGLY + #.938 HO2 + #.938 NO2 + #.062 RCNO3 + #.025 CROOH + #.025 CO + #-0.948 XC	9.13E-12
2MBUTDAL_P1 + NO = NO2 + #.749 MGLY + #.749 HO2 + #.251 CO2 + #.251 HCHO + #.251 OH + #-0.749 XC	9.13E-12
2MBUTDAL_P1 + NO3 = NO2 + #.749 MGLY + #.749 HO2 + #.251 CO2 + #.251 HCHO + #.251 OH + #-0.749 XC	2.30E-12
2MBUTDAL_P1 + HO2 = #.9 CROOH + #.1 MGLY + #-5.5 XC	1.27E-11
2MBUTDAL_P1 + SumRO2 = SumRO2 + #.624 MGLY + #.374 HO2 + #.25 CROOH + #.126 CO2 + #.126 HCHO + #.126 OH + #-2.124 XC	2.03E-13
2MBUTDAL_P1 + SumRCO3 = SumRCO3 + #.799 MGLY + #.599 HO2 + #.201 CO2 + #.201 HCHO + #.201 OH + #-0.799 XC	1.37E-11
2MBUTDAL_R3 = RCNO3 + OH + XC	0.60
2MBUTDAL_R3 + NO = RCNO3 + #.938 CO + #.938 HO2 + #.938 NO2 + #.062 XC + #.062 XN	9.13E-12
2MBUTDAL_P2 + NO = #.938 NO2 + #.469 MACO3 + #.284 MALAH + #.284 HO2 + #.185 MGLY + #.185 MEO2 + #.185 CO + #.062 RCNO3 + #.247 XC + #.185 SumRO2 + #.469 SumRCO3	9.13E-12
2MBUTDAL_P2 + NO3 = NO2 + #.5 MACO3 + #.303 MALAH + #.303 HO2 + #.197 MGLY + #.197 MEO2 + #.197 CO + #.197 XC + #.197 SumRO2 + #.5 SumRCO3	2.30E-12
2MBUTDAL_P2 + HO2 = #.45 RUOOH + #.45 HPALD + #.05 BACL + #.05 MALAH + #-0.45 XC	1.78E-11
2MBUTDAL_P2 + SumRO2 = SumRO2 + #.277 MALAH + #.25 MACO3 + #.152 HO2 + #.125 BACL + #.125 OLEP + #.125 HFON52M4 + #.098 MGLY + #.098 MEO2 + #.098 CO + #-0.277 XC + #.098 SumRO2 + #.25 SumRCO3	2.57E-12

Reaction [a]	k(298) [b]
2MBUTDAL_P2 + SumRCO3 = SumRCO3 + #.4 MACO3 + #.342 MALAH + #.242 HO2 + #.158 MGLY + #.158 MEO2 + #.158 CO + #.1 BACL + #.158 XC + #.158 SumRO2 + #.4 SumRCO3	1.37E-11
3-Hexene-2,5-dione (formed from 2,5-dimethylfuran)	
3HXE25DO + OH = 3HXE25DO_P1 + SumRO2	4.71E-11
3HXE25DO + NO3 = 3HXE25DO_P3 + SumRO2	1.80E-18
3HXE25DO + O3 = MGLY + #.5 3HXE25DO_P2 + #.5 RCHO2 + #.5 OH + #.5 CO + #.5 SumRO2	1.64E-14
3HXE25DO_P1 + NO = #.93 NO2 + #.743 MECO3 + #.743 RCHO + #.372 MGLY + #.186 HO2 + #.07 RCNO3 + #.146 XC + #.743 SumRCO3	9.13E-12
3HXE25DO_P1 + NO3 = NO2 + #.8 MECO3 + #.8 RCHO + #.401 MGLY + #.2 HO2 + #-0.003 XC + #.8 SumRCO3	2.30E-12
3HXE25DO_P1 + HO2 = #.9 CROOH + #.1 BACL + #-1.6 XC	1.95E-11
3HXE25DO_P1 + SumRO2 = SumRO2 + #.4 MECO3 + #.4 RCHO + #.25 BACL + #.25 KET2 + #.2 MGLY + #.1 HO2 + #.5 XC + #.4 SumRCO3	2.57E-12
3HXE25DO_P1 + SumRCO3 = SumRCO3 + #.64 MECO3 + #.64 RCHO + #.32 MGLY + #.2 BACL + #.16 HO2 + #.4 XC + #.64 SumRCO3	1.37E-11
3HXE25DO_P2 + NO = NO2 + #.749 MGLY + #.749 HO2 + #.251 CO2 + #.251 HCHO + #.251 OH + #-0.749 XC	9.13E-12
3HXE25DO_P2 + NO3 = NO2 + #.749 MGLY + #.749 HO2 + #.251 CO2 + #.251 HCHO + #.251 OH + #-0.749 XC	2.30E-12
3HXE25DO_P2 + HO2 = #.9 CROOH + #.1 MGLY + #-5.5 XC	1.27E-11
3HXE25DO_P2 + SumRO2 = SumRO2 + #.624 MGLY + #.374 HO2 + #.25 CROOH + #.126 CO2 + #.126 HCHO + #.126 OH + #-2.124 XC	2.03E-13
3HXE25DO_P2 + SumRCO3 = SumRCO3 + #.799 MGLY + #.599 HO2 + #.201 CO2 + #.201 HCHO + #.201 OH + #-0.799 XC	1.37E-11
3HXE25DO_P3 + NO = #.935 RCNO3 + #.847 NO2 + #.782 MECO3 + #.065 MACO3 + #.065 HCHO + #.371 XC + #.218 XN + #.847 SumRCO3	9.13E-12
3HXE25DO_P3 + NO3 = NO2 + #.924 MECO3 + #.924 RCNO3 + #.076 MACO3 + #.076 HCHO + #.076 XC + #.076 XN + SumRCO3	2.30E-12
3HXE25DO_P3 + HO2 = #.924 RCNO3 + #.069 HPALD + #.008 AFG3 + #1.911 XC + #.076 XN	1.95E-11
3HXE25DO_P3 + SumRO2 = SumRO2 + #.924 RCNO3 + #.462 MECO3 + #.038 MACO3 + #.038 HCHO + #.038 AFG3 + #.962 XC + #.076 XN + #.5 SumRCO3	2.39E-12
3HXE25DO_P3 + SumRCO3 = SumRCO3 + #.924 RCNO3 + #.739 MECO3 + #.061 MACO3 + #.061 HCHO + #.015 AFG3 + #.431 XC + #.076 XN + #.8 SumRCO3	1.37E-11
5-Hydroxy-2(5H)-furanone (formed from furan)	
HFON52 + OH = #.933 HFON52_P1 + #.067 MALAH + #.067 HO2 + #.933 SumRO2	3.84E-11
HFON52 + O3 = RCHO2 + XC	5.07E-17
HFON52 + NO3 = #.864 HFON52_P2 + #.136 MALAH + #.136 HO2 + #.136 XN + #.864 SumRO2	4.08E-15

Reaction [a]	k(298) [b]
HFON52_P1 + NO = #.974 NO2 + #.968 HO2 + #.691 MGLY + #.277 RCHO + #.026 RCNO3 + #.007 R2CO3 + #.694 XC + #.007 SumRCO3	9.13E-12
HFON52_P1 + NO3 = NO2 + #.993 HO2 + #.709 MGLY + #.284 RCHO + #.007 R2CO3 + #.716 XC + #.007 SumRCO3	2.30E-12
HFON52_P1 + HO2 = #.935 ROOH + #.065 BACL + #-0.935 XC	1.61E-11
HFON52_P1 + SumRO2 = SumRO2 + #.497 HO2 + #.355 MGLY + #.25 OTH3 + #.164 BACL + #.142 RCHO + #.086 KET2 + #.003 R2CO3 + #.186 XC + #.003 SumRCO3	2.57E-12
HFON52_P1 + SumRCO3 = SumRCO3 + #.795 HO2 + #.567 MGLY + #.227 RCHO + #.131 BACL + #.069 KET2 + #.005 R2CO3 + #.438 XC + #.005 SumRCO3	1.37E-11
HFON52_P2 + NO = #1.462 NO2 + #.513 RCNO3 + #.487 HO2 + #.388 RCHO + #.099 MGLY + #.099 XC + #.025 XN	9.13E-12
HFON52_P2 + NO3 = #1.5 NO2 + #.5 RCNO3 + #.5 HO2 + #.399 RCHO + #.101 MGLY + #.101 XC	2.30E-12
HFON52_P2 + HO2 = RCNO3	1.61E-11
HFON52_P2 + SumRO2 = SumRO2 + #.75 RCNO3 + #.25 NO2 + #.25 HO2 + #.199 RCHO + #.051 MGLY + #.051 XC	2.57E-12
HFON52_P2 + SumRCO3 = SumRCO3 + #.6 RCNO3 + #.4 NO2 + #.4 HO2 + #.319 RCHO + #.081 MGLY + #.081 XC	1.37E-11
5-Methyl-5-hydroxy-2(5H)-furanone (formed from 2-methyl and 2,5-dimethylfurans)	
HFON52M5 + OH = HFON52M5_P1 + SumRO2	3.61E-11
HFON52M5 + O3 = RCHO2 + #2 XC	5.07E-17
HFON52M5 + NO3 = #.967 HFON52M5_P2 + #.033 MALAH + #.033 MEO2 + #.033 XN + SumRO2	3.65E-15
HFON52M5_P1 + NO = #.938 NO2 + #.932 HO2 + #.627 MGLY + #.305 RCHO + #.062 RCNO3 + #.006 R2CO3 + #1.633 XC + #.006 SumRCO3	9.13E-12
HFON52M5_P1 + NO3 = NO2 + #.993 HO2 + #.668 MGLY + #.325 RCHO + #.007 R2CO3 + #1.675 XC + #.007 SumRCO3	2.30E-12
HFON52M5_P1 + HO2 = #.935 ROOH + #.065 BACL + #.065 XC	1.78E-11
HFON52M5_P1 + SumRO2 = SumRO2 + #.497 HO2 + #.334 MGLY + #.25 OTH3 + #.164 BACL + #.163 RCHO + #.086 KET2 + #.003 R2CO3 + #1.165 XC + #.003 SumRCO3	2.57E-12
HFON52M5_P1 + SumRCO3 = SumRCO3 + #.795 HO2 + #.534 MGLY + #.26 RCHO + #.131 BACL + #.069 KET2 + #.005 R2CO3 + #1.405 XC + #.005 SumRCO3	1.37E-11
HFON52M5_P2 + NO = #1.407 NO2 + #.531 RCNO3 + #.469 HO2 + #.374 RCHO + #.095 MGLY + #1.095 XC + #.062 XN	9.13E-12
HFON52M5_P2 + NO3 = #1.5 NO2 + #.5 RCNO3 + #.5 HO2 + #.399 RCHO + #.101 MGLY + #1.101 XC	2.30E-12
HFON52M5_P2 + HO2 = RCNO3 + XC	1.78E-11
HFON52M5_P2 + SumRO2 = SumRO2 + #.75 RCNO3 + #.25 NO2 + #.25 HO2 + #.199 RCHO + #.051 MGLY + #1.051 XC	2.57E-12
HFON52M5_P2 + SumRCO3 = SumRCO3 + #.6 RCNO3 + #.4 NO2 + #.4 HO2 + #.319 RCHO + #.081 MGLY + #1.081 XC	1.37E-11
4-Methyl-5-hydroxy-2(5H)-furanone (formed from 3-methylfuran)	

Reaction [a]	k(298) [b]
HFON52M4 + OH = #.944 HFON52M4_P1 + #.056 MALAH + #.056 HO2 + #-0.056 XC + #.944 SumRO2	4.62E-11
HFON52M4 + O3 = RCHO2 + #2 XC	1.63E-16
HFON52M4 + NO3 = HFON52M4_P2 + SumRO2	7.03E-14
HFON52M4_P1 + NO = #.938 HO2 + #.938 NO2 + #.518 KET2 + #.42 MGLY + #.062 RCNO3 + #.384 XC	9.13E-12
HFON52M4_P1 + NO3 = HO2 + NO2 + #.553 KET2 + #.447 MGLY + #.341 XC	2.30E-12
HFON52M4_P1 + HO2 = #.957 ROOH + #.043 BACL + #.043 XC	1.78E-11
HFON52M4_P1 + SumRO2 = SumRO2 + #.5 HO2 + #.393 OTH3 + #.276 KET2 + #.224 MGLY + #.107 BACL + #.672 XC	1.10E-12
HFON52M4_P1 + SumRCO3 = SumRCO3 + #.915 HO2 + #.553 KET2 + #.362 MGLY + #.085 BACL + #.256 XC	1.37E-11
HFON52M4_P2 + NO = #1.876 NO2 + #.909 MGLY + #.062 RCNO3 + #.029 RCHO + #1.909 XC + #.062 XN	9.13E-12
HFON52M4_P2 + NO3 = #2 NO2 + #.969 MGLY + #.031 RCHO + #1.969 XC	2.30E-12
HFON52M4_P2 + HO2 = RCNO3 + XC	1.78E-11
HFON52M4_P2 + SumRO2 = SumRO2 + #.5 NO2 + #.5 RCNO3 + #.485 MGLY + #.015 RCHO + #1.485 XC	2.57E-12
HFON52M4_P2 + SumRCO3 = SumRCO3 + #.8 NO2 + #.775 MGLY + #.2 RCNO3 + #.025 RCHO + #1.775 XC	1.37E-11
3-Methyl-5-hydroxy-2(5H)-furanone (formed from 3-methylfuran)	
HFON52M3 + OH = #.957 HFON52M3_P1 + #.043 MALAH + #.043 HO2 + #-0.043 XC + #.957 SumRO2	5.98E-11
HFON52M3 + O3 = HFON52M3_P2 + OH + SumRO2	1.63E-16
HFON52M3 + NO3 = HFON52M3_P3 + SumRO2	7.03E-14
HFON52M3_P1 + NO = #.938 NO2 + #.658 R2CO3 + #.28 HO2 + #.155 RCHO + #.125 BACL + #.062 RCNO3 + #1.658 XC + #.658 SumRCO3	9.13E-12
HFON52M3_P1 + NO3 = NO2 + #.701 R2CO3 + #.299 HO2 + #.165 RCHO + #.133 BACL + #1.705 XC + #.701 SumRCO3	2.30E-12
HFON52M3_P1 + HO2 = ROOH	1.78E-11
HFON52M3_P1 + SumRO2 = SumRO2 + #.457 OTH3 + #.351 R2CO3 + #.149 HO2 + #.083 RCHO + #.067 BACL + #.043 KET2 + #1.261 XC + #.351 SumRCO3	4.40E-13
HFON52M3_P1 + SumRCO3 = SumRCO3 + #.701 R2CO3 + #.264 HO2 + #.132 BACL + #.132 RCHO + #.034 KET2 + #1.637 XC + #.701 SumRCO3	1.37E-11
HFON52M3_P2 + NO = #.938 R2CO3 + #.938 HCHO + #.938 NO2 + #.062 RCNO3 + XC + #.938 SumRCO3	9.13E-12
HFON52M3_P2 + NO3 = R2CO3 + HCHO + NO2 + XC + SumRCO3	2.30E-12
HFON52M3_P2 + HO2 = BACL + XC	1.78E-11
HFON52M3_P2 + SumRO2 = SumRO2 + #.5 R2CO3 + #.5 HCHO + #.5 BACL + XC + #.5 SumRCO3	2.03E-13
HFON52M3_P2 + SumRCO3 = SumRCO3 + #.8 R2CO3 + #.8 HCHO + #.2 BACL + XC + #.8 SumRCO3	1.37E-11
HFON52M3_P3 + NO = RCNO3 + #.938 HO2 + #.938 NO2 + XC + #.062 XN	9.13E-12

Reaction [a]	k(298) [b]
HFON52M3_P3 + NO3 = RCNO3 + HO2 + NO2 + XC	2.30E-12
HFON52M3_P3 + HO2 = RCNO3 + XC	1.78E-11
HFON52M3_P3 + SumRO2 = SumRO2 + RCNO3 + #.5 HO2 + XC	2.57E-12
HFON52M3_P3 + SumRCO3 = SumRCO3 + RCNO3 + #.8 HO2 + XC	1.37E-11
3H-furan-2-one (formed from 2-butene 1,4-dial photolysis)	
3HF2ONE + OH = 3HF2ONE_P1 + SumRO2	4.45E-11
3HF2ONE + O3 = #42.886 NROG + #.547 CO2 + #.453 3HF2ONE_R1 + #.453 OH + #.06 3HF2ONE_P2 + #.06 HO2 + #1.461 XC + #.06 SumRO2	2.52E-17
3HF2ONE + NO3 = 3HF2ONE_P3 + SumRO2	2.45E-13
3HF2ONE_P1 + NO = #.974 RCHO + #.974 HO2 + #.974 NO2 + #.026 RCNO3	9.13E-12
3HF2ONE_P1 + NO3 = RCHO + HO2 + NO2	2.30E-12
3HF2ONE_P1 + HO2 = #.911 ROOH + #.089 OTH1 + #-0.822 XC	1.61E-11
3HF2ONE_P1 + SumRO2 = SumRO2 + #.5 RCHO + #.5 HO2 + #.25 OTH3 + #.222 OTH1 + #.028 KET2 + #.166 XC	2.57E-12
3HF2ONE_P1 + SumRCO3 = SumRCO3 + #.8 RCHO + #.8 HO2 + #.177 OTH1 + #.023 KET2 + #.131 XC	1.37E-11
3HF2ONE_R1 = 3HF2ONE_P4 + SumRO2	0.60
3HF2ONE_R1 + NO = #.974 HO2 + #.974 NO2 + #.956 MGLY + #.956 CO + #.026 RCNO3 + #.018 BACL	9.13E-12
3HF2ONE_P2 + NO = #.99 NO2 + #.742 MGLY + #.742 HO2 + #.249 R2CO3 + #.249 HCHO + #.01 RCNO3 + #-0.262 XC + #.249 SumRCO3	9.13E-12
3HF2ONE_P2 + NO3 = NO2 + #.749 MGLY + #.749 HO2 + #.251 R2CO3 + #.251 HCHO + #-0.251 XC + #.251 SumRCO3	2.30E-12
3HF2ONE_P2 + HO2 = #.9 ROOH + #.1 MGLY + #-1.8 XC	1.44E-11
3HF2ONE_P2 + SumRO2 = SumRO2 + #.624 MGLY + #.374 HO2 + #.25 OTH1 + #.126 R2CO3 + #.126 HCHO + #-0.126 XC + #.126 SumRCO3	2.03E-13
3HF2ONE_P2 + SumRCO3 = SumRCO3 + #.799 MGLY + #.599 HO2 + #.201 R2CO3 + #.201 HCHO + #-0.201 XC + #.201 SumRCO3	1.37E-11
3HF2ONE_P3 + NO = #1.949 NO2 + #.974 RCHO + #.026 RCNO3 + #.025 XN	9.13E-12
3HF2ONE_P3 + NO3 = #2 NO2 + RCHO	2.30E-12
3HF2ONE_P3 + HO2 = RCNO3	1.61E-11
3HF2ONE_P3 + SumRO2 = SumRO2 + #.5 RCHO + #.5 NO2 + #.5 RCNO3	2.57E-12
3HF2ONE_P3 + SumRCO3 = SumRCO3 + #.8 RCHO + #.8 NO2 + #.2 RCNO3	1.37E-11
3HF2ONE_P4 + NO = #.974 NO2 + #.942 BACL + #.942 HO2 + #.032 MGLY + #.026 RCNO3 + #.016 R2CO3 + #.016 CO2 + #.016 OH + #-0.032 XC + #.016 SumRCO3	9.13E-12
3HF2ONE_P4 + NO3 = NO2 + #.967 BACL + #.967 HO2 + #.033 MGLY + #.017 R2CO3 + #.017 CO2 + #.017 OH + #-0.035 XC + #.017 SumRCO3	2.30E-12
3HF2ONE_P4 + HO2 = #.9 ROOH + #.1 BACL + #-0.9 XC	1.61E-11
3HF2ONE_P4 + SumRO2 = SumRO2 + #.733 BACL + #.483 HO2 + #.25 ROOH + #.017 MGLY + #.008 R2CO3 + #.008 CO2 + #.008 OH + #-0.265 XC + #.008 SumRCO3	2.57E-12
3HF2ONE_P4 + SumRCO3 = SumRCO3 + #.973 BACL + #.773 HO2 + #.027 MGLY + #.013 R2CO3 + #.013 CO2 + #.013 OH + #-0.025 XC + #.013 SumRCO3	1.37E-11

Reaction [a]	k(298) [b]
5-Methyl-3H-furan-2-one (formed from 4-oxo-2-pentenal photolysis)	
3HF2ONM5 + OH = 3HF2ONM5_P1 + SumRO2	7.52E-11
3HF2ONM5 + O3 = #49.717 NROG + #.547 CO2 + #.453 3HF2ONM5_R1 + #.453 OH + #.06 3HF2ONM5_P2 + #.06 HO2 + #1.948 XC + #.06 SumRO2	8.11E-17
3HF2ONM5 + NO3 = 3HF2ONM5_P3 + SumRO2	9.68E-12
3HF2ONM5_P1 + NO = #.938 RCHO + #.938 HO2 + #.938 NO2 + #.062 RCNO3 + XC	9.13E-12
3HF2ONM5_P1 + NO3 = RCHO + HO2 + NO2 + XC	2.30E-12
3HF2ONM5_P1 + HO2 = ROOH	1.78E-11
3HF2ONM5_P1 + SumRO2 = SumRO2 + #.5 RCHO + #.5 HO2 + #.488 OTH3 + #.012 KET2 + #.976 XC	1.23E-13
3HF2ONM5_P1 + SumRCO3 = SumRCO3 + #.99 RCHO + #.99 HO2 + #.01 KET2 + #.98 XC	1.37E-11
3HF2ONM5_R1 = 3HF2ONM5_P4 + SumRO2	0.60
3HF2ONM5_R1 + NO = #.938 HO2 + #.938 NO2 + #.921 MGLY + #.921 CO + #.062 RCNO3 + #.018 BACL + #.996 XC	9.13E-12
3HF2ONM5_P2 + NO = #.974 NO2 + #.73 MGLY + #.73 HO2 + #.245 R2CO3 + #.245 HCHO + #.026 RCNO3 + #.726 XC + #.245 SumRCO3	9.13E-12
3HF2ONM5_P2 + NO3 = NO2 + #.749 MGLY + #.749 HO2 + #.251 R2CO3 + #.251 HCHO + #.749 XC + #.251 SumRCO3	2.30E-12
3HF2ONM5_P2 + HO2 = #.9 ROOH + #.1 MGLY + #-0.8 XC	1.61E-11
3HF2ONM5_P2 + SumRO2 = SumRO2 + #.624 MGLY + #.374 HO2 + #.25 OTH1 + #.126 R2CO3 + #.126 HCHO + #.874 XC + #.126 SumRCO3	2.03E-13
3HF2ONM5_P2 + SumRCO3 = SumRCO3 + #.799 MGLY + #.599 HO2 + #.201 R2CO3 + #.201 HCHO + #.799 XC + #.201 SumRCO3	1.37E-11
3HF2ONM5_P3 + NO = #1.876 NO2 + #.938 RCHO + #.062 RCNO3 + XC + #.062 XN	9.13E-12
3HF2ONM5_P3 + NO3 = #2 NO2 + RCHO + XC	2.30E-12
3HF2ONM5_P3 + HO2 = RCNO3 + XC	1.78E-11
3HF2ONM5_P3 + SumRO2 = SumRO2 + #.5 RCHO + #.5 NO2 + #.5 RCNO3 + XC	2.57E-12
3HF2ONM5_P3 + SumRCO3 = SumRCO3 + #.8 RCHO + #.8 NO2 + #.2 RCNO3 + XC	1.37E-11
3HF2ONM5_P4 + NO = #.938 NO2 + #.907 BACL + #.907 HO2 + #.062 RCNO3 + #.031 MGLY + #.016 R2CO3 + #.016 CO2 + #.016 OH + #.967 XC + #.016 SumRCO3	9.13E-12
3HF2ONM5_P4 + NO3 = NO2 + #.967 BACL + #.967 HO2 + #.033 MGLY + #.017 R2CO3 + #.017 CO2 + #.017 OH + #.965 XC + #.017 SumRCO3	2.30E-12
3HF2ONM5_P4 + HO2 = #.9 ROOH + #.1 BACL + #.1 XC	1.78E-11
3HF2ONM5_P4 + SumRO2 = SumRO2 + #.733 BACL + #.483 HO2 + #.25 ROOH + #.017 MGLY + #.008 R2CO3 + #.008 CO2 + #.008 OH + #.735 XC + #.008 SumRCO3	2.57E-12
3HF2ONM5_P4 + SumRCO3 = SumRCO3 + #.973 BACL + #.773 HO2 + #.027 MGLY + #.013 R2CO3 + #.013 CO2 + #.013 OH + #.975 XC + #.013 SumRCO3	1.37E-11
4-Methyl-3H-furan-2-one (formed from 2-methyl-2-butene-1,4-dial photolysis)	
3HF2ONM4 + OH = 3HF2ONM4_P1 + SumRO2	3.73E-11
3HF2ONM4 + O3 = 3HF2ONM4_P2 + OH + SumRO2	8.11E-17
3HF2ONM4 + NO3 = 3HF2ONM4_P3 + SumRO2	8.61E-15

Reaction [a]	k(298) [b]
3HF2ONM4_P1 + NO = #.938 KET2 + #.938 HO2 + #.938 NO2 + #.062 RCNO3 + #-0.876 XC	9.13E-12
3HF2ONM4_P1 + NO3 = KET2 + HO2 + NO2 + #-1 XC	2.30E-12
3HF2ONM4_P1 + HO2 = #.925 ROOH + #.075 OTH1 + #.15 XC	1.78E-11
3HF2ONM4_P1 + SumRO2 = SumRO2 + #.5 KET2 + #.5 HO2 + #.312 OTH3 + #.188 OTH1 + #.188 XC	1.94E-12
3HF2ONM4_P1 + SumRCO3 = SumRCO3 + #.849 KET2 + #.849 HO2 + #.151 OTH1 + #-0.547 XC	1.37E-11
3HF2ONM4_P2 + NO = #.938 NO2 + #.469 R2CO3 + #.469 HCHO + #.469 MECO3 + #.469 MGLY + #.062 RCNO3 + #.531 XC + #.938 SumRCO3	9.13E-12
3HF2ONM4_P2 + NO3 = NO2 + #.5 R2CO3 + #.5 HCHO + #.5 MECO3 + #.5 MGLY + #.5 XC + SumRCO3	2.30E-12
3HF2ONM4_P2 + HO2 = #.9 ROOH + #.05 MGLY + #.05 BACL + #.15 XC	1.78E-11
3HF2ONM4_P2 + SumRO2 = SumRO2 + #.375 MGLY + #.25 R2CO3 + #.25 HCHO + #.25 KET2 + #.25 MECO3 + #.125 BACL + #.375 XC + #.5 SumRCO3	1.39E-12
3HF2ONM4_P2 + SumRCO3 = SumRCO3 + #.5 MGLY + #.4 R2CO3 + #.4 HCHO + #.4 MECO3 + #.1 BACL + #.7 XC + #.8 SumRCO3	1.37E-11
3HF2ONM4_P3 + NO = #1.876 NO2 + #.938 KET2 + #.062 RCNO3 + #-0.876 XC + #.062 XN	9.13E-12
3HF2ONM4_P3 + NO3 = #2 NO2 + KET2 + #-1 XC	2.30E-12
3HF2ONM4_P3 + HO2 = RCNO3 + XC	1.78E-11
3HF2ONM4_P3 + SumRO2 = SumRO2 + #.5 KET2 + #.5 NO2 + #.5 RCNO3	2.57E-12
3HF2ONM4_P3 + SumRCO3 = SumRCO3 + #.8 KET2 + #.8 NO2 + #.2 RCNO3 + #-0.6 XC	1.37E-11

[a] Reactions are given in the format used by the SAPRC modeling program (Carter, 2020), model species for stable reactants and products are described in Table B2. Species with suffix "_P" and "_R" are lumped peroxy intermediates.

[b] Rate constants are for 298K and are in units of cm^3 $molec^{-1}$ s^{-1} if bimolecular and sec^{-1} if unimolecular. If this is a photolysis reaction, the overall quantum yield (assumed to be wavelength-independent) is shown. The absorption cross sections sued for all photolysis reactions listed here are in the photolysis set AFGS.

Table B6: Listing of reactions of the furans and their explicitly represented products for implementation with the SAPRC-07/-11 mechanisms.

Reaction [a]	k(298) [b]
Furan	
FURAN + OH = #.309 RO2C + #.008 RO2XC + #.76 BUTEDIAL + #.76 HO2 + #.232 xHO2 + #.156 xHFONS + #.075 xRCHO + #.293 yROOH + #.008 zRNO3 + #.024 yHFONS	3.97E-11
FURAN + NO3 = #1.288 RO2C + #.034 RO2XC + #.653 xHO2 + #.313 xNO2 + #.653 xHFONS + #.313 xRCHO + #.322 yROOH + #.026 zRNO3 + #.008 zRNO7 + #.1 yHFONS + #.9 yRNO3	1.36E-12
FURAN + O3 = RCHO	2.41E-18
2-Methylfuran	
2M-FURAN + OH = #.612 RO2C + #.04 RO2XC + #.44 4OX2PEAL + #.44 HO2 + #.346 xHO2 + #.432 xHFONS + #.087 xRCHO + #.173 xMEO2 + #.623 yROOH + #.04 zRNO3 + #.03 yHFONS	7.31E-11
2M-FURAN + NO3 = #1.094 RO2C + #.072 RO2XC + #.463 xHO2 + #.147 xNO2 + #.009 xOH + #.772 xHFONS + #.147 xRCHO + #.308 xMEO2 + #.176 yROOH + #.062 zRNO3 + #.002 zRNO4 + #.008 zRNO5 + #.054 yHFONS + #.946 yRNO3	2.57E-11
2M-FURAN + O3 = #.192 RO2C + #.013 RO2XC + #.613 OH + #.14 CO2 + #.052 xHO2 + #.14 xOH + #.591 RCHO + #.204 OLE2 + #.052 xCO + #.192 xMACR + #.134 yROOH + #.013 zRNO3 + #.015 yBACL	2.00E-17
3-Methylfuran	
3M-FURAN + OH = #.695 RO2C + #.046 RO2XC + #.27 2MBUTDAL + #.27 HO2 + #.684 xHO2 + #.675 xHFONS + #.01 xRCHO + #.667 yROOH + #.046 zRNO3 + #.073 yHFONS	8.73E-11
3M-FURAN + NO3 = #.951 RO2C + #.063 RO2XC + #.924 xHO2 + #.013 xNO2 + #.81 xHFONS + #.013 xRCHO + #.128 yROOH + #.062 zRNO3 + #.001 zRNO6 + #.1 yHFONS + #.9 yRNO3	1.26E-11
3M-FURAN + O3 = #.409 RCHO + #.591 PROD2	2.05E-17
2,5-Dimethylfuran	
25M-FUR + OH = #.747 RO2C + #.106 RO2XC + #.28 3HXE25DO + #.28 HO2 + #.116 xHO2 + #.498 xHFONS + #.116 xRCHO + #.498 xMEO2 + #.852 yROOH + #.106 zRNO3	1.26E-10
25M-FUR + NO3 = #1.037 RO2C + #.147 RO2XC + #.121 xNO2 + #.04 xOH + #.692 xHFONS + #.121 xRCHO + #.692 xMEO2 + #.224 yROOH + #.147 zRNO3 + yRNO3	5.80E-11
25M-FUR + O3 = #.438 RO2C + #.062 RO2XC + #1.5 OH + #.319 CO2 + #.119 xHO2 + #.319 xOH + #.5 OLE2 + #.119 xCO + #.438 xMACR + #.328 yROOH + #.062 zRNO3 + #.037 yBACL	4.19E-16
2-Butene-1,4-dial (formed from furan)	
BUTEDIAL + HV = #.59 OH + #.59 HO2 + #.41 HFONS + #.59 ALK3	qy=2.88E-1

Reaction [a]	k(298) [b]
BUTEDIAL + OH = #.045 RO2C + #.001 RO2XC + #.954 OH + #.045 xHO2 + #.758 ALK3 + #.195 ROOH + #.004 xCO + #.041 xGLY + #.041 xMGLY + #.004 xROOH + #.001 zRNO3	4.22E-11
BUTEDIAL + NO3 = #.008 RO2C + #.991 OH + #.008 xHO2 + #.955 HNO3 + #.955 ALK3 + #.037 RNO3 + #.008 xCO + #.008 xRNO3	2.07E-15
BUTEDIAL + O3 = #.667 HO2 + #.606 CO2 + #.273 HCHO + #.334 CO + GLY + #.394 RCOOH	1.60E-18
4-Oxo-2-penteneal (formed from 2-methylfuran)	
4OX2PEAL + HV = #.699 OH + #.699 ALK3 + #.699 MEO2	qy=3.42E-1
4OX2PEAL + OH = #.585 RO2C + #.038 RO2XC + #.253 CO2 + #.144 xHO2 + #.253 xOH + #.377 MACO3 + #.009 xCO + #.09 xGLY + #.19 xMGLY + #.262 xRCHO + #.178 xROOH + #.178 xMECO3 + #.467 yROOH + #.038 zRNO3 + #.052 yBACL	5.65E-11
4OX2PEAL + NO3 = #.064 RO2C + #.005 RO2XC + #.009 CO2 + #.009 xOH + #.931 HNO3 + #.931 MACO3 + #.064 xRNO3 + #.055 xMECO3 + #.004 zRNO3 + #.068 yRNO3	9.99E-15
4OX2PEAL + O3 = #.129 RO2C + #.129 OH + #.495 HO2 + #.45 CO2 + #.129 xHO2 + #.202 HCHO + #.377 CO + #.258 GLY + #.742 MGLY + #.421 RCOOH + #.129 xMGLY + #.116 yROOH + #.013 yMGLY	4.80E-18
4OX2PEAL + HV = #.699 OH + #.699 ALK3 + #.699 MEO2	qy=0.342
2-Methyl-2-butene-1,4-dial (formed from 3-methylfuran)	
2MBUTDAL + HV = #.656 RO2C + #.043 RO2XC + #.699 HO2 + #.328 xHO2 + #.328 xAFG3 + #.328 xMACO3 + #.629 yROOH + #.043 zHFONS + #.035 yAFG3 + #.035 yBACL	4.14E-11
2MBUTDAL + OH = #.055 RO2C + #.004 RO2XC + #.941 OH + #.055 xHO2 + #.25 ROOH + #.691 AFG3 + #.007 xCO + #.01 xGLY + #.078 xMGLY + #.01 xBACL + #.007 xROOH + #.004 zRNO3	3.13E-15
2MBUTDAL + NO3 = #.106 RO2C + #.007 RO2XC + #.887 OH + #.106 xHO2 + #.408 HNO3 + #.478 RNO3 + #.408 AFG3 + #.106 xCO + #.106 xRNO3 + #.007 zRNO3	4.80E-18
3-Hexene-2,5-dione (formed from 2,5-dimethylfuran)	
3HXE25DO + OH = #.93 RO2C + #.07 RO2XC + #.186 xHO2 + #.372 xMGLY + #.743 xRCHO + #.743 xMECO3 + #.9 yROOH + #.07 zRNO3 + #.1 yBACL	4.69E-11
3HXE25DO + NO3 = #.846 RO2C + #.154 RO2XC + #.076 HNO3 + #.065 xHCHO + #.782 xRNO3 + #.782 xMECO3 + #.065 xMACO3 + #.069 yROOH + #.154 zRNO3 + #.008 yAFG3 + #.924 yRNO3	1.80E-18
3HXE25DO + O3 = #.5 RO2C + #.5 OH + #.5 xHO2 + #.5 CO + MGLY + #.5 RCOOH + #.5 xMGLY + #.45 yROOH + #.05 yMGLY	1.64E-14
Lumped furanones and hydroxyfuranones	
HFONS + OH = #.909 RO2C + #.024 RO2XC + #.067 HO2 + #.903 xHO2 + #.067 ALK3 + #.645 xMGLY + #.258 xRCHO + #.006 xRCO3 + #.872 yROOH + #.024 zRNO3 + #.061 yBACL	3.83E-11

Reaction [a]	k(298) [b]
HFONS + NO3 = #.842 RO2C + #.022 RO2XC + #.136 HO2 + #.421 xHO2 + #.421 xNO2 + #.136 HNO3 + #.136 ALK3 + #.085 xMGLY + #.336 xRCHO + #.421 xRNO3 + #.022 zRNO3 + #.864 yRNO3	4.08E-15
HFONS + O3 = RCOOH	5.07E-17
SAPRC-07 or SAPRC-11 peroxy radical operator species [c]	
Operators representing formation of compounds after peroxy + NO --> NO2 reactions (Prod=3HXE25DO, 4OX2PEAL, HFONS, ROOH, NO3)	
x(Prod) = (Prod)	RO2RO
x(Prod) =	RO2XRO
Operators representing formation of compounds after peroxy + HO2 reactions (Prod) = HFONS, MALAH, MGLY, BACL, RNO3, AFG3	
y(Prod) =	RO2RO
y(Prod) = (Prod)	RO2HO2
y(Prod) = PROD2	RO2RO2M
Operator representing the formation of organic nitrate after peroxy + NO reactions	
zHFONS = HFONS + #-1 XN	RO2NO
zHFONS = PROD2 + HO2	RO222NN
zHFONS =	RO2XRO

[a] Reactions are given in the format used by the SAPRC modeling programs (Carter, 2020), model species for stable reactants and products are described on Table B2.

[b] Rate constants are for 298K and are in units of cm^{3} molec^{-1} s^{-1} if bimolecular and sec^{-1} if unimolecular. If this is a photolysis reaction, the overall quantum yield (assumed to be wavelength-independent) is shown. The absorption cross sections sued for all photolysis reactions listed here are in the photolysis set AFGS.

[c] See the SAPRC-07 documentation for a discussion of the treatment of peroxy radical reactions and operators.(Carter, 2009) The rate constants for these "reactions" are calculated from the coefficients given in the rate constant column, which are calculated from total rates of various peroxy radical reactions, whose total concentrations are the sum of the operators RO2R and RO2XC. These coefficients are calculated as follows:

RO2NO = k(RO2+NO)[NO]
RO22NN = k(RO2+NO3)[NO3] + 0.5 k(RO2+MEO2)[MEO2] + 0.5 k(RO2+RO2){[RO2C]+ [RO2XC])
RO2XRO = k(RO2+HO2)[HO2] + k(RO2+MECO3){[MECO3]+[RCO3]+[BZCO3]+ [MACO3]) + 0.5 k(RO2+MEO2)[MEO2] + 0.5 k(RO2+RO2){[RO2C]+ [RO2XC])
RO2HO2 = k(RO2+HO2)[HO2]; RO2RO2M = k(RO2+MECO3){[MECO3]+[RCO3]+[BZCO3]+ [MACO3]) + 0.5 k(RO2+MEO2)[MEO2] + 0.5 k(RO2+RO2){[RO2C]+ [RO2XC])
RO2RO = k(RO2+NO)[NO] + k(RO2+NO3)[NO3] + 0.5 k(RO2+MEO2)[MEO2] + 0.5 k(RO2+RO2) {[RO2C]+[RO2XC])

B.2 Additional Mechanism Schematics

(a) Furan

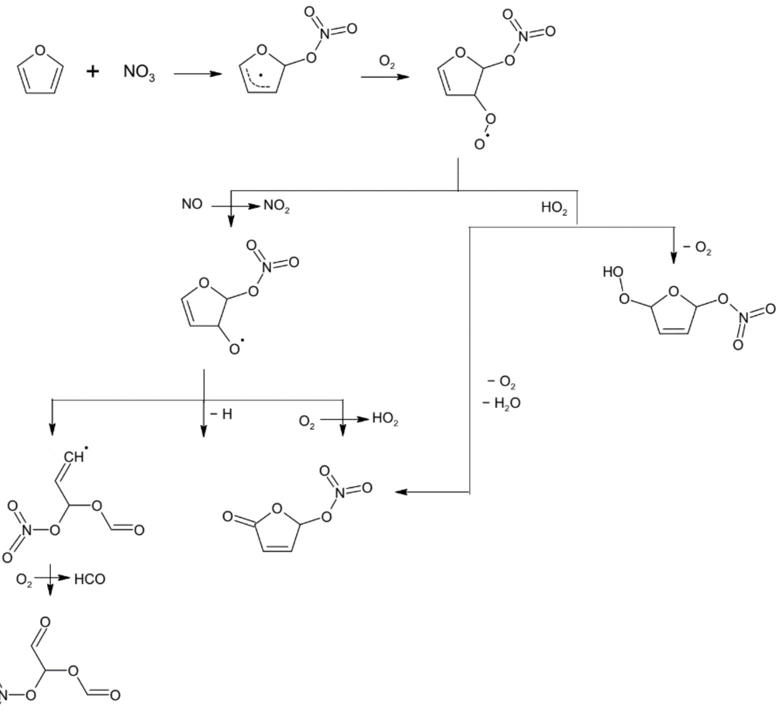

Figure B1: Schematic of the NO_3-initiated oxidation of furans in the detailed furans mechanism at 298K and atmospheric pressure in the presence of NO_x. For figure clarity, only the major reaction pathways of furans peroxy radicals are shown in this figure.

(b) 2-MF

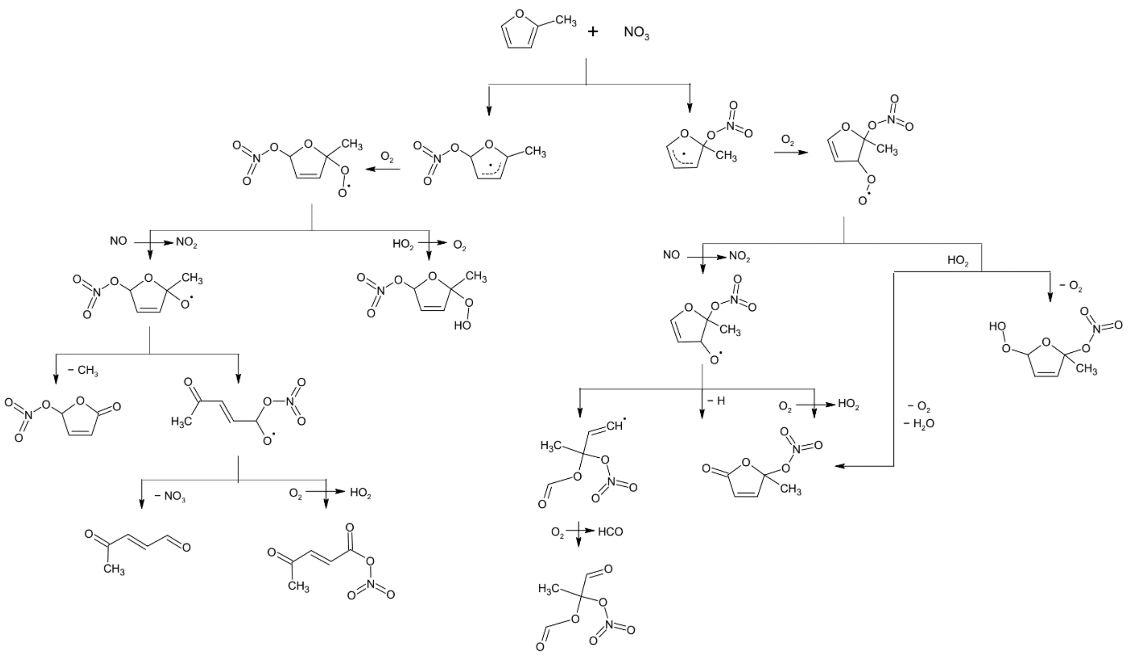

Figure B1 (continued): Schematic of the NO_3-initiated oxidation of furans in the detailed furans mechanism at 298K and atmospheric pressure in the presence of NO_x. For figure clarity, only the major reaction pathways of furans peroxy radicals are shown in this figure.

(c) 3-MF

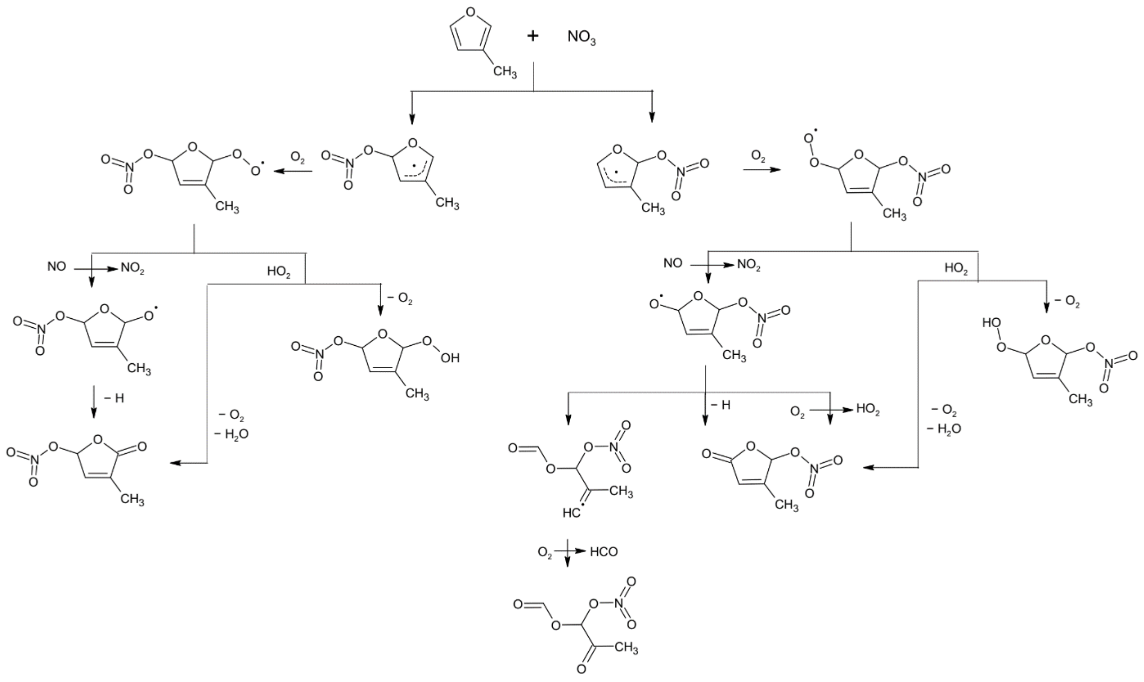

Figure B1 (continued): Schematic of the NO3-initiated oxidation of furans in the detailed furans mechanism at 298K and atmospheric pressure in the presence of NOx. For figure clarity, only the major reaction pathways of furans peroxy radicals are shown in this figure.

(d) 2,5-MF

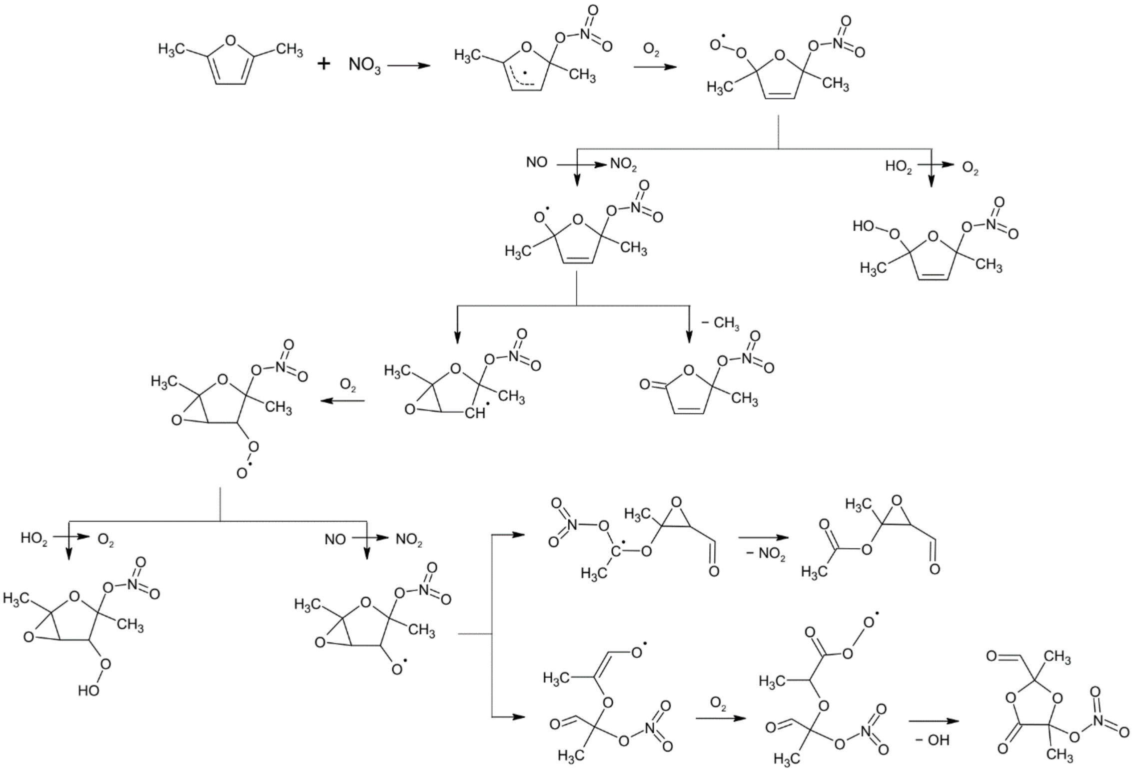

Figure B1 (continued): Schematic of the NO3-initiated oxidation of furans in the detailed furans mechanism at 298K and atmospheric pressure in the presence of NOx. For figure clarity, only the major reaction pathways of furans peroxy radicals are shown in this figure.

(a) 2-MF

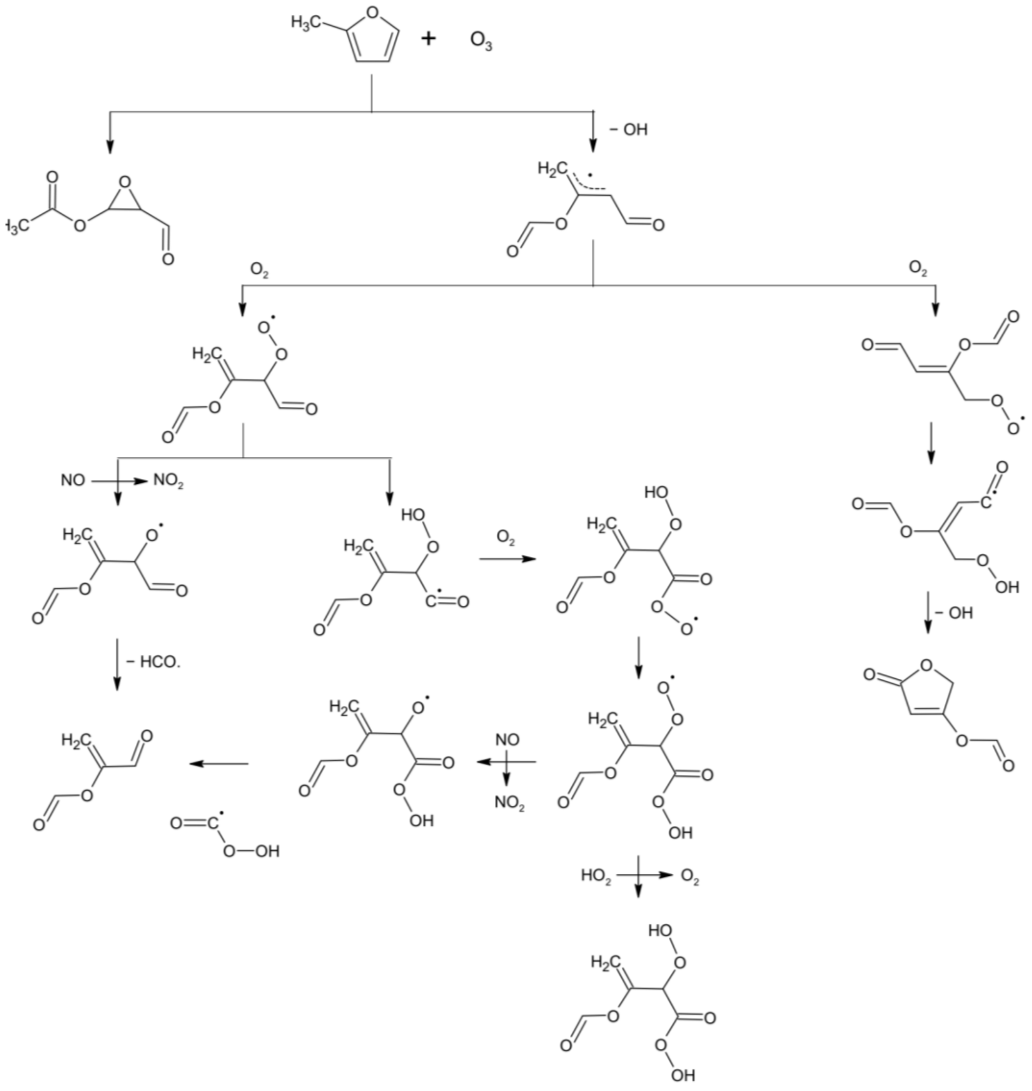

Figure B2: Schematic of the O$_3$-initiated oxidation of furans in the detailed furans mechanism at 298K and atmospheric pressure in the presence of NO$_x$. For figure clarity, only the major reaction pathways of furans peroxy radicals are shown in this figure.

(b) 2,5-DMF

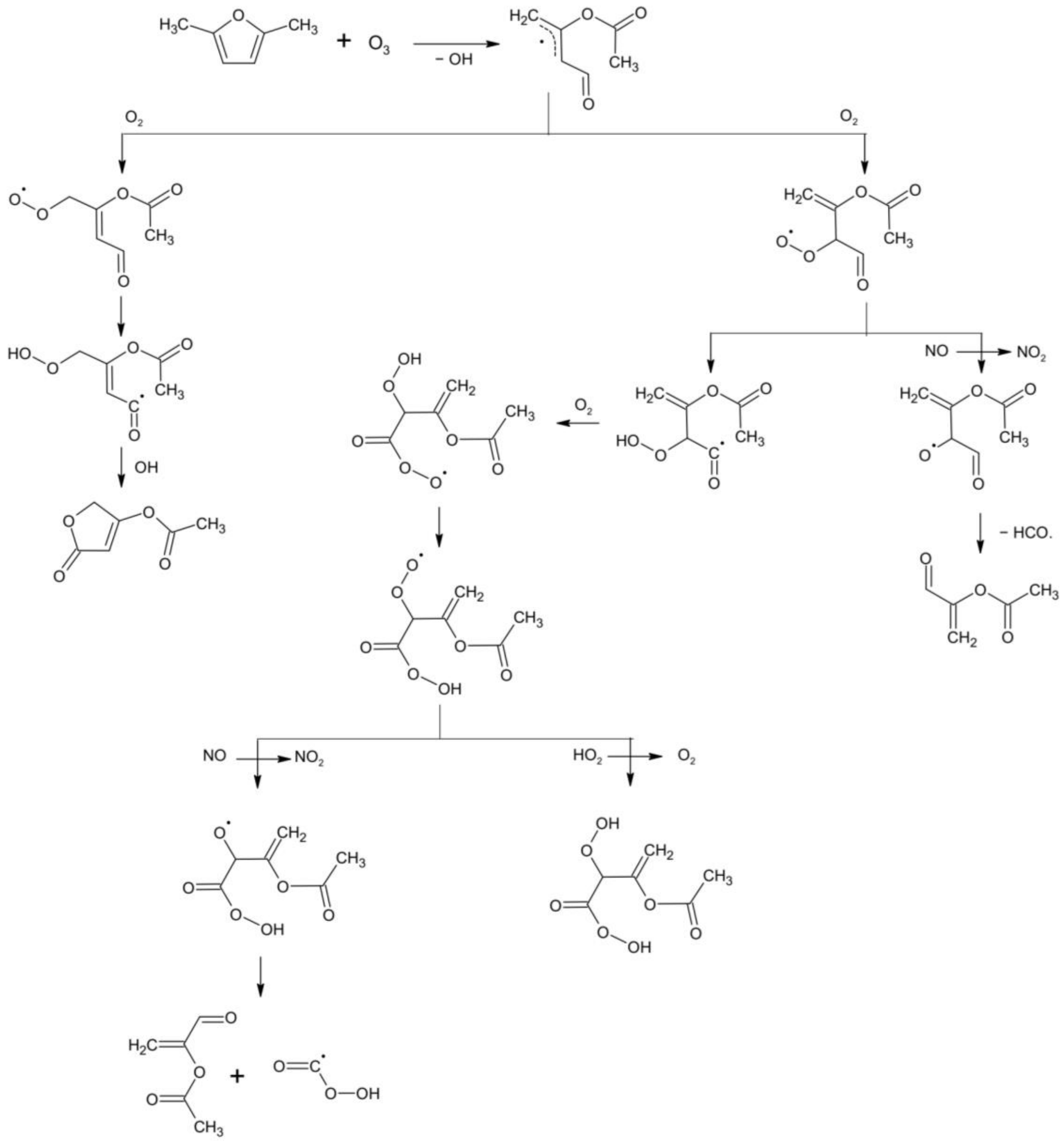

Figure B2 (continued): Schematic of the O_3-initiated oxidation of furans in the detailed furans mechanism at 298K and atmospheric pressure in the presence of NO_x. For figure clarity, only the major reaction pathways of furans peroxy radicals are shown in this figure.

B.3 Additional Results

Table B7: Fractions of furans react with different oxidants in each experiment, and fractions of total peroxy radical reactions of each type, calculated based on "Standard_S18Base" simulation results.

Group	Run ID	Fraction of Furan Reaction			Fraction of RO_2 Reaction [a]			
		OH	NO_3	O_3	NO	HO_2	NO_3	RO_2s
Furan-1	ITC711	84%	15%	1%	99%	0.7%	0.1%	-
	ITC713	92%	7%	1%	>99%	-	-	-
	ITC715	90%	8%	1%	>99%	-	-	-
	ITC743	85%	14%	1%	>99%	0.2%	-	-
Furan-2	EPA355A	99%	0%	0%	>99%	-	-	-
	EPA355B	99%	1%	0%	98%	1.7%	-	0.2%
	EPA371A	100%	0%	0%	>99%	-	-	-
	EPA371B	98%	2%	0%	99%	1.3%	-	-
Furan-3	EPA1402A	78%	10%	12%	50%	49%	0.4%	0.1%
	EPA1403A	69%	22%	9%	56%	43%	-	0.3%
	EPA1403B	68%	22%	9%	56%	44%	-	0.3%
	EPA1448A	78%	10%	12%	54%	46%	-	1.0%
2-MF	EPA356A	88%	10%	2%	>99%	0.1%	-	-
	EPA356B	87%	10%	3%	94%	5%	-	0.6%
	EPA996A	84%	13%	3%	97%	3%	-	0.2%
	EPA996B	84%	13%	3%	97%	3%	-	0.2%
	EPA999A	60%	4%	36%	51%	44%	-	5%
	EPA999B	64%	7%	29%	62%	33%	-	5%
3-MF	EPA358A	87%	10%	3%	>99%	0.1%	-	-
	EPA358B	83%	12%	5%	88%	10%	-	1.2%
	EPA359A	87%	11%	2%	>99%	-	-	-
	EPA359B	84%	12%	4%	94%	5%	-	0.4%
	EPA418A	90%	8%	2%	>99%	-	-	-
	EPA418B	89%	9%	3%	94%	5%	-	0.6%
2,5-DMF	EPA357A	86%	5%	9%	>99%	0.1%	-	-
	EPA357B	79%	5%	16%	86%	12%	-	1.8%

[a] Ratios of integrated reaction rates for the reaction of the total peroxy radical species, SumRO2, with the indicated reactant, divided by the total integrated reaction rates at the end of the experiment. "RO_2s" refers to the sum of reactions of SumRO2 with SumRO2 and with SumRCO3.

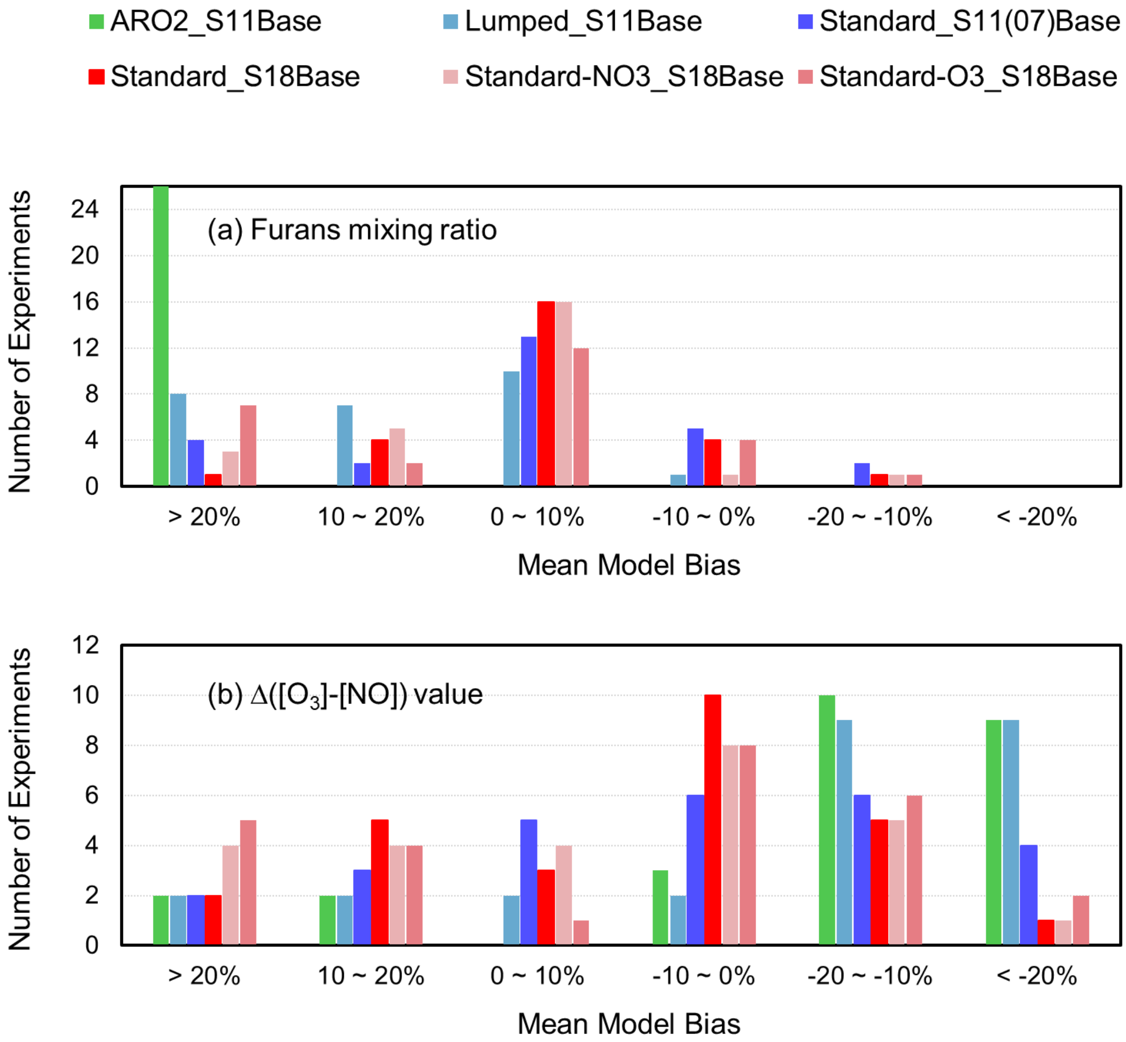

Figure B3: Classification of mean normalized bias by the number of experiments for a) furans mixing ratios; b) Δ([O3]-[NO]) during the experiment using mechanisms listed in Table 2.5.

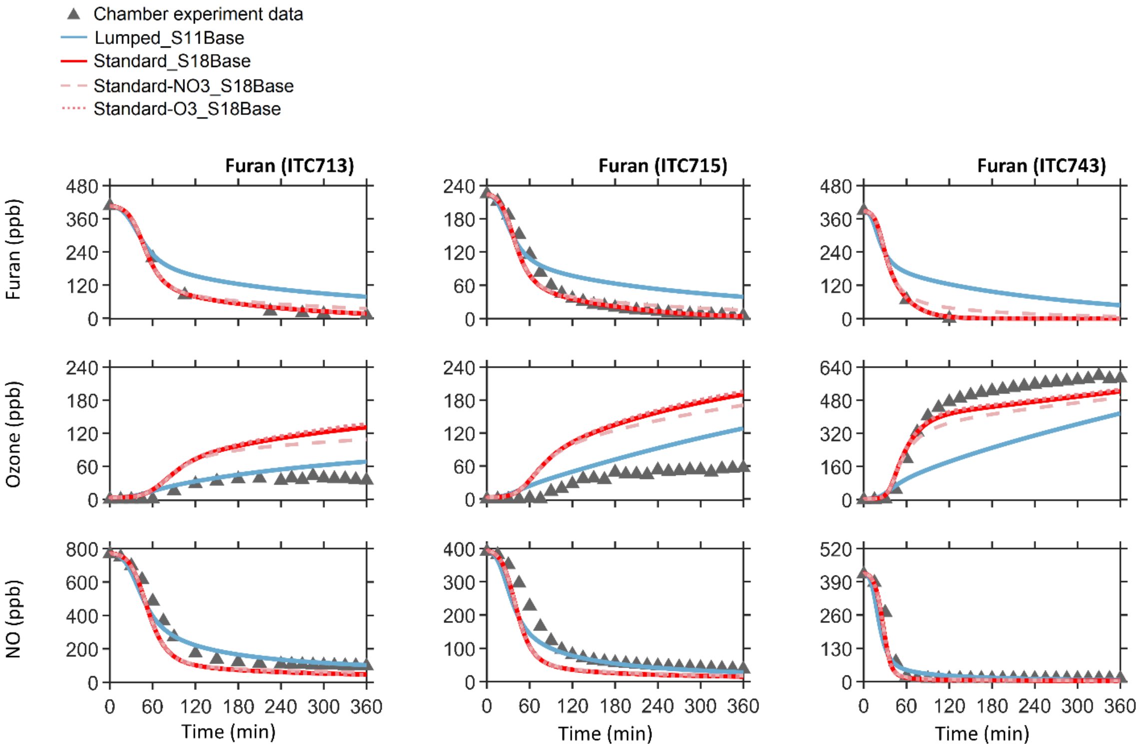

Figure B4: Comparison of chamber data (triangles) and model simulation results (lines) for the photooxidation of furan in the presence of NO_x ("Furan-1" group).

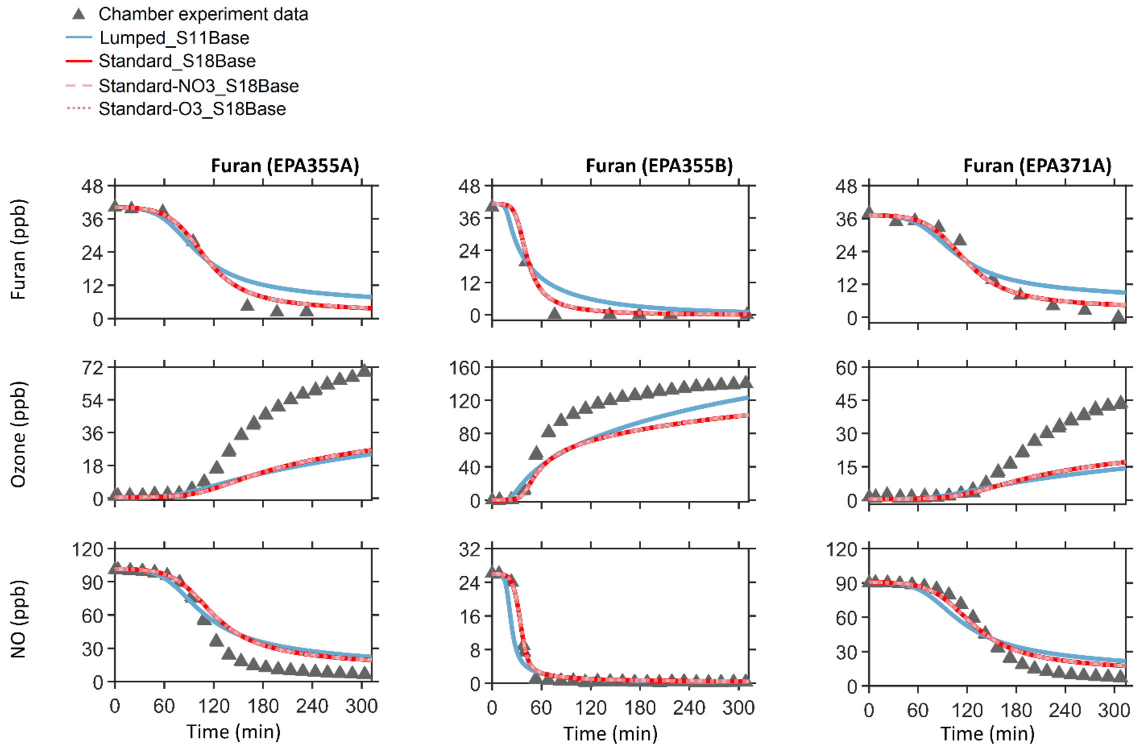

Figure B5: Comparison of chamber data (triangles) and model simulation results (lines) for the photooxidation of furan in the presence of NO_x (“Furan-2” group).

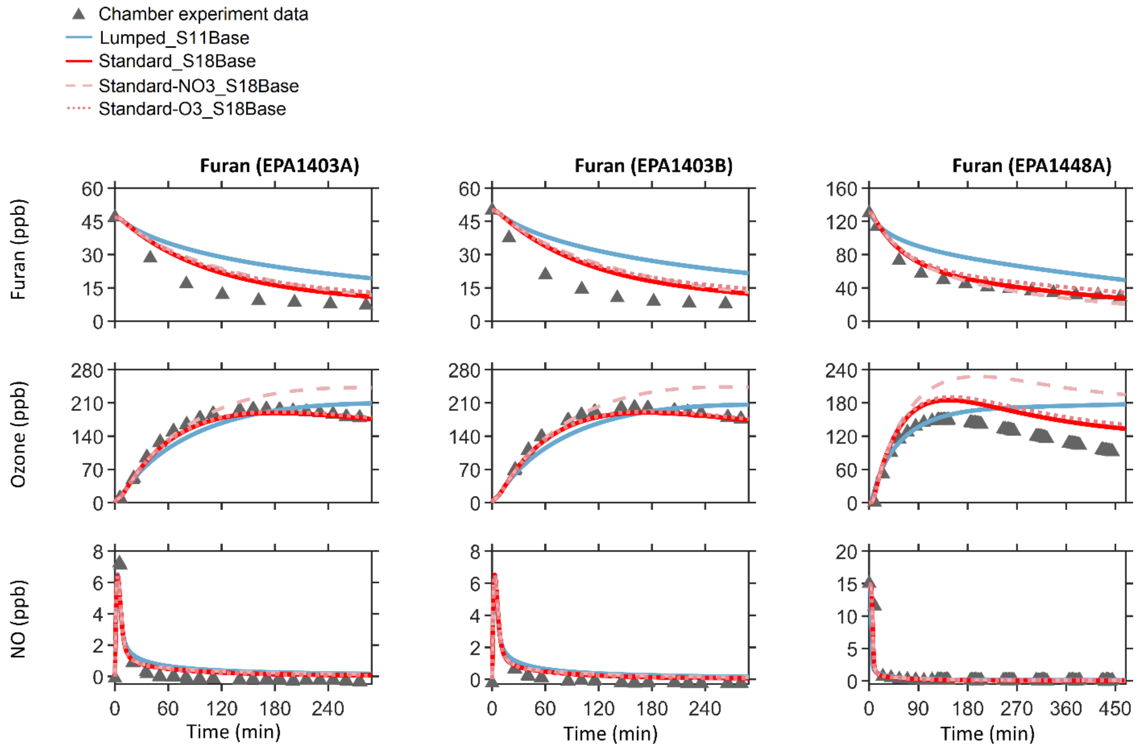

Figure B6: Comparison of chamber data (triangles) and model simulation results (lines) for the photooxidation of furan in the presence of NO_x (“Furan-3” group).

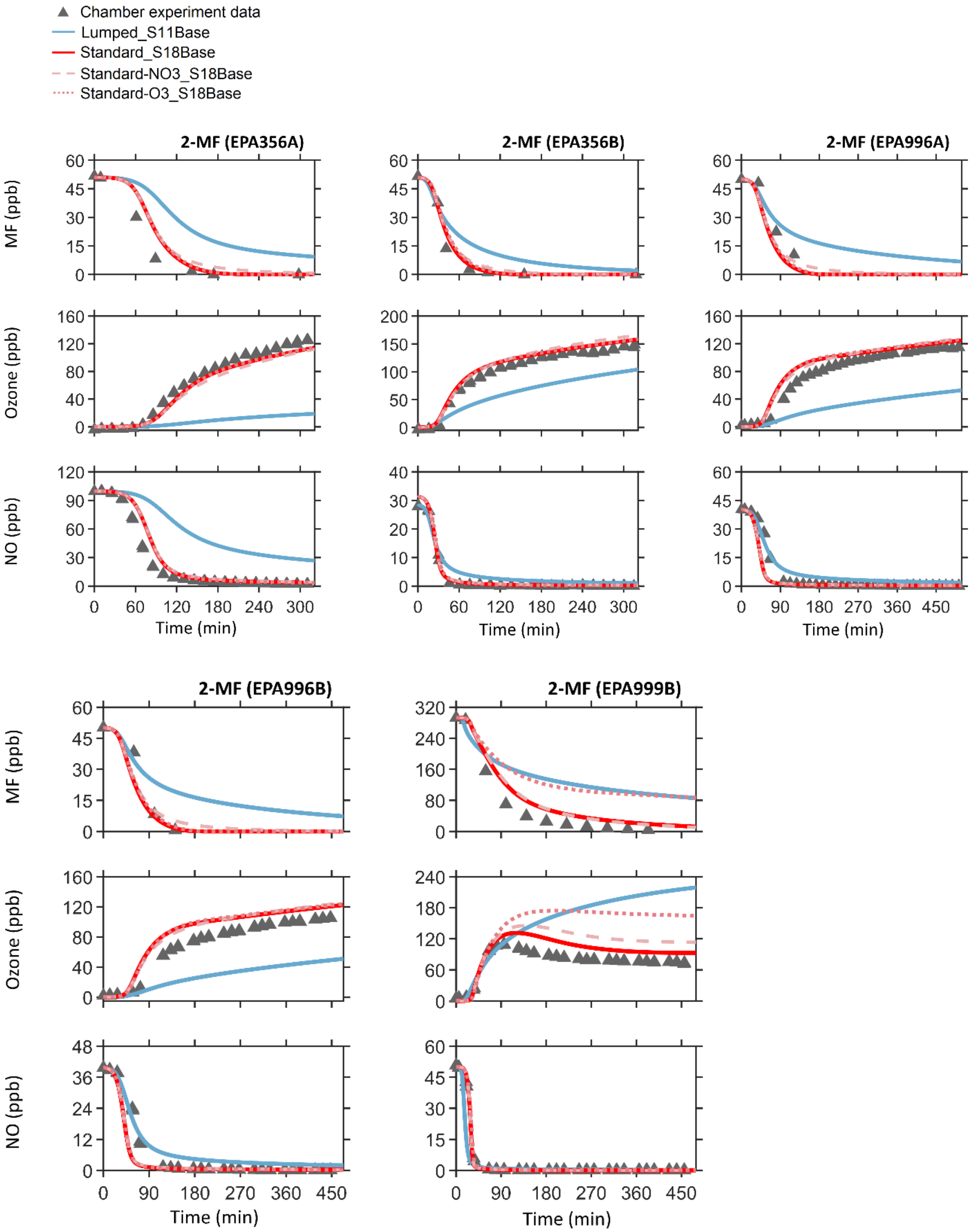

Figure B7: Comparison of chamber data (triangles) and model simulation results (lines) for the photooxidation of 2-methylfuran in the presence of NO_x ("2-MF" group).

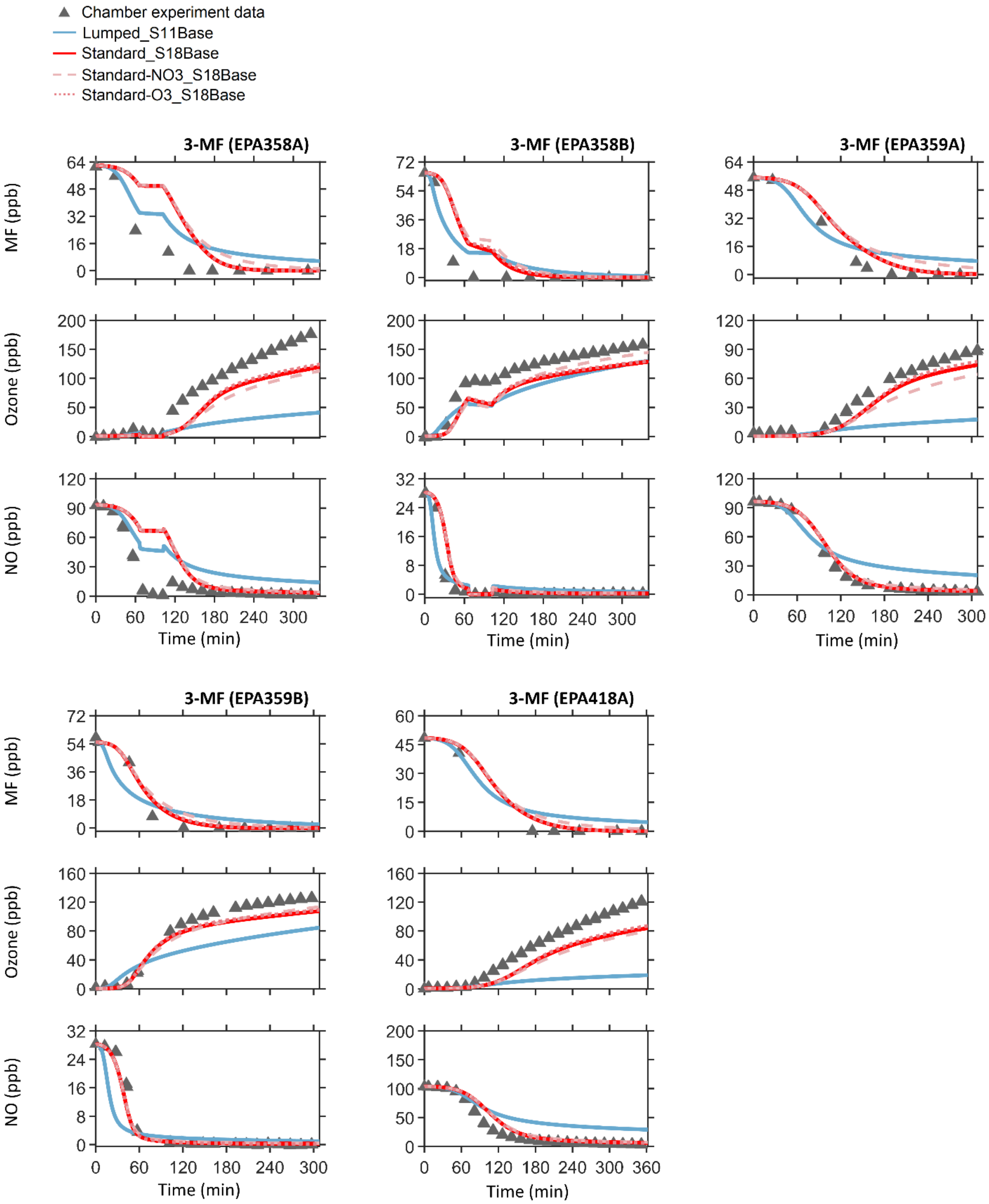

Figure B8: Comparison of chamber data (triangles) and model simulation results (lines) for the photooxidation of 3-methylfuran in the presence of NO_x ("3-MF" group).

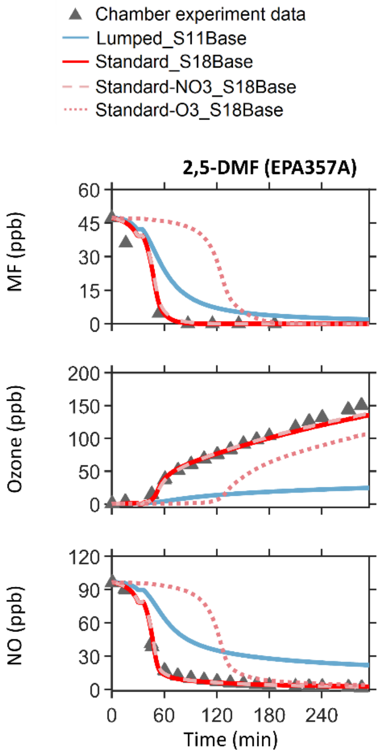

Figure B9: Comparison of chamber data (triangles) and model simulation results (lines) for the photooxidation of 2,5-dimethylfuran in the presence of NO_x ("2,5-DMF" group).

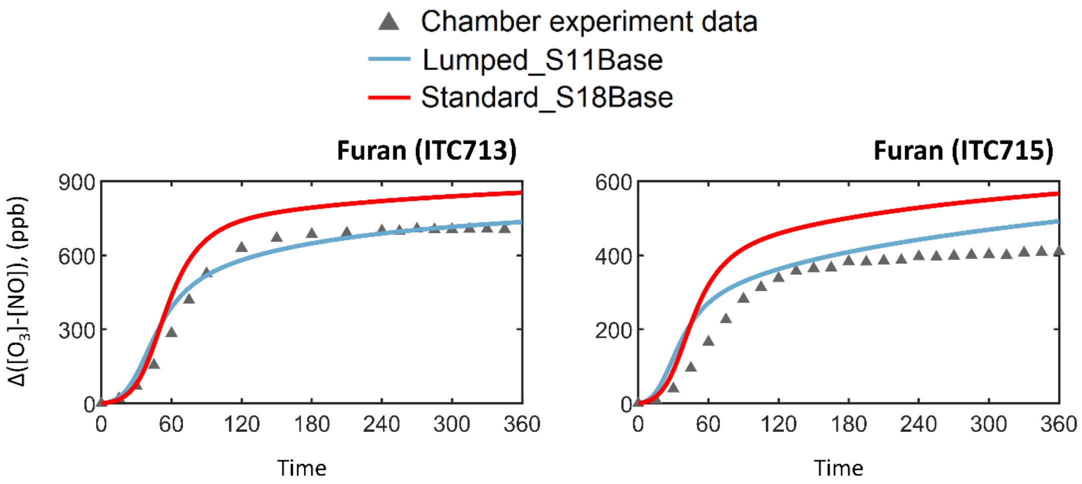

Figure B10: Comparison of model simulations of furan experiments between "Lumped_S11Base" and "Standard_S18Base" for Δ([O3]-[NO]).

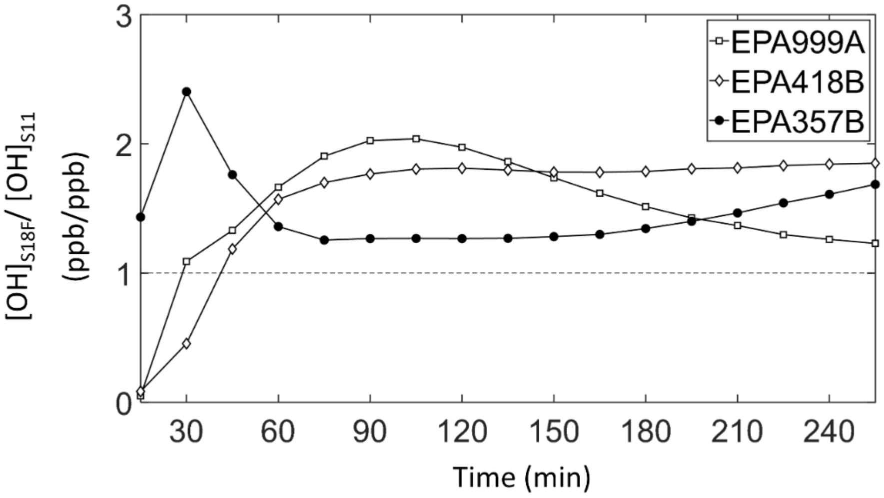

Figure B11: The ratio of simulated OH mixing ratios between the detailed furans mechanism ("S18F" short for "Standard_S18Base") and lumped furans mechanism in SAPRC-11 ("S11" short for "Lumped_S11Base") as a function of time (from 15 minutes to 255 minutes, 15-minute intervals).

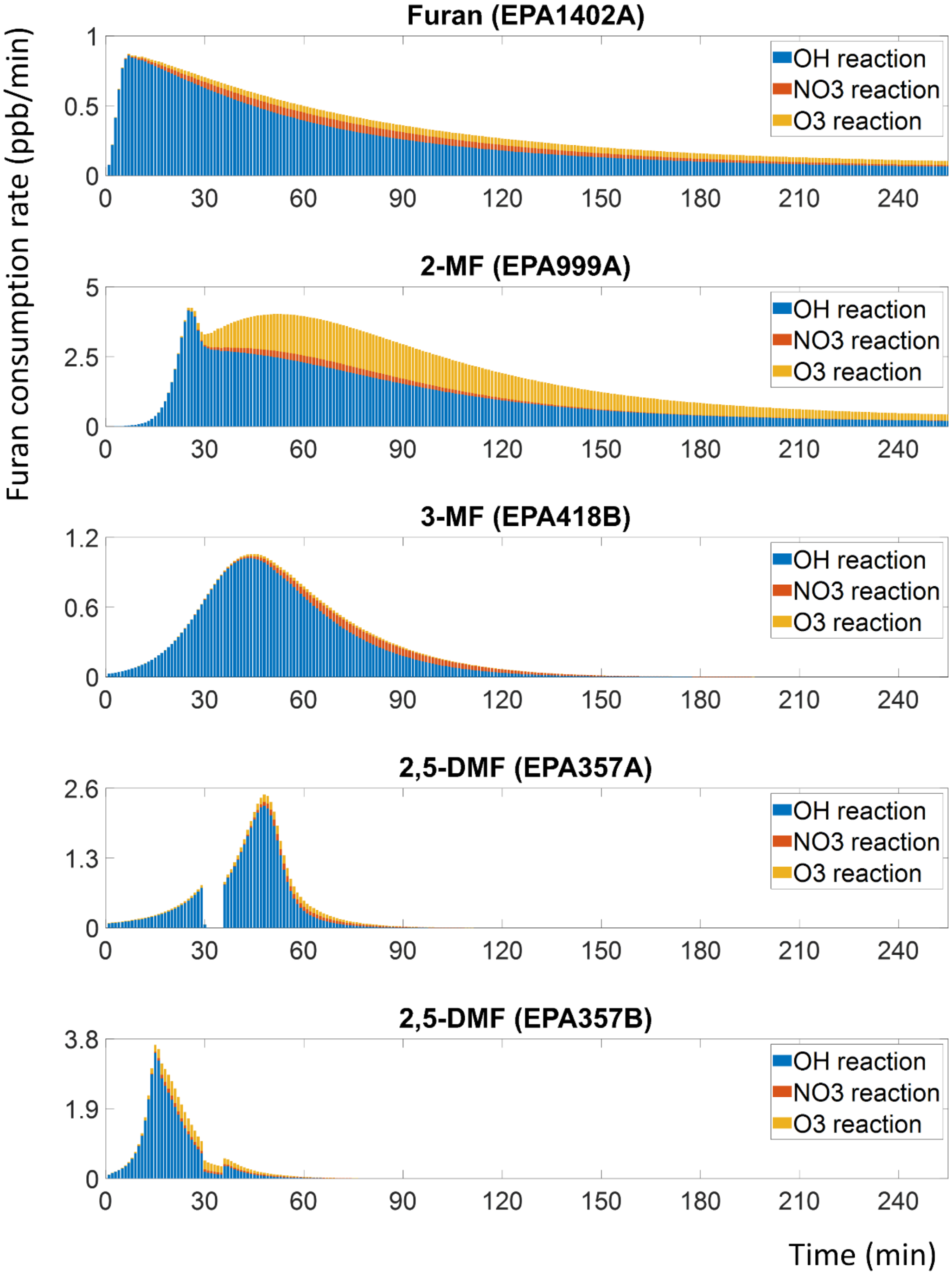

Figure B12: Time dependence for the consumption rate of furans in EPA1402A, EPA999A, EPA418B, EPA357A and EPA357B in "Standard_S18Base" simulations.

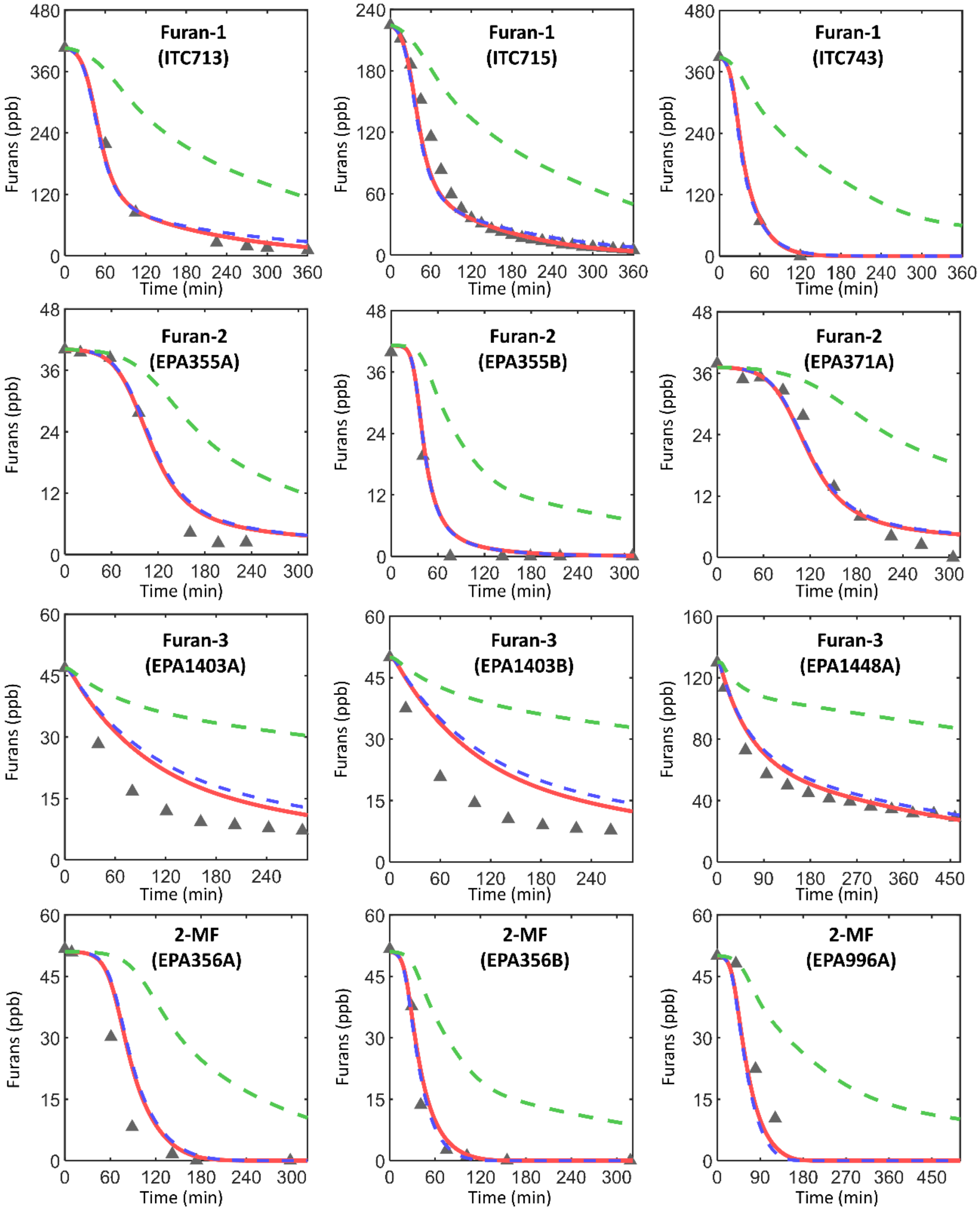

Figure B13: Model simulation comparison of furans mixing ratio for representative furan and methylfuran experiments using the standard mechanisms developed in this work and the mechanism where furans are lumped with higher aromatics.

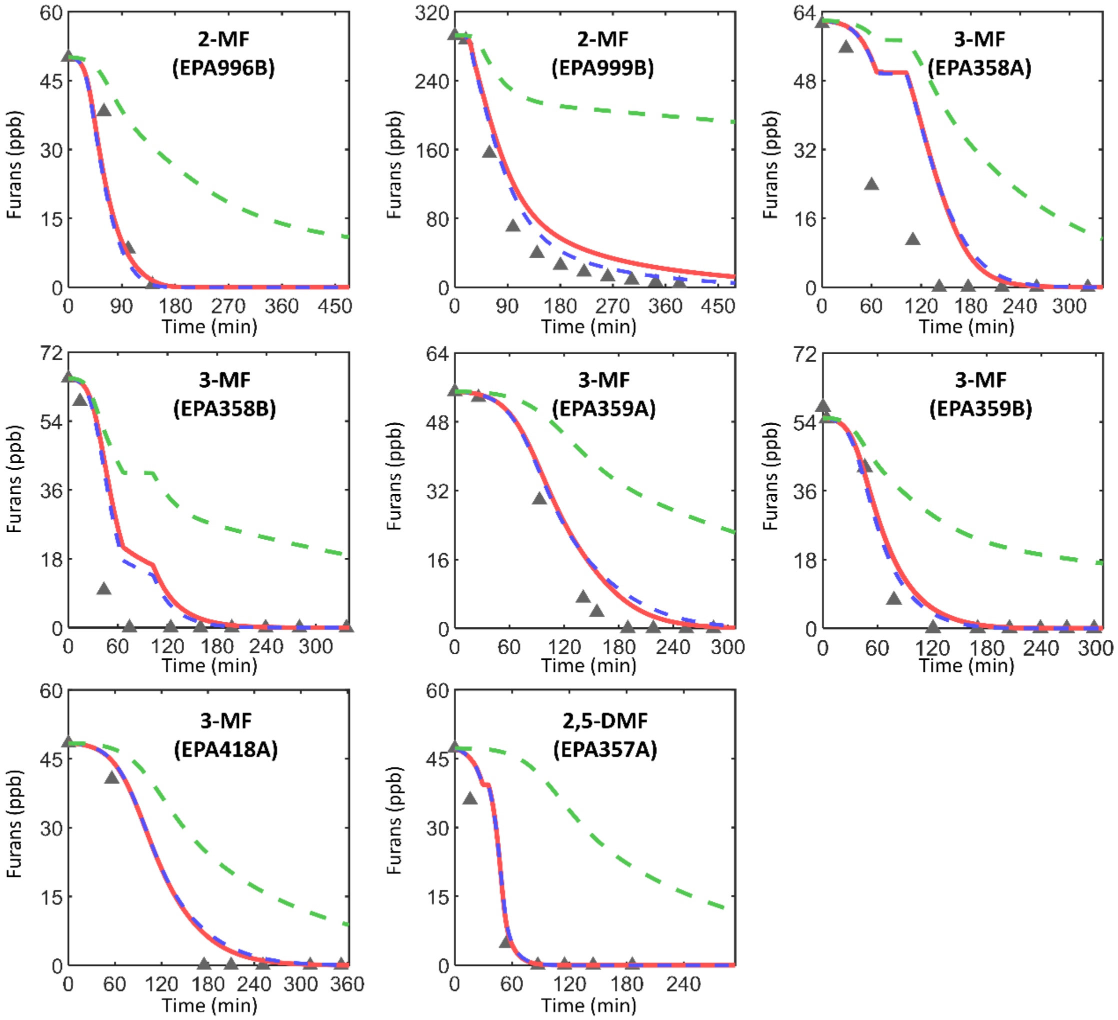

Figure B13 (continued): Model simulation comparison of furans mixing ratio for representative furan and methylfuran experiments using the standard mechanisms developed in this work and the mechanism where furans are lumped with higher aromatics.

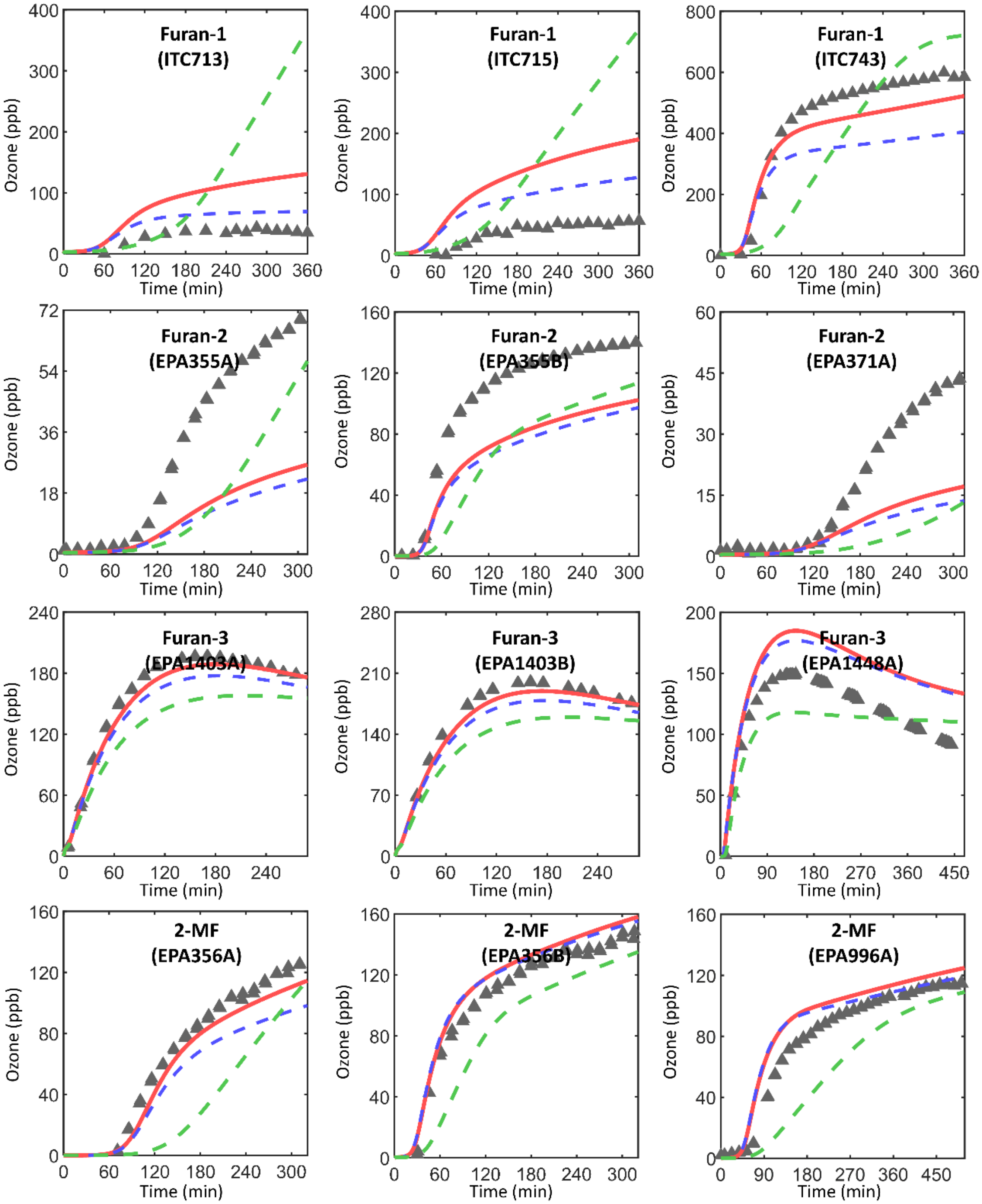

Figure B14: Model simulation comparison of O_3 formation for representative furan and methylfuran experiments using the standard mechanisms developed in this work and the mechanism where furans are lumped with higher aromatics.

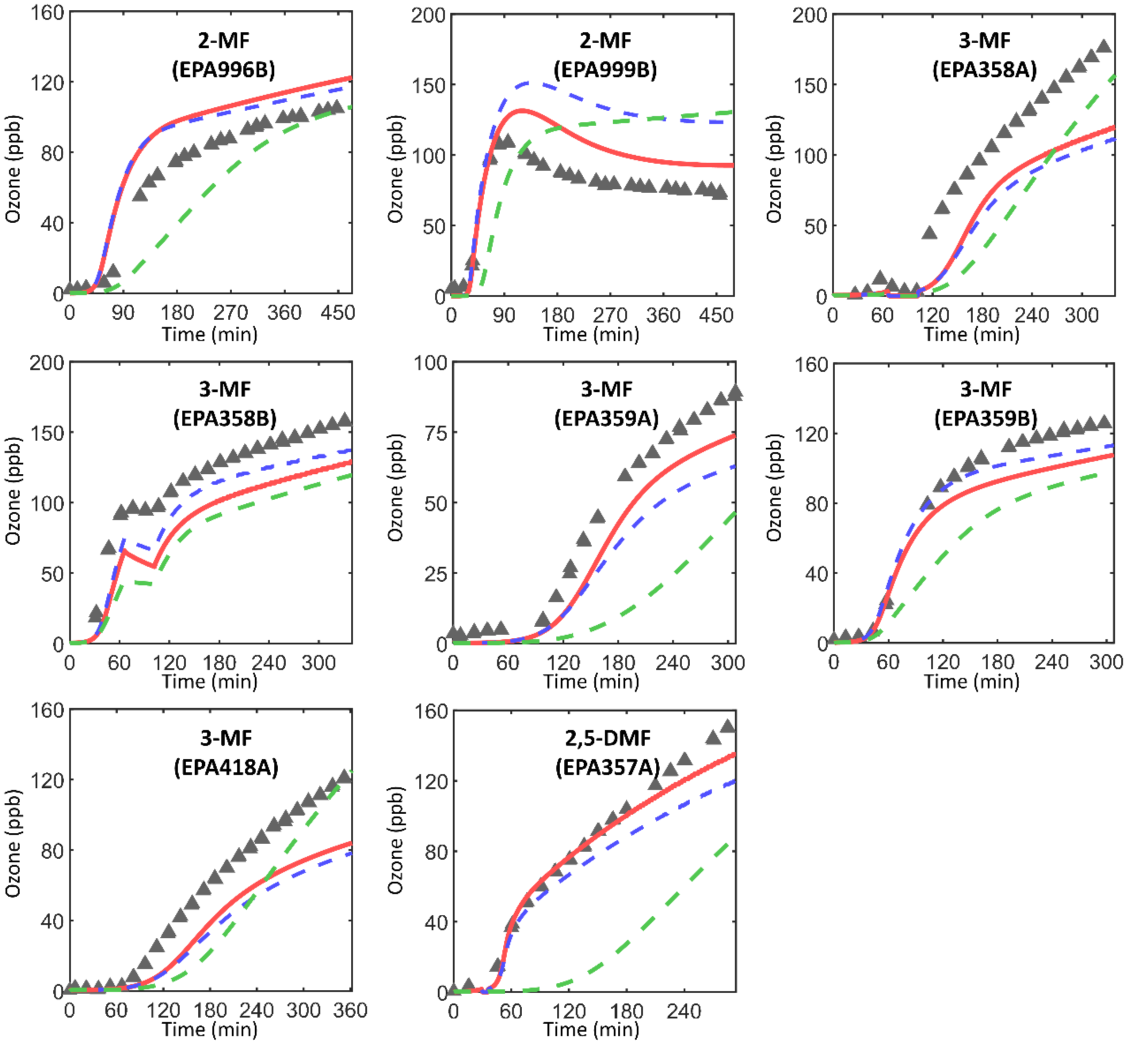

Figure B14 (continued): Model simulation comparison of O3 formation for representative furan and methylfuran experiments using the standard mechanisms developed in this work and the mechanism where furans are lumped with higher aromatics.

B.4 Initiation Reactions in Chamber Experiments

The oxidation reactions in the furan + NO_x experiments are driven by chain reactions involving OH radicals, which react with the furans or their products to form organic radicals that eventually regenerate OH (i.e., radical initiators). The furans and some of their products also react with O_3 and NO_3 radicals, and dicarbonyl aldehyde products photolyze, which can cause radical initiation and enhance OH levels. Although O_3 and NO_3 are not present before the lights are turned on, O_3 is rapidly formed in the photostationary state from the photolysis of NO_2; NO_3 is formed from the reaction of the O_3 with NO_2. Radical formation is also initiated by a chamber radical source that is attributed to the light-induced offgasing and subsequent rapid photolysis of HONO. The OH formed from HONO offgassing is an important radical source in chamber experiments that do not have VOCs that are or form radical initiators. It also plays a role in initiating reactions in some furans experiments used in this study. Model simulations of these experiments suggest that initiation rates are not sensitive to reasonable variations of the magnitude of this OH source. The rates of radical initiation during the first stages (100 minutes) of representative furans experiments are shown in Figure B15, demonstrating the relative importance of dominant initiation reactions as a function of time.

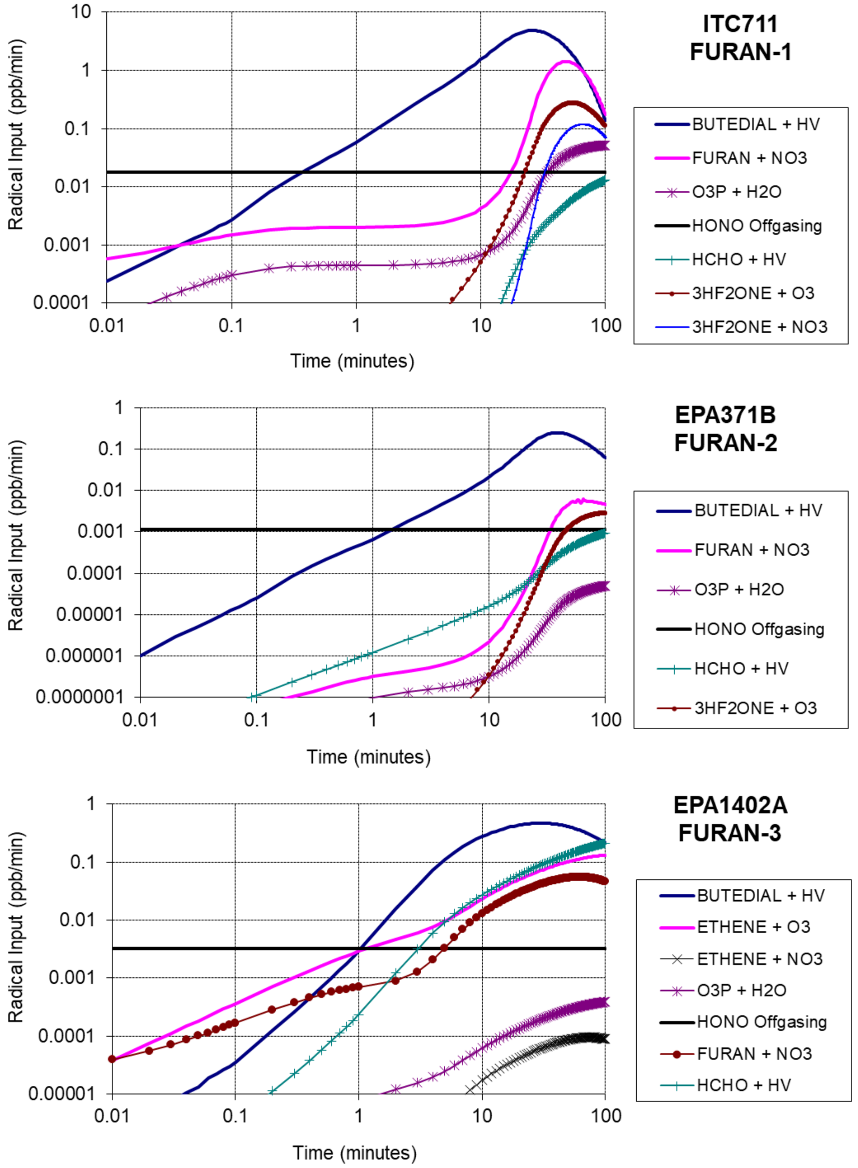

Figure B15: Radical initiation rates for reactions that are important in the first 100 minutes, shown for six representative experiments.

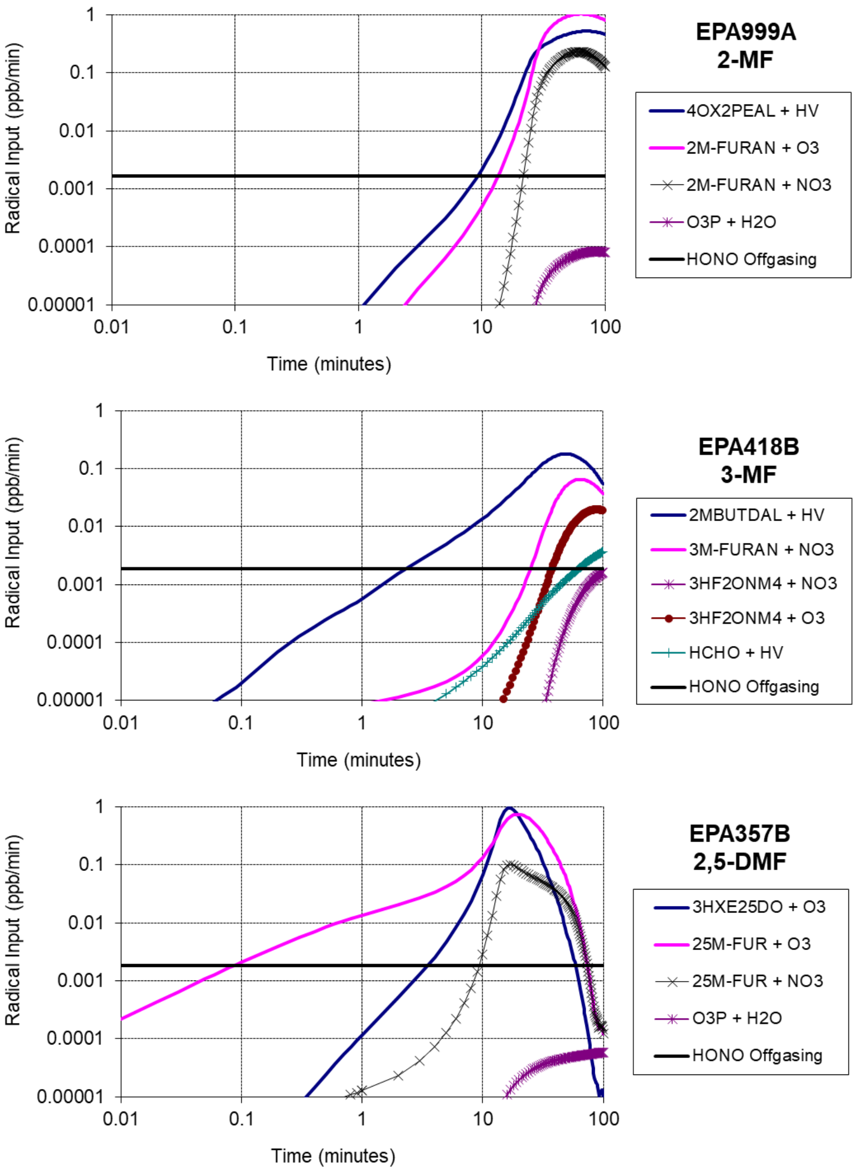

Figure B15 (continued): Radical initiation rates for reactions that are important in the first 100 minutes, shown for six representative experiments.

References

Alvarado, A., Atkinson, R., & Arey, J. (1996). Kinetics of the gas-phase reactions of NO3 radicals and O3 with 3-methylfuran and the OH radical yield from the O3 reaction. *International Journal of Chemical Kinetics*, *28*(12), 905-909. https://doi.org/10.1002/(SICI)1097-4601(1996)28:12<905::AID-KIN7>3.0.CO;2-R

Aschmann, S. M., Nishino, N., Arey, J., & Atkinson, R. (2011). Kinetics of the Reactions of OH Radicals with 2- and 3-Methylfuran, 2,3- and 2,5-Dimethylfuran, and E- and Z-3-Hexene-2,5-dione, and Products of OH + 2,5-Dimethylfuran. *Environmental Science and Technology*, *45*(5), 1859-1865. https://doi.org/10.1021/es103207k

Atkinson, R., Aschmann, S. M., & Carter, W. P. L. (1983). Kinetics of the reactions of O3 and OH radicals with furan and thiophene at 298 ± 2 K. *International Journal of Chemical Kinetics*, *15*(1), 51-61. https://doi.org/10.1002/kin.550150106

Bierbach, A., Barnes, I., Becker, K. H., & Wiesen, E. (1994). Atmospheric chemistry of unsaturated carbonyls: butenedial, 4-oxo-2-pentenal, 3-hexene-2,5-dione, maleic anhydride, 3h-furan-2-one, and 5-methyl-3h-furan-2-one. *Environmental Science and Technology*, *28*(4), 715-729. https://doi.org/10.1021/es00053a028

Cabañas, B., Baeza, M. T., Martín, P., Salgado, S., Villanueva, F., Monedero, E., & Wirtz, K. (2005). Products and mechanism of the NO3 reaction with thiophene. *Journal of Atmospheric Chemistry*, *51*(3), 317-335. https://doi.org/10.1007/s10874-005-3580-5

Calvert, J. G., Orlando, J. J., Stockwell, W. R., & Wallington, T. J. (2015). *The Mechanisms of Reactions Infuencing Atmospheric Ozone*. https://doi.org/10.15713/ins.mmj.3

Carter, W. P. L. (2020). *Gateway to the SAPRC Mechanism Generation System*. http://mechgen.cert.ucr.edu/

Kind, I., Berndt, T., Böge, O., & Rolle, W. (1996). Gas-phase rate constants for the reaction of NO3 radicals with furan and methyl-substituted furans. *Chemical Physics Letters*, *256*(6), 679-683. https://doi.org/10.1016/0009-2614(96)00513-1

Liu, X., Jeffries, H. E., & Sexton, K. G. (1999). Atmospheric photochemical degradation of 1,4-unsaturated dicarbonyls. *Environmental Science and Technology*, *33*(23), 4212-4220. https://doi.org/10.1021/es990469y

Martín, P., Cabañas, B., Colmenar, I., Salgado, M. S., Villanueva, F., & Tapia, A. (2013). Reactivity of E-butenedial with the major atmospheric oxidants. *Atmospheric Environment*, *70*, 351-360. https://doi.org/10.1016/j.atmosenv.2013.01.041

Matsumoto, J. (2011). Kinetics of the reactions of ozone with 2,5-dimethylfuran and its atmospheric implications. *Chemistry Letters*, *40*(6), 582-583. https://doi.org/10.1246/cl.2011.582

Newland, M. J., Rea, G. J., Thüner, L. P., Henderson, A. P., Golding, B. T., Rickard, A. R., Barnes, I., & Wenger, J. (2019). Photochemistry of 2-butenedial and 4-oxo-2-pentenal under atmospheric boundary layer conditions. *Physical Chemistry Chemical Physics*, *21*(3), 1160-1171. https://doi.org/10.1039/c8cp06437g

Tapia, A., Villanueva, F., Salgado, M. S., Cabañas, B., Martínez, E., & Martín, P. (2011). Atmospheric degradation of 3-methylfuran: kinetic and products study. *Atmospheric Chemistry and Physics*, *11*(7), 3227-3241. https://doi.org/10.5194/acp-11-3227-2011

Tuazon, E. C., Atkinson, R., & Carter, W. P. L. (1985). Atmospheric chemistry of cis-and trans-3-hexene-2, 5-dione. *Environmental Science and Technology*, *19*(3), 265-269. https://doi.org/10.1021/es00133a009

Yuan, Y., Zhao, X., Wang, S., & Wang, L. (2017). Atmospheric oxidation of furan and methyl-substituted furans initiated by hydroxyl radicals. *Journal of Physical Chemistry A*, *121*(48), 9306-9319. https://doi.org/10.1021/acs.jpca.7b09741

Appendix C: Supplementary Information for Chapter 3

C.1 Listing of Mechanisms

Table C1: Model species and reactions of phenols in SAPRC-18-STD.

[a]	Rate Coefficient [b]	Reaction [c]
PHEN: phenol		
R)	4.50E-13 -2.442	;PHEN + OH = #.730 HO2 + #.100 BZO + #.170 OH + #.200 RO2C + #.700 SVPHE + #.030 AFG1 + #.170 OLEA1 + #.030 GLY + #.200 SumRO2 + #-0.730 XC
R)	4.50E-12	;PHEN + NO3 = #.130 HNO3 + #.730 HO2 + #.100 BZO + #.170 OH + #.200 RO2C + #.870 NPHE + #.030 AFG1 + #.170 OLEA1 + #.030 GLY + #.200 SumRO2 + #-1.050 XC
SVPHE: based on catechol; lumped model species for unspecified semi-volatile, non-nitrogen-containing products of the reactions of OH and NO3 with phenolic compounds		
R)	2.00E-10	;SVPHE + OH = #.600 HO2 + #.200 BZO + #.200 OH + #.400 RO2C + #.400 OTHN + #.100 AFG2A + #.100 AFG2B + #.600 OLEA1 + #.100 GLY + #.100 MGLY + #.400 SumRO2 + #-4.200 XC
R)	1.70E-10	;SVPHE + NO3 = #.400 HNO3 + #.600 HO2 + #.200 BZO + #.200 OH + #.400 RO2C + #.200 NPHE + #.400 RNNO3 + #.100 AFG2A + #.100 AFG2B + #.600 OLEA1 + #.100 GLY + #.100 MGLY + #.400 SumRO2 + #-4.600 XC
CRES: based on o-cresol; lumped model species for cresol isomers		
R)	1.60E-12 -1.985	;CRES + OH = #.785 HO2 + #.100 BZO + #.115 OH + #.200 RO2C + #.700 SVPHE + #.043 AFG2A + #.043 AFG2B + #.115 OLEA1 + #.043 GLY + #.043 MGLY + #.200 SumRO2 + #.122 XC
R)	1.40E-11	;CRES + NO3 = #.185 HNO3 + #.785 HO2 + #.100 BZO + #.115 OH + #.200 RO2C + #.815 NPHE + #.043 AFG2A + #.043 AFG2B + #.115 OLEA1 + #.043 GLY + #.043 MGLY + #.200 SumRO2 + #.132 XC
XYNL: based on 2,4-dimethylphenol; lumped model species for xylenols and higher alkylphenols		
R)	7.30E-11	;XYNL + OH = #.726 HO2 + #.100 BZO + #.174 OH + #.330 RO2C + #.570 SVPHE + #.078 AFG2A + #.078 AFG2B + #.174 OLEA1 + #.078 GLY + #.078 MGLY + #.330 SumRO2 + #1.118 XC

R)	3.12E-11	;XYNL + NO3 = #.256 HNO3 + #.726 HO2 + #.100 BZO + #.174 OH + #.330 RO2C + #.744 NPHE + #.078 AFG2A + #.078 AFG2B + #.174 OLEA1 + #.078 GLY + #.078 MGLY + #.330 SumRO2 + #.644 XC

[a] “R)” indicates the starting line of the reaction.

[b] If only have one number, it represents the constant rate constant in unit of 10^{-11} cm^3 $molecule^{-1}$ s^{-1}; If there are three numbers, this is the standard extended Arrhenius temperature dependence: $k = A \cdot \exp(-Ea/RT) \cdot T^B$, the input is A, E_a and B; If it is PF=MVK-16, represent the rate constant for the photolysis reaction calculated using the absorption cross sections and quantum yields in MVK-16.PHF file (Carter, 2020).

[c] Reactions staring with a sign “R)” in first column; More details about other model species can be found in Carter (2020).

Table C2: Model species and reactions of phenols in standard MG-PHEN.

[a]	Rate Coefficient [b]	Reaction [c]
PHENOL: phenol		
R)	4.70E-13 -2.424 0.00	;PHENOL + OH = #.49 PHENOL_P1 + #.449 HO2 + #.189 XYNL + #.126 OLEA1 + #.104 OLEA2 + #.062 BZO + #.029 OLEP + #-0.91 XC + #.49 SumRO2
R)	4.50E-12	;PHENOL + NO3 = BZO + XN
R)	9.05E-12	;PHENOL_P1 + NO = #.879 HO2 + #.879 NO2 + #.461 BUDAL + #.461 MGLY + #.418 GLY + #.407 AFG4A + #.121 RPNO3 + #.011 AFG1 + #-0.714 XC
R)	2.30E-12	;PHENOL_P1 + NO3 = HO2 + NO2 + #.524 BUDAL + #.524 MGLY + #.476 GLY + #.463 AFG4A + #.013 AFG1 + #-0.537 XC
R)	1.95E-11	;PHENOL_P1 + HO2 = #.987 RAOOH + #.013 OTHN + #-2.052 XC
R)	2.57E-12	;PHENOL_P1 + SumRO2 = SumRO2 + #.5 HO2 + #.5 OLEP + #.262 BUDAL + #.262 MGLY + #.238 GLY + #.232 AFG4A + #.006 AFG1 + #-2.268 XC
R)	1.37E-11	;PHENOL_P1 + SumRCO3 = SumRCO3 + #.8 HO2 + #.42 BUDAL + #.42 MGLY + #.38 GLY + #.37 AFG4A + #.2 OLEP + #.01 AFG1 + #-1.23 XC
CATECHOL: catechol		
R)	6.23E-11	;CATECHOL + OH = #.774 HO2 + #.386 OLEP + #.197 CATECHOL_P1 + #.132 OLEA1 + #.123 XYNL + #.087 OLEA2 + #.045 LVKS + #.03 BZO + #-2.228 XC + #.197 SumRO2
R)	6.43E-11	;CATECHOL + NO3 = BZO + XN
R)	9.13E-12	;CATECHOL_P1 + NO = #.876 HO2 + #.876 NO2 + #.438 AFG2A + #.438 MGLY + #.438 BUDAL + #.438 BACL + #.124 RPNO3 + #-1.562 XC
R)	2.30E-12	;CATECHOL_P1 + NO3 = HO2 + NO2 + #.5 AFG2A + #.5 MGLY + #.5 BUDAL + #.5 BACL + #-1.5 XC
R)	1.95E-11	;CATECHOL_P1 + HO2 = OTHN + #-6 XC
R)	2.57E-12	;CATECHOL_P1 + SumRO2 = SumRO2 + #.5 HO2 + #.5 OLEP + #.25 AFG2A + #.25 MGLY + #.25 BUDAL + #.25 BACL + #-2.75 XC
R)	1.37E-11	;CATECHOL_P1 + SumRCO3 = SumRCO3 + #.8 HO2 + #.4 AFG2A + #.4 MGLY + #.4 BUDAL + #.4 BACL + #.2 OLEP + #-2 XC
HCHDO: 2-hydroxy-3,5-cyclohexadienone		
R)	1.73E-10	;HCHDO + OH = #.989 HCHDO_P1 + #.011 BACL + #.011 HO2 + #.022 XC + #.989 SumRO2
R)	3.77E-17	;HCHDO + O3 = #.75 AFG2A + #.643 HO2 + #.613 OH + #.25 RCHO + #.137 CO2 + #1.113 XC
R)	PF=MVK-16	;HCHDO + HV = OLEP + CO + #-5 XC
R)	9.05E-12	;HCHDO_P1 + NO = #.931 NO2 + #.747 HO2 + #.542 MGLY +

		#.204 AFG2A + #.185 MACO3 + #.069 RCNO3 + #2.269 XC + #.185 SumRCO3
R)	2.30E-12	;HCHDO_P1 + NO3 = NO2 + #.802 HO2 + #.582 MGLY + #.219 AFG2A + #.198 MACO3 + #2.367 XC + #.198 SumRCO3
R)	1.95E-11	;HCHDO_P1 + HO2 = #.759 RUOOH + #.219 OTHN + #.021 BACL + #-1.266 XC
R)	2.57E-12	;HCHDO_P1 + SumRO2 = SumRO2 + #.401 HO2 + #.291 MGLY + #.202 LVKS + #.195 OLEP + #.11 AFG2A + #.099 MACO3 + #.053 BACL + #.05 AFG3 + #.103 XC + #.099 SumRCO3
R)	1.37E-11	;HCHDO_P1 + SumRCO3 = SumRCO3 + #.641 HO2 + #.466 MGLY + #.175 AFG2A + #.159 MACO3 + #.118 LVKS + #.043 BACL + #.04 AFG3 + #1.735 XC + #.159 SumRCO3
O-CRESOL: o-cresol		
R)	1.60e-12 -1.985 0.00	;O-CRESOL + OH = #.541 HO2 + #.42 O-CRESOL_P1 + #.168 OLEP + #.129 OLEA1 + #.114 XYNL + #.07 OLEA2 + #.06 LVKS + #.039 BZO + #-0.72 XC + #.42 SumRO2
R)	1.40E-11	;O-CRESOL + NO3 = BZO + XC + XN
R)	9.05E-12	;O-CRESOL_P1 + NO = #.815 HO2 + #.815 NO2 + #.389 MGLY + #.304 AFG2A + #.249 BACL + #.249 BUDAL + #.225 AFG4A + #.181 RPNO3 + #.14 GLY + #.038 BALD + #.003 RHNO3 + #-0.597 XC + #.001 XN
R)	2.30E-12	;O-CRESOL_P1 + NO3 = HO2 + NO2 + #.479 MGLY + #.374 AFG2A + #.307 BACL + #.307 BUDAL + #.277 AFG4A + #.172 GLY + #.041 BALD + #-0.502 XC
R)	2.11E-11	;O-CRESOL_P1 + HO2 = #.787 RAOOH + #.172 OTHN + #.041 ROOH + #-1.565 XC
R)	2.03E-12	;O-CRESOL_P1 + SumRO2 = SumRO2 + #.5 HO2 + #.479 OLEP + #.24 MGLY + #.187 AFG2A + #.154 BACL + #.154 BUDAL + #.139 AFG4A + #.086 GLY + #.031 BALD + #.01 XYNL + #-1.702 XC
R)	1.37E-11	;O-CRESOL_P1 + SumRCO3 = SumRCO3 + #.834 HO2 + #.418 MGLY + #.334 AFG2A + #.246 BACL + #.246 BUDAL + #.222 AFG4A + #.157 OLEP + #.138 GLY + #.041 BALD + #-0.913 XC
24M-PHEN: 2,4-dimethylphenol		
R)	7.30E-11	;24M-PHEN + OH = #.877 HO2 + #.658 OLEP + #.112 24M-PHEN_P1 + #.105 OLEA2 + #.062 XYNL + #.036 OLEA1 + #.017 LVKS + #.011 BZO + #-1.44 XC + #.112 SumRO2
R)	3.12E-11	;24M-PHEN + NO3 = BZO + #2 XC + XN
R)	9.13E-12	;24M-PHEN_P1 + NO = #.746 HO2 + #.746 NO2 + #.373 MGLY + #.291 AFG2A + #.254 RPNO3 + #.239 BACL + #.239 AFG1 + #.216 AFG4 + #.134 GLY +

		#-0.105 XC
R)	2.30E-12	;24M-PHEN_P1 + NO3 = HO2 + NO2 + #.5 MGLY + #.39 AFG2A + #.32 BACL + #.32 AFG1 + #.29 AFG4 + #.18 GLY + #-0.14 XC
R)	2.11E-11	;24M-PHEN_P1 + HO2 = #.641 RAOOH + #.359 OTHN + #-1.436 XC
R)	1.36E-12	;24M-PHEN_P1 + SumRO2 = SumRO2 + #.5 OLEP + #.5 HO2 + #.25 MGLY + #.195 AFG2A + #.16 BACL + #.16 AFG1 + #.145 AFG4 + #.09 GLY + #-1.07 XC
R)	1.37E-11	;24M-PHEN_P1 + SumRCO3 = SumRCO3 + #.894 HO2 + #.458 MGLY + #.348 AFG2A + #.29 AFG4 + #.256 BACL + #.256 AFG1 + #.18 GLY + #.106 OLEP + #-0.288 XC

[a] "R)" indicates the starting line of the reaction.

[b] If only have one number, it represents the constant rate constant in unit of 10^{-11} cm^3 $molecule^{-1}$ s^{-1}; If there are three numbers, this is the standard extended Arrhenius temperature dependence: $k = A \cdot \exp(-Ea/RT) \cdot T^B$, the input is A, E_a and B; If it is PF=MVK-16, represent the rate constant for the photolysis reaction calculated using the absorption cross sections and quantum yields in MVK-16.PHF file (Carter, 2020).

[c] Reactions staring with a sign "R)" in first column; More details about other model species can be found in Carter (2020).

Table C3: Model species and reactions of phenols in MG-PHEN-MOD.

[a]	Rate Coefficient [b]	Reaction [c]
PHENOL: phenol		
R)	4.70E-13 -2.424 0.00	;PHENOL + OH = #.95 PHENOL_A1 + #.05 BZO
R)	4.50E-12	;PHENOL + NO3 = BZO + HNO3
R)	5.10E-13	;PHENOL_A1 + O2 = #.25 PHENOL_P1 + #.75 CATECHOL + #.75 HO2
R)	3.00E-11	;PHENOL_A1 + NO2 = CATECHOL + HONO
R)	1.10E+06	;PHENOL_P1 = #.996 HCHDO + #.996 HO2 + #.004 PHENOL_P2 + #-1.992 XC + #.004 SumRO2
R)	9.05E-12	;PHENOL_P1 + NO = OLEA1 + HO2 + NO2
R)	6.82E-12	;PHENOL_P1 + HO2 = #.5 OLEA1 + #.5 HO2 + #.5 OH + #.5 RUOOH
R)	9.13E-12	;PHENOL_P2 + NO = #.876 HO2 + #.876 NO2 + #.438 AFG2A + #.438 GLY + #.438 BUDAL + #.438 MGLY + #.124 RPNO3 + #-1.124 XC
R)	2.30E-12	;PHENOL_P2 + NO3 = HO2 + NO2 + #.5 AFG2A + #.5 GLY + #.5 BUDAL + #.5 MGLY + #-1 XC
R)	1.95E-11	;PHENOL_P2 + HO2 = RAOOH + #-2 XC
R)	2.57E-12	;PHENOL_P2 + SumRO2 = SumRO2 + #.5 HO2 + #.5 OLEP + #.25 AFG2A + #.25 GLY + #.25 BUDAL + #.25 MGLY + #-2.5 XC
R)	1.37E-11	;PHENOL_P2 + SumRCO3 = SumRCO3 + #.8 HO2 + #.4 AFG2A + #.4 GLY + #.4 BUDAL + #.4 MGLY + #.2 OLEP + #-1.6 XC
CATECHOL: catechol		
R)	1.04E-10	;CATECHOL + OH = #.774 HO2 + #.386 OLEP + #.197 CATECHOL_P1 + #.132 OLEA1 + #.123 XYNL + #.087 OLEA2 + #.045 LVKS + #.03 BZO + #-2.228 XC + #.197 SumRO2
R)	9.80E-11	;CATECHOL + NO3 = BZO + XN
R)	9.13E-12	;CATECHOL_P1 + NO = #.876 HO2 + #.876 NO2 + #.438 AFG2A + #.438 MGLY + #.438 BUDAL + #.438 BACL + #.124 RPNO3 + #-1.562 XC
R)	2.30E-12	;CATECHOL_P1 + NO3 = HO2 + NO2 + #.5 AFG2A + #.5 MGLY + #.5 BUDAL + #.5 BACL + #-1.5 XC
R)	1.95E-11	;CATECHOL_P1 + HO2 = OTHN + #-6 XC
R)	2.57E-12	;CATECHOL_P1 + SumRO2 = SumRO2 + #.5 HO2 + #.5 OLEP + #.25 AFG2A + #.25 MGLY + #.25 BUDAL + #.25 BACL + #-2.75 XC
R)	1.37E-11	;CATECHOL_P1 + SumRCO3 = SumRCO3 + #.8 HO2 + #.4 AFG2A + #.4 MGLY + #.4 BUDAL + #.4 BACL + #.2 OLEP + #-2 XC
HCHDO: 2-hydroxy-3,5-cyclohexadienone		
R)	1.73E-10	;HCHDO + OH = #.989 HCHDO_P1 + #.011 BACL + #.011 HO2 + #.022 XC + #.989 SumRO2

R)	3.77E-17	;HCHDO + O3 = #.75 AFG2A + #.643 HO2 + #.613 OH + #.25 RCHO + #.137 CO2 + #1.113 XC
R)	PF=MVK-16	;HCHDO + HV = OLEP + CO + #-5 XC
R)	9.05E-12	;HCHDO_P1 + NO = #.931 NO2 + #.747 HO2 + #.542 MGLY + #.204 AFG2A + #.185 MACO3 + #.069 RCNO3 + #2.269 XC + #.185 SumRCO3
R)	2.30E-12	;HCHDO_P1 + NO3 = NO2 + #.802 HO2 + #.582 MGLY + #.219 AFG2A + #.198 MACO3 + #2.367 XC + #.198 SumRCO3
R)	1.95E-11	;HCHDO_P1 + HO2 = #.759 RUOOH + #.219 OTHN + #.021 BACL + #-1.266 XC
R)	2.57E-12	;HCHDO_P1 + SumRO2 = SumRO2 + #.401 HO2 + #.291 MGLY + #.202 LVKS + #.195 OLEP + #.11 AFG2A + #.099 MACO3 + #.053 BACL + #.05 AFG3 + #.103 XC + #.099 SumRCO3
R)	1.37E-11	;HCHDO_P1 + SumRCO3 = SumRCO3 + #.641 HO2 + #.466 MGLY + #.175 AFG2A + #.159 MACO3 + #.118 LVKS + #.043 BACL + #.04 AFG3 + #1.735 XC + #.159 SumRCO3
O-CRESOL: o-cresol		
R)	1.60E-12 -1.985 0.00	;O-CRESOL + OH = #.73 XYNL + #.73 HO2 + #.2 O-CRESOL_P1 + #.07 BZO + #-0.66 XC + #.2 SumRO2
R)	1.42E-11	;O-CRESOL + NO3 = BZO + XC + XN
R)	9.05E-12	;O-CRESOL_P1 + NO = #.811 AFG4 + #.811 GLY + #.811 HO2 + #.811 NO2 + #.189 RPNO3 + #-0.189 XC
R)	2.30E-12	;O-CRESOL_P1 + NO3 = AFG4 + GLY + HO2 + NO2
R)	2.11E-11	;O-CRESOL_P1 + HO2 = OTHN + #-5 XC
R)	3.71E-16	;O-CRESOL_P1 + SumRO2 = SumRO2 + #.5 OLEP + #.5 AFG4 + #.5 GLY + #.5 HO2 + #-1.5 XC
R)	1.37E-11	;O-CRESOL_P1 + SumRCO3 = SumRCO3 + AFG4 + GLY + HO2
24M-PHEN: 2,4-dimethylphenol		
R)	7.40E-11	;24M-PHEN + OH = #.877 HO2 + #.658 OLEP + #.112 24M-PHEN_P1 + #.105 OLEA2 + #.062 XYNL + #.036 OLEA1 + #.017 LVKS + #.011 BZO + #-1.44 XC + #.112 SumRO2
R)	3.12E-11	;24M-PHEN + NO3 = BZO + #2 XC + XN
R)	9.13E-12	;24M-PHEN_P1 + NO = #.746 HO2 + #.746 NO2 + #.373 MGLY + #.291 AFG2A + #.254 RPNO3 + #.239 BACL + #.239 AFG1 + #.216 AFG4 + #.134 GLY + #-0.105 XC
R)	2.30E-12	;24M-PHEN_P1 + NO3 = HO2 + NO2 + #.5 MGLY + #.39 AFG2A + #.32 BACL + #.32 AFG1 + #.29 AFG4 + #.18 GLY + #-0.14 XC
R)	2.11E-11	;24M-PHEN_P1 + HO2 = #.641 RAOOH + #.359 OTHN + #-1.436 XC
R)	1.36E-12	;24M-PHEN_P1 + SumRO2 = SumRO2 + #.5 OLEP + #.5 HO2 + #.25 MGLY + #.195 AFG2A + #.16 BACL + #.16 AFG1 +

R)	1.37E-11	#.145 AFG4 + #.09 GLY + #-1.07 XC ;24M-PHEN_P1 + SumRCO3 = SumRCO3 + #.894 HO2 + #.458 MGLY + #.348 AFG2A + #.29 AFG4 + #.256 BACL + #.256 AFG1 + #.18 GLY + #.106 OLEP + #-0.288 XC

[a] “R)” indicates the starting line of the reaction.

[b] If only have one number, it represents the constant rate constant in unit of 10^{-11} cm^{3} molecule^{-1} s^{-1}; If there are three numbers, this is the standard extended Arrhenius temperature dependence: $k = A \cdot \exp(-Ea/RT) \cdot T^{B}$, the input is A, E_a and B; If it is PF=MVK-16, represent the rate constant for the photolysis reaction calculated using the absorption cross sections and quantum yields in MVK-16.PHF file (Carter, 2020).

[c] Reactions staring with a sign “R)” in first column; More details about other model species can be found in Carter (2020).

Table C4: Model species and reactions of phenols in SAPRC-18-PHEN.

[a]	Rate Coefficient [b]	Reaction [c]
PHEN: phenol		
R)	4.70E-13 -2.424 0.00	;PHEN + OH = #.95 PHEN_A1 + #.05 BZO
R)	4.50E-12	;PHEN + NO3 = BZO + HNO3
R)	5.10E-13	;PHEN_A1 + O2 = #.25 PHEN_P1 + #.75 CATECHOL + #.75 HO2
R)	3.00E-11	;PHEN_A1 + NO2 = CATECHOL + HONO
R)	1.10E+06	;PHEN_P1 = #.996 HCHDO + #.996 HO2 + #.004 PHEN_P2 + #-1.992 XC + #.004 SumRO2
R)	9.05E-12	;PHEN_P1 + NO = OLEA1 + HO2 + NO2
R)	6.82E-12	;PHEN_P1 + HO2 = #.5 OLEA1 + #.5 HO2 + #.5 OH + #.5 RUOOH
R)	9.13E-12	;PHEN_P2 + NO = #.876 HO2 + #.876 NO2 + #.438 AFG2A + #.438 GLY + #.438 BUDAL + #.438 MGLY + #.124 RPNO3 + #-1.124 XC
R)	2.30E-12	;PHEN_P2 + NO3 = HO2 + NO2 + #.5 AFG2A + #.5 GLY + #.5 BUDAL + #.5 MGLY + #-1 XC
R)	1.95E-11	;PHEN_P2 + HO2 = RAOOH + #-2 XC
R)	2.57E-12	;PHEN_P2 + SumRO2 = SumRO2 + #.5 HO2 + #.5 OLEP + #.25 AFG2A + #.25 GLY + #.25 BUDAL + #.25 MGLY + #-2.5 XC
R)	1.37E-11	;PHEN_P2 + SumRCO3 = SumRCO3 + #.8 HO2 + #.4 AFG2A + #.4 GLY + #.4 BUDAL + #.4 MGLY + #.2 OLEP + #-1.6 XC
SVPHE: based on catechol; lumped model species for unspecified semi-volatile, non-nitrogen-containing products of the reactions of OH and NO3 with phenolic compounds		
R)	1.04E-10	;SVPHE + OH = #.774 HO2 + #.386 OLEP + #.197 SVPHE_P1 + #.132 OLEA1 + #.123 XYNL + #.087 OLEA2 + #.045 LVKS + #.03 BZO + #-2.228 XC + #.197 SumRO2
R)	9.80E-11	;SVPHE + NO3 = BZO + XN
R)	9.13E-12	;SVPHE_P1 + NO = #.876 HO2 + #.876 NO2 + #.438 AFG2A + #.438 MGLY + #.438 BUDAL + #.438 BACL + #.124 RPNO3 + #-1.562 XC
R)	2.30E-12	;SVPHE_P1 + NO3 = HO2 + NO2 + #.5 AFG2A + #.5 MGLY + #.5 BUDAL + #.5 BACL + #-1.5 XC
R)	1.95E-11	;SVPHE_P1 + HO2 = OTHN + #-6 XC
R)	2.57E-12	;SVPHE_P1 + SumRO2 = SumRO2 + #.5 HO2 + #.5 OLEP + #.25 AFG2A + #.25 MGLY + #.25 BUDAL + #.25 BACL + #-2.75 XC
R)	1.37E-11	;SVPHE_P1 + SumRCO3 = SumRCO3 + #.8 HO2 + #.4 AFG2A + #.4 MGLY + #.4 BUDAL + #.4 BACL + #.2 OLEP + #-2 XC
HCHDO: 2-hydroxy-3,5-cyclohexadienone		
R)	1.73E-10	;HCHDO + OH = #.989 HCHDO_P1 + #.011 BACL +

		#.011 HO2 + #.022 XC + #.989 SumRO2
R)	3.77E-17	;HCHDO + O3 = #.75 AFG2A + #.643 HO2 + #.613 OH + #.25 RCHO + #.137 CO2 + #1.113 XC
R)	PF=MVK-16	;HCHDO + HV = OLEP + CO + #-5 XC
R)	9.05E-12	;HCHDO_P1 + NO = #.931 NO2 + #.747 HO2 + #.542 MGLY + #.204 AFG2A + #.185 MACO3 + #.069 RCNO3 + #2.269 XC + #.185 SumRCO3
R)	2.30E-12	;HCHDO_P1 + NO3 = NO2 + #.802 HO2 + #.582 MGLY + #.219 AFG2A + #.198 MACO3 + #2.367 XC + #.198 SumRCO3
R)	1.95E-11	;HCHDO_P1 + HO2 = #.759 RUOOH + #.219 OTHN + #.021 BACL + #-1.266 XC
R)	2.57E-12	;HCHDO_P1 + SumRO2 = SumRO2 + #.401 HO2 + #.291 MGLY + #.202 LVKS + #.195 OLEP + #.11 AFG2A + #.099 MACO3 + #.053 BACL + #.05 AFG3 + #.103 XC + #.099 SumRCO3
R)	1.37E-11	;HCHDO_P1 + SumRCO3 = SumRCO3 + #.641 HO2 + #.466 MGLY + #.175 AFG2A + #.159 MACO3 + #.118 LVKS + #.043 BACL + #.04 AFG3 + #1.735 XC + #.159 SumRCO3

CRES: based on o-cresol; lumped model species for cresol isomers

R)	1.60E-12 -1.985 0.00	;CRES + OH = #.73 XYNL + #.73 HO2 + #.2 CRES_P1 + #.07 BZO + #-0.66 XC + #.2 SumRO2
R)	1.42E-11	;CRES + NO3 = BZO + XC + XN
R)	9.05E-12	;CRES_P1 + NO = #.811 AFG4 + #.811 GLY + #.811 HO2 + #.811 NO2 + #.189 RPNO3 + #-0.189 XC
R)	2.30E-12	;CRES_P1 + NO3 = AFG4 + GLY + HO2 + NO2
R)	2.11E-11	;CRES_P1 + HO2 = OTHN + #-5 XC
R)	3.71E-16	;CRES_P1 + SumRO2 = SumRO2 + #.5 OLEP + #.5 AFG4 + #.5 GLY + #.5 HO2 + #-1.5 XC
R)	1.37E-11	;CRES_P1 + SumRCO3 = SumRCO3 + AFG4 + GLY + HO2

XYNL: based on 2,4-dimethylphenol; lumped model species for xylenols and higher alkylphenols

R)	7.40E-11	;XYNL + OH = #.877 HO2 + #.658 OLEP + #.112 XYNL_P1 + #.105 OLEA2 + #.062 XYNL + #.036 OLEA1 + #.017 LVKS + #.011 BZO + #-1.44 XC + #.112 SumRO2
R)	3.12E-11	;XYNL + NO3 = BZO + #2 XC + XN
R)	9.13E-12	;XYNL_P1 + NO = #.746 HO2 + #.746 NO2 + #.373 MGLY + #.291 AFG2A + #.254 RPNO3 + #.239 BACL + #.239 AFG1 + #.216 AFG4 + #.134 GLY + #-0.105 XC
R)	2.30E-12	;XYNL_P1 + NO3 = HO2 + NO2 + #.5 MGLY + #.39 AFG2A + #.32 BACL + #.32 AFG1 + #.29 AFG4 + #.18 GLY + #-0.14 XC
R)	2.11E-11	;XYNL_P1 + HO2 = #.641 RAOOH + #.359 OTHN + #-1.436 XC
R)	1.36E-12	;XYNL_P1 + SumRO2 = SumRO2 + #.5 OLEP + #.5 HO2 +

R)	1.37E-11	#.25 MGLY + #.195 AFG2A + #.16 BACL + #.16 AFG1 + #.145 AFG4 + #.09 GLY + #-1.07 XC ;XYNL_P1 + SumRCO3 = SumRCO3 + #.894 HO2 + #.458 MGLY + #.348 AFG2A + #.29 AFG4 + #.256 BACL + #.256 AFG1 + #.18 GLY + #.106 OLEP + #-0.288 XC

[a] "R)" indicates the starting line of the reaction.

[b] If only have one number, it represents the constant rate constant in unit of 10^{-11} cm^3 $molecule^{-1}$ s^{-1}; If there are three numbers, this is the standard extended Arrhenius temperature dependence: $k = A \cdot \exp(-Ea/RT) \cdot T^B$, the input is A, E_a and B; If it is PF=MVK-16, represent the rate constant for the photolysis reaction calculated using the absorption cross sections and quantum yields in MVK-16.PHF file (Carter, 2020).

[c] Reactions staring with a sign "R)" in first column; More details about other model species can be found in Carter (2020).

C.2 Additional Results

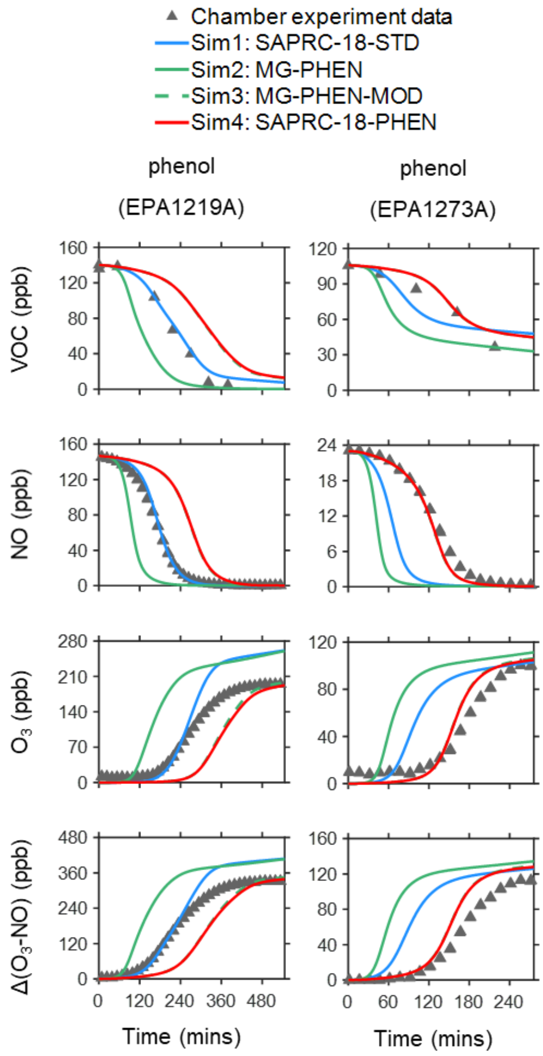

Figure C1: Comparison of chamber data (triangles) and model simulation results (lines) for the photooxidation of phenol in the presence of NO_x.

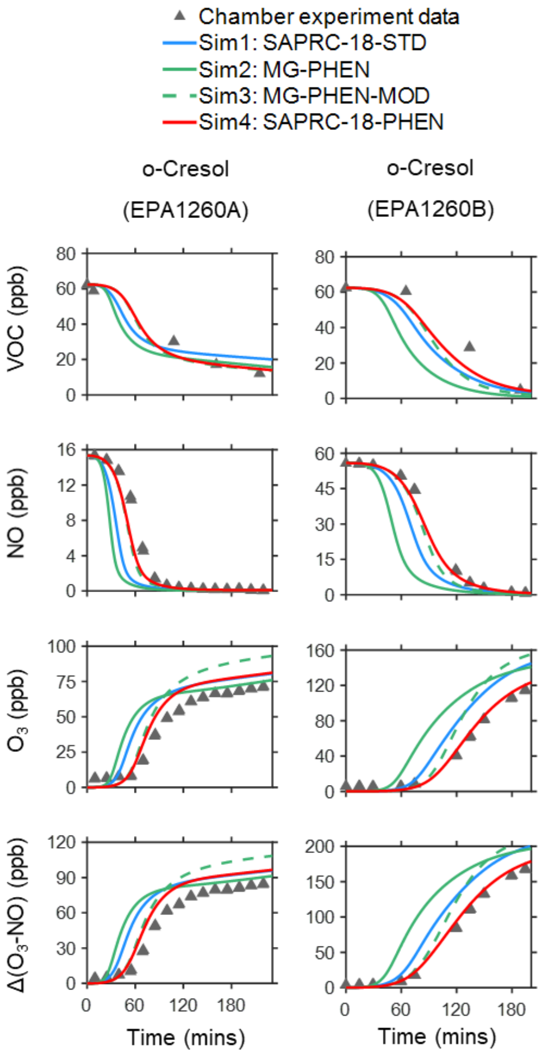

Figure C2: Comparison of chamber data (triangles) and model simulation results (lines) for the photooxidation of o-cresol in the presence of NO_x.

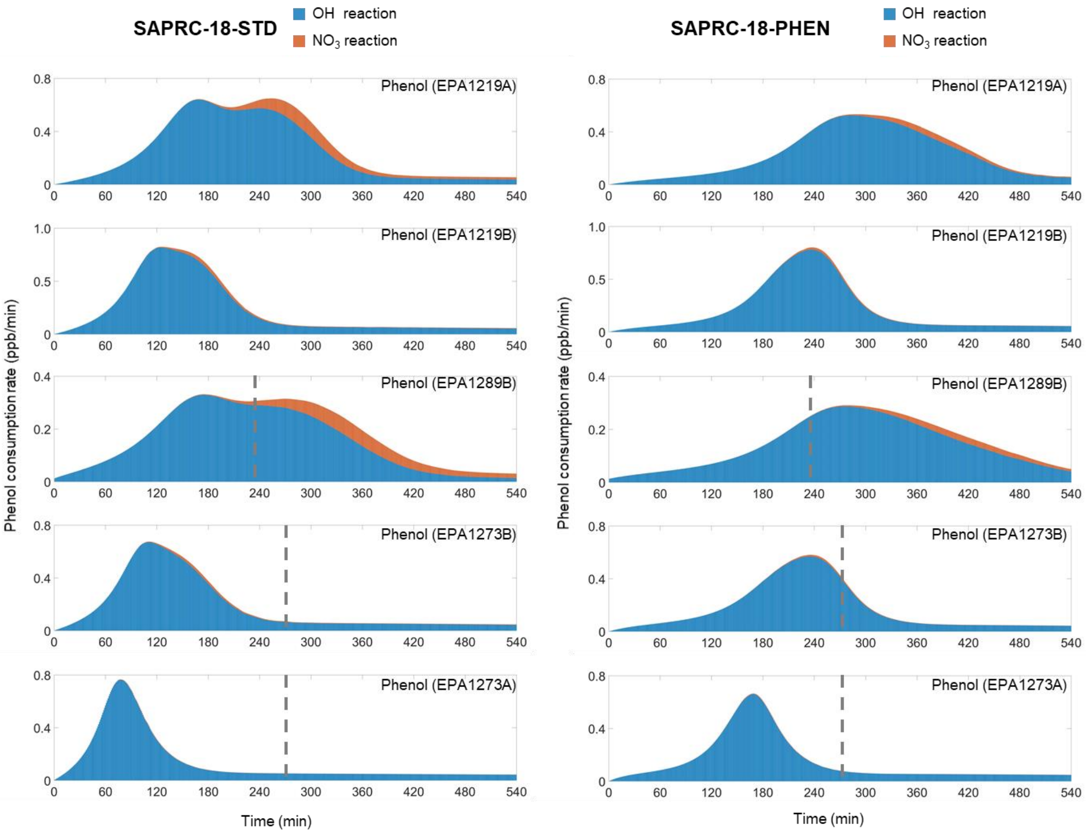

Figure C3: Time dependence for the consumption rate of phenol in SAPRC-18-STD and SAPRC-18-PHEN simulations.

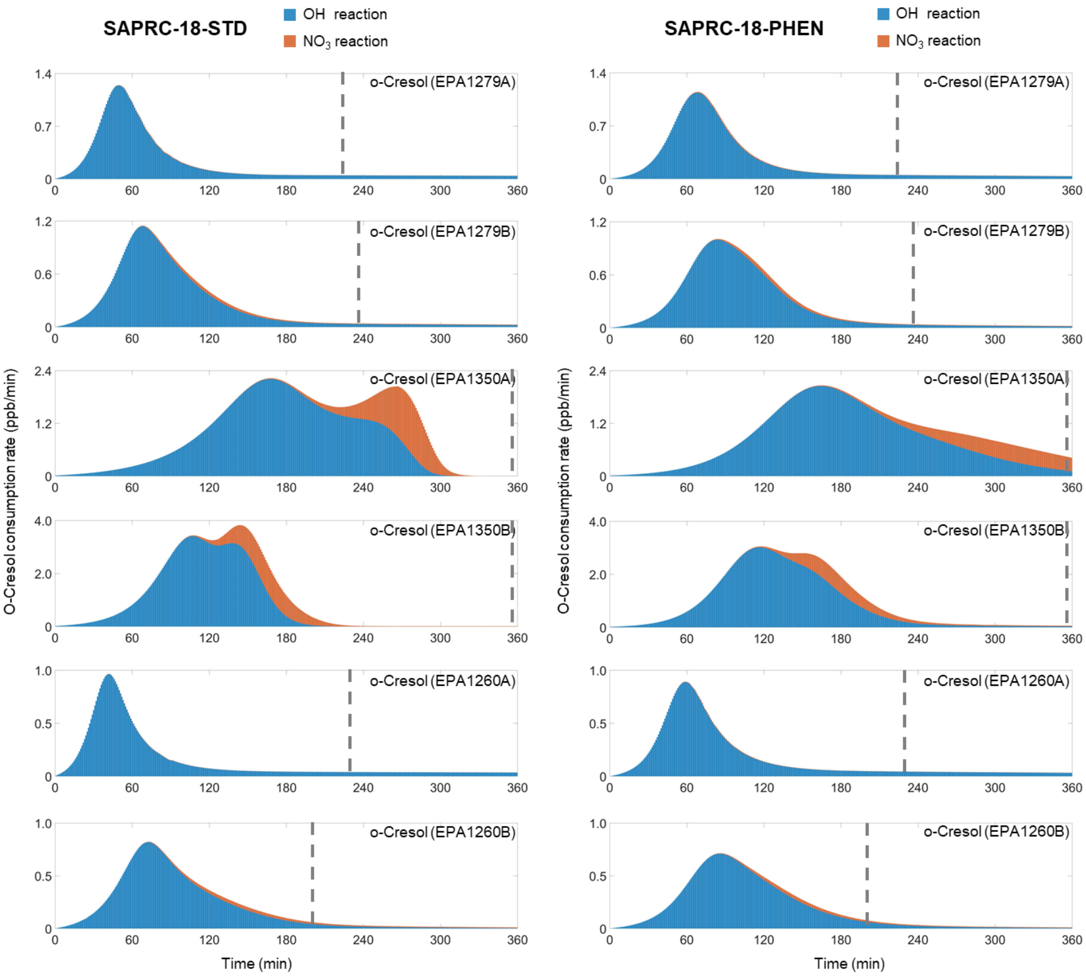

Figure C4: Time dependence for the consumption rate of o-cresol in SAPRC-18-STD and SAPRC-18-PHEN simulations.

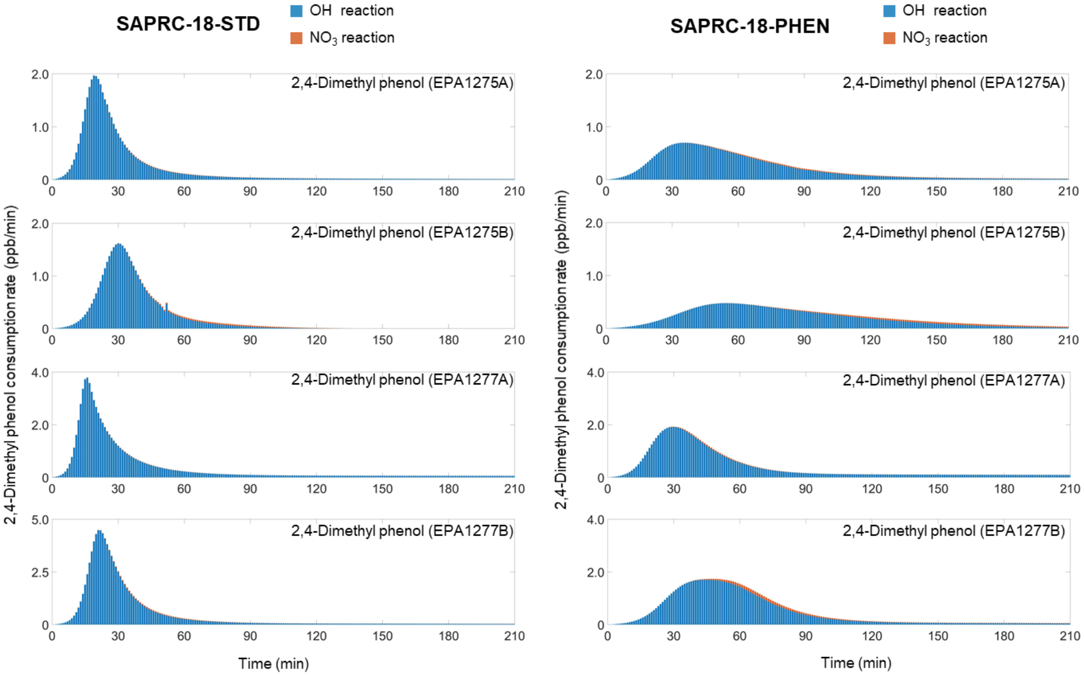

Figure C5: Time dependence for the consumption rate of 2,4-DMP in SAPRC-18-STD and SAPRC-18-PHEN simulations.

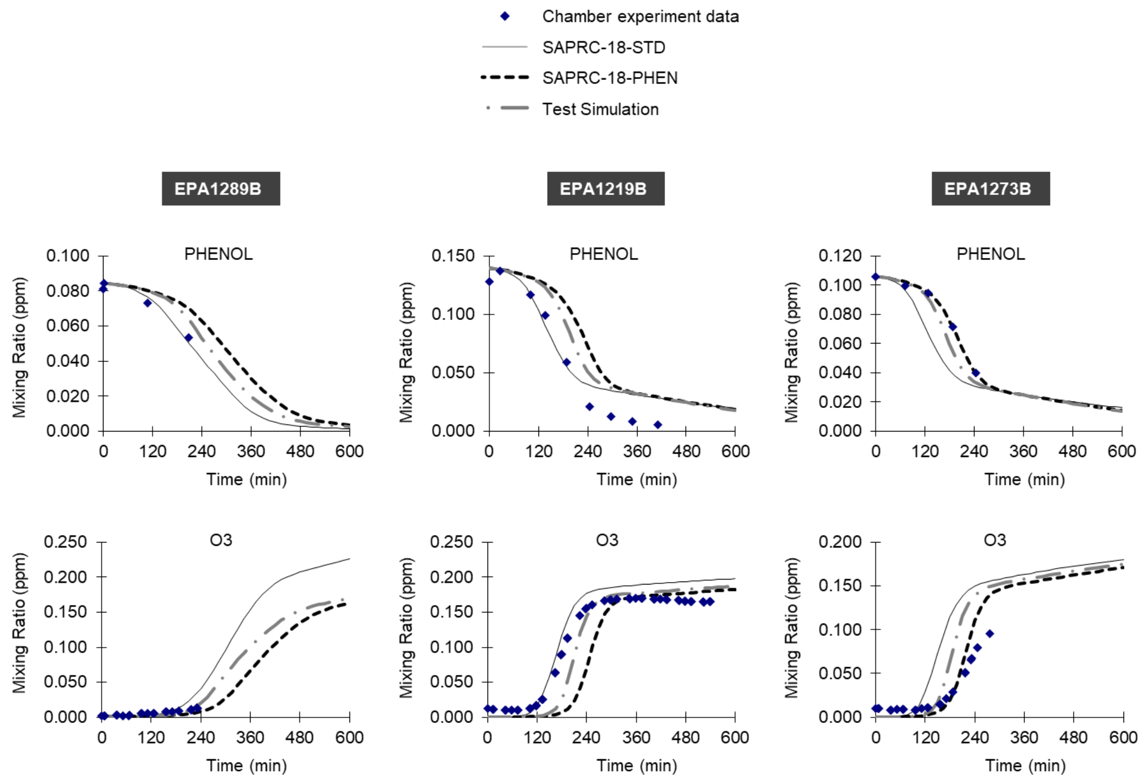

Figure C6: Comparison of chamber data (diamond) and model simulation results (lines) for the photooxidation of phenol in the presence of NO_x.

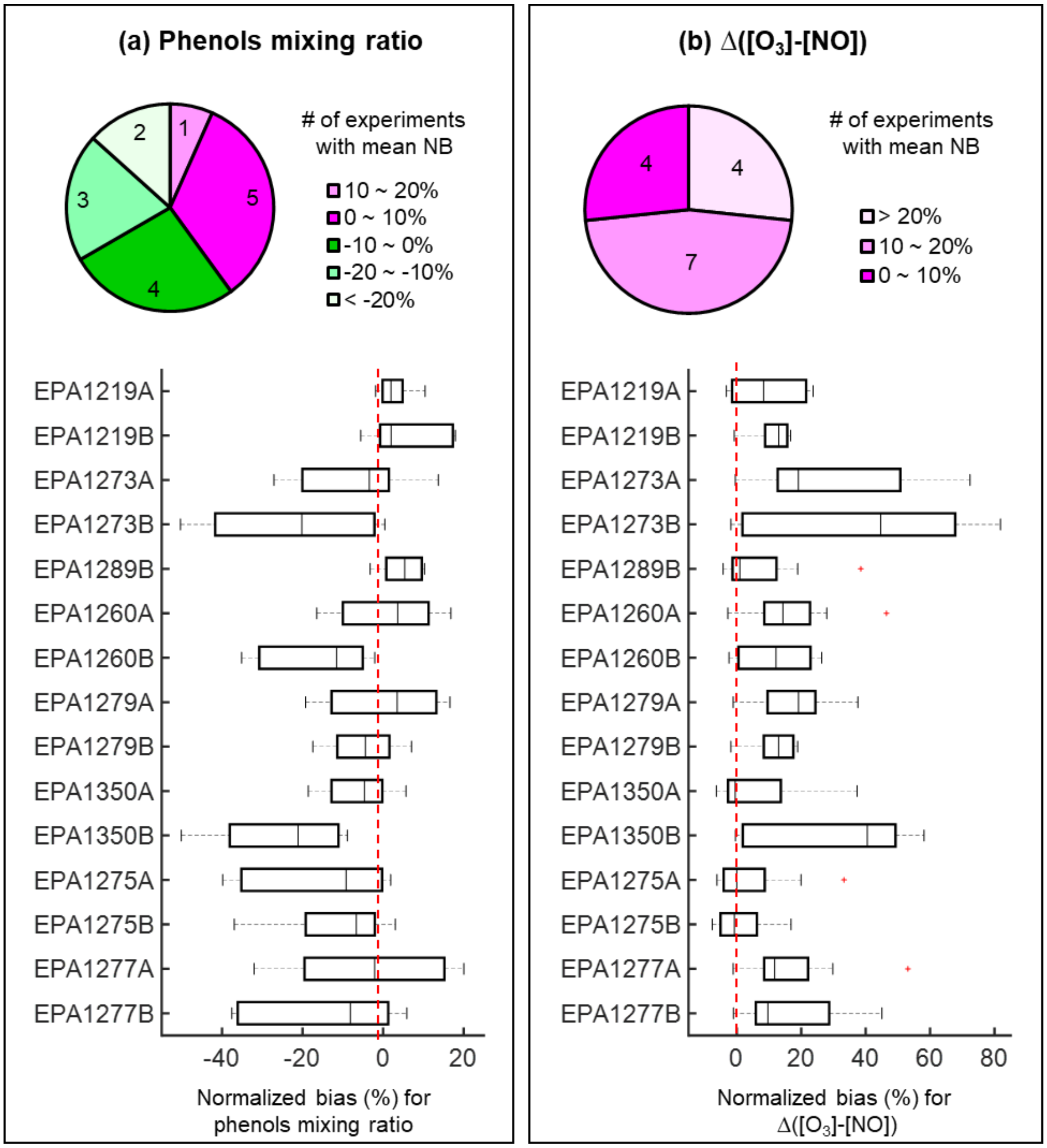

Figure C7: Normalized bias for the standard SAPRC-18-STD mechanism: a) phenols mixing ratios; b) Δ([O3]-[NO]). Pie chart: classification of mean normalized bias by the number of experiments. Box-and-whisker plots: distribution and median of the normalized bias over the duration of the experiment.

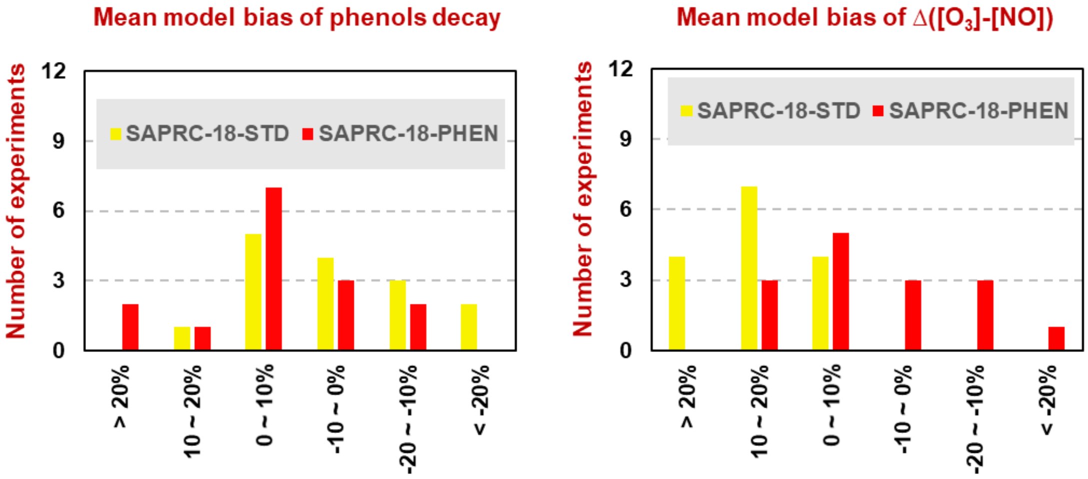

Figure C8: Classification of mean normalized bias by the number of experiments for a) phenols mixing ratios; b) Δ([O3]-[NO]) values.

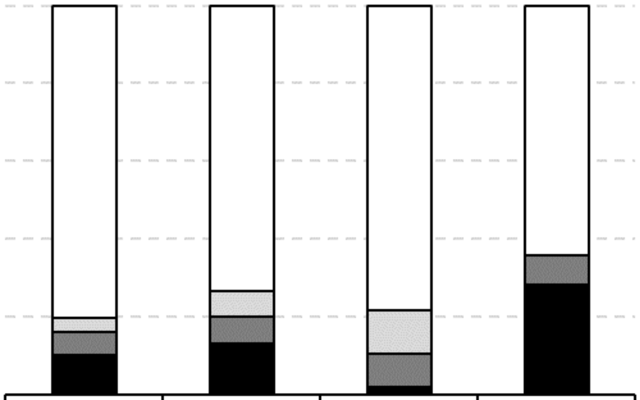

	Phenol	o-Cresol	m-Cresol	p-Cresol
□ Dihydroxybenzene	0.804	0.734	0.783	0.641
□ Benzoquinone	0.037	0.068	0.113	0
▨ Nitrophenol	0.058	0.068	0.087	0.076
■ Other	0.101	0.13	0.017	0.283

Figure C9: Molar yields of major products in the OH-initiated oxidation of phenols at (298±2) K and 1000 mbar calculated based on Olariu et al. (2002).

References

Carter, W. P. L. (2020). *Documentation of the SAPRC-18 Mechanism; Report to California Air Resources Board Contract No. 11-761, May, 2020*. https://intra.engr.ucr.edu/~carter/SAPRC/18/

Olariu, R. I., Klotz, B., Barnes, I., Becker, K. H., & Mocanu, R. (2002). FT-IR study of the ring-retaining products from the reaction of OH radicals with phenol, o-, m-, and p-cresol. *Atmospheric Environment*, *36*(22), 3685-3697. https://doi.org/10.1016/S1352-2310(02)00202-9

Appendix D: Supplementary Information for Chapter 4

Table D1: Weighted fractions of total peroxy radical bimolecular reactions of each type, calculated based on SAPRC simulations.

Expt.	$[HC]_0$ (ppb)	$[HC]_0/[NO_x]_0$ (ppbv/ppbv)	SOA Yield	Total RO_2 [a] (ppb)	Fraction of total RO_2 Reaction			
					NO	HO_2	NO3	RO_2s [b]
WO1	7	7	0.15	15	0.06	0.94	0.00	0.00
WO2	9	9	0.08	18	0.04	0.96	0.00	0.00
WO3	28	28	0.27	54	0.04	0.95	0.00	0.00
WO4	57	57	0.28	99	0.05	0.92	0.00	0.03
WO5	120	120	0.27	141	0.05	0.79	0.00	0.16
WO6	223	223	0.19	165	0.04	0.66	0.00	0.30
W1	7	0.08	0.36	37	0.96	0.04	0.00	0.00
W2	25	0.18	0.33	114	0.98	0.02	0.00	0.00
W3	32	0.51	0.64	139	0.90	0.10	0.00	0.00
W4	43	5.91	0.41	110	0.49	0.50	0.00	0.01
W5	60	0.64	0.60	249	0.91	0.09	0.00	0.00
W6	131	1.33	0.59	445	0.84	0.14	0.00	0.01
W7	172	2.88	0.52	455	0.74	0.21	0.00	0.04

[a] Total RO_2 is calculated as the summation of RO_2 that undergo bimolecular reactions.
[b] "RO2s" refers to the sum of RO_2 reacting with RO_2 and with RCO_3.

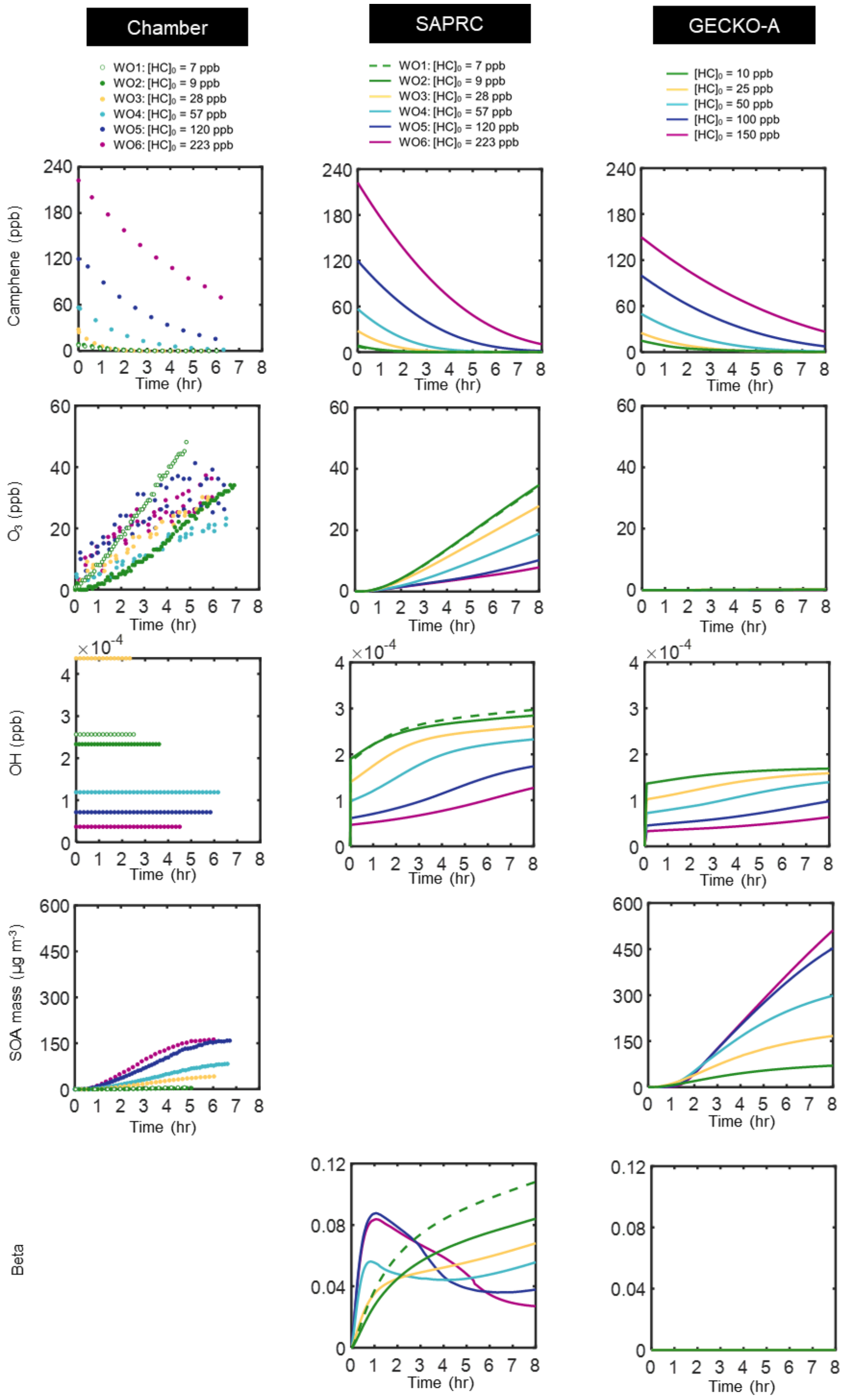

Figure D1a: Comparison of chamber data (circles) and model simulation results (lines) for the photo-oxidation of camphene (without added NO$_x$). Two blank figures were due to measurement and modeling limitation.

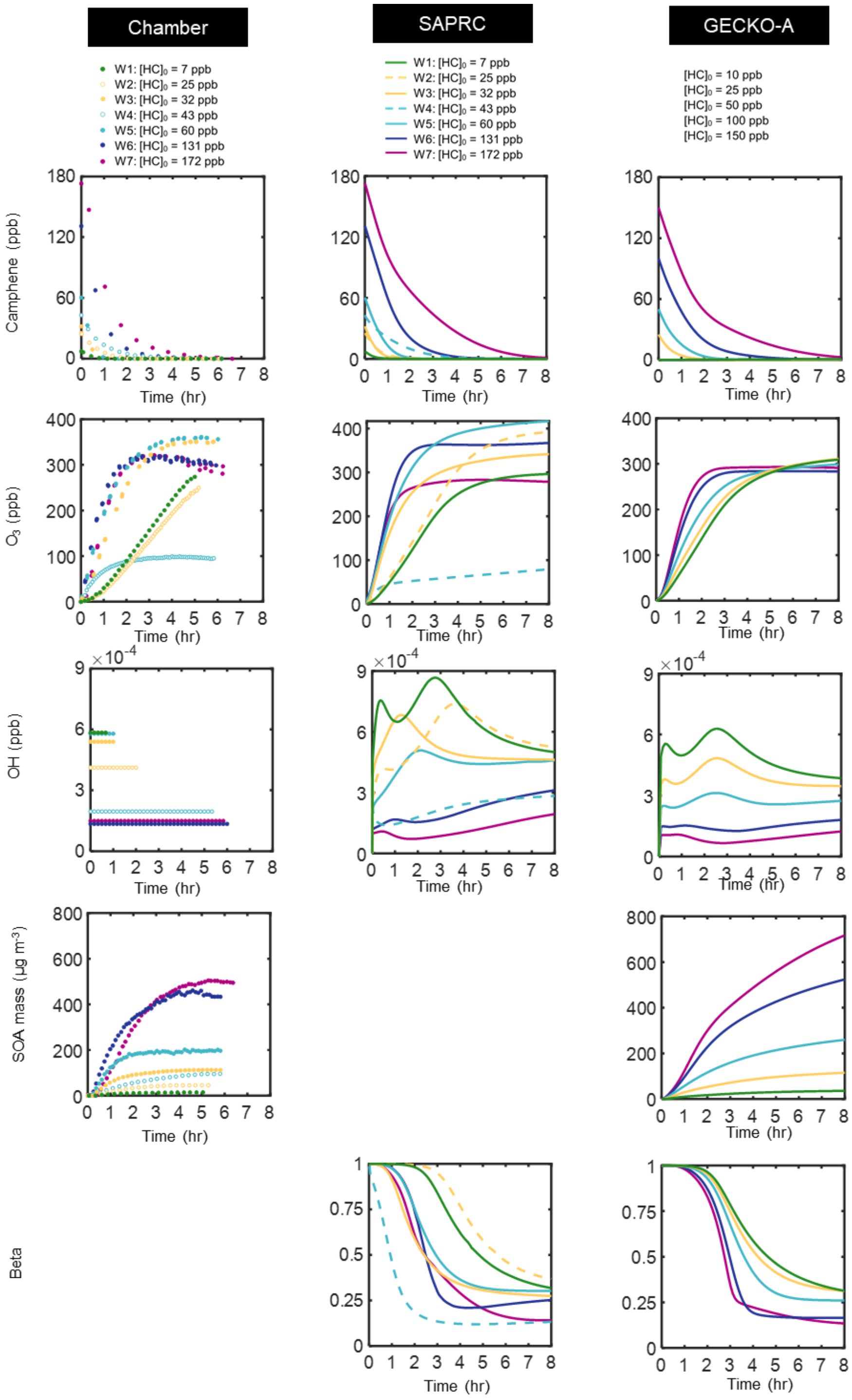

Figure D1b: Comparison of chamber data (circles) and model simulation results (lines) for the photo-oxidation of camphene (without added NO_x). Two blank figures were due to measurement and modeling limitation.

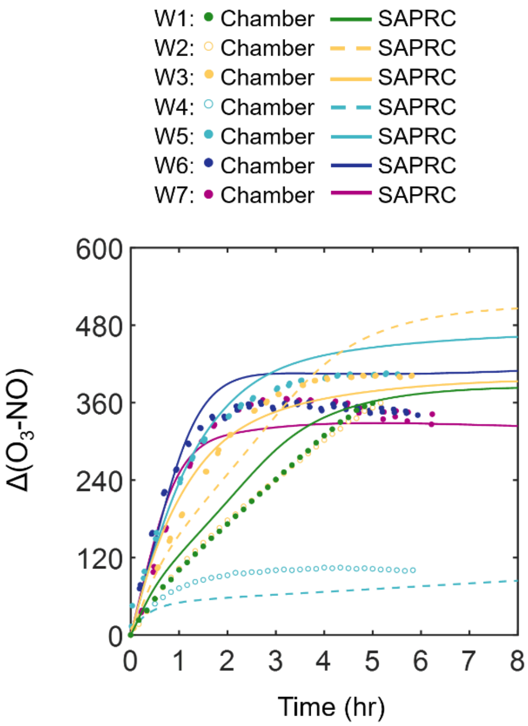

Figure D2: Comparison of the chamber data (circles) and SAPRC model simulation results (lines) for camphene photooxidation experiments with added NO$_x$.

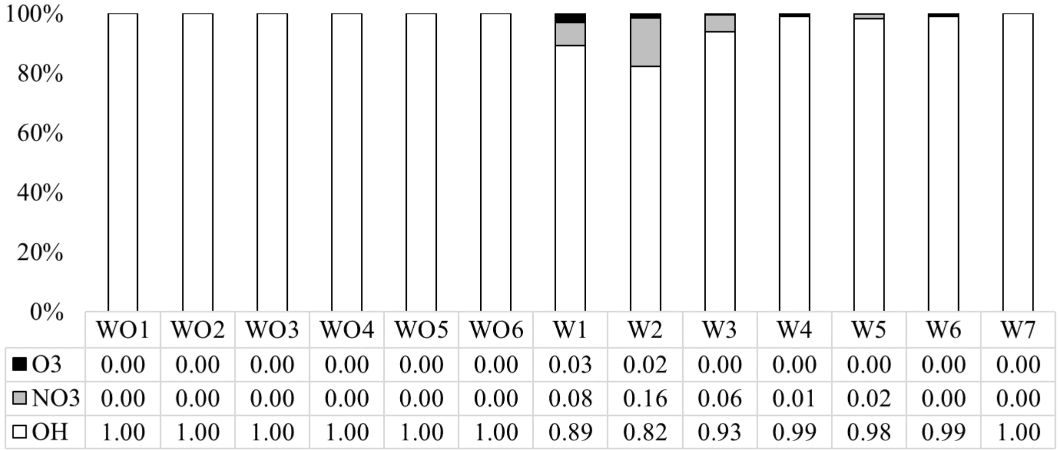

	WO1	WO2	WO3	WO4	WO5	WO6	W1	W2	W3	W4	W5	W6	W7
■ O3	0.00	0.00	0.00	0.00	0.00	0.00	0.03	0.02	0.00	0.00	0.00	0.00	0.00
▨ NO3	0.00	0.00	0.00	0.00	0.00	0.00	0.08	0.16	0.06	0.01	0.02	0.00	0.00
□ OH	1.00	1.00	1.00	1.00	1.00	1.00	0.89	0.82	0.93	0.99	0.98	0.99	1.00

Figure D3: Fractional precursor reactivity for each experiment (with added NO$_x$ and without added NO$_x$) based on SAPRC simulations).

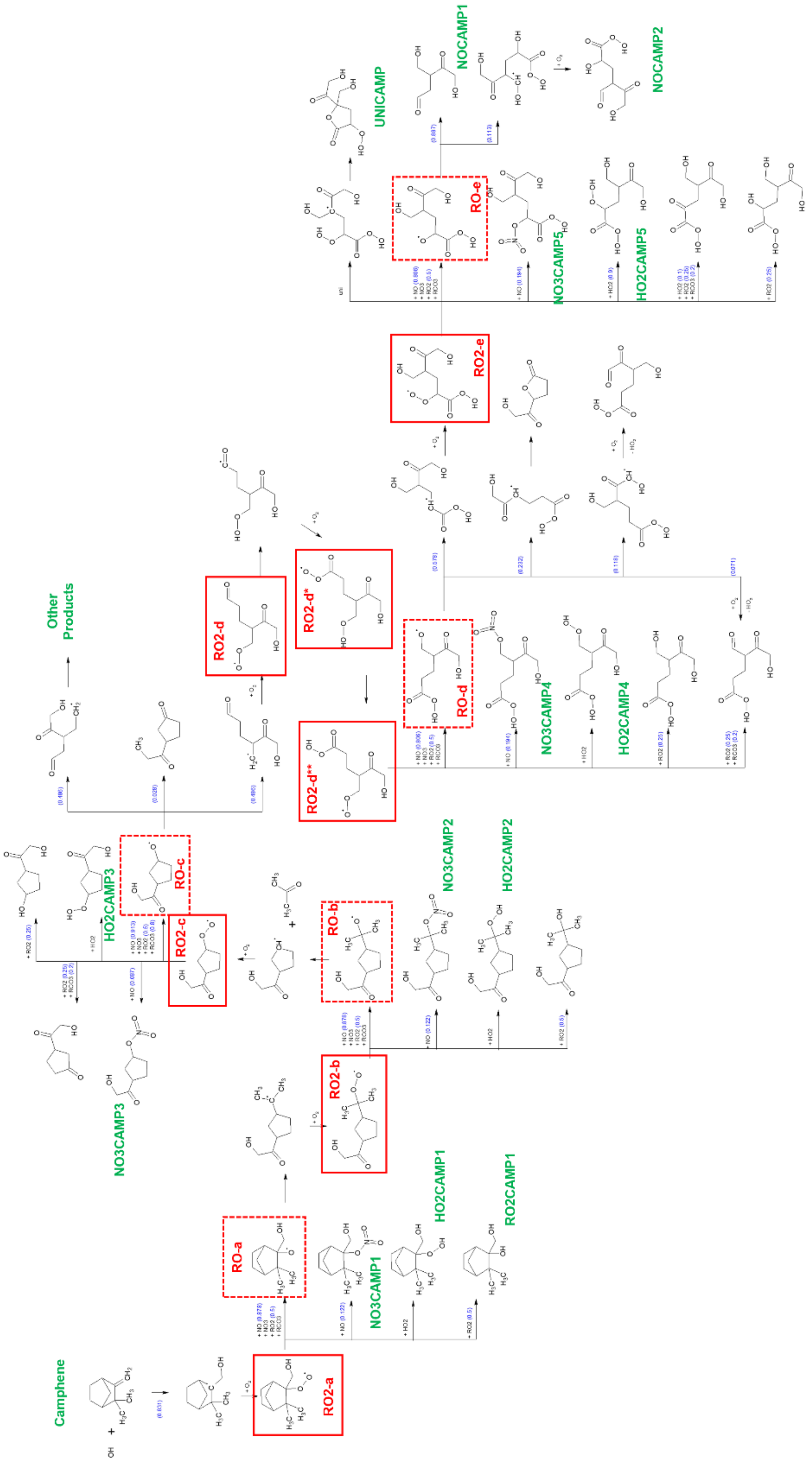

Figure D4: Detailed schematic of the OH-initiated oxidation of camphene at 298 K and atmospheric pressure with added NO$_x$ as in SAPRC.

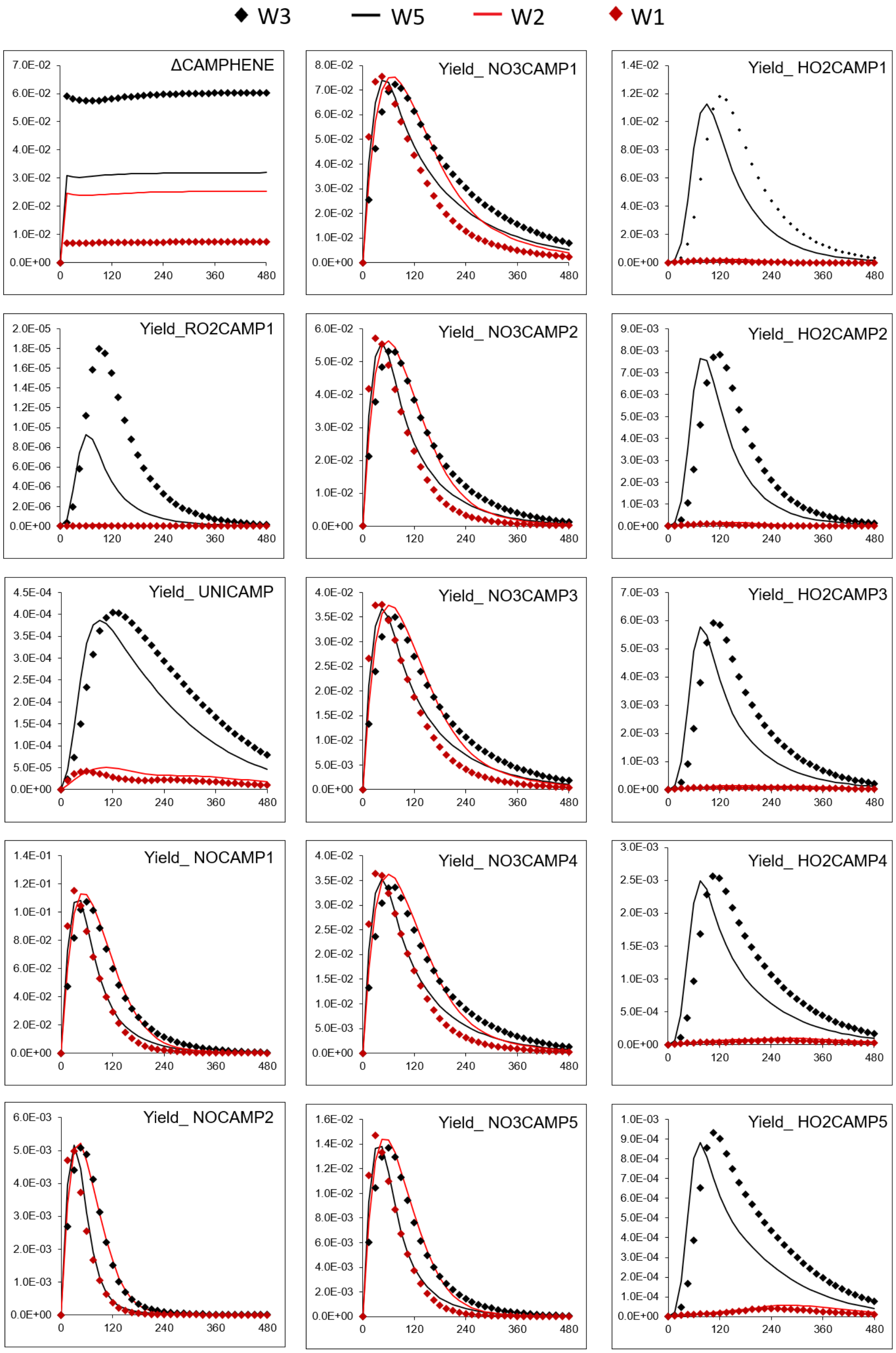

Figure D5: Time-resolved product yield distributions for W3, W5, W1 and W2 predicted by SAPRC. The yield of the product is calculated as: Yield = Δ[product] / Δ[camphene].

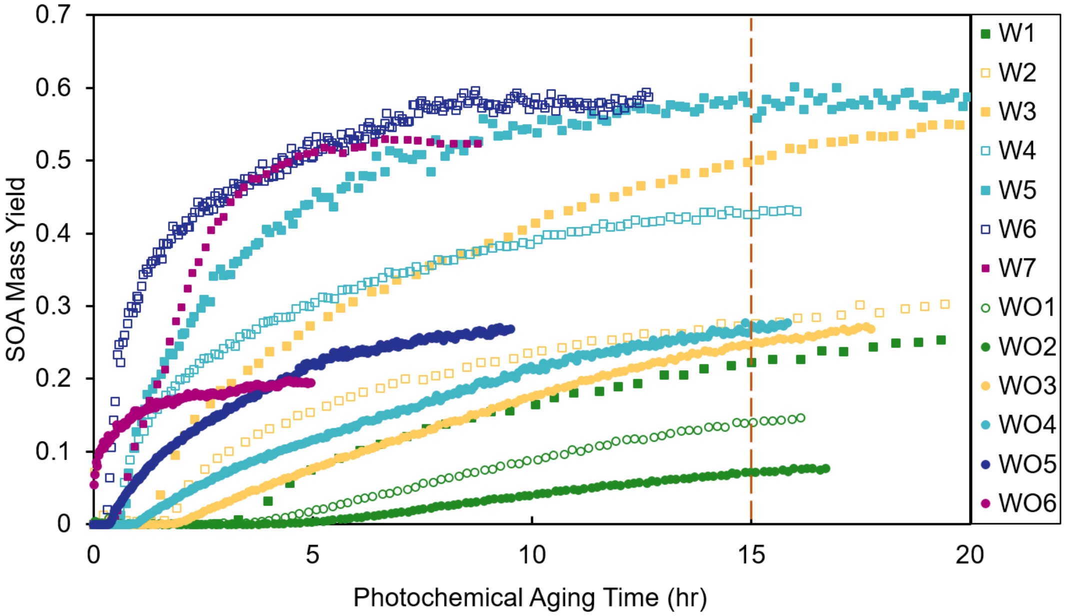

Figure D6: SOA mass yields as functions of photochemical aging time in experiments with added NOx (squares); and experiments without added NOx (circles) with cutoff line at 15 hours to highlight a single aging time across experiments.